

An Extended Modal Approach for Nonlinear Aeroelastic Simulations of Highly Flexible Aircraft Structures

vorgelegt von
Dipl.-Ing.
Markus Raimund Ritter
ORCID: 0000-0003-3828-0397

von der Fakultät V – Verkehrs- und Maschinensysteme
der Technischen Universität Berlin
zur Erlangung des akademischen Grades

Doktor der Ingenieurwissenschaften
- Dr.-Ing. -

genehmigte Dissertation

Promotionsausschuss:

Vorsitzender: Prof. Dr.-Ing. Dieter Peitsch
Gutachter: Prof. Dr.-Ing. Robert Luckner
Gutachter: Prof. Carlos E. S. Cesnik
Gutachter: Prof. Dr.-Ing. Wolf-Reiner Krüger
Gutachter: Prof. Dr.-Ing. Lorenz Tichy

Tag der wissenschaftlichen Aussprache: 17. Oktober 2018

Berlin 2019

Acknowledgements

This thesis is the result of a collaboration between the Active Aeroelasticity and Structures Research Laboratory (A²SRL) of the University of Michigan, the Department of Flight Mechanics, Flight Control and Aeroelasticity of the Technische Universität Berlin, and the DLR Institute of Aeroelasticity.

I would like to first thank Prof. Robert Luckner for his support of this thesis. I have always enjoyed his pleasant way and the discussions about flight mechanics which helped me to get a better understanding of the X-HALE's involved flight dynamics characteristics.

To my supervisor Prof. Carlos E. S. Cesnik from the University of Michigan, who gave me the opportunity for a wonderful collaboration and who has since kept on supporting and pushing the subject of this thesis. I am very thankful for the time he spend with reviewing our papers and the countless Telecons and Emails. Hopefully, we'll have more common research projects and publications in future whenever opportunity permits. I am especially grateful to the support of Prof. Cesnik's students at the A²SRL during the two internships in Ann Arbor. Ryan Clock, Ryan Kitson, Jessica Jones, Renato R. Medeiros and Patrícia Teixeira not only introduced me to the American culture and the lovely city of Ann Arbor, but also invested hard work and time in technical discussions and the generation of aeroelastic reference data with UM/NAST.

For Prof. Wolf Krüger, who always took the time to discuss problems of this work and pushed me to finish this document. I am thankful for his personable manner and the way he shapes and develops our department and its colleagues.

Prof. Lorenz Tichy was willing to help out as fourth supervisor on short notice. I am very pleased with his help and the support of this work.

I would like to thank my colleagues at the Institute of Aeroelasticity and especially at the Loads Analysis and Aeroelastic Design department for their great support and motivation. Furthermore, I would like to mention the help of Johannes Dillinger, Felix Wienke, and David Quero-Martín.

I am forever grateful to my wife Carmen and my children Nicolas and Jannis for accepting the countless hours I spend in the office at the evening and on the weekend. The work had definitely not been possible without their immeasurable support.

The work is dedicated to my parents. Their support not only made my studies possible, but also promoted my passion of building and flying radio controlled model aircraft as a youth. This hobby took me to my current profession and certainly to this thesis, too.

Abstract

Some classes of aircraft are characterized by highly flexible wings undergoing large structural deformations in steady and maneuvering flight. In most cases this flexibility is the result of a high aspect ratio, which is in turn forced by dedicated design criteria such as the reduction of the induced drag. Prominent examples for such configurations are High Altitude Long Endurance (HALE) aircraft as well as modern, high performance sailplanes of the Open Class. The design and the analysis of highly flexible aircraft put high demands on the methods and tools employed. Multidisciplinary analysis taking into account aerodynamics, flight mechanics, and structural dynamics is indispensable where nonlinearities due to large rigid-body motions and large structural deflections are inherent in each of these disciplines.

For the structural part, only few methods exist to date for the calculation of general aircraft structures subjected to large deformations. Commercial finite element solvers are mostly limited to clamped structures in their nonlinear solution capabilities, i.e. concurrent rigid-body motions are inadmissible. On the other hand, sophisticated methods incorporating nonlinear rigid-body as well as nonlinear elastic motions have been developed mainly for beam-type structures but not for complex and three-dimensional models.

In aeroelasticity, the modal approach is a well-established and elegant method for simulating and analyzing the dynamic behavior of aircraft structures. However, its applicability is limited to small structural deformations and an extension into the nonlinear regime with respect to large geometric deflections would be desirable.

The goal of this thesis is thus the extension of the modal approach towards large geometric deformations of highly flexible aircraft structures. The extensions include stiffness terms of higher order as well as higher-order modal components for the calculation of the nonlinear displacement field. It is shown that the method is applicable to different kinds of structural models composed of beam and shell elements with anisotropic material properties. Furthermore, an integrated set of equations based on these extensions is presented that allows the nonlinear time-domain simulation of the free-flying elastic aircraft in steady and unsteady maneuvering flight with large structural deformations.

In the first part of the thesis, the two extensions are presented in detail. The linear relation between load and structural displacements given in the classical modal approach is extended by generalized stiffness terms that depend quadratically and cubically on the generalized coordinates. The higher-order stiffness terms are derived by a series expansion of the strain energy of the structure which is formulated as a nonlinear function of deformation. The linear transformation between modal and Euclidean space by the eigenvectors of the structure is extended by higher (second-, third-, and fourth-) order mode components to approximate the geometrically nonlinear displacement field. The higher-order stiffness and mode components of the structure are determined in a preprocessing step where a series of nonlinear static solutions are

generated using a commercial finite element solver. Higher-order polynomials are fitted to the solutions, the polynomial coefficients then correspond to the higher-order components.

The second part introduces the extensions described above into the governing equations of motion of the free-flying elastic aircraft. The governing equations are derived using Lagrange's equations of the second kind where particular attention is paid to admit as few assumptions as possible. One widely applied assumption in aeroelastic analysis of free-flying aircraft is the mean axes condition to inertially decouple rigid-body and elastic degrees of freedom. This assumption requires the frequencies of the typical rigid-body and elastic modes of the aircraft to be largely separated and is limited to small structural deformations. By contrast, flight dynamics of highly flexible aircraft is characterized by strong inertial coupling between flight mechanic and elastic degrees of freedom due to low structural frequencies. Consequently, the governing equations derived in this thesis consider inertial coupling between rigid-body and elastic motions.

The third part presents applications of the method to three different test cases with increasing complexity. First, the basics of the method are outlined by a simple beam structural model in static structural response. The second test case is a slender wing box represented by a full 3D finite element model with anisotropic materials. The third test case is the very flexible *X-HALE* unmanned aerial vehicle from the University of Michigan. Static structural and aeroelastic responses as well as free-flight maneuver simulations with unsteady excitation of the aircraft by gust and tail inputs demonstrate further capabilities and the limits of the method.

Zusammenfassung

Einige Flugzeugkonfigurationen sind durch hochflexible Tragflügel, die zu großen strukturellen Deformationen in stationären und beschleunigten Flugzuständen führen, gekennzeichnet. In den meisten Fällen ist diese Flexibilität das Resultat einer hohen Streckung, die wiederum durch bestimmte Auslegungskriterien vorgegeben wird, wie beispielsweise die Reduzierung des induzierten Widerstandes. Bekannte Beispiele für derartige Konfigurationen sind *High Altitude Long Endurance* Flugzeuge sowie moderne Hochleistungssegelflugzeuge der offenen Klasse.

Die Auslegung und Analyse dieser hochflexiblen Flugzeuge stellen hohe Anforderungen an die verwendeten Methoden und Programme. So sind multidisziplinäre Analysen mit Berücksichtigung der Aerodynamik, Flugmechanik und Strukturmechanik unabdingbar. Hierbei sind Nichtlinearitäten aufgrund großer Starrkörperbewegungen und großer elastischer Deformationen inhärent in jeder der Disziplinen.

Für die Strukturmechanik stehen gegenwärtig allerdings nur wenige Methoden zur Berechnung großer Deformationen allgemeiner Strukturen zur Verfügung. Kommerzielle Finite-Elemente-Programme können nichtlineare Analysen meist nur für eingespannte Systeme durchführen, d. h. gleichzeitige Starrkörperbewegungen sind unzulässig. Andererseits sind Methoden, die nichtlineare Starrkörper- und elastische Bewegungen berücksichtigen, fast ausschließlich für balkenartige Strukturen und nicht für komplexe Modelle entwickelt worden.

Der Modalansatz stellt für die Aeroelastik eine etablierte und elegante Methode zur Simulation und Analyse des dynamischen Verhaltens von Flugzeugstrukturen dar. Seine Anwendbarkeit ist allerdings auf kleine strukturelle Deformationen beschränkt. Eine Erweiterung in den nichtlinearen Bereich bezüglich großer Deformationen wäre daher wünschenswert.

In Folge dessen ist das Ziel dieser Arbeit die Erweiterung des Modalansatzes zur Berücksichtigung großer Deformationen von hochflexiblen Flugzeugstrukturen. Eine Erweiterung sind generalisierte Steifigkeitsterme höherer Ordnung, eine andere sind Modekomponenten höherer Ordnung zur Berechnung des nichtlinearen Verschiebungsfeldes. Es wird gezeigt, dass die Methode auf verschiedene Arten von Strukturmodellen bestehend aus Balken- und Schalenelementen mit anisotropen Materialeigenschaften anwendbar ist. Weiterhin wird ein Satz an Gleichungen vorgestellt, der die nichtlineare Simulation von stationären und instationären Manövern des freifliegenden elastischen Flugzeuges mit großen strukturellen Deformationen im Zeitbereich ermöglicht.

Im ersten Teil der vorliegenden Arbeit werden die zwei Erweiterungen ausführlich erläutert. Die dem klassischen Modalansatz zugrunde liegende lineare Beziehung zwischen Last und struktureller Verformung wird um generalisierte Steifigkeitsterme erweitert, die quadratisch und kubisch von den generalisierten Koordinaten abhängen. Die Steifigkeitsterme höherer Ordnung werden von einer Reihenentwicklung der Dehnungsenergie abgeleitet, welche als nichtlineare Funktion der Deformationen formuliert ist. Die lineare Abbildung zwischen modalem und euklidischem Raum mittels der strukturellen Eigenvektoren wird um Modekomponen-

ten höherer (zweiter, dritter, vierter) Ordnung zur Approximation des geometrisch nichtlinearen Verschiebungsfeldes erweitert. Die genannten Steifigkeits- und Modekomponenten höherer Ordnung des Strukturmodells werden im Preprocessing mittels einer Serie von statischen, geometrisch nichtlinearen Lösungen, die mit einem kommerziellen Finite-Elemente-Programm erzeugt werden, bestimmt. Schließlich werden diese Lösungen durch Polynome höherer Ordnung approximiert; die Polynomkoeffizienten entsprechen folglich den Steifigkeits- und Modekomponenten höherer Ordnung.

Im zweiten Teil werden die genannten Erweiterungen in die Bewegungsgleichungen des freifliegenden elastischen Flugzeuges übernommen, welche mit den Lagrangeschen Gleichungen zweiter Art hergeleitet werden. Hierbei sollen so wenig Annahmen wie möglich eingeräumt werden. Für aeroelastische Analysen freifliegender Flugzeuge weit verbreitet ist die *mean axes* Annahme zur Entkopplung von Starrkörper- und elastischer Bewegung durch Vernachlässigung bestimmter Inertiallasten. Diese Annahme bedingt einen großen Frequenzabstand von flugmechanischen und elastischen Eigenbewegungsformen und ist auf kleine strukturelle Deformationen limitiert. Im Gegensatz dazu ist das flugdynamische Verhalten hochflexibler Flugzeuge charakterisiert durch ausgeprägte Kopplungen von Starrkörper- und elastischen Freiheitsgraden, die durch niederfrequente strukturelle Moden hervorgerufen werden. Aus diesem Grund beinhalten die in dieser Arbeit hergeleiteten Bewegungsgleichungen Kopplungen durch Inertiallasten.

Im dritten Teil werden Anwendungen der entwickelten Methode auf drei Testfälle mit steigender Komplexität vorgestellt. Zuerst werden die grundlegenden Eigenschaften der Methode anhand eines statisch belasteten, einfachen Balkenmodells dargestellt. Der zweite Testfall ist ein hochgestreckter Flügelkasten, modelliert als dreidimensionales Finite-Elemente-Modell mit anisotropen Materialien. Der dritte Testfall ist das hochflexible *X-HALE* UAV der University of Michigan. Statische strukturelle und aeroelastische Simulationen sowie Freiflugmanöver mit instationärer Anregung durch Böen und Höhenrudereingaben demonstrieren letztendlich weitere Fähigkeiten und die Grenzen der Methode.

Contents

Acknowledgements	iii
Abstract	v
Zusammenfassung	vii
List of Figures	xiii
List of Tables	xvii
List of Symbols	xix
Chapter	
1 Introduction	1
1.1 Motivation	1
1.2 State of the Art	5
1.2.1 Nonlinear Finite Element Methods for the Modeling of Large Deformations	6
1.2.2 Modeling of Nonlinear Beam-type Structures	9
1.2.3 Static and Dynamic Reduced-Order Modeling of Aircraft Structures and Substructures	11
1.2.4 Modal Expansions for Aeroelastic and Structural Dynamics Applications .	13
1.2.5 Modeling of the Free-flying Elastic Aircraft with Large Deformations	14
1.2.6 Governing Equations of the Free-flying Flexible Aircraft	15
1.2.7 Integrated Simulation Models and Frameworks	17
1.3 Objectives and Outline of the Dissertation	21
1.3.1 Objectives of this Work	21
1.3.2 Dissertation Outline	23
2 Structural and Flight Dynamics Equations of Motion	25
2.1 Derivation of the Static Equation of Motion	25
2.1.1 Higher-order Strain Energy Formulation	25

2.1.2	Higher-order Deformation Representation	30
2.1.3	Calculation of the Generalized Forces	35
2.1.4	Static and Dynamic Governing Equations of the Proposed Method	37
2.1.5	Recapitulation and Solution Sequence of the Proposed Method	38
2.2	Inertially Coupled Equations of Motion for the Free-flying Flexible Aircraft	38
2.2.1	Definition of Kinematical Relations	40
2.2.2	Definition of the Kinetic Energy	42
2.2.3	Definition of the Potential Energy	46
2.2.4	Definition of the Generalized Forces	46
2.2.5	Lagrange's Equations of the Second Kind in Quasi- and Modal Coordinates	47
2.2.6	Matrix Form of the Equations of Motion	48
2.2.7	Simplified Equations of Motions	49
2.2.8	First-Order System of the Equations of Motion	49
2.3	Calculation of the Linear and Higher-Order Stiffness and Mode Components	50
2.3.1	Two-dimensional Polynomial Surface Fitting to Nonlinear Solutions	51
2.3.2	Calculation of the Higher-Order Stiffness and Mode Tensors from Polynomial Coefficients	53
2.3.3	Exemplary Calculation of the Higher-Order Components for a Beam Structure	56
2.3.4	Residual-based Evaluation of the Stencil Size and the Amplitude Dependency	58
3	The Aeroelastic Model of the Free-flying Aircraft	67
3.1	Calculation of Aerodynamic Forces by a Vortex-lattice Method	67
3.1.1	Basics of Aerodynamic Potential Theory	68
3.1.2	Spatial Discretization and Details of the Unsteady Vortex-lattice Implementation	70
3.1.3	Steady Vortex-lattice Method	74
3.1.4	Enhancements of the Steady and Unsteady Vortex-lattice Method	75
3.2	Interface of Aerodynamic and Structural Model	76
3.3	The Aeroelastic Model – Simulations in the Time Domain	77
3.4	Trim Approach for Steady Straight Horizontal Flight	79
4	Numerical Studies	85
4.1	Cantilever Beam Test Case	86
4.1.1	Static Validation of the Higher-Order Stiffness Tensors and Mode Components	87
4.1.2	Static Simulations and Validation with Selected Force Fields	92
4.2	High Aspect Ratio Composite Wingbox Test Case	98

4.2.1	Static Response Simulations and Validation	101
4.2.2	Static Aeroelastic Simulations and Validation	104
4.3	X-HALE UAV Test Case	109
4.3.1	Key Features of the X-HALE UAV	109
4.3.2	Setup of the Structural and Aerodynamic Simulation Models	110
4.3.3	Verification of the Structural Model	117
4.3.4	Validation of Static Coupling Simulations with UM/NAST Results	121
4.3.5	Trim Simulations for Steady Straight Horizontal Flight	122
4.3.6	Unsteady Maneuver Simulations	125
5	Conclusion and Outlook	137
5.1	Summary and Main Conclusions	137
5.2	Key Contributions of this Dissertation	139
5.3	Outlook and Future Research	140
Appendices		
A	Matrices of the Nonlinear Flight Dynamics EOMs	143
A.1	Matrices of the Nonlinear Flight Dynamics EOMs without mean axes assumptions	143
A.2	Matrices of the Linearized Flight Dynamics EOMs	145
B	Frames of Reference and Flight Mechanic Matrices	147
C	Longitudinal Dynamics of the X-HALE	151
D	Properties of the Cantilever Beam Test Case	153
	Bibliography	157

List of Figures

1.1	Generic cantilever beam subject to tip load.	4
1.2	Kinematical concept and description of the corotational formulation.	8
2.1	Generic cantilever beam subject to tip load.	31
2.2	Kinematic relations of a pendulum with approximations of tip displacements. . .	32
2.3	Approximation of a circular arc.	33
2.4	Differences between arc line and polynomial approximations.	33
2.5	Linear, quadratic, cubic, and fourth-order mode components of a generic beam. .	35
2.6	Exemplary deformation fields of the first bending mode for the generic beam. . .	36
2.7	Static and dynamic solution sequence of the proposed method without rigid-body DOFs.	39
2.8	Inertial (geodetic) and body-fixed frames for definition of kinematical relations. .	41
2.9	Stencil of width five and exemplary solutions of \mathbf{N}_{ij}	51
2.10	Nonlinear and linear strain energies, and their difference for the first out-of-plane bending mode of the beam test case.	57
2.11	Nonlinear and linear strain energies, and their difference.	57
2.12	Displacements calculated by a geometrically nonlinear FE simulation for the first out-of-plane bending mode of the beam test case.	58
2.13	Strain energies for the first in-plane bending mode of the beam test case.	59
2.14	Nonlinear displacements for the first in-plane bending mode of the beam test case.	59
2.15	Strain energies for a combination of the first out-of-plane and in-plane bending mode of the beam test case.	60
2.16	Nonlinear displacements for a combination of the first out-of-plane and in-plane bending mode of the beam test case.	60
2.17	Dependency of the ratio of the ten lowest identified linear stiffness terms to reference values from Nastran.	61
2.18	Difference between identified linear mode components and reference values from Nastran.	62

2.19	Convergence of the quadratic mode components as function of the stencil size.	63
2.20	Convergence of the cubic mode components as function of the stencil size.	64
2.21	Convergence of the fourth-order mode components as function of the stencil size.	64
2.22	Residuals of eigenvectors and eigenvalues for the first out-of-plane bending mode.	65
2.23	Residuals of quadratic, cubic, and fourth-order mode components of the first out-of-plane bending mode.	66
3.1	Discretization of a cambered lifting surface with vortex rings and details of the grid metric.	71
3.2	Wing and wake of the vortex-lattice method discretized by vortex rings.	73
3.3	Solution sequence of the unsteady vortex-lattice method.	74
3.4	Wake panels of the steady vortex-lattice method.	75
3.5	Setup of the coupling model.	78
3.6	Deflection of a control surface by means of tilting the normal vectors of its panels.	79
3.7	Solution sequence of the aeroelastic program.	80
4.1	FE model of the 16 m beam test case.	86
4.2	Comparison of the static displacement fields obtained by different methods, the first bending mode shape was selected for ϕ^i	88
4.3	Comparison of the static displacement fields obtained by different methods, the first in-plane bending mode shape was selected for ϕ^i	89
4.4	Comparison of the static displacement fields obtained by different methods, the second bending mode shape was selected for ϕ^i	89
4.5	Comparison of the static displacement fields obtained by different methods with a combination of the first and the second out-of-plane bending mode.	90
4.6	Comparison of the static displacement fields obtained by different methods with a combination of the first and the (reversed) second bending mode.	91
4.7	Comparison of the static displacement fields for a force field defined by a combination of the first vertical and the first horizontal (in-plane) bending mode.	92
4.8	Comparison of the static displacement fields for a force field defined by a combination of the first vertical bending and the first torsion mode.	93
4.9	Comparison of the static displacement fields obtained by different methods.	94
4.10	Comparison of the static displacement fields obtained by different methods.	95
4.11	Comparison of the static displacement fields for a combination of forces in the x and in the z direction applied at the tip of the beam.	96
4.12	Comparison of the static displacement fields for a combination of forces in the x and in the z direction applied at each node of the beam.	97
4.13	Comparison of the static displacement fields for a combination of forces in the negative y and in the positive z direction applied at each node of the beam.	98

4.14 Comparison of the static displacement fields for a combination of forces along the x , the y , and the z axes and a torsion moment applied at each node of the beam.	99
4.15 Changes in linear stiffness of ten modes of the beam test case as function of a constant force field.	100
4.16 Layout of the wingbox made from CFRP shell elements with details and material thicknesses.	101
4.17 Selected normal mode shapes of the wing box test case.	102
4.18 Nodes on the upper side of the wingbox for which deformations will be plotted.	102
4.19 Comparison of the static displacement fields obtained by different methods for tip forces with values from 1000 to 7000 N applied in the z direction at the wingtip.	103
4.20 Comparison of the static displacement fields obtained by different methods for different elliptical force fields applied along the z direction at each node of the wingbox.	104
4.21 Comparison of the static displacement fields obtained by different methods for different elliptical and tilted force fields with components in z and y direction.	104
4.22 Vortex-lattice aerodynamic model of the wingbox test case.	106
4.23 Comparison of static aeroelastic coupling results of the wingbox.	106
4.24 Increase of the aerodynamically effective surface area of the wing due to structural deformation.	107
4.25 Cut loads (forces) at the wing root as function of AoA.	107
4.26 Cut loads (moments) at the wing root as function of AoA.	108
4.27 Concept of the X-HALE UAV developed by the University of Michigan.	110
4.28 X-HALE 6 meter span RRV in turn maneuver and on ground.	110
4.29 Structural model of the X-HALE UAV build with beam finite elements.	112
4.30 The lowest twelve mode shapes of the X-HALE structural model obtained from a normal modes analysis.	113
4.31 Vortex-lattice aerodynamic grid of the X-HALE.	114
4.32 Lift, drag, and moment coefficients of the EMX 07 reflex airfoil for Reynolds number varying from $1.95 \cdot 10^5$ to $2.5 \cdot 10^5$	115
4.33 Lift, drag, and pitching moment coefficients of the rigid X-HALE model as function of the AoA.	116
4.34 Lift force per length in the z direction of the rigid X-HALE aerodynamic model for different AoAs.	116
4.35 Coupling model of the X-HALE UAV.	117
4.36 Comparison of the static displacement field obtained by different methods for forces from 2 N to 14 N (in steps of 2 N) applied along the z direction at the wingtip.	118

4.37 Comparison of the static displacement field obtained by different methods for forces from 0.2 N to 1.8 N (in steps of 0.2 N) applied along the z direction at each node of the wing beam.	118
4.38 Displacement field of two methods from static coupling simulations for different AoAs.	119
4.39 Lift in aerodynamic axes for different AoAs.	120
4.40 Displacement fields of two methods from static coupling simulations with varying tail deflections.	120
4.41 Displacement fields of static coupling simulations from four methods for different AoAs.	121
4.42 Results of the trim simulations of the X-HALE for flight velocities of 15, 16, 17, and 18 m/s.	122
4.43 Structural deformation of the right wing of the X-HALE for four trim velocities, without drag.	124
4.44 Structural deformation of the right wing of the X-HALE for four trim velocities, with induced and viscous drag.	125
4.45 Structural deformation of the right wing of the X-HALE for a trim velocity of 16 m/s and three different structural solutions.	126
4.46 Elastic and rigid-body responses of symmetric tail input maneuver with tail rotation of one degree.	128
4.47 Comparison of the responses from the proposed method and UM/NAST in terms of elastic deformation and rigid-body reaction, amplitude of tail rotation is one degree.	129
4.48 Elastic and rigid-body responses of symmetric tail input maneuver with tail rotation of two degrees.	130
4.49 Comparison of the responses from the proposed method and UM/NAST in terms of elastic deformation and rigid-body reaction, amplitude of tail rotation is two degrees.	131
4.50 Illustration of the DARPA gust.	132
4.51 DARPA gust encounter simulation with disturbance velocity in the z_g direction of -0.5 m/s.	133
4.52 DARPA gust encounter simulation with disturbance velocity in the z_g direction of -1.5 m/s.	135
B.1 Two inertial (geodetic) and body-fixed frames of reference with different axes orientations.	150

List of Tables

4.1	Eigenvalues of the ten lowest modes of the beam model.	87
4.2	Eigenvalues of eight selected modes of the generic wingbox model.	101
4.3	Aerodynamic and mass properties of the X-HALE UAV.	111
4.4	Eigenvalues of the twelve lowest modes of the X-HALE FE model.	113
C.1	Selected longitudinal stability derivatives of the X-HALE.	152
C.2	Short-period mode and phugoid of the X-HALE.	152
D.1	Node ids and locations (with respect to the Nastran basic coordinate system) of the nodes of the beam test case FE model introduced in Section 4.1.	154
D.2	Moments of inertia of the cross-sections of the beam test case FE model.	155
D.3	Properties of concentrated masses defined at particular nodes of the beam test case FE model.	156

List of Symbols

Abbreviations

AIC	Aerodynamic Influence Coefficients
AoA	Angle of Attack
AR	Aspect Ratio
BDF	Backward Differentiation Formula
c.m.	center of mass
CBEAM	MSC Nastran finite beam element
CFD	Computational Fluid Dynamics
CFRP	Carbon Fiber Reinforced Plastic
CONM2	MSC Nastran concentrated mass element
DARPA	Defense Advanced Research Projects Agency
DLM	Doublet-Lattice Method
DLR	Deutsches Zentrum für Luft- und Raumfahrt, German Aerospace Center
DOF	Degree of Freedom
EOM	Equations of Motion
ERAST	Environmental Research Aircraft and Sensor Technology
FEM	Finite Element Method
H.O.T.	Higher Order Terms
HALE	High Altitude Long Endurance
IMU	Inertial Measurement Unit
INS	Inertial Navigation System
MAT2	MSC Nastran material definition

MDA	Multidisciplinary Analysis
ModGen	Model Generator, DLR toolbox for generation of Nastran FE models
MSC	MSC Software Corporation, provider of proprietary simulation software
NACA	National Advisory Committee for Aeronautics
NAST	Nonlinear Aeroelastic Simulation Toolbox
Nastran	NASA Structural Analysis, proprietary FE analysis program
ODE	Ordinary Differential Equation
RBE2	MSC Nastran Rigid-Body Element
RBF	Radial Basis Function
RHS	Right Hand Side
RRV	Risk Reduction Vehicle
SPLINE1	MSC Nastran surface spline for aeroelastic applications
TPS	Thin Plate Spline
UAV	Unmanned Aerial Vehicle
UM	University of Michigan
VLM	Vortex-Lattice Method
ZAERO	Proprietary aeroelastic simulation software from ZONA Technology

Greek symbols

α	Angle of attack
β	Angle of sideslip
Δ	Increment
$\dot{\alpha}$	Time derivative of angle of attack
η	Tail plane deflection, stencil size
Λ	Aspect ratio
ν	Unit normal vector
$\omega_{0,P}$	Frequency of the phugoid (rad/s)
$\omega_{0,SP}$	Frequency of the short-period mode (rad/s)
∂	Symbol of partial-derivative
Φ	Roll angle; Velocity potential

π	Total potential energy (e.g. of a body)
Ψ	Yaw angle
ρ	Density of fluid
ρ_∞	Reference density of fluid (for incompressible flow field)
Θ	Pitch angle
φ	Amplitude of the pendulum

Indexes

η	Stencil Size
0	Value at steady trim state
A	aerodynamic
a	Index for scaling factor of force field
b	w.r.t. body-fixed frame of reference; Index for scaling factor of force field
D	Induced drag part of aerodynamic forces; Drag (derivatives)
e	elastic
eff	effective (circulation)
F	propulsive
f	Axes index of body-fixed frame according to ISO-1151
g	w.r.t. geodetic frame of reference
L	Lift
m	Number of generalized coordinates; Pitching moment
N	Number of nodes; Number of aerodynamic panels
n	Load step (in nonlinear FE theory)
o	Axes index of normal earth-fixed frame according to ISO-1151
P	Phugoid
q	pitch rate
r	rotational
root	Value at root section
S	Index of integration over surface; Steady part of aerodynamic forces; Structural
SP	Short-period mode

t	translational; Exponent of polynomial
U	Unsteady part of aerodynamic forces
V	Index of integration over volume

Latin symbols and Scalars

\bar{c}	Mean chord
\bar{q}	Dynamic pressure
Δc_p	Difference of pressure coefficient between upper and lower side of aerodynamic panel
Δt	Timestep size
A_i	Area of aerodynamic panel
b	Width of aerodynamic panel; Span
c	Chord length of aerodynamic panel
C_D	Drag coefficient (air-path axes)
C_L	Lift coefficient (air-path axes)
C_X	Drag coefficient (body axes)
C_Z	Lift coefficient (body axes)
C_{MY}	Pitching moment coefficient (body axes)
C_{my}	Pitching moment coefficient (air-path axes)
dm_i	Discrete mass element
ds	Infinitesimal surface element
dv	Infinitesimal volume element
f	Frequency (Hz)
$F_{x,y,z}$	Force in direction of x,y,z axis
g	Magnitude of gravity vector
k	Coefficient of quadratic displacements (pendulum example)
L	Length of the pendulum; Lagrange variable
m	Aircraft mass
$M_{x,y,z}$	Moment about x,y,z axis
O	Origin of reference frame

p	Roll rate of body-fixed frame resolved in body-fixed frame
q	Pitch rate of body-fixed frame resolved in body-fixed frame
r	Yaw rate of body-fixed frame resolved in body-fixed frame
S	Wing area
T	Kinetic energy; Period time
U	Strain energy
u	Location of mass point in the y direction (pendulum example); x-component of translational velocity of body-fixed frame resolved in body-fixed frame; x-component of flow velocity
U_g	Gravitational potential energy
U_p	Total potential energy of the aircraft
U_{linear}	Linear part of strain energy
V	Potential energy of applied loads; Airspeed
v	Location of mass point in the z direction (pendulum example); y-component of translational velocity of body-fixed frame resolved in body-fixed frame; y-component of flow velocity
v_i	Trim parameter
w	z-component of translational velocity of body-fixed frame resolved in body-fixed frame; z-component of flow velocity
x,y,z	General notation for axes of cartesian coordinates
${}^p R_0^{rot}$	Residual to evaluate convergence of rotational terms of linear mode component
${}^p R_0^{trans}$	Residual to evaluate convergence of translational terms of linear mode component
${}^p R_1^{trans}$	Residual to evaluate convergence of translational terms of quadratic mode component

Matrices

ϵ_{ij}	(Green-Lagrange) strain tensor
Ω^2	Natural eigenvalues
ϕ	Eigenvector, structural mode shape
τ_{ij}	(2nd Piola-Kirchhoff) stress tensor
H	Coupling matrix
I	Identity matrix

\mathbf{J}	Tensor of inertia of the undeformed aircraft; Jacobian matrix (for trim approach)
\mathbf{J}_i	Local tensor of inertia of discrete mass point dm_i
\mathbf{K}	Stiffness matrix (of discretized structure)
\mathbf{K}^t	Tangent stiffness matrix (of discretized structure)
\mathbf{M}	Nodal mass matrix (of discretized structure); Generalized mass matrix
$\mathbf{M}_{b\Phi}$	Transformation matrix (used to relate the time rate of change of the Euler angles, $\dot{\Phi}$, and the angular velocity of the body-fixed frame, Ω_b)
\mathbf{M}_{bg}	Orthogonal transformation matrix used to transform vectors from geodetic to body-fixed frame
\mathbf{P}_{ij}	Matrix of polynomial scaling factors
\mathbf{N}_{ij}	Vector of nonlinear solutions (strain energy or nodal displacements)
$\dot{\mathbf{J}}$	Time derivative of tensor of inertia of the deformed aircraft
$\overline{\mathbf{D}}$	Gyroscopic matrix of the EOMs for the flexible aircraft (rigid-body and elastic DOFs)
$\overline{\mathbf{J}}$	Tensor of inertia of the deformed aircraft
$\overline{\mathbf{K}}$	Stiffness matrix of the EOMs for the flexible aircraft (rigid-body and elastic DOFs)
$\overline{\mathbf{M}}$	Mass matrix of the EOMs for the flexible aircraft (rigid-body and elastic DOFs)
AIC	Matrix of aerodynamic influence coefficients
${}^p\Phi_0$	Linear mode component
${}^pG_1^i$	Linear stiffness term

Operators

δX	Variation
\dot{X}	Time derivative (w.r.t. inertial system)
$\frac{D}{Dt}$	Substantial derivative
\dot{X}	Time derivative w.r.t. body-fixed frame
$\nabla \cdot \mathbf{x}$	Divergence of vector field \mathbf{x}
$\nabla \times \mathbf{x}$	Curl of vector field \mathbf{x}
∇x	Gradient of scalar field x
∇^2	Laplace operator
\tilde{r}	Skew-symmetric matrix of (3×1) vector r

Tensors of rank > 2

B	Tensor considering second-order effects of deformation on the tensor of inertia of the undeformed aircraft
h_{pk}	Cross product of elastic modes p and k
ΔJ	Tensor considering first-order effects of deformation on the tensor of inertia of the undeformed aircraft
$\Delta^2 J$	Tensor considering second-order effects of deformation on the tensor of inertia of the undeformed aircraft
$\overline{r\mathbf{m}}$	Offset of center of mass w.r.t. origin of body-fixed frame
${}^p\Phi_1^i$	Quadratic mode component
${}^p\Phi_2^{ij}$	Cubic mode component
${}^p\Phi_3^{ijk}$	Fourth-order mode component
${}^p\overline{\Phi\mathbf{m}}$	Mean axes constraint for translational rigid-body motion
${}^p\overline{r\Phi\mathbf{m}}$	Mean axes constraint for rotational rigid-body motion
${}^pG_2^{ij}$	Quadratic stiffness term
${}^pG_3^{ijk}$	Cubic stiffness term

Vectors

Δ	Discrete nodal translations and rotations
Γ	Circulation of the vortex rings of the aerodynamic panel
Ω_b	Angular rates of body-fixed frame resolved in body-fixed frame
ψ	Discrete nodal translations and rotations
ζ	Vorticity of the flow field
a	Discrete nodal translations and rotations
B	Vector field of applied loads
F	Discrete nodal loads (forces and moments); Resultant of propulsive forces w.r.t the axes of the body-fixed frame
f	External nodal forces and moments w.r.t Cartesian coordinates
g	Gravity vector resolved in geodetic frame
n_i	Normal of aerodynamic panel i

P	Discrete nodal loads (forces and moments); Location of body-fixed frame w.r.t. geodetic frame resolved in body-fixed frame
P_g	Location of body-fixed frame w.r.t. geodetic frame, resolved in geodetic frame
P_g^0	Initial location of body-fixed frame w.r.t. geodetic frame, resolved in geodetic frame
Q	Generalized Forces
q	Generalized Coordinates
Q^A	Resultant of aerodynamic moments w.r.t the axes of the body-fixed frame
RHS	Kinematic boundary conditions at collocation points of aerodynamic panels
r	Internal force field w.r.t Cartesian coordinates; Location of mass point w.r.t. undeformed structure
R^A	Resultant of aerodynamic forces w.r.t the axes of the body-fixed frame
R_i	Location of mass point dm_i resolved in the body-fixed frame
r_i	Quarter-chord line of aerodynamic panel i
R_r	Residual vector of rotational DOFs (for trim approach)
R_t	Residual vector of translational DOFs (for trim approach)
s	Scaling factors for discrete nodal displacements
$T^{(\nu)}$	Traction vector field applied on body surface
u	Displacement field; Vector of nodal displacements w.r.t Cartesian coordinates; Velocity field
u_b	Flow velocity at collocation point on aerodynamic panel
V_b	Translational velocity of body-fixed frame resolved in body-fixed frame
V_i	Velocity of mass point dm_i resolved in the geodetic frame
$V_{bodystreamwise}$	Velocities induced by the streamwise segments of the bound vortex rings and all segments of the wake vortex rings
$V_{elastic}$	Disturbance velocity at collocation point on aerodynamic panel induced by structural deformation
V_{gust}	Disturbance velocity at collocation point on aerodynamic panel induced by gust, resolved in body-fixed frame
V_{RB}	Flow velocity at collocation point on aerodynamic panel due to onflow and rigid-body motion
V_{wake}	Disturbance velocity at collocation point on aerodynamic panel induced by wake panels, resolved in body-fixed frame

\mathbf{X}	Vector of aircraft state variables (rigid-body and elastic DOFs)
\mathbf{x}_{ij}	Vector of polynomial coefficients from which higher-order stiffness and mode components are derived
$\tilde{\mathbf{n}}_i$	Tilted normal of aerodynamic panel i
$\underline{\Phi}$	Euler angles, $\underline{\Phi} = [\Phi \Theta \Psi]^T$
$\underline{\Phi}^0$	Initial value of the Euler angles
${}^{ab}\mathbf{F}_{ij}$	Nodal force field for excitation of particular modes

Chapter 1

Introduction

The first chapter of this dissertation provides an introduction into the problem of geometrically large deformations in aeroelastic analysis. A general description of the problem and motivations for the engagement with it are given in Section 1.1. The state of the art in the modeling of large deformations for aircraft structures in different scenarios – from simply supported beam models to the free-flying aircraft – as well as an in-depth description of the previous works in the field are provided in Section 1.2. Particular objectives of this work and its new contributions are outlined in Section 1.3 together with a brief description of the five chapters of the thesis.

1.1 Motivation

The importance of multidisciplinary analysis (MDA) in future aircraft design and evaluation increases continuously. Nowadays, concepts such as fixed-wing type, very flexible Unmanned Aerial Vehicles (UAV) and High Altitude Long Endurance (HALE) type of aircraft are about to establish and ask for the early inclusion of more disciplines into the aircraft design process, such as aeroelasticity, flight dynamics, structural dynamics, and control [1, 2]¹. Nonlinearities are inherent properties of the static and dynamic behavior of such vehicles and thus become an inevitable part of the analyses methods [3, 4, 5]. Furthermore, the realization of new and radical ideas for future manned and unmanned aircraft concepts carries great risks; it will only have a chance if the designer masters the intrinsic and mutual effects of any of the disciplines involved [6].

Processing these issues demands highly sophisticated methods and tools for the design and the analysis. It is intended that the numerical simulation tools used in conceptual and preliminary design are integrated such that they consider the mutual interaction of aerodynamics, flight mechanics, and structural dynamics a priori [6]. Only by these means a global nonlinear aeroelastic analysis of the system considered becomes possible.

¹Zephyr, the High Altitude Pseudo-Satellite, <http://www.airbus.com/defence/uav/zephyr.html>

Such dependencies can be illustrated by simple examples. From an aerodynamic point of view, one of the key design features that supports achieving higher efficiency is an increased aspect ratio to reduce the induced drag. This inevitably leads to an increased wing span which, in turn, leads to greater flexibility of the wing, that is even more increased if a light, high performance structural construction is used. Jet transports have ever since been pushed to higher flight velocities. Airfoils with reduced thicknesses can help to further increase the Mach number due to reduced transonic effects, but also at the costs of higher flexibility of the wing. In most of such cases, the high flexibility is not a particular design goal but must be taken into account in the analyses. On the other hand, highly flexible wings can be a desired feature. For jet transports an increase in passenger comfort and the reduction of structural loads is expected if the energy of atmospheric disturbances can be absorbed and damped by more flexible parts of the wings.

Regarding the fidelity and applicability of the disciplines involved in more detail, one quickly realizes that the aerodynamic analysis capabilities are already far advanced. CFD methods that solve the steady and unsteady Navier-Stokes equations on volume grids are becoming state of the art even in industry [7]. For flexible aircraft, a popular approach is to extend the rigid-body flight mechanic model by (steady) aerodynamic corrections to consider structural elasticity [8]. Progress was made in the past to establish methods that account for the interaction of flight mechanic and structural degrees of freedom (DOFs) due to frequency proximity [9, 10]. As an example, the widely used approach of frequency separation and thus an independent analysis of the flight dynamic and aeroelastic behavior of elastic aircraft loses its validity for certain fixed-wing UAVs and long-range jet transports [11].

The structural part, however, lags behind in some aspects. The calculation of static and dynamic structural deflections in aeroelastic simulations are typically based on a linear description of the airframe either by stiffness and mass matrices or modal data where eigenvectors and corresponding eigenvalues in the frequency range of interest are used. In order to save computational costs and consider thousands of load case scenarios (as typically present in an industrial loads computation process for jet transport), the structural and aeroelastic mathematical models are expressed in the frequency domain. Such kinds of structural methods have limited if any applicability to the problem of geometrically nonlinear aeroelasticity, where the emphasis turns to time domain solutions and coupled aeroelasticity/flight dynamics analysis. Complex 3D finite element (FE) models are used to represent the characteristics of the structure, but almost all of them are restricted to geometrically linear calculations. As mentioned above, structural nonlinearities are entering the scene of jet transport design, and thus it is desirable to use the 3D FE models in the loads computation process. Nonlinear static aeroelastic analysis (e.g. for trimmed flight) can be done with those complex models by coupling of a FE program with an appropriate aerodynamic method. Unfortunately, no general structural method exists that can be used with arbitrary FE models to perform nonlinear, dynamic aeroelastic analyses. An approach to overcome this problem is the conversion of the complex

FE model into an equivalent beam-type structure and the application of a nonlinear beam theory. Indeed, geometrically-exact beam-based formulations coupled with appropriate unsteady aerodynamics make the current state of the art for example in frameworks for the aeroelastic simulation of highly flexible UAVs [12]. On the other hand, beam formulations may not be sufficient to model complex structural details of general aircraft wings. Overall, this reveals the deficiency of a static and dynamic structural method that is both simple in use (comparable to the modal approach widely used in aeroelasticity), applicable to complex 3D FE models, and considers geometrically nonlinear effects due to large deformations.

The goal of this thesis is the development of a new method for the geometrically nonlinear, aeroelastic simulation of highly flexible aircraft structures undergoing large displacements. Specifically, the modal approach based on shape functions and generalized coordinates is to be extended to account for its two major shortcomings that emerge at large deformations. The first one is the linear relation between the applied structural forces and the resulting displacement field, it is to be corrected to account for nonlinear force-displacement relations, which are encountered especially in plate-like structures. The second one is the geometrically linear mapping between generalized and nodal coordinates. Considering, for instance, slender structures at large, nonlinear deformations, the paths of the nodes appear as curved rather than straight lines, which corresponds to a nonlinear mapping between generalized and nodal coordinates. For the simulation of free-flying, highly flexible aircraft in maneuvering flight, the method is to be extended by rigid-body motions. An aeroelastic framework based on the method together with an appropriate aerodynamic method is to be developed that enables the nonlinear flight dynamic simulation in the time domain. The method should be applicable to complex 3D FE models built from beam, shell, and plate elements possibly with anisotropic material characteristics. Other sources of structural nonlinearities, provoked e.g. by damping mechanisms or particular material behavior (e.g. plasticity or viscoelasticity), are not considered here.

Some examples for envisaged application of the proposed method are suggested briefly for motivation. As will be shown in the thesis, the method can be used to reliably calculate structural deformations up to approximately 25% of the semi-span. Only very few aircraft configurations will exhibit such large deflections during normal operation. However, the X-HALE UAV from University of Michigan was developed particularly for that purpose and is used as a challenging test case for the proposed method in this thesis. Its planform and proportions are based on the well-known HELIOS prototype developed in the ERAST program (Environmental Research Aircraft and Sensor Technology), whose accident has triggered global activities to develop sophisticated simulation methods for highly flexible aircraft. Other examples of aircraft showing large deflections in flight include high-performance sailplanes of the Open Class. Finally one must admit that the complexity involved in the description and simulation of highly flexible aircraft grant the aeroelastician a wide field for broad and multidisciplinary research activities.

A very simple but illustrative example for motivation is shown in Fig. 1.1. A generic, 1m

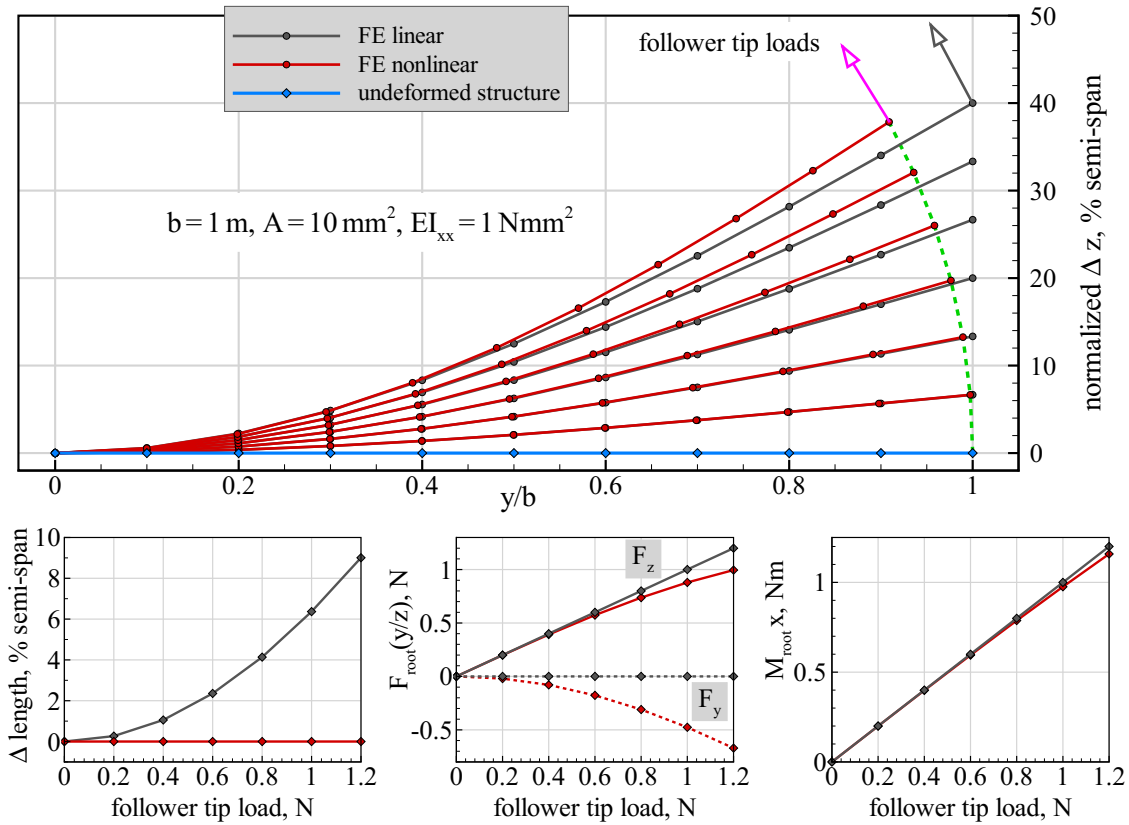


Figure 1.1: Generic cantilever beam subject to tip load (the linear solution only considers the force components in the z direction). Differences between linear and nonlinear FE calculations manifest in the length of the beam, the shear forces, and the root bending moment.

span cantilever beam is subjected to a follower tip force – to resemble the nonconservative characteristic of aerodynamic loads – and the displacement field is calculated by a linear and a nonlinear FE method, respectively. Essential differences between the solutions in terms of the displacement field and the constraint forces at the root can be identified by means of this example. Most significant are the differences of the nodal displacements in the z and in the y direction, the linear FE solution leads to an artificial increase of the length of the beam as the tip load is increased. Considering that the beam resembles an aircraft wing, this effect directly affects the aerodynamic forces since the area of the wing is increased as well. Furthermore, the linear FE solution is not able to take the rotation of the load into account since it only considers the force components acting in the z direction. The shear forces in the y and in the z direction and the bending moment about the x axis are diverging with increasing level of deformation. However, an interesting counteracting effect is depicted by the plot of the linear and nonlinear bending moments which show acceptable agreement also at higher deformations of the beam. The nonlinear FE solution considers the rotation of the applied force and keeps the length of the beam constant, resulting in a root bending moment which is similar to the one calculated

by non-follower load but increased beam length (the linear case). Aside from the impact on loads, the two solution methods will lead to different distributions and locations of masses with respect to the origin and will thus generate different inertial forces if e.g. the clamping section is accelerated as in the case of a maneuvering aircraft.

1.2 State of the Art

As mentioned in the introduction, a new method is to be developed for the geometrically non-linear, aeroelastic simulation of the free-flying elastic aircraft with large deformations. In this thesis, aeroelastic simulation comprises the disciplines aerodynamics, structural dynamics, and flight mechanics. The overall motion of an unconstrained, flexible aircraft in free-flight (the physical model thereof is introduced in Section 2.2) is composed of the rigid-body motion of a body-fixed reference frame and the elastic structural deformations (possibly large and geometrically nonlinear) with respect to this reference frame. The rigid-body motion, including translational and rotational DOFs, is described by the laws of conservation of translational and rotational momentum, the physical formulation of this type of motion is well-established. Thus this section is focused to provide an overview of the state of the art of methods for the nonlinear structural dynamics part of the physical model of a flexible aircraft in free flight².

The nonlinearities accounted for are limited to *geometrical nonlinearities*, defined as significant deviation from linear structural behavior (linear force-displacement, stress-strain, or kinematic relations) caused by structural deformations. This classification comprises effects such as the stiffening of plates subjected to transverse loads or e.g. helicopter rotor blades loaded by centrifugal forces, for both systems the structural deformations leading to nonlinear effects might be low compared to e.g. the thickness of the plate or the length of the blade. Another example is a structure which undergoes very large deformations with respect to its dimensions, but whose material strains are within the linear regime (which is, for instance, the case for very flexible aircraft or deployable devices such as parachutes).

The method developed in this thesis is related to and builds on different works published by other researchers, thus a detailed description and discussion of their work and distinctive features is given. Methods used by research institutions and industry are considered. Before, methods for the modeling of nonlinear structural dynamics within the FE method and the most important nonlinear beam theories are depicted. The nonlinear FE methods are of particular importance for the proposed method because they are used to calculate validation results as well as the higher-order stiffness and mode components, which form the basis of the method.

The topics discussed in the following subsections comprise:

- Nonlinear finite element methods for the modeling of large deflections

²It must be mentioned at this point that the rigid-body and the elastic motions are in general coupled by inertia, gyroscopic, elastic, and external forces. This fact necessitates an extension of structural dynamics methods which are formulated for clamped systems by rigid-body DOFs (as is the case in this thesis).

- Modeling of nonlinear beam-type structures
- Static and dynamic reduced-order modeling of aircraft structures and substructures
- Modal expansions for aeroelastic and structural dynamic applications
- Modeling and simulation of the free-flying elastic aircraft with large deformations

1.2.1 Nonlinear Finite Element Methods for the Modeling of Large Deformations

Analytical analysis of aircraft structures is limited in many aspects. Mostly an appropriate simplification of the structure is required to be applicable to elementary structural methods, such as analytical beam or plate theories. The constraints become worse if geometrically nonlinear, large displacements are to be considered and analyzed. So far, no closed form analytical solution for the calculation of the geometrically nonlinear displacement field of a beam structure exists. Numerical methods are the state of the art for the mechanical simulation of aerospace structures not only for this reason. Aircraft are complex designs especially from a structural point of view; sophisticated methods such as the FEM are thus required to enable the transfer of the real design into a simulation model composed of beam, shell, solid, and mass elements.

In general, linear structural analysis a priori assumes a linear relation that maps a displacement field \mathbf{u} (composed of translations and rotations) to a force field \mathbf{f} (composed of forces and moments) where the transformation matrix is the stiffness matrix of the structure, \mathbf{K} (a finite element discretization of the system is assumed and time-dependent terms are omitted):

$$\mathbf{K}\mathbf{u} = \mathbf{f} . \quad (1.1)$$

Stress becomes a linear function of strain, material and geometric properties of the elements are constant. Also boundary conditions do not change with respect to the initial configuration as loads are applied [13]. Furthermore, the stiffness matrix is assumed constant and determined based on the undeformed, initial state of the system. The inverse operation, i.e., the calculation of the displacement field corresponding to a prescribed force field is always unique but requires the inversion of the stiffness matrix. The solution of the problem defined by Eq. 1.1 can be calculated in a single step, i.e. no iterative solution sequence is required.

By contrast, nonlinear analyses are different in many aspects. In general, a number of nonlinearities must be considered, such as material nonlinearities due to creep or yield, contact nonlinearities, or distinctive changes of the geometry of the system. In nonlinear analyses, the stiffness properties of the system become a function of the current state of deformation. This in turn asks for an iterative solution procedure due to the mutual dependency of stiffness and deformation. Loads are typically applied in steps and the stiffness matrix is updated (a tangent stiffness matrix is calculated) following the convergence of a criterion based for example on the sum of the work of internal and external forces in each step. Hence, the balance of internal

and external forces and moments (equilibrium conditions) are enforced with respect to the deformed geometry. This can be expressed mathematically as the equilibrium of the applied forces ${}^n \mathbf{f}$ and the nodal forces ${}^n \mathbf{r}$ (resulting from the internal stresses of the finite elements), both at load step n [13]

$${}^{(n)} \mathbf{f} - {}^{(n)} \mathbf{r} = \mathbf{0} . \quad (1.2)$$

This expression of equilibrium must hold for the instantaneous, current configuration. Considering a load increment denoted by $n + 1$, the same relation holds

$${}^{(n+1)} \mathbf{f} - {}^{(n+1)} \mathbf{r} = \mathbf{0} . \quad (1.3)$$

Now it is assumed that the solution for the displacements, ${}^{(n)} \mathbf{u}$, is known at load increment n . The increment $\Delta \mathbf{r}$ of the internal forces corresponding to the increase of internal stresses from load step n to $n + 1$ can be expressed as

$${}^{(n+1)} \mathbf{r} = {}^{(n)} \mathbf{r} + \Delta \mathbf{r} , \quad (1.4)$$

where vector $\Delta \mathbf{r}$ is approximated by a tangent stiffness matrix ${}^{(n)} \mathbf{K}^t$

$$\Delta \mathbf{r} = {}^{(n)} \mathbf{K}^t \Delta \mathbf{u} . \quad (1.5)$$

Here, $\Delta \mathbf{u}$ denotes a vector of incremental displacements. The tangent stiffness matrix is defined as

$${}^{(n)} \mathbf{K}^t = \frac{\partial {}^{(n)} \mathbf{r}}{\partial {}^{(n)} \mathbf{u}} , \quad (1.6)$$

it contains a *geometric* and the linear stiffness matrix \mathbf{K} . Inserting Eq.(1.5) and (1.4) into Eq.(1.3) yields the following system of linear equations for the displacement increment

$${}^{(n)} \mathbf{K}^t \Delta \mathbf{u} = {}^{(n+1)} \mathbf{f} - {}^{(n)} \mathbf{r} \quad (1.7)$$

which can be solved for the vector of incremental displacements, $\Delta \mathbf{u}$. The absolute displacements for the next load increment are the sum of the node positions of the last step and the increment

$${}^{(n+1)} \mathbf{u} = {}^{(n)} \mathbf{u} + \Delta \mathbf{u} . \quad (1.8)$$

Structurally nonlinear problems involving large displacements and rotations can be classified into two main categories. First, the large displacement, small strain problem, and second, the large displacement, large strain problem. Throughout this thesis, the nonlinearities considered are limited to geometrically large displacements and small strains. By rule of thumb (and as will be shown quantitatively in the following chapters), displacements are taken as large for normalized deformations greater than approximately ten percent of the semi-span in the case of

e.g. aircraft wings³. In large deformation analyses, the displacement of an element is generally split into two parts, a rigid-body motion with large and finite translations and rotations, and an elastic motion. Considering geometrically nonlinear analyses within the FEM, three methods are currently used for kinematical descriptions: First, the *Total Lagrangian*, second, the *Updated Lagrangian*, and third, the *Corotational Formulation*.

Both Lagrangian methods use a finite element mesh which is attached to the material and moves with it. The total Lagrangian method uses the initial, undeformed configuration of the structure to calculate the equilibrium of inner and outer loads. The determination of the tangent stiffness matrix accounts for stresses and changes of the geometry from the last load step. In contrast, the updated Lagrangian method uses the configuration of the last load step to calculate the load equilibrium and the tangent stiffness matrix [13, 14].

The corotational method is most recently developed. Although it also belongs to the group of Lagrangian methods since the computational mesh follows the elements in space as they move, *each* finite element is accompanied by a *local reference frame* that moves with the element. Stresses, strains, and the elastic deformations of the element are calculated with respect to this reference frame, as depicted in Fig. 1.2. Using an appropriate method for the calculation

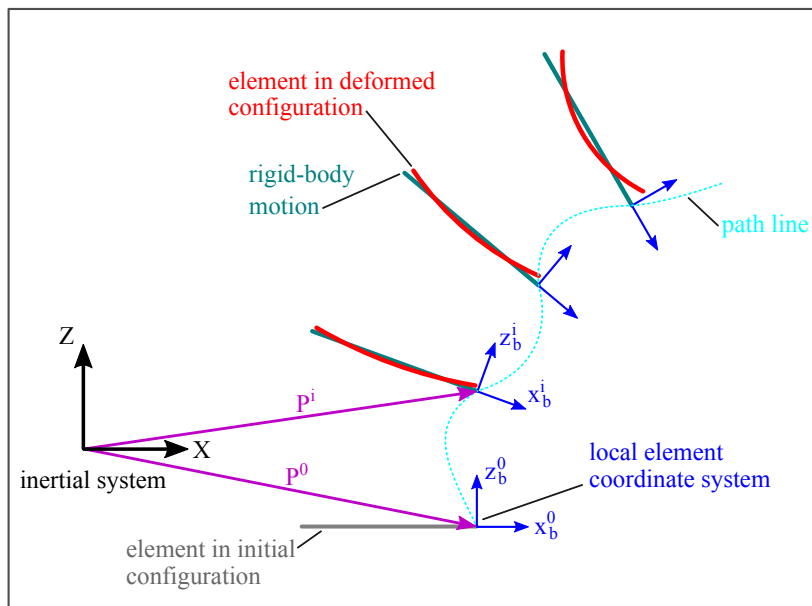


Figure 1.2: Kinematical concept and description of the corotational formulation.

of rotations (e.g. quaternions), the rigid-body motion of the element can become arbitrarily large [15]. Assuming small strains within an element, linear structural theories are sufficient and the main nonlinearity is due to the large rigid-body translations and rotations. A further

³In the context of this work, slender structures such as aircraft wings are considered. The expression *large deformation* may be quantified differently depending on the system considered. For example, the analysis of a plate structure can yield nonlinear effects due to bending-membrane coupling for deformations within the thickness of the plate.

advantage of this method is that existing (linear) finite elements can be reused, leading to the element-independent corotational formulation [15]. However, due to its newness and an ongoing research effort, this formulation has not found its way into commercial finite element programs yet. The idea of separating the rigid-body and elastic degrees of freedom of a body or an element seems natural and is comparable (to a certain extent) to the approaches used in multibody system dynamics with elastic components [16, 17], and to the approach applied for the derivation of the equations of motion of the free-flying flexible aircraft, derived in Section 2.2.

All nonlinear FE simulations shown in this thesis are performed by MSC Nastran, applying solution sequence *SOL 400*⁴. The nonlinear simulations are used both for the determination of the higher-order stiffness and mode components which are required for the proposed method (Sections 2.1.1 and 2.1.2), and also as general reference solutions for validation (Section 4). MSC Nastran uses both the total and the updated Lagrangian method for nonlinear analysis in the solution sequence *SOL 400*. The choice for a particular method is made either by the user or by Nastran based on the finite element model provided and the type of solution and nonlinearities involved. The load is applied in a number of increments in order to account for changes of the model in terms of the stiffness matrix (tangential stiffness), the boundary conditions, or the material properties. In order to account for the nonlinearities in the strain-displacement relations, the Green-Lagrange strain tensor is employed in combination with its work conjugate, the second Piola-Kirchhoff stress tensor. The components of both tensors are invariant against rigid-body translations and rotations of the corresponding element, which is a necessary requirement [16]. A Newton-Raphson method is used to find the solution for each load increment [14].

Although a large number of finite elements is supported by the nonlinear MSC Nastran solutions, the drawback with respect to the simulation of highly flexible aircraft is that the structural model is not allowed to undergo rigid-body motions. However, a simple method to analyze for example the stability of a highly flexible aircraft at a steady state, trimmed flight condition (with large deformations) is the linearization about that state which can be performed with Nastran. The structural dynamic characteristics can then be represented by a set of preloaded eigenvalues, where the trim state has been calculated with clamping.

1.2.2 Modeling of Nonlinear Beam-type Structures

Geometrically exact beam theories provide an elegant way to consider large deformations provided that the structure considered can be represented satisfyingly by beam elements. The term *geometrically exact* denotes that no assumptions (e.g. small angle approximation) were made for kinematic relations and exact equilibrium conditions are used with respect to the deformed reference line of the beam for the derivation of the governing equations. Depending

⁴*SOL 400 is the nonlinear static and implicit transient analysis, SOL 106 the nonlinear static analysis* [18].

on the choice of the independent degrees of freedom (displacements, velocities and internal forces, strains), three different formulations for nonlinear beam finite elements can be derived which are widely used for structural dynamic and aeroelastic analyses. The *displacement-based* formulation can be seen as a geometrically nonlinear extension of classical beam theories. A parametrization of the finite rotations of the nodes of the beam element by e.g. Euler angles or quaternions must be introduced which increases the computational effort. *Intrinsic* beam equations use translational and rotational internal velocities and stress resultants as independent variables rather than displacements. The governing equations are comparable to Euler's equations for the unconstrained rigid body moving in space. Displacements and rotations can be obtained by direct time integration of the velocities [5, 19]. The formulations for the kinematic relations used in the intrinsic beam theory correspond to a total Lagrangian description. Intrinsic beam formulations offer advantages in dynamic aeroelastic applications, since the translational velocities are a part of the independent variables that determine the aerodynamic forces. The fluid-structure interaction process is simplified because the implicit coupling of velocities and displacements at the interface of the fluid and the structure can be realized with less effort. *Strain-based* beam theories assume constant strain distributions for the extension, the bending in two directions, and the twist over a finite beam element and use them as independent variables [4]. The strain-based formulation provides an elegant way for the comparison of experimental and simulation data because strains can be measured relatively easily even in flight tests of scaled aircraft. Parts of the reference data for validation of the proposed method (introduced in Chapter 4 of this thesis) have been simulated with the UM/NAST toolbox from the University of Michigan which uses the strain-based beam formulation. Palacios and co-workers provide an overview of the methods and outline how they can be derived from a single set of equations [5].

Although the nonlinear beam theories are sophisticated methods, the structural discretization and reduction can pose a large problem. UAV configurations with wings of high slenderness and comparatively stiff fuselage and empennage are particularly suitable for a structural discretization by beams. Using a nonlinear beam theory to model e.g. a jet transport with highly flexible wings necessitates a reduction of the mostly complex structure into an equivalent beam model, though. Depending on the structural model considered, this task involves assumptions regarding the exact condensation of masses or stiffnesses of the corresponding cross sections of the full FE model [20]. Details must be omitted to a particular extent, and the process can become time consuming. As an example, the coupled nature of vertical and chordwise bending deformations present in a typical 3D wingbox structure changes the camber of the wing. This effect is not accounted for if the structure is represented by beams. However, for the structural models of jet transport aircraft used in industrial loads processes this approach can be promising because the commonly applied condensation of these models into a *loads-reference-axis model* (also referred to as *stick model*) to reduce the number of DOFs yields a discretization that resembles a beam model [11].

Concerning the modeling of geometrically large deformations, the method proposed in this thesis follows another approach. Besides the application of a nonlinear Lagrangian method or a nonlinear beam theory, a 3D FE model of a typical aircraft structure is described by a higher-order modal representation accounting for nonlinearities in the stiffness and in the deformation behavior. A static and dynamic structural condensation is realized by a modal representation of the structure, but the topology of the model in terms of the underlying geometry (the FE mesh) is kept.

1.2.3 Static and Dynamic Reduced-Order Modeling of Aircraft Structures and Substructures

The development and application of reduced-order models (ROMs) to nonlinear problems in structural dynamics started some decades ago. Similar to the work proposed in this thesis, the goal was both to overcome the restrictions of linear methods in terms of geometrical nonlinearities and to avoid the computational effort that comes with the application of nonlinear FE models. Muravyov determines nonlinear modal coefficients for arbitrary FE models and includes quadratic and cubic stiffness terms in the modal equations of motion. The determination process is based on the prescription of particular displacement fields to render a series of linear and nonlinear static problems which are then solved to determine the nodal forces corresponding to the imposed displacements. The nonlinear stiffness terms are then obtained from the nodal forces [21, 22]. In contrast to that, the method proposed in this work prescribes a series of static force fields and uses the resulting nonlinear strain energy and displacement fields to determine the higher-order coefficients.

Extensive research in the field of nonlinear structural ROMs was done by Mignolet and co-workers in recent years who have given detailed descriptions for the derivation of static and dynamic nonlinear structural governing equations including quadratic and cubic stiffness coefficients (generalized Duffing equation) [23, 24]. Fields of application are primarily plate structures and curved beams subjected to discrete loads, dynamic pressure (sound) and thermal loads. Nonlinearities are pronounced in plates subjected to out-of plane loads because of the intrinsic coupling of bending and membrane deformation. This behavior is satisfyingly represented by a cubic stiffness term. Coupling of several generalized coordinates is considered by the quadratic and cubic stiffness coefficients, which are tensors of third and fourth-order, respectively. As will be explained in detail in the following sections, geometrically nonlinear structural behavior includes nonlinearities not only in the force-displacement relation – which can be considered by the higher-order stiffness tensors – but also in terms of the displacement field. Mignolet uses a set of linear and *dual modes* (which are determined in pre-processing) to calculate the nodal displacements as function of the generalized coordinates. Considering e.g. a cantilever beam, the dual mode of the first bending mode can be seen as an orthogonal mode that yields in-plane displacements. However, for the calculation of the nodal displacement field,

both the linear and the dual modes are multiplied by the generalized coordinate (which is in contrast to the quadratic modes described in the following that are multiplied by the square of the generalized coordinates). The determination of the stiffness coefficients (the ROM parameters) is done in a pre-processing step by a series of nonlinear static FE simulations with the full model using a commercial FE software. A very good survey of different methods (e.g. prescription of nodal displacements or forces) to determine the higher-order stiffness tensors and dual modes of arbitrary structures using commercial FE codes is given in the paper of Mignolet [23]. It must be mentioned that besides plate structures and generic beams, the method was successfully applied to the modeling of the complex wing of the Predator unmanned aircraft system by Wang et al. MSC Nastran was used to identify the nonlinear coefficients of the ROM and the importance of the dual modes to capture transverse displacements for that application is emphasized. Furthermore, the stability of the nonlinear ROM is investigated and improved by neglecting selected stiffness terms of higher order [25].

A drawback of this method is the effect caused by inertia forces in dynamic applications involving large displacements. In such cases, the mass properties (or the mass matrix, respectively) of the system are dependent on the generalized coordinates. For plate structures, this poses no problem since the magnitude of deformations causing nonlinear behavior is still of the order of the plate thickness. Applying the method to slender, highly flexible beam structures with deformations in the range of 20% and more normalized displacements with respect to semi-span requires the consideration of the state-dependency of the modal mass to improve the calculation of inertia forces. A method for the extension of the nonlinear ROMs to account for this shortcoming was introduced by Medeiros who introduces higher-order terms into the formulation of the kinetic energy of slender wing structures [26].

Nonlinear Normal Modes (NNMs) basically describe the resonant frequency and response of a structure governed by nonlinear differential equations as a function of response amplitude or energy. The nonlinearity is introduced into the equation e.g. by cubic stiffness terms. A general introduction and overview of the theory of NNMs is given in an article of Kerschen et al. [27]. Kuether and Allen describe methods based on NNMs to simplify the dynamic analysis of large, complex FE structures [28, 29, 30]. The idea of their method is to assemble (nonlinear) structural subcomponents and determine their dynamic behavior; the nonlinear dynamics of the assembly as a whole are predicted based on the dynamics of the subcomponents. Two substructuring methods that can be used in conjunction with detailed FE models are presented by Kuether [28], where the second one is based on creating a reduced-order model of a structure by applying a series of static loads to a nonlinear FE model. Quadratic and cubic stiffness terms are used to consider nonlinear force-displacement behavior and the coupling of individual modes.

1.2.4 Modal Expansions for Aeroelastic and Structural Dynamics Applications

This thesis builds strongly upon the concept of modal expansion as introduced by Segalman and Dohrmann in terms of the quadratic mode components. Here, the concept of higher-order modes is further developed for a more accurate representation of geometrically nonlinear, large displacements. It must be mentioned that the method of the quadratic mode components has been used by several researchers to yield a linear stiffness term which is a function of deformation and the force field applied to the structure. This feature is essential for aeroelastic applications since the in-plane force components caused by rotation of aerodynamic lifting surfaces are captured.

As will be shown, the kinematically nonlinear displacement field of large deformations can be reconstructed by shape functions of higher-order. The *method of quadratic modes* was successfully applied by Segalman and Dohrmann to improve the kinematical and dynamical description of rotating structures (beams) undergoing large displacements up to second order. A shape function orthogonal to the normal mode (the quadratic component) is multiplied with the square of the independent variable (generalized coordinate) and accounts for the foreshortening of beams. An approach for the calculation of the quadratic components based on a series of nonlinear static solutions and numerical differentiation using finite differences is described in their work [31, 32, 33, 34]. Van Zyl derives the quadratic mode shapes for truss elements by energy considerations and uses them for the calculation of T-Tail flutter, where the kinematic relations at horizontal and vertical tail planes are improved [35, 36]. Van Zyl also showed that by applying modal expansion, the linear stiffness term becomes a function of deformation due to the quadratic mode components (this important feature will be outlined in detail in subsection 2.1.3). More recently, Farao builds upon this work and derives the quadratic mode shapes for elastic beams. He successfully applies them to the modeling of the NASA common research model (CRM) for which he first builds an equivalent beam model. The deformation results, as a vertical tip load is applied, clearly show that the approach much better conserves the length of the structure under large deformations in contrast to a linear structural method [37].

The important relation between the tangent stiffness matrix mentioned in Section 1.2.1 and the quadratic mode shapes is outlined by several authors in the theory of multibody system dynamics with flexible bodies. In general, multibody systems use either modal or nodal coordinate formulations [17]. If time-dependent modal coordinates are used in combination with a suitable frame of reference, the *linear* mapping from generalized (modal) to physical (nodal) coordinates can be realized by mode shapes. However, multibody systems often deal with rotating structures such as helicopter or wind turbine blades which are subject to centrifugal stiffening due to centrifugal loads. If a nodal formulation is used, this effect can be considered by a tangent stiffness matrix; the quadratic mode components can be seen as its counterpart in modal space (this will be pointed out in the following chapters). This relation and the use of

quadratic mode components in multibody system dynamics is described in the work of Wallrapp and Wiedemann [17, 38, 39].

1.2.5 Modeling of the Free-flying Elastic Aircraft with Large Deformations

For aircraft characterized by a comparatively high structural stiffness, a simulation approach that assumes a separation of flight mechanic and elastic DOFs can be used without introducing large errors. In such cases, flight dynamics and loads analyses (maneuver simulation, gust and turbulence encounter) can even be done with the rigid aircraft and stability analyses (flutter) are then based on the natural (in-vacuo) mode shapes and corresponding eigenvalues of the aircraft in its undeformed configuration. This approach can be justified because the magnitudes of the aerodynamic and structural loads induced by the elastic deformations are well below those induced by the rigid-body motions. However, only few aircraft fall in this category.

If a pronounced structural flexibility of the aircraft is noticeable, the interaction between the rigid-body and the elastic degrees of freedom must be taken into account for flight dynamics and loads analysis. For most transport aircraft, the lowest structural modes (in terms of frequency) show the largest contribution to the steady and unsteady structural deformations during flight, thus a strong interaction with flight mechanic rigid-body modes (mainly the short-period mode) is to be expected. This in turn renders the approach of separating the rigid-body and elastic degrees of freedom ad absurdum and demands their concurrent solution. Typical frameworks for such aeroelastic analyses used in academic and industrial context are Nastran and ZAERO. Both are limited to the aerodynamics represented by the doublet-lattice method, such as small displacements of lifting surfaces and compressible but isentropic and inviscid flow but are able to handle complex (but linear) 3D FE models. The main field of application of these methods is the static aeroelastic analysis, including trim, as well as unsteady maneuver loads simulations including gust and turbulence encounter as well as flutter [18, 40]. Both Nastran and ZAERO make use of rigid-body and elastic mode shapes to represent the motion of the aircraft. The governing equations of motion using rigid-body modes are the result of further linearization of the mean axes equations given by Waszak and Schmidt and are only valid for very small rigid-body motions superimposing a steady state (as is typical for most gust encounter scenarios). If an aircraft shows large rigid-body motions and comparatively small structural deflections in ordinary flight maneuvers (as will be the case for most jet transport), the application of Waszak and Schmidt's mean axes equations of motion might be justified. However, as will be shown, using the mean axes assumptions for flight dynamics poses several problems. It is per se limited to free-free (unclamped) structural models and its validity for larger structural deflections is still discussed [41]. Despite the high computational costs, frameworks using aerodynamic methods of high fidelity (CFD) for steady and unsteady flight dynamics and loads analyses with linear structural dynamics are gaining popularity, even though most of them are restricted to linear structural dynamics [6, 42].

One of the goals of this thesis is the flight dynamic simulation of free-flying highly flexible aircraft in the time domain. According to Silvestre, the term *very flexible* is related in this context to an aircraft which experiences large elastic displacements in flight for which the assumptions necessary for the application of linear structural methods are violated [43]. Several authors have demonstrated approaches and methods for flight dynamics simulations of very flexible aircraft. In terms of large geometric deformations, most of them are based on beam-type representations of the underlying structural model [3, 4, 44]. However, as mentioned, most of those beam models are highly sophisticated with only few assumptions or limitations regarding e.g. the overall magnitude of deformations. Also large, nonlinear rigid-body motions can be part of the solution. To the author's knowledge, no framework is available and no publication has demonstrated the use of a general, geometrically nonlinear structural dynamics method (for complex 3D FE models) in flight dynamics simulations including unbounded rigid-body motions so far.

1.2.6 Governing Equations of the Free-flying Flexible Aircraft

In the following, approaches for the derivation of governing equations of the free-flying elastic aircraft, in which elastic structural deformations are described by a number of shape functions multiplied by time-dependent generalized coordinates (modal approach), are reviewed. From a historical point of view, completely independent methods were used for the calculation of either the flight mechanic or the aeroelastic characteristics (e.g. divergence and flutter) of an aircraft. Structural deformations and vibrations were assumed to be small and of high frequency which allows the use of a decoupled approach, even if rigid-body motions are large and nonlinear [8](pp. 168-175). The effect of elasticity on the stability and control of aircraft was recognized as significant as wings became slender and the flexibility of the whole airframe was increased. One of the first approaches to consider this effect was to introduce steady correction factors into the rigid aircraft equations and into the aerodynamic derivatives to account for structural flexibility [8, 45]. A first set of equations of motion of an unrestrained flexible aircraft is given by Bisplinghoff and Ashley [46]. Equilibrium conditions and Hamilton's principle are used for the derivation of the inertially uncoupled translational, rotational, and structural differential equations which are consequently linearized to enable a simplified calculation of small disturbances from steady rectilinear flight. Structural deformations are calculated by a set of free vibration modes of the undeformed structure.

The choice of an adequate body-reference coordinate system for the kinematical description of the coupled rigid-body and structural degrees of freedom is an elementary issue in the works described next. The widely used mean axes system is a non-inertial reference system which is not fixed to a material point of the body but moves with the body. It effectively decouples rigid-body and elastic degrees of freedom by assuming that the relative translational and angular momentum due to elastic deformation becomes zero at every instant [45]. However, inertial

coupling can be re-introduced by e.g., cross coupling of different modes or discrete mass offsets in the structural model [10, 47]. The main reason for the application and use of the mean axes assumptions is the resulting set of equations of motion which is greatly simplified because inertial coupling is almost completely removed. As will be shown in the following sections, the numerical solution is then considerably simpler due to a lower condition number of the mass matrix of the system. However, modern numerical solution techniques for ODEs and the computational resources available nowadays compensate for this disadvantage. Furthermore, it must be mentioned that the equations of motion remain coupled by the aerodynamic forces anyway.

Milne gives a derivation of the equations of motion of an unconstrained elastic body based on the conservation of linear and angular momenta [45]. He discusses three particular choices of body axes. First, *attached axes*, in which the origin remains at one particular material point of the structure and an axis of orientation follows the tangent of a curve formed by the material points originally defining the axis of orientation. Second, *mean axes*, to reduce inertial coupling between rigid-body and elastic degrees of freedom as mentioned above. Third, *principal axes*, which are preferably combined with locating the origin at the instantaneous center of mass of the body. Milne further describes the three body axis with illustrative examples to explain differences between mean and principle axes [48].

Etkin uses normal modes of free vibration with the mean axes assumptions and adds an additional structural equation (derived from Lagrange's equations) for every mode to the rigid-body equations of motion [8]. The resulting equations of motion are inertially decoupled, the author also mentions that in practice only a few of the lowest mode shapes need to be considered to calculate structural deflections.

The well-known work of Waszak and Schmidt describes the derivation of closed-form expressions for the flight dynamics of aeroelastic vehicles [9, 49]. Equations of motion for the flexible aircraft are developed from Lagrange's equations and the principle of virtual work. The mean axes system is applied together with free vibration modes of an unconstrained body to locate the origin and define a proper orientation of the body axis, the resulting equations are only coupled through the aerodynamic forces. An aerodynamic strip theory is used to determine generalized aerodynamic forces.

Buttrill, Zeiler, and Arbuckle derive the equations of motion of an elastic aircraft with concentrated masses using Lagrangian mechanics [10]. Although the authors make use of the mean axes conditions for the final equations of motion, it is pointed out in the derivation which terms in the energy expressions must be kept if mode shapes of a clamped structure are to be used for the calculation of structural deformations. The final governing equations account for changes in the vehicle's tensor of inertia due to deformation, second-order momentum coupling between elastic and rotational degrees of freedom is considered by cross-coupling of deformation and deformation rates of different modes.

A comparison of the studies and equations of motion from Waszak as well as from Schmidt and Buttrill, Zeiler, and Arbuckle is given in Waszak, Buttrill, and Schmidt [50].

Meirovitch uses a Lagrangian approach to derive hybrid equations of motion for flexible bodies (spacecraft) in terms of *quasi-coordinates*, where the body can undergo arbitrary rigid-body motion in addition to elastic deformations [51]. With regard to the kinematical description of aircraft flight dynamics, the concept of quasi-coordinates is seen to be advantageous since it allows an elegant expression of translational and rotational motions in components along the body axes of the aircraft. If these motions are expressed in body axes, the corresponding velocities (translational and rotational) are referred to as *quasi-velocities*. However, the quasi-velocities cannot be integrated to obtain displacements or angles in an inertial frame of reference, but a differential equation is used to link the kinematic relations between ordinary and quasi coordinates (and velocities), as outlined in Section 2.2.1.

Meirovitch and Tuzcu argue against the mean axes concept in aeroelastic applications [41]. Their equations of motion of a flexible structure are given in body axes rather than mean axes, hence terms accounting for inertial coupling between rigid-body and elastic degrees of freedom are part of the state equations of motion.

Reschke derives inertially coupled equations of motion for the elastic aircraft [47, 52] using Lagrange's equations in quasi-coordinates. A discretized structural model with lumped masses is used and the mean axes assumptions are introduced. However, Reschke considers offsets of discrete masses in the lumped mass model with respect to structural nodes and obtains inertially coupled equations of motion.

1.2.7 Integrated Simulation Models and Frameworks

Besides the use of shape functions, several other approaches are adopted for the calculation of structural deformations together with rigid-body motions of flexible aircraft. Most notably are nonlinear beam theories which have become very important mainly for the modeling of *very flexible aircraft*. However, different approaches such as the use of multibody simulation software in combination with adequate aerodynamic methods are gaining attraction. In addition to the equations of motions for flexible aircraft mentioned in the previous section, integrated simulation models and programs have been developed and successfully applied to aeroelastic simulations. Selected works are reviewed in the following including the modeling of the steady and unsteady aerodynamic forces. A rough distinction can be made between integral simulation models and approaches in which the relevant disciplines (aerodynamics, structural dynamics, and rigid-body motions) are treated independently and coupled spatially and temporarily. An integral aircraft simulation model is based on a coupled set of governing equations of motion that includes the steady and unsteady aerodynamic forces and is written in state-space form. The approach for the simulation of the free-flying elastic aircraft applied in this thesis treats the aerodynamic method and the structural and flight mechanic methods independently of

each other. Approaches of this type are mainly used if one of the disciplines is handled by an independent, i.e., stand-alone or commercial program. A typical example in flight dynamics and loads analysis of flexible aircraft is the use of a mid- or high-fidelity aerodynamic solver (e.g. vortex-lattice or CFD) for the calculation of the aerodynamic forces coupled with a simpler, modal-based structural solver.

Linear and Nonlinear Rigid-Body Motion and Linear Structural Dynamics

Looye introduces an object-oriented, integral simulation framework based on the equations of motion derived by Waszak and Schmidt [53]. A lumped mass model is used and the tensor of inertia of the aircraft is assumed constant as the aircraft deforms. In addition to the mean axes, local reference systems are attached to particular material points of the aircraft to attach e.g. engines or sensor models. The kinematics of these local points are described by the motion of the mean axes (with respect to an inertial system), plus the elastic deformations. A doublet-lattice aerodynamic model provides the unsteady aerodynamic forces which are transformed into the time domain using a rational function approximation.

Meirovitch and Tuzcu describe time domain simulations of flexible aircraft using a unified formulation to treat the aircraft as a single system [54, 55]. The elasticity of the aircraft is modeled by flexible components (each having their own shape functions) for the fuselage, the wing, and the empennage, where a set of reference frames is attached to different parts of the aircraft that act as different body systems. However, all elastic motions of the components are finally related to a body system attached at the undeformed fuselage acting as reference frame for the entire aircraft. The use of mean axes is explicitly avoided, and the equations of motions are formulated in terms of quasi-coordinates.

Kier develops integral aircraft models for flight loads analysis based on the equations of motion derived by Waszak and Schmidt with the extensions of Reschke [56]. Dynamic loads of a large jet transport aircraft obtained from different aerodynamic theories (quasi-steady vortex-lattice method, extended strip theory with indicial functions, and doublet-lattice method with rational function approximation) are discussed. Kier's results prove the superiority of the doublet-lattice method for gust load calculation of large elastic aircraft.

Silvestre and Luckner introduce a methodology for modeling coupled flight dynamics and aeroelasticity in the time domain, also based on the equations by Waszak and Schmidt [43, 57]. A strip theory is used for the calculation of aerodynamic forces in the time domain expressed as a set of differential equations; the method is successfully applied to time response simulations of a Stemme S6 motor glider.

An approach to the integral modeling of flexible aircraft is given by Mauermann [58]. The inertially decoupled equations of motion are combined with an unsteady, wake-shedding potential-flow solver (unsteady vortex-lattice method) and solved in the time domain. The ap-

proach is used to calculate structural loads of a large jet transport in a wake vortex encounter scenario.

Ritter and co-workers use linearized and inertially decoupled equations of motion to calculate structural loads of an elevator input maneuver and a gust encounter scenario of a large transport aircraft [11, 42, 59]. For the gust encounter simulations, small translational and rotational disturbances superimpose the trimmed flight state, thus rigid-body mode shapes are used to represent rigid-body motions. Compared to the previous methods, a separated approach is used in the sense that an external CFD solver calculates the unsteady aerodynamic forces. A *Conventional-Serial-Staggered* algorithm is used for the weak temporal coupling of aerodynamics and structural dynamics.

Linear and Nonlinear Rigid-Body Motion and Geometrically Nonlinear Structural Dynamics

An integral aircraft simulation model based on geometrically nonlinear beam elements for arbitrary large displacements and potential-flow aerodynamics was developed by Drela [60]. A full Newton method is used to solve the coupled nonlinear equations of motion in the time domain, frequency response and eigenvalue analysis are also performed. The model is applied to simulate an asymmetrical gust encounter and to determine the static stability of a lightweight sailplane. Based on this work, Drela also developed the program *ASWING* for the calculation of static and dynamic loads as well as deformations of flexible aircraft and gives detailed derivations of the underlying physical and mathematical models⁵. An unsteady lifting line theory links the nonlinear equations of motion.

Patil et al. present a similar framework to simulate *High-altitude long-endurance* (HALE) type aircraft where intrinsic beam equations are used to represent the structural dynamics and the finite-state model of Peters is used for the calculation of aerodynamic loads [3]. The necessity to include the nonlinear flexibility effects in the trim, flutter, and stability analysis of highly flexible aircraft because of significant changes in the aerodynamic loads due to deflection is clearly pointed out.

Cesnik and co-workers derive the governing equations of motion and introduce a framework for very flexible aircraft based on a geometrically nonlinear, strain-based beam structural model in combination with nonlinear rigid-body motions [4, 61, 62]. A potential-flow finite state aerodynamic model calculates steady and unsteady aerodynamic forces, the equations of motion and aerodynamic loads are integrated simultaneously using a modified Newmark method. The program is known as the *University of Michigan Nonlinear Aeroelastic Simulation Toolbox (UM/NAST)*. It features modules for the calculation of steady trim conditions and flutter speeds, and enables the simulation of nonlinear rigid-body motions with linearized structural solutions. The program was applied for the modeling of several HALE aircraft [1, 20, 63]; it is

⁵ASWING 5.81 Technical Description, <http://web.mit.edu/drela/Public/web/aswing/>

also used to calculate nonlinear aeroelastic reference solutions for the validation of the method proposed in this thesis. It must be mentioned that the latest version uses a geometrically nonlinear vortex-lattice method to calculate steady and unsteady aerodynamic forces [64].

Aeroelastic modeling using geometrically exact intrinsic beam models with velocities and strains as independent variables is the content of the work of Palacios and co-workers [65]. An evaluation of different structural dynamics models to be used in frameworks for nonlinear flight dynamics simulations of very flexible aircraft, including displacement and strain-based, as well as intrinsic, geometrically nonlinear composite beams is discussed [5]. Murua et al. introduce an aeroelastic program based on a geometrically exact, nonlinear composite beam model (intrinsic formulation) combined with an unsteady vortex-lattice method which is finally linearized in time and space to obtain an integral, linear state-space model of the aeroelastic system [44]. A detailed overview of the theoretical derivation and the implementation is given in the thesis of Murua [66]. Several nonlinear aeroelastic test cases demonstrate the power of his aeroelastic tool.

The geometrically nonlinear simulation programs mentioned above make use of nonlinear beam theories which are not able to handle complex 3D FE models. A few methods have been developed to account for such structural models in nonlinear flight dynamics simulations. The application of ROMs of nonlinear structures subjected to large deformations is worth mentioning in this regard. In a recent publication, Howcroft et al. apply different methods to investigate the effects of large structural deformations on the aeroelastic behavior of a highly loaded, high aspect ratio wing. An approach based on a weighted sum of continuous shape profiles (which are able to reflect e.g. shortening effects) are tested besides nonlinear beam theories and a rigid element multi body method. Very good agreement between the different methods is obtained for a nonlinear structural test case in static tip loading. As expected, large differences between linearized and fully nonlinear structural solutions are obtained as the deformation of the tip reaches values greater than 30% of the semi-span [67].

Multibody simulation techniques can also be combined with aerodynamic solvers of different fidelities. They have been successfully used for the modeling of high aspect ratio wings and HALE aircraft. Two advantages follow from this approach. First, a highly flexible structure can be modeled easily by linking a set of rigid or elastic bodies with joints where the stiffness properties of the entire structure are represented for example by torsion springs connected to the joints. A local frame of reference is attached to each of the bodies and the elastic deformations are expressed in terms of the local body frame. Since the translational and the rotational motions of the local frames are almost unrestricted, the structure as a whole can take states of high deformation, even if strains and deformations of the local elements are small (this approach is comparable to the corotational formulation described in Section 1.2.1). Second, components attached to the main structure by joints (such as flaps, control surfaces, or even a complex landing gear setup) can be considered without effort even if large motions relative to each other occur. The inclusion of flight mechanics in the aeroelastic simulation is straight

forward because a coordinate system serving as body (aircraft) reference frame can easily be attached to one of the joined bodies. However, as was mentioned for the reduction of a 3D FEM to an equivalent beam model, the setup of the joined bodies goes hand in hand with major simplifications of the structure.

Krüger uses the multibody dynamics program *SIMPACT* for aeroelastic analyses of the *HELIOS* UAV [68]. Different rigid segments with particular mass and aerodynamic properties are coupled to setup the simulation model; torsion springs and dampers connecting the segments define the structural characteristics of the aircraft. An integral simulation model with the possibility for linearization around selected trim states was built with this approach. Trim analyses for different mass configurations clearly show nonlinear trends in the trim variables as the deformations increase, an investigation of the phugoid offers an explanation for the dynamically unstable behavior of the *HELIOS* as the deformation of the wing reaches very high values.

Castellani simulates a generic, flexible aircraft with a high aspect ratio wing using a nonlinear FE and a multibody approach in combination with strip theory aerodynamics [69]. The normalized tip deflections of the wing reach values up to 50% of the semi-span, significant differences between the linear and nonlinear results arise in terms of the trim angles of attack and the structural loads.

1.3 Objectives and Outline of the Dissertation

1.3.1 Objectives of this Work

In the previous sections the current state of the art for the numerical modeling of geometrically large displacements for aeroelastic applications was pointed out. Advantages and disadvantages of the particular methods became evident. Methods applicable to general 3D FE models based on Lagrangian formulations (either the total or updated, or the corotational) are involved and computationally extensive from a practical perspective; the extension of the theoretical formulations to include rigid-body degrees of freedom can become a complex task. Even though such methods are implemented in a number of commercial FE software packages, they are limited to clamped structures, i.e. the flight dynamic simulation of free-flying elastic aircraft with nonlinear rigid-body motions is not possible to date. Nonlinear beam theories may require complex conversions of 3D finite element models accompanied by the neglect of important structural details. Considering this creates the desire for a computationally inexpensive structural dynamics method applicable to general finite element structures which combines large rigid-body motions and geometrically nonlinear deformations. The goal of this thesis is to propose such a method to fill this gap. Starting point is the modal approach because of the many benefits it already holds especially for aeroelastic applications. Its two major drawbacks w.r.t. large deflections are corrected systematically.

The first drawback is the linear force-displacement relation represented in modal space by the eigenvalues and the (in vacuo) eigenvectors of the structure. The second one is the linear mapping between the modal (generalized) and the nodal (physical) space also by means of the (in vacuo) eigenvectors of the structure. The latter results in a geometrically linear nodal displacement field omitting significant nonlinear effects such as foreshortening and coupling of deformations due to external force fields superimposed in a certain way. As an example, the coupling of out-of plane bending and torsion deformations at a cantilever beam induces in-plane bending deformations which are not reflected by linear solutions. The linear force-displacement relation is extended by quadratic and cubic stiffness terms (tensors) in the governing equation of motion, which is formulated in modal space. Modes shapes of quadratic, cubic, and fourth-order – referred to as *higher-order mode components* in this thesis – render the linear mapping from modal to Euclidean (physical) space nonlinear and hence allow for highly curved nodal displacement fields. A key feature of the proposed method is the consideration of the coupling effects which appear in nonlinear solutions if modes are superimposed by the higher-order stiffness and mode components. In the classical modal approach this coupling is nonexistent. A further drawback of the modal approach is the inability to consider changes in the stiffness properties of the structure as the applied loads or deformations are increased. As mentioned in Section 1.2.1, this is accounted for by the tangent stiffness matrix in nonlinear finite element analyses. However, the quadratic mode components used in the proposed method, which can be seen as the equivalent to the tangent stiffness matrix in modal space, provide an elegant way to account for load and deformation dependent changes of the stiffness properties (this feature is of high importance in aeroelastic applications due to the nonconservative nature of the aerodynamic forces). As will be shown, the proposed method assumes that even in the case of large structural deflections (beyond the linear regime), the nodal deformation field can still be expressed by the superposition of shape functions (the mode components), i.e. mode shapes can be identified in geometrically nonlinear solutions as well as in linear ones. The numerical studies serve as proof of this assumption.

A further goal of this thesis is the extension of the proposed method by rigid-body DOFs to simulate the free-flying elastic aircraft. Emphasis is put on the derivation of a set of integral (rigid-body and elastic DOFs) governing equations of motion in which as less assumptions as possible are made concerning the structural deformations. The widely used mean axes constraints, which provide a means of inertial decoupling of the rigid-body and the elastic motion are not applied in this work because of two reasons. First, they assume small structural deflections a priori [9, 10]. The second, a more practical, reason is that the higher-order stiffness and mode shape components which form the basis of the proposed method, can only be calculated for clamped structural models. A series of geometrically nonlinear simulations is required to extract these higher-order components, as described in Section 2.3. MSC Nastran is used for the structural solution, and by now has no option to apply a *nonlinear* inertia relief in combination with large geometric deflections. Thus the extracted linear and the higher-order

mode components have clamped boundary conditions. Such modes, on the other hand, do not fulfill the mean axes constraints per definitionem [10]. The circumvention of this problem requires a different formulation of the flight dynamic equations in which terms are included that account for the inertial coupling between rigid-body and elastic DOFs.

1.3.2 Dissertation Outline

This thesis is organized in chapters that describe the theoretical basis of the proposed method, discuss simulation results of three test cases, and give a summary of the main conclusions and recommendations for future work.

In Chapter 2, both the governing equation of the proposed method without rigid-body DOFs as well as the flight dynamics equations of motion are derived. The derivation of the governing equation without rigid-body DOFs is composed of two parts following the two extensions mentioned above. First, a Taylor series expansion is applied to the strain energy of the structure, which is assumed to be a nonlinear function of deformation. The application of Castigliano's first theorem to this strain energy function yields a nonlinear, static structural governing equation with quadratic and cubic generalized stiffness terms. Second, another Taylor series expansion is applied to a particular, nonlinear nodal displacement field from which the higher-order (quadratic, cubic, and fourth-order) mode components are determined. Rigid-body DOFs are added by deriving the governing equations of motion of the free-flying elastic aircraft using Lagrange's equations of the second kind in quasi and modal coordinates. As mentioned above, no simplifications (such as mean axes constraints) are applied to obtain equations in which rigid-body and elastic DOFs are coupled by inertia and gyroscopic forces. The higher-order stiffness and mode terms are identified in a preprocessing step by a series of nonlinear, static solutions with the structural model. Polynomials of higher order are fitted to the results, the polynomial coefficients then correspond to the higher-order components. This process is outlined in detail and a convergence study shows the influence of important parameters such as amplitudes and numbers of nonlinear solutions on the higher-order components.

Chapter 3 describes the setup and details of the program used for the steady and unsteady aeroelastic simulations of the test cases. Its aerodynamic solver is based on the unsteady vortex-lattice method with extensions that account for the calculation of induced and viscous drag forces (which is an important aspect if vehicles operating at low Reynolds numbers, such as the X-HALE, are considered). The data transfer between the aerodynamic and the structural model is done by a coupling method based on spatial interpolation functions, the concept of the *coupling model* used for beam-type structural models is explained. A brief explanation of the theory of the vortex-lattice method is followed by the description of the method applied for the fluid-structure interaction process.

Chapter 4 demonstrates applications of the proposed method to three test cases with increasing complexity. Starting with a simple clamped beam structure, the basics of the method

are outlined in static structural response. The influences of the coupling terms and the linear stiffness term (which is a function of deformation and structural loads) are elaborated in this test case. The second test case is a tapered slender wing box of high aspect ratio represented by a 3D FE model. It is built from shell elements where anisotropic material properties are used to model the fiber reinforced plastic structure. The steady structural and aeroelastic response is simulated and validated with fully nonlinear reference solutions. Additionally, the influence of linearized structural solutions in the aeroelastic simulation on steady structural loads is analyzed. Finally, the X-HALE UAV from the University of Michigan is simulated using the proposed method. The model is first verified in a number of static structural and aeroelastic simulations using MSC Nastran as a reference. Subsequently, trim simulations for steady horizontal flight are performed and the results used as initial conditions for the unsteady free-flight maneuver simulations. Symmetric sinusoidal tail deflections as well as gust encounter scenarios provide a challenging test case for the proposed method including rigid-body degrees of freedom. The nonlinear reference solutions for validation of the trim and maneuver simulations are provided by the UM/NAST aeroelastic solver from the University of Michigan, which is described briefly in Section 1.2.7. Detailed information about the setup and characteristics of the aerodynamic (vortex-lattice) and the structural models are given for all three test cases. Furthermore, emphasis is put on a rigorous verification and validation of the results of the proposed method with nonlinear reference solutions, either from MSC Nastran or from UM/NAST. Linear structural and aeroelastic results are added whenever it appears meaningful and to provide additional insight into the differences between nonlinear and linear solutions.

The work is summarized in Chapter 5, where the most important findings are recapitulated and conclusions are drawn. The new scientific contributions of the thesis are highlighted; ideas for improvements and future topics of research for the proposed method are suggested.

Chapter 2

Structural and Flight Dynamics Equations of Motion

The theoretical derivation of the proposed method is the content of this chapter. In Section 2.1, the static and the dynamic equations of the proposed method are derived where only elastic DOFs are considered. Rigid-body motions are incorporated in Section 2.2. This splitting is chosen intentionally because the method can be used equally well to model fixed structures and the derivation is laid out more clearly in this way. The final governing EOMs of the free-flying flexible aircraft are then given in an integral form. Finally, a method for the calculation of the higher-order stiffness and mode components based on polynomial fitting is introduced in Section 2.3.

2.1 Derivation of the Static Equation of Motion

2.1.1 Higher-order Strain Energy Formulation

A mechanical system consisting of a restrained, continuous elastic body subjected to internal and external loads is considered first. The total potential energy of the body, π , is given as the sum of the total strain energy, U , and the potential energy of the applied loads, V . Furthermore, the total potential energy of the system is constant. This statement is expressed as [70]:

$$\pi = U + V = \text{const.} \quad (2.1)$$

Assuming linear elastic material behavior (Hooke's law), and neglecting the influence of temperature, the total strain energy U in the body is given as the following function (here and on what follows, variables with equal indices are summed over their range):

$$U = \frac{1}{2} \int_V \tau_{ij} \epsilon_{ij} dv \quad (i, j = 1, 2, 3) \quad , \quad (2.2)$$

where τ_{ij} and ϵ_{ij} are the stress and strain component pairs. Finite strain theory is applied here by employing the second Piola-Kirchhoff stress tensor and the Green-Lagrange strain tensor for τ_{ij} and ϵ_{ij} , respectively. The work done by the applied loads V can be expressed as

$$V = - \int_V B_i u_i dv - \int_S T_i^{(\nu)} u_i ds , \quad (2.3)$$

where B_i represents the components of the applied body forces, u_i the components of the displacement field, and $T_i^{(\nu)}$ denotes the traction vector applied on the body surface. Traction on the boundary can be related to stresses via *Cauchy's formula* [70]

$$T_i^{(\nu)} = \tau_{ij} \nu_j \quad (2.4)$$

with ν as the unit outward normal vector. Introducing a variation of both the total strain energy and the external work by employing the variational operator δ yields

$$\delta\pi = \delta(U + V) = \int_V \tau_{ij} \delta\epsilon_{ij} dv - \int_V B_i \delta u_i dv - \int_S T_i^{(\nu)} \delta u_i ds , \quad (2.5)$$

where $\delta\epsilon_{ij}$ denotes the variation of the strain field and δu_i a virtual displacement field. The virtual displacement field must be consistent with the constraints imposed by the boundary conditions of the system, and from that the kinematic compatibility of the strain field directly follows. Invoking the principle of minimum total potential energy results in

$$\delta\pi = 0 . \quad (2.6)$$

Therefore, the variation of the total strain energy equals the negative variation of the external work

$$\delta U = -\delta V . \quad (2.7)$$

Introducing a discretization of the structure by finite elements with N nodes, the work of the external forces is reduced to discrete nodal loads (forces and moments), denoted as \mathbf{P}_i , multiplied by nodal translations and rotations, denoted as $\mathbf{\Delta}_i$. These nodal displacements are the result of the deformation of the body at point (i) in the direction of the applied loads, \mathbf{P}_i . The total potential energy is then given as

$$\pi = U - \sum_{k=1}^N \mathbf{P}_k \mathbf{\Delta}_k . \quad (2.8)$$

Taking the first variation of this expression leads to the first Castigliano theorem which states that the partial derivative of the strain energy (U) with respect to an arbitrary displacement (Δ_i) at a point (i) equals the load (\mathbf{P}_i) at this point in the direction of the displacement [70, 71],

$$\frac{\partial U}{\partial \Delta_i} = \mathbf{P}_i \quad (i = 1, \dots, N) . \quad (2.9)$$

The theorem similarly holds for nonlinear force-displacement relations and can be generalized by the introduction of generalized displacements \mathbf{q} and generalized forces \mathbf{Q} [70],

$$\frac{\partial U}{\partial \mathbf{q}_i} = \mathbf{Q}_i . \quad (2.10)$$

Now a vector ψ that contains discrete displacements for every node of the structure is defined as a linear combination in the following way:

$$\psi \equiv \sum_{i=1}^m s_i \mathbf{a}^i , \quad (2.11)$$

where s_i denotes a scalar value which is an element of the vector \mathbf{s} ,

$$\mathbf{s} \equiv (s_1, s_2, \dots, s_m)^T , \quad (2.12)$$

and

$$\mathbf{a}^i = (\Delta_1, \dots, \Delta_N)^T \quad (2.13)$$

contains constant (and for now arbitrary) displacements for each node. The upper bound of the summation in Eq.(2.11), m , is equal to the number of generalized coordinates of the final governing equation that is to be derived in the following sections. Now the total strain energy, Eq.(2.2), is assumed to be a *nonlinear* and continuously differentiable function of the externally applied displacements ψ , which are a function of the scalar value s_i only, and expanded in a Taylor series centered at zero (since the internal energy is zero for zero deformation)

$$\begin{aligned} U(\mathbf{s}) &= \sum_{i=1}^m \frac{\partial U}{\partial s_i} s_i \\ &+ \frac{1}{2!} \sum_{i=1}^m \sum_{j=1}^m \frac{\partial^2 U}{\partial s_i \partial s_j} s_i s_j \\ &+ \frac{1}{3!} \sum_{i=1}^m \sum_{j=1}^m \sum_{k=1}^m \frac{\partial^3 U}{\partial s_i \partial s_j \partial s_k} s_i s_j s_k \\ &+ \frac{1}{4!} \sum_{i=1}^m \sum_{j=1}^m \sum_{k=1}^m \sum_{l=1}^m \frac{\partial^4 U}{\partial s_i \partial s_j \partial s_k \partial s_l} s_i s_j s_k s_l + H.O.T. \end{aligned} \quad (2.14)$$

Application of the first Castigliano theorem and partial differentiation of the strain energy defined in Eq.(2.14) yields a governing equation with stiffness terms that quadratically and cubically depend on s , which is the desired nonlinear force-deformation relation. The term $\frac{1}{2!} \sum_{i=1}^m \sum_{j=1}^m \frac{\partial^2 U}{\partial s_i \partial s_j}$ in Eq.(2.14) is comparable to the linear stiffness matrix of the structure. The Taylor series is carried out up to the fourth order so to capture up to cubic nonlinearities on the stiffness.

In general – and additionally to a deformation field as the one given by ψ – two approaches are possible in order to “excite” the structure and to identify the nonlinear force-displacement relations [23]:

1. A *displacement field* can be imposed on the structure’s degrees of freedom. A nonlinear static FE simulation solves for the unknown forces at each structural node as a result of the applied displacements.
2. A *force field* can be imposed on the structure. A nonlinear static FE simulation yields the corresponding deformation field.

The second approach will be applied for the further derivation because the imposition of a forced field turned out to be much easier from a practical point of view in a nonlinear structural solution than the imposition of a deformation field. The question arises what “shape” the force field should have. In the preceding formulas, *nodal* coordinates were used. The goal of this work is to obtain a governing equation based on generalized coordinates with corresponding shape functions (eigenvectors in the linear case). In the following, the natural (in vacuo) eigenvalues and corresponding eigenvectors of the structure are assumed to be available. Using one eigenvector, a nodal force field (denoted as F^i) can be defined in the following way:

$$\mathbf{F}_i = \mathbf{K} \phi^i q_i , \quad (2.15)$$

where \mathbf{K} denotes the linear stiffness matrix of the structure, q_i a scaling factor (for now), and ϕ^i denotes the column vector of one of the natural eigenvectors of the structure. Applying this force field in a nonlinear FE simulation results in nodal displacements u_i which are a function of the scaling parameter q_i . Using a comparatively small value for q_i – which in turn yields small deformations – results in a deformation field that qualitatively equals the mode shape ϕ^i . Increasing the value of q_i in the nonlinear simulation at some point results in a deformation field that shows significant differences to the linear deformation field (cf. Fig. 1.1). This becomes obvious if for example the first bending mode shape is applied to ϕ^i . The linear part of the deformation field consists of pure transverse displacements, whereas for larger values of q_i in-plane deformations significantly emerge. In summary, the following reasons support the application of a force field (and especially one that is chosen according to Eq. 2.15) to excite the nonlinearities in a FE simulation:

1. Imposing a force field onto the structure and solving for the displacements in a nonlinear static FE simulation turned out to be simpler from a practical point of view than imposing a displacement field and solving for the forces.
2. The force field according to Eq.(2.15) yields a deformation field that equals the eigenvector ϕ^i for the linear case (small values of q_i).
3. In the nonlinear case (large q_i), nonlinearities in the strain energy and/or the deformation field are excited.

In the following, the nonlinear energy part is further considered. If the structure is loaded by the force field defined in Eq.(2.15), the strain energy can be seen as a function of the scaling parameter q_i (the nodal stiffness matrix and the eigenvector are constants). The Taylor series expansion of the internal strain energy as function of the scaling parameters q_i is then given by

$$\begin{aligned}
U(\mathbf{q}) &= \frac{1}{2!} \sum_{i=1}^m \sum_{j=1}^m \frac{\partial^2 U}{\partial q_i \partial q_j} q_i q_j \\
&+ \frac{1}{3!} \sum_{i=1}^m \sum_{j=1}^m \sum_{k=1}^m \frac{\partial^3 U}{\partial q_i \partial q_j \partial q_k} q_i q_j q_k \\
&+ \frac{1}{4!} \sum_{i=1}^m \sum_{j=1}^m \sum_{k=1}^m \sum_{l=1}^m \frac{\partial^4 U}{\partial q_i \partial q_j \partial q_k \partial q_l} q_i q_j q_k q_l + H.O.T. \quad (2.16)
\end{aligned}$$

The term $\sum_{i=1}^m \frac{\partial U}{\partial q_i} q_i$ is omitted since no energy contribution as a linear function of q_i exists. Using the first Castigliano theorem again and applying a partial differentiation with respect to \mathbf{q} centered at zero yields the governing equation of the structure as a function of \mathbf{q} ,

$$\begin{aligned}
\frac{\partial U}{\partial q_p} &= \sum_{i=1}^m \frac{\partial^2 U}{\partial q_i \partial q_p} q_i \\
&+ \frac{1}{2!} \sum_{i=1}^m \sum_{j=1}^m \frac{\partial^3 U}{\partial q_i \partial q_j \partial q_p} q_i q_j \\
&+ \frac{1}{3!} \sum_{i=1}^m \sum_{j=1}^m \sum_{k=1}^m \frac{\partial^4 U}{\partial q_i \partial q_j \partial q_k \partial q_p} q_i q_j q_k + H.O.T. \quad (p = 1, \dots, m) \quad (2.17)
\end{aligned}$$

The following definitions are introduced for a more compact notation:

$${}^p G_1^i \equiv \left. \frac{\partial^2 U}{\partial q_i \partial q_p} \right|_{\mathbf{q}=0}, \quad (2.18a)$$

$${}^p G_2^{ij} \equiv \left. \frac{1}{2!} \frac{\partial^3 U}{\partial q_i \partial q_j \partial q_p} \right|_{\mathbf{q}=0}, \quad (2.18b)$$

$${}^p G_3^{ijk} \equiv \left. \frac{1}{3!} \frac{\partial^4 U}{\partial q_i \partial q_j \partial q_k \partial q_p} \right|_{\mathbf{q}=0}. \quad (2.18c)$$

The idea of the proposed method is to take the ${}^p G_n$ stiffness tensors as generalized stiffnesses and the \mathbf{q} as generalized coordinates. In this way, the following equation with the generalized coordinates as independent variables is obtained and used as the basis for the method:

$${}^p G_1^i q_i + {}^p G_2^{ij} q_i q_j + {}^p G_3^{ijk} q_i q_j q_k = Q^p \quad (p = 1, \dots, m). \quad (2.19)$$

Here the summation convention is used again. Since the strain energy defined in Eq.(2.16) was developed up to the fourth order, the resultant governing equation (2.19) contains a quadratic and a cubic stiffness term. The linear stiffness term, ${}^p G_1^i$, is a second-order tensor that equals the eigenvalues of the structure in the sense of the (linear) modal approach. A coupling of two modes would be enabled by off-diagonal entries. However, as will be shown in the following sections, the linear stiffness term is a diagonal matrix as is the matrix of the structure's eigenvalues. The quadratic and the cubic stiffness terms, ${}^p G_2^{ij}$, and ${}^p G_3^{ijk}$, are third- and fourth-order tensors, respectively. They enable the coupling of three and four modes by the corresponding entries. It must be mentioned that a nonzero value of the ${}^p G_2^{ij}$ term indicates a non-isotropic structural behavior ¹. It must also be mentioned that the linear case can always be recovered by omitting the stiffness terms of higher order in Eq. (2.19). The static governing equation derived above is similar to higher-order structural governing equations introduced by other researchers [23]. However, in this work it is derived using a higher-order definition of the strain energy of the structure.

2.1.2 Higher-order Deformation Representation

The second extension of the modal approach is the geometrically nonlinear displacement field. In the context of this section, flexible aircraft structures and their sub-components (mainly the wings) are considered. For such cases, the nonlinearity in the deformation field is pronounced by large displacements compared to a characteristic length of the structure, such as the wingspan. By contrast – and depending on the boundary conditions – plate structures

¹Applying a force field to such a structure would result in a softening or hardening in the corresponding direction of deformation, and a hardening or softening if the sign of the force field changes.

show nonlinear force-displacement behavior even for the case of deformations which are in the order of the thickness of the plate (due to membrane-bending coupling). Therefore, the expression *large deformation* is roughly defined as a normalized wingtip deflection larger than approximately 10% w.r.t. semi-span. Regarding the nodal displacement field for such large deformations manifests significant differences to the linear case. An illustrative example of these differences is given by the generic beam example in the introduction, the upper part of the plot is shown again in Fig. 2.1. Differences are significant in terms of the maximum deformation in

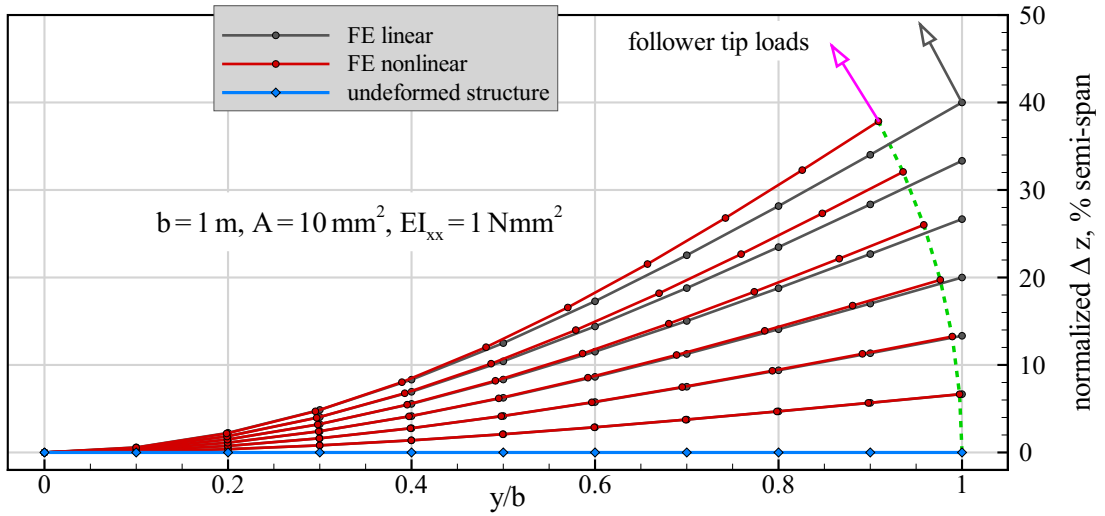


Figure 2.1: Generic cantilever beam subject to tip load, deformation field calculated by linear and nonlinear FE method.

the z , but also in the y direction. Furthermore, these differences are increasing progressively – mostly noticeable by means of the displacements in the y direction – with increasing amplitude of deformation, as illustrated by the green dashed line. The deformation field of the nonlinear FE solution evidently includes higher-order "deformation components". Since the length of the beam can be assumed to be constant even for large bending deformations, the true, i.e. non-linear kinematic deformation field must be composed not only of displacements in the z , but also in the y direction, which are by first approximation a quadratic function of the deformation amplitude, as will be shown. For small deformation analysis (linear case), these in-plane deformations can usually be neglected without introducing large errors.

The objective now is to define and include these higher-order deformation components. Therefore, a more rigorous derivation is given starting with a simple mathematical pendulum

as the one illustrated in Fig. 2.2. The kinematic relations in a Cartesian frame of reference are given by the trigonometric relations

$$v = \sin(\varphi) L \quad (2.20a)$$

$$u = \cos(\varphi) L \quad (2.20b)$$

Assuming small values for the amplitude φ of the pendulum, the small-angle approximation is

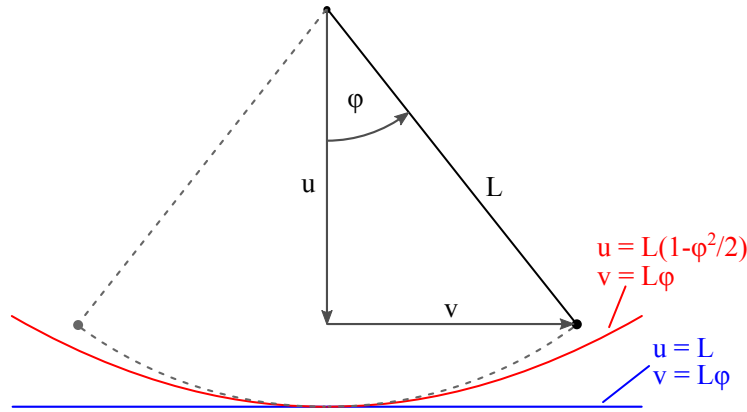


Figure 2.2: Kinematic relations on a pendulum; linear and parabolic approximation of the tip displacement plotted by blue and red lines.

used to simplify the analytical calculation of the motion of the pendulum. This simplification makes use of the Taylor series expansion of the sine and cosine functions:

$$\sin(\varphi) = \varphi - \frac{\varphi^3}{3!} + \frac{\varphi^5}{5!} + H.O.T. \quad (2.21a)$$

$$\cos(\varphi) = 1 - \frac{\varphi^2}{2!} + \frac{\varphi^4}{4!} + H.O.T. \quad (2.21b)$$

An extension of the small-angle approximation would have to include higher-order terms of the sine and cosine series expansions. Considering higher-order expressions for the approximation of a circular arc by adding the quadratic, cubic, and fourth-order terms given by Eqs.(2.21) yields the plots depicted in Fig. 2.3. Including the quadratic term yields a very good approximation of the arc up to an angle of approximately 25° . As expected, including the cubic and fourth-order terms further improves the approximation and reduces the difference to the actual line of the arc in both the z and the y direction. The error, defined here as difference between the arc's line and the polynomial approximations is plotted in Fig. 2.4 for a unit circle. Differences in the z direction are of course equal for the linear and the quadratic, as well as for the cubic and the fourth-order approximations. The same holds for the differences in the y direction for the quadratic and the cubic terms. As can be identified from these differences, using a fourth-order polynomial yields a very good approximation of the arc up to an angle

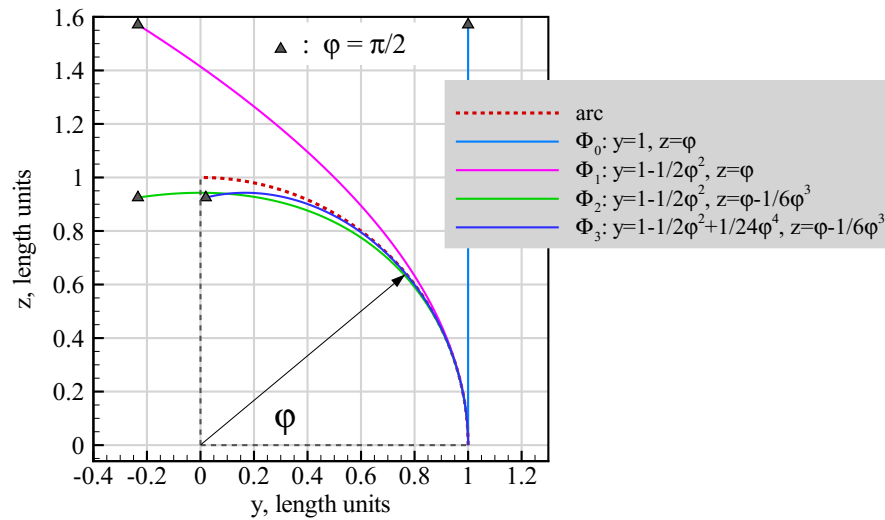


Figure 2.3: Approximation of a circular arc by linear, quadratic, cubic, and fourth-order polynomials as defined by the formulas in the legend.

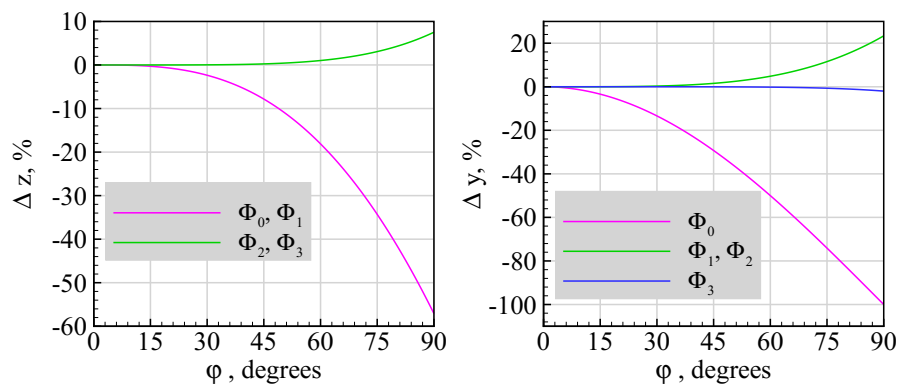


Figure 2.4: Differences in the z and in the y direction between the line of the arc and its polynomial approximations.

of approximately 45° . Approximating the nodal displacement field of a geometrically nonlinear structural simulation by shape functions of linear, quadratic, cubic, and fourth-order is the second extension of the proposed method.

In the context of this work, the nodal deformation field as a result of a nonlinear mapping of the force field defined in Eq.(2.15) is expanded in a Taylor series centered at zero which is truncated after the fourth term

$$\begin{aligned}
\mathbf{u}(\mathbf{q}) = & \sum_{i=1}^m \frac{\partial \mathbf{u}}{\partial q_i} q_i \\
& + \frac{1}{2!} \sum_{i=1}^m \sum_{j=1}^m \frac{\partial^2 \mathbf{u}}{\partial q_i \partial q_j} q_i q_j \\
& + \frac{1}{3!} \sum_{i=1}^m \sum_{j=1}^m \sum_{k=1}^m \frac{\partial^3 \mathbf{u}}{\partial q_i \partial q_j \partial q_k} q_i q_j q_k \\
& + \frac{1}{4!} \sum_{i=1}^m \sum_{j=1}^m \sum_{k=1}^m \sum_{l=1}^m \frac{\partial^4 \mathbf{u}}{\partial q_i \partial q_j \partial q_k \partial q_l} q_i q_j q_k q_l + H.O.T. \tag{2.22}
\end{aligned}$$

The constant term is omitted here. Substitution similar as defined above for the strain energy (Eq. 2.18) yields the following approximation for the nodal deformation field in Cartesian coordinates:

$$\mathbf{u}(\mathbf{q}) = {}^p\Phi_0 q_p + {}^p\Phi_1^i q_p q_i + {}^p\Phi_2^{ij} q_p q_i q_j + {}^p\Phi_3^{ijk} q_p q_i q_j q_k \ . \tag{2.23}$$

The (amplitude-dependent) mode shape with higher-order components is obtained by partial differentiation of the displacement field with respect to the generalized coordinates,

$${}^p\Phi(\mathbf{q}) = \frac{\partial \mathbf{u}}{\partial q_p} = {}^p\Phi_0 + 2 {}^p\Phi_1^i q_i + 3 {}^p\Phi_2^{ij} q_i q_j + 4 {}^p\Phi_3^{ijk} q_i q_j q_k \ , \tag{2.24}$$

where the sum is taken again over repeated indices. The term ${}^p\Phi_0$ can be seen as the equivalent of the normal modes of the structure. In the context of this thesis, the third-order tensor ${}^p\Phi_1^i$ is referred to as the *quadratic mode component*, the fourth-order tensor ${}^p\Phi_2^{ij}$ as the *cubic mode component*, and the fifth-order tensor ${}^p\Phi_3^{ijk}$ as the *fourth-order mode component*. As described above for the strain energy, these higher-order tensors enable the coupling of several modes with respect to the nodal deformation field due to the mixed partial derivatives in Eq.(2.22). Staying with the generic beam example from Fig. 2.1, the mode components of the first bending mode are plotted in Fig. 2.5 for illustration. For simplicity, only the non-zero components are considered. In this example, the quadratic component accounts for the in-plane displacements of the nodes of the beam in the (negative) y direction, the cubic component has negative sign and thus reduces the deformation in the z direction. The contribution from the fourth-order component acts in the y direction and has positive sign, it thus reduces the in-plane displacement of the quadratic component. Starting from the linear mode component, the natural amplitudes of the higher-order components are roughly two orders of magnitude smaller in this example. The contributions of the different mode components to the deformation field are shown illustratively for the first bending mode in Fig. 2.6. Proper values were chosen for

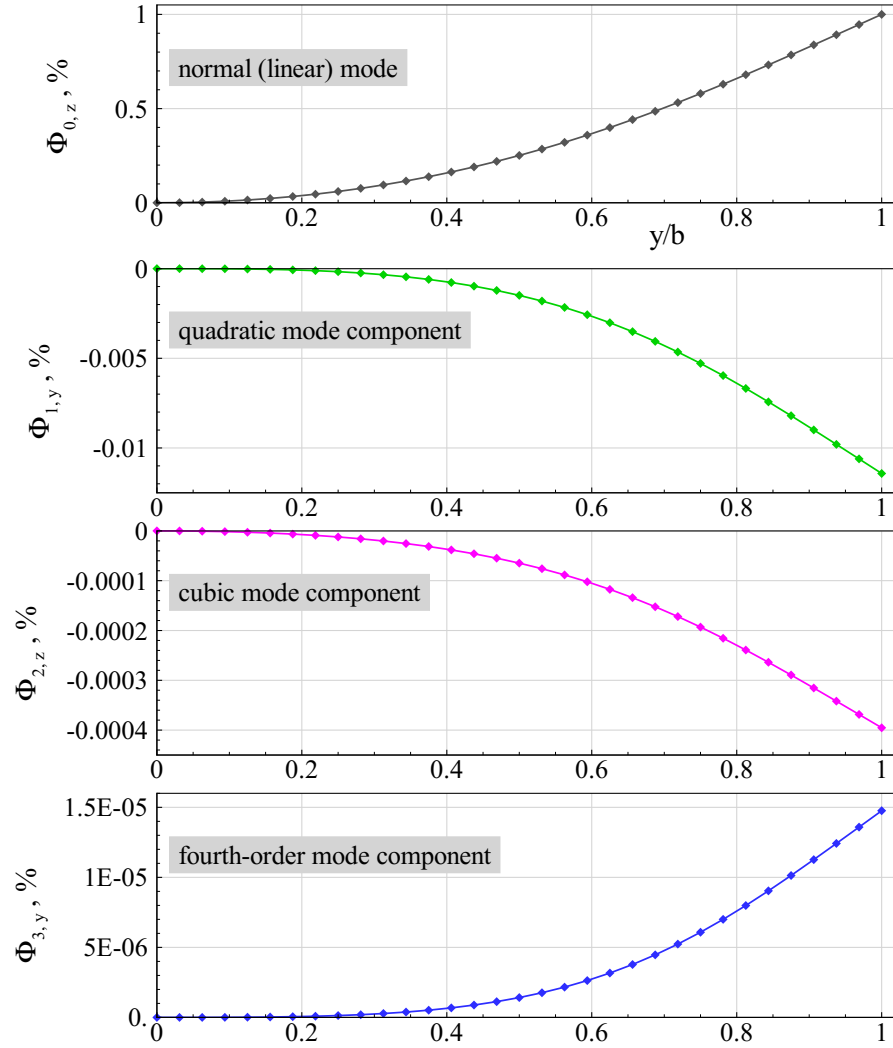


Figure 2.5: Linear, quadratic, cubic, and fourth-order mode components of the first bending mode of a generic beam. The maximum deflection of the linear mode is normalized to one.

q_1 and the nodal coordinates were calculated using Eq.(2.23). In contrast to the approximation of the arc (Fig. 2.3), where the quadratic component showed a large influence on the error of the approximation even for small angles, the quadratic and the cubic mode component almost equally contribute to the deformation field. The influence of the fourth-order term is rather small in this case and thus the approximation of the deformation field by higher-order modes can be seen as converged by considering mode components up to the fourth order.

2.1.3 Calculation of the Generalized Forces

According to Eq.(2.19), the right hand side of the modal governing equation consists of the generalized forces, Q^p , which are determined in the following by the application of the principle

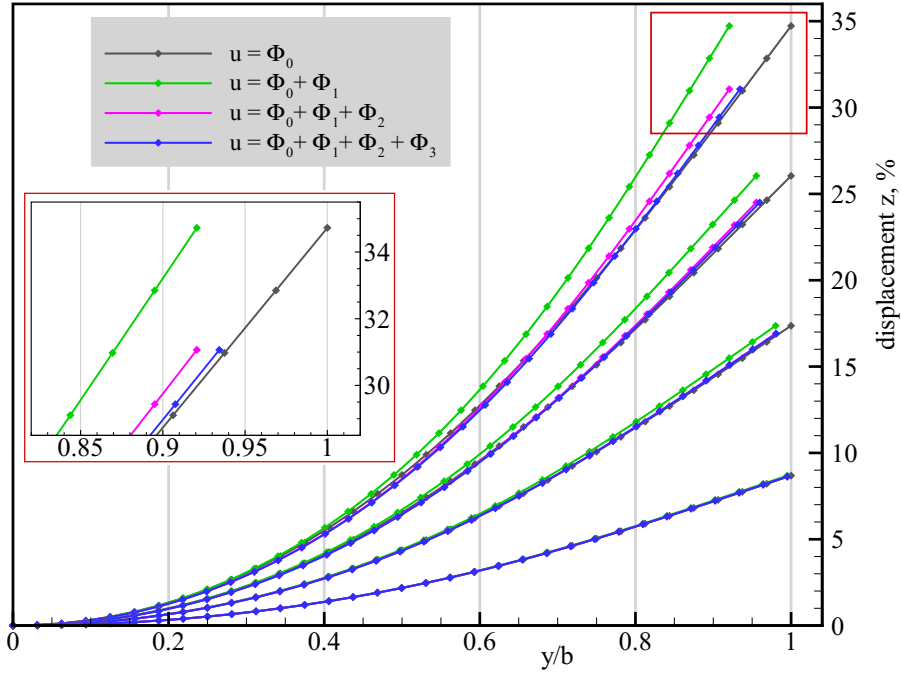


Figure 2.6: Exemplary deformation fields of the first bending mode shape for different values (amplitudes) for q_1 for the generic beam.

of virtual work. Using virtual displacements in Cartesian coordinates, the virtual work of the external loads is calculated as

$$\delta V = \delta \mathbf{u}^T \mathbf{f} , \quad (2.25)$$

where \mathbf{f} denotes the nonconservative external forces and moments. The virtual displacements $\delta \mathbf{u}$ can be expressed by the generalized coordinates and the corresponding mode components, as given by Eq.(2.23). In this work, however, only the linear and the quadratic mode components are considered which follows the approach used by van Zyl [36].

Expansion of the virtual physical displacements using the linear and the quadratic mode components yields

$$\delta V = \delta q_p^T \left({}^p \Phi_0^T + {}^p \Phi_1^{iT} q_i \right) \mathbf{f} . \quad (2.26)$$

Thus the generalized forces are given as

$$Q^p = {}^p \Phi_0^T \mathbf{f} + {}^p \Phi_1^{iT} \mathbf{f} q_i . \quad (2.27)$$

For the linear modal approach, only the linear mode components are used to calculate the generalized forces. The extension by the quadratic mode component yields an expression for the generalized forces which are linearly dependent on the generalized coordinates. This dependency results in important benefits which will be described in the next subsection. An expression for the generalized forces including the quadratic and the cubic mode components

has not been investigated in this work (although it should be possible in general); this step can be seen as a topic for future work.

2.1.4 Static and Dynamic Governing Equations of the Proposed Method

Combining Eqs.(2.19) and (2.27) yields the static governing equation of the proposed method:

$$({}^pG_1^i - {}^p\Phi_1^{iT} \mathbf{f}) q_i + {}^pG_2^{ij} q_i q_j + {}^pG_3^{ijk} q_i q_j q_k = {}^p\Phi_0^T \mathbf{f} . \quad (2.28)$$

Compared to the classical modal approach, the term ${}^pG_1^i$, which corresponds to the eigenvalues of the linear system, is amended by the product of the transposed of the quadratic mode component matrix and the external force field. This additional stiffness parameter is proportional to the force field applied to the structure and induces additional coupling of the otherwise (in the linear sense) uncoupled eigenvectors. This feature is of particular importance in aeroelastic applications as will be demonstrated in the following sections. If, for instance, a typical aeroelastic problem that consists of large deformations of a wing-like structure is considered, aerodynamic forces will have significant in-plane components (as seen in a body-fixed system located at the origin) due to the rotation of the lifting surfaces. In the classical modal approach, these components are normally disregarded since e.g. bending modes only have displacements in the out-of-plane direction. However, these force components are taken into account for the proposed method by the quadratic mode component.

The dynamic formulation is obtained by adding an inertia term to Eq.(2.28). The governing equation is then given as:

$${}^pM^i \ddot{q}_i + \left({}^pG_1^i - {}^p\Phi_1^{iT} \mathbf{f} \right) q_i + {}^pG_2^{ij} q_i q_j + {}^pG_3^{ijk} q_i q_j q_k = {}^p\Phi_0^T \mathbf{f} , \quad (2.29)$$

where M denotes the generalized mass matrix. Eq.(2.29) describes a *Duffing oscillator* without damping in the case of a single DOF system [72]. Due to the cubic nonlinearity, a wide range of solutions could be obtained in general, from harmonic oscillations to chaotic behavior. However, as will be shown in the following sections, the aircraft structures and components considered are characterized by very low values of the quadratic and cubic stiffness terms, and thus the dynamic solutions of Eq.(2.29) are very similar to the solutions of the harmonic oscillator. In the case of e.g. plate-like structures, the quadratic and cubic nonlinearities can be much more pronounced, though [24].

In the context of this thesis, Eq.(2.29) is solved by numerical methods. The governing equation can be converted into an equivalent system of ordinary differential equations (ODEs) of first order, for which implicit solvers are especially suited due to the stiffness of the system, which is of course a function of the magnitude of the cubic stiffness term. In the absence of the

inertia term (static governing equation), the resulting governing equation consists of a coupled system of nonlinear equations, which can be solved by the Newton-Raphson method.

2.1.5 Recapitulation and Solution Sequence of the Proposed Method

The important results of the derivations presented in this section are recapitulated as follows. The two most limiting disadvantages of the classical modal approach, namely the (linear) function relating applied forces and structural displacements by the linear stiffness term, as well as the linear transformation from generalized to nodal (cartesian) coordinates using normal modes are resolved by the following extensions:

- Nonlinear force-displacement function by the quadratic and cubic stiffness tensors ${}^pG_2^{ij}$ and ${}^pG_3^{ijk}$, defined by Eq.(2.16). A coupling of up to three modes is enabled by these higher-order stiffness terms.
- Higher-order mode components are used to calculate the nonlinear nodal displacement field as function of the generalized coordinates (mapping from generalized to nodal coordinates), defined by Eq.(2.23). The nonlinear deformation field is thus composed of linear, quadratic, cubic, and fourth-order parts.
- The quadratic mode components are considered for the calculation of the generalized forces leading to an extended linear stiffness term in the governing equation which becomes a function of the applied loads, defined by Eq.(2.27). This feature is especially important for aeroelastic applications since it considers the in-plane component of e.g. aerodynamic forces which appear in large deformations and rotations of lifting surfaces.

Figure 2.7 illustrates the static and the dynamic solution sequences of the proposed method. For aeroelastic applications, the nonconservative nature of the aerodynamic forces, which is in general a nonlinear function of the displacements and rotations of lifting surfaces, requires an iterative solution process, as is depicted in the figure.

2.2 Inertially Coupled Equations of Motion for the Free-flying Flexible Aircraft

This section describes the derivation of the flight dynamic governing equations of motion for the free-flying flexible aircraft with inertial coupling between rigid-body and elastic degrees of freedom. The goal is an integral set of equations with the rigid-body and the elastic degrees of freedom as independent variables, expressed by a set of coupled, ordinary differential equations of first order. To this end, the dynamic structural governing equation introduced in the previous section is extended by rigid-body degrees of freedom using Lagrange's equations of the second kind. As mentioned in the introduction, one issue comes with the calculation of the

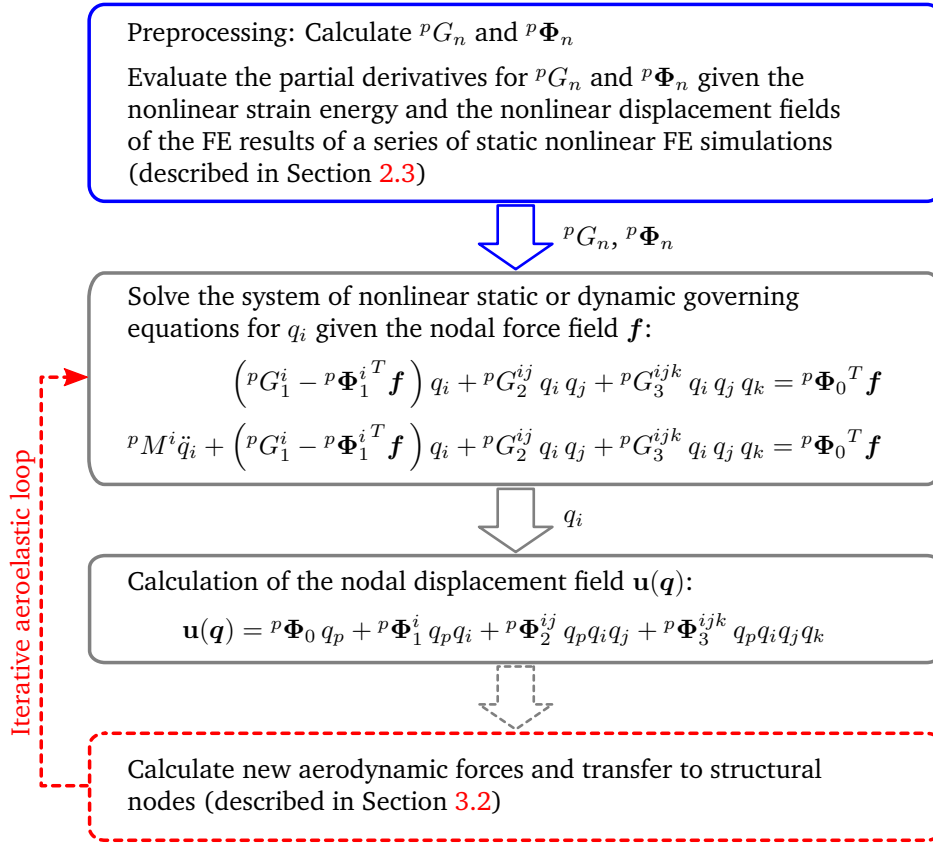


Figure 2.7: Static and dynamic solution sequence of the proposed method without rigid-body DOFs.

higher-order stiffness terms and mode components. All the test cases and simulations depicted in this thesis use structural models built for use with MSC Nastran, in which geometrically nonlinear static simulations with large deformations can be performed for clamped structures only. Unfortunately, no *inertia relief* exists for such solution sequences in MSC Nastran. Consequently, calculating the higher-order stiffness and mode components is by now not possible for unclamped (free-free) structures, with the consequence that a simplified flight dynamics description using the concept of the *practical mean axes* is not acceptable here. The mean axes constraints – a mathematical formulation of these constraints is given in the following – can be used to decouple rigid-body and elastic degrees of freedom with respect to inertial forces. This results in a simplified flight dynamics governing equation of motion with a smaller condition number of the mass matrix [51, 10]. They are automatically fulfilled by mode shapes of an unclamped, free-free structural model. In the general case, i.e. if mode shapes of a clamped structural model are to be used, these conditions will be non-zero and manifest in inertial coupling terms in the governing equations, which are derived in this section. It must be mentioned

that the equations of motion of the free-flying elastic aircraft with inertial coupling (no mean axes assumption) have been introduced based on a derivation using Lagrange's equations in quasi- and modal coordinates by Meirovitch [41]. The derivation in this chapter, however, uses a lumped mass model of the structure with discrete masses and a strain energy formulation with quadratic and cubic stiffness terms as described in Section 2.1.1.

2.2.1 Definition of Kinematical Relations

Two coordinate frames of reference are used for the definition of the kinematical relations and magnitudes. A geodetic, earth-fixed frame and a body-fixed frame, both are depicted in Fig. 2.8. The geodetic frame is an unaccelerated inertial system with its unit vectors denoted by x_g , y_g , and z_g . In the following, the coordinate frame fixed to a material point of the aircraft in its undeformed position is denoted as *body-fixed frame* or *body frame*, its basis is defined by the unit vectors x_b , y_b , and z_b ². The summation index i refers to a discrete mass element dm_i of the lumped mass model, with n denoting the number of mass points. The location of the body-fixed frame in the geodetic frame is defined by vector P_g , resolved in the geodetic frame. The same vector resolved in the body frame is denoted as P . Another vector, the attitude, is required to fully define how the body-fixed frame is placed in the geodetic frame. In this work, the set of Euler angles,

$$\underline{\Phi} = [\Phi \Theta \Psi]^T, \quad (2.30)$$

is used [73]. Angular rates of the body frame resolved in the body frame are denoted by vector Ω_b ,

$$\Omega_b = [p \ q \ r]^T. \quad (2.31)$$

The vector r_i defines the position of the mass point in the body frame with respect to the undeformed structure, and u_i is the displacement of the mass point due to structural deformation, also resolved in the body frame. Thus the vector that defines the location of the mass point resolved in the body frame, denoted as R_i , is given by the sum

$$R_i = P + r_i + u_i. \quad (2.32)$$

The velocity of the mass point resolved in the geodetic frame is given by the following total time derivative (also with respect to the geodetic frame) of the position vector R_i and is denoted as V_i [47],

$$V_i = \dot{R}_i = \dot{P} + \Omega_b \times P + \dot{u}_i + \Omega_b \times (r_i + u_i), \quad (2.33)$$

²The orientation of the axes of the inertial and the body-fixed frame is not conform with those of reference frames typically applied to flight dynamics analyses. The reason for this particular axes orientation is the setup and construction of the structural (FE) model, which is typically based on a coordinate system in which the x axis points positive from nose to tail and the z axis points positive upwards. This orientation was adopted for convenience and will be used in the following (the relation to the commonly applied *ISO-1151* reference systems is depicted in Appendix B).

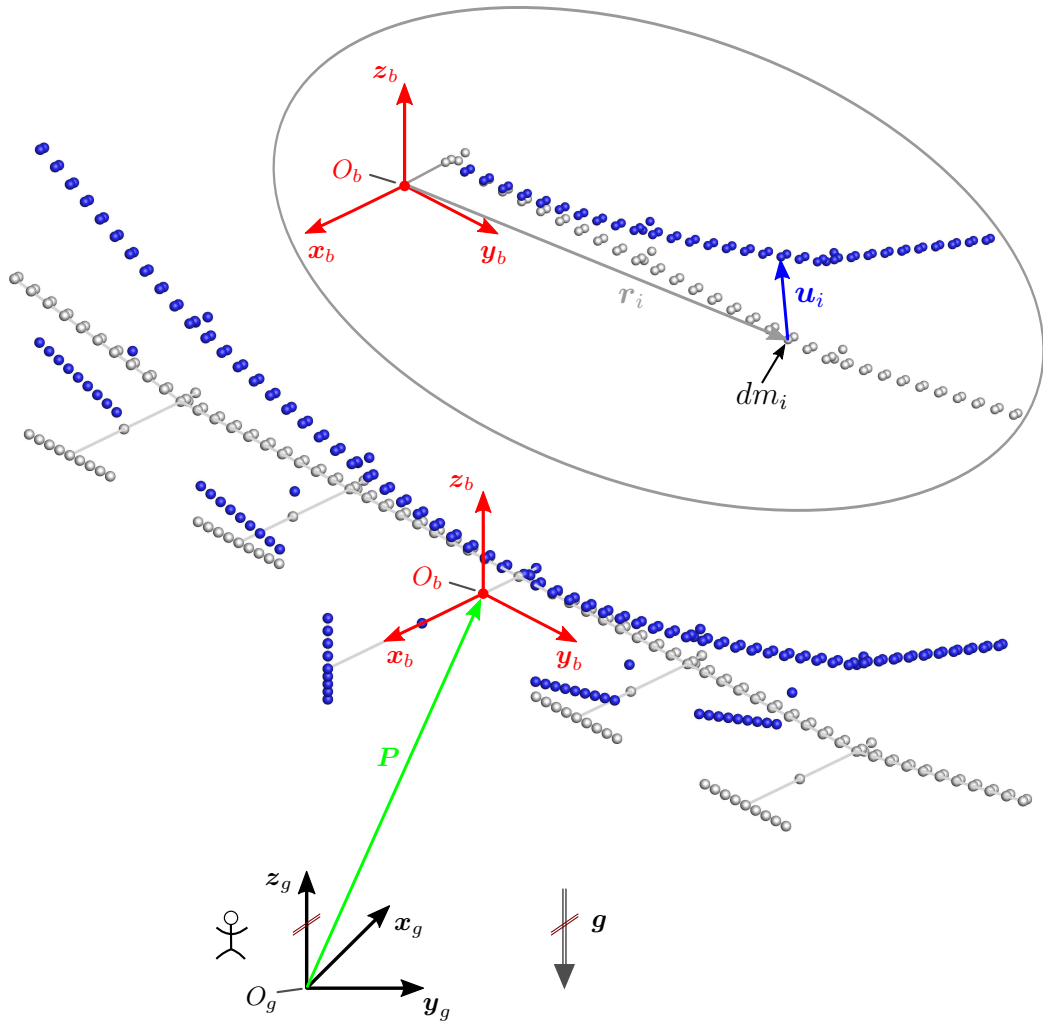


Figure 2.8: Inertial (geodetic) and body-fixed frames with indices g and b (in this case, the body-fixed frame is fixed to a material point of the undeformed body). Mass point dm_i in undeformed position, r_i , and displacement due to structural deformation, u_i . The choice of axes directions was made for convenience, it is not conform to general axes layouts applied in flight mechanics (such as those of *ISO-1151*)

where a standard kinematic relation was used to define the transformation between the time derivative of an arbitrary vector in an inertial and in a rotating system [74, p. 174]. A ring above a variable denotes its time rate of change with respect to the body frame. The term $\dot{\mathbf{P}} + \mathbf{\Omega}_b \times \mathbf{P}$ corresponds to the translational velocity of the body frame resolved in the body frame,

$$\mathbf{V}_b = \dot{\mathbf{P}} = \dot{\mathbf{P}} + \mathbf{\Omega}_b \times \mathbf{P} , \quad (2.34)$$

with the velocity components along the body axes denoted as

$$\mathbf{V}_b = [u \ v \ w]^T . \quad (2.35)$$

Transformation of a vector resolved in the geodetic frame into the body-fixed frame requires a transformation matrix built from direction cosines which is denoted by M_{bg} . This matrix is can be used to resolve the position vector \mathbf{P}_g in the body-fixed frame,

$$\mathbf{P} = M_{bg} \mathbf{P}_g , \quad (2.36)$$

and to calculate the kinematic relation between the time derivative of the position vector \mathbf{P}_g and the translational velocity of the body frame [73],

$$\mathbf{V}_b = M_{bg} \dot{\mathbf{P}}_g . \quad (2.37)$$

Relating the angular velocity of the body frame, $\boldsymbol{\Omega}_b$, to the time rate of change of the Euler angles requires another transformation matrix denoted by $M_{b\Phi}$ [73],

$$\boldsymbol{\Omega}_b = M_{b\Phi} \dot{\boldsymbol{\Phi}} . \quad (2.38)$$

The rotation matrices and further relations of flight mechanic states are detailed in Appendix B.

2.2.2 Definition of the Kinetic Energy

Application of Lagrange's equations requires to express the kinetic and the potential energy of the system. The kinetic energy of the aircraft as a whole is given by the sum of the kinetic energies of its n discrete masses dm_i ,

$$T = \frac{1}{2} \sum_{i=1}^n \mathbf{V}_i^T \mathbf{V}_i dm_i + \frac{1}{2} \boldsymbol{\Omega}_b^T \sum_{i=1}^n \mathbf{J}_i \boldsymbol{\Omega}_b , \quad (2.39)$$

where the local tensor of inertia of an individual mass point is denoted by \mathbf{J}_i . Summing the individual discrete masses of the aircraft yields its total mass, m ,

$$m = \sum_{i=1}^n dm_i . \quad (2.40)$$

Inserting the velocity defined by Eqs.(2.33) and (2.34) into Eq.(2.39) results in the following expression for the kinetic energy of the structure [10]:

$$\begin{aligned}
T = & \frac{1}{2} \mathbf{V}_b^T \mathbf{V}_b m & (2.41) \\
& + \frac{1}{2} \sum_{i=1}^n \dot{\mathbf{u}}_i^T \dot{\mathbf{u}}_i dm_i \\
& + \frac{1}{2} \boldsymbol{\Omega}_b^T \left[\sum_{i=1}^n [(\mathbf{r}_i^T \mathbf{r}_i) \mathbf{I} - \mathbf{r}_i \mathbf{r}_i^T] dm_i \right] \boldsymbol{\Omega}_b \\
& + \frac{1}{2} \boldsymbol{\Omega}_b^T \left[\sum_{i=1}^n [(\mathbf{u}_i^T \mathbf{r}_i + \mathbf{r}_i^T \mathbf{u}_i) \mathbf{I} - \mathbf{u}_i \mathbf{r}_i^T - \mathbf{r}_i \mathbf{u}_i^T] dm_i \right] \boldsymbol{\Omega}_b \\
& + \frac{1}{2} \boldsymbol{\Omega}_b^T \left[\sum_{i=1}^n [(\mathbf{u}_i^T \mathbf{u}_i) \mathbf{I} - \mathbf{u}_i \mathbf{u}_i^T] dm_i \right] \boldsymbol{\Omega}_b \\
& + \boldsymbol{\Omega}_b^T \left[\sum_{i=1}^n (\mathbf{u}_i \times \dot{\mathbf{u}}_i) dm_i \right] \\
& + \mathbf{V}_b^T \left[\boldsymbol{\Omega}_b \times \left(\sum_{i=1}^n \mathbf{r}_i dm_i \right) \right] \\
& + \mathbf{V}_b^T \left[\boldsymbol{\Omega}_b \times \left(\sum_{i=1}^n \mathbf{u}_i dm_i \right) \right] \\
& + \mathbf{V}_b^T \left[\sum_{i=1}^n \dot{\mathbf{u}}_i dm_i \right] \\
& + \boldsymbol{\Omega}_b^T \left[\sum_{i=1}^n (\mathbf{r}_i \times \dot{\mathbf{u}}_i) dm_i \right] \\
& + \frac{1}{2} \boldsymbol{\Omega}_b^T \sum_{i=1}^n \mathbf{J}_i \boldsymbol{\Omega}_b .
\end{aligned}$$

The nodal displacements \mathbf{u}_i (including translational and rotational components) of a mass point dm_i due to structural deformation will now be expressed by the modal approach. For simplicity, only the linear ${}^p\Phi_0$ components are used for now. The inclusion of the higher-order mode components in the expression for the kinetic energy is not considered in this work but will be done in future. However, the quadratic mode components are used for the calculation of the generalized forces, cf. Eq.(2.27), and all higher-order mode components are used for the calculation of the nodal displacement field, cf. Eq.(2.23), in the final governing equations of motion. Thus for the kinetic energy, \mathbf{u}_i is calculated as

$$\mathbf{u}_i = {}^p\Phi_0^i q_p \quad (p = 1, \dots, m) , \quad (2.42)$$

with the corresponding time derivative given as

$$\dot{\mathbf{u}}_i = {}^p\Phi_0^i \dot{q}_p . \quad (2.43)$$

Equation (2.43) is inserted into Eq.(2.41) to express nodal deformations as function of generalized coordinates. The resulting terms of Eq.(2.41) are discussed now.

$$\frac{1}{2} \sum_{i=1}^n \dot{\mathbf{u}}_i^T \dot{\mathbf{u}}_i dm_i = \frac{1}{2} {}^pM^k \dot{q}_k \dot{q}_p \quad (2.44)$$

denotes the modal kinetic energy of the elastic deformations where ${}^pM^k$ is the generalized mass matrix. Definitions for the tensor of inertia and its derivatives are introduced in the following to simplify the equations of motion [10]. The tensor of inertia of the undeformed aircraft with the local inertia contributions is given by the following expression

$$\mathbf{J} \equiv \sum_{i=1}^n \left[(\mathbf{r}_i^T \mathbf{r}_i) \mathbf{I} - \mathbf{r}_i \mathbf{r}_i^T \right] dm_i + \sum_{i=1}^n \mathbf{J}_i . \quad (2.45)$$

The first-order effect of deformation on the inertia tensor of the system is considered by the $(3 \times 3 \times m)$ tensor $\Delta \mathbf{J}$,

$$\begin{aligned} & \sum_{i=1}^n \left[(\mathbf{u}_i^T \mathbf{r}_i + \mathbf{r}_i^T \mathbf{u}_i) \mathbf{I} - \mathbf{u}_i \mathbf{r}_i^T - \mathbf{r}_i \mathbf{u}_i^T \right] dm_i \\ &= \underbrace{\left[\sum_{i=1}^n \left((2\mathbf{r}_i^T {}^p\Phi_0^i) \mathbf{I} - {}^p\Phi_0^i \mathbf{r}_i^T - \mathbf{r}_i {}^p\Phi_0^{iT} \right) dm_i \right]}_{\Delta \mathbf{J}_p} q_p , \end{aligned} \quad (2.46)$$

where the (3×3) submatrices of the respective generalized coordinate are symmetric, i.e.,

$$\Delta \mathbf{J}_p = \Delta \mathbf{J}_p^T . \quad (2.47)$$

Second-order effects of deformation on the inertia tensor are considered by the $(m \times 3 \times 3 \times m)$ tensor \mathbf{B} ,

$$\sum_{i=1}^n [(\mathbf{u}_i^T \mathbf{u}_i) \mathbf{I} - \mathbf{u}_i \mathbf{u}_i^T] dm_i = \underbrace{\left[\sum_{i=1}^n \left(({}^p\Phi_0^{iT k} {}^p\Phi_0^i) \mathbf{I} - {}^p\Phi_0^{i k} {}^p\Phi_0^{iT} \right) dm_i \right]}_{\mathbf{B}_{pk}} q_p q_k . \quad (2.48)$$

Again, the submatrices are symmetric,

$$\mathbf{B}_{pk}^T = \mathbf{B}_{kp} . \quad (2.49)$$

The following definition is introduced for a compact notation:

$$\Delta^2 J_{pk} \equiv B_{pk} + B_{kp} . \quad (2.50)$$

Second-order momentum coupling between elastic modes and angular momentum is taken into account by the following cross product of modes p and k , denoted by the $(m \times 3 \times m)$ tensor \mathbf{h} [10],

$$\sum_{i=1}^n (\mathbf{u}_i \times \dot{\mathbf{u}}_i) dm_i = \underbrace{\left[\sum_{i=1}^n \left({}^p \Phi_0^i \times {}^k \Phi_0^i \right) dm_i \right]}_{\mathbf{h}_{pk}} q_p \dot{q}_k , \quad (2.51)$$

where

$$\mathbf{h}_{pk} = -\mathbf{h}_{kp} . \quad (2.52)$$

If the origin of the body-fixed frame is located at the center of mass of the undeformed structure, the seventh term of Eq.(2.41) will be zero. This removes inertial coupling between the translational and rotational angular momentum. The location of the origin of the body-fixed frame with respect to the undeformed aircraft structure is not restricted here and can be chosen according to practical needs. However, a location in the plane of symmetry of the aircraft is of course favorable in most cases. The eighth, ninth, and tenth term of Eq.(2.41) can be set to zero only if the mean axes conditions are employed. These conditions can be approximated if the eigenvectors of an unrestrained structure are used in Eq.(2.42) [10]. If the eigenvectors of a clamped structure are to be used for the calculation of elastic deformations, coupling between elastic and translational and angular momentum occurs which is considered by the following contributions to the kinetic energy defined in Eq.(2.41):

$$\mathbf{V}_b^T \left[\boldsymbol{\Omega}_b \times \left(\sum_{i=1}^n \mathbf{u}_i dm_i \right) \right] = \mathbf{V}_b^T \left[\boldsymbol{\Omega}_b \times \left(\left[\sum_{i=1}^n {}^p \Phi_0^i dm_i \right] q_p \right) \right] , \quad (2.53)$$

$$\mathbf{V}_b^T \left[\sum_{i=1}^n \dot{\mathbf{u}}_i dm_i \right] = \mathbf{V}_b^T \left[\left[\sum_{i=1}^n {}^p \Phi_0^i dm_i \right] \dot{q}_p \right] , \quad (2.54)$$

$$\boldsymbol{\Omega}_b^T \left[\sum_{i=1}^n (\mathbf{r}_i \times \dot{\mathbf{u}}_i) dm_i \right] = \boldsymbol{\Omega}_b^T \left[\left[\sum_{i=1}^n (\mathbf{r}_i \times {}^p \Phi_0^i) dm_i \right] \dot{q}_p \right] . \quad (2.55)$$

The following definitions are introduced to avoid lengthy expressions in the following derivations:

$$\overline{\mathbf{r}\mathbf{m}} \equiv \sum_{i=1}^n \mathbf{r}_i dm_i \quad (3 \times 1) \text{ vector} \quad (2.56a)$$

$${}^p\overline{\Phi\mathbf{m}} \equiv \sum_{i=1}^n {}^p\Phi_0^i dm_i \quad (3 \times 1) \text{ vector} \quad (2.56b)$$

$${}^p\overline{\mathbf{r}\Phi\mathbf{m}} \equiv \sum_{i=1}^n (\mathbf{r}_i \times {}^p\Phi_0^i) dm_i \quad (3 \times 1) \text{ vector} \quad (2.56c)$$

2.2.3 Definition of the Potential Energy

Contributions to the total potential energy of the system are made by the gravitational potential energy, U_g , and the strain energy:

$$\begin{aligned} U_p &= U_g + U & (2.57) \\ &= - \sum_{i=1}^n \mathbf{R}_i^T (\mathbf{M}_{bg} \mathbf{g}) dm_i + \frac{1}{2} \left({}^pG_1^i q_p q_i + {}^pG_2^{ij} q_p q_i q_j + {}^pG_3^{ijk} q_p q_i q_j q_k \right) . \end{aligned}$$

Similar as for the kinetic energy and for simplicity, no higher-order mode components are considered for the strain energy so far. Considering only the linear mode component ${}^p\Phi_0^i$ for the calculation of structural deformations in the potential energy definition yields:

$$U_p = - \sum_{i=1}^n (\mathbf{P} + \mathbf{r}_i + {}^p\Phi_0^i q_p)^T (\mathbf{M}_{bg} \mathbf{g}) dm_i + \frac{1}{2} \left({}^pG_1^i q_p q_i + {}^pG_2^{ij} q_p q_i q_j + {}^pG_3^{ijk} q_p q_i q_j q_k \right) , \quad (2.58)$$

where the gravity vector, resolved in the geodetic frame, is denoted as \mathbf{g} :

$$\mathbf{g} = [0 \ 0 \ -g]^T . \quad (2.59)$$

2.2.4 Definition of the Generalized Forces

The nonconservative generalized forces and moments for translational and rotational momentum as well as for the structural work are denoted as \mathbf{Q}_t , \mathbf{Q}_r , and Q^p , respectively. In this thesis, the generalized forces of the translational and angular momentum are composed of aerodynamic and propulsive (thrust) forces and moments only:

$$\mathbf{Q}_t = \mathbf{R}^A + \mathbf{F} , \quad (2.60a)$$

$$\mathbf{Q}_r = \mathbf{Q}^A + \mathbf{Q}^F . \quad (2.60b)$$

Here, \mathbf{R}^A denotes the resulting aerodynamic forces acting on the aircraft with respect to the axes of the body-fixed frame, and \mathbf{F} denotes the resulting propulsive forces, also resolved in the body-fixed frame. Accordingly, \mathbf{Q}^A are the resulting aerodynamic moments, and \mathbf{Q}^F denotes the propulsive moments, both resolved in the body-fixed frame. The generalized forces of the structural governing equation are calculated by Eq.(2.27).

2.2.5 Lagrange's Equations of the Second Kind in Quasi- and Modal Coordinates

In the following, the governing equations of motion for the translational, the rotational, and the elastic degrees of freedom are derived. Therefore, the energy expressions given in the previous sections are inserted into Lagrange's equations of the second kind in quasi- and modal coordinates [51, 41]. The Lagrange variable L is defined as the difference of the kinetic and the total potential energy:

$$L = T - U_p . \quad (2.61)$$

Lagrange's equations for the system considered are given as follows [51]:

Linear momentum in quasi-coordinates:

$$\frac{d}{dt} \Big|_b \frac{\partial L}{\partial \mathbf{V}_b} + \boldsymbol{\Omega}_b \times \left(\frac{\partial L}{\partial \mathbf{V}_b} \right) - M_{bg} \frac{\partial L}{\partial \mathbf{P}} = \mathbf{Q}_t \quad (2.62)$$

Rotational momentum in quasi coordinates:

$$\frac{d}{dt} \Big|_b \frac{\partial L}{\partial \boldsymbol{\Omega}_b} + \mathbf{V}_b \times \left(\frac{\partial L}{\partial \mathbf{V}_b} \right) + \boldsymbol{\Omega}_b \times \left(\frac{\partial L}{\partial \boldsymbol{\Omega}_b} \right) - (M_{b\Phi}^T)^{-1} \frac{\partial L}{\partial \boldsymbol{\Theta}} = \mathbf{Q}_r \quad (2.63)$$

Elastic deformation in modal coordinates:

$$\frac{d}{dt} \Big|_b \frac{\partial L}{\partial \dot{q}_p} - \frac{\partial L}{\partial q_p} = Q^p \quad (2.64)$$

Using the expressions for the kinetic and the potential energy defined above and taking the partial derivatives yields the inertially coupled equations of motion.

The linear momentum equation of motion is given as

$$\begin{aligned} & \dot{\mathbf{V}}_b m + \dot{\boldsymbol{\Omega}}_b \times \left[\overline{\mathbf{r}m} + {}^p \overline{\boldsymbol{\Phi}m} q_p \right] + {}^p \overline{\boldsymbol{\Phi}m} \ddot{q}_p + \\ & \boldsymbol{\Omega}_b \times \left[\mathbf{V}_b m + \boldsymbol{\Omega}_b \times \left[\overline{\mathbf{r}m} + {}^p \overline{\boldsymbol{\Phi}m} q_p \right] + 2 {}^p \overline{\boldsymbol{\Phi}m} \dot{q}_p \right] - (M_{bg} \mathbf{g}) m = \mathbf{Q}_t . \end{aligned} \quad (2.65)$$

The rotational momentum equation of motion is given as:

$$\begin{aligned} & \overline{\mathbf{J}}\dot{\boldsymbol{\Omega}}_b + \dot{\overline{\mathbf{J}}}\boldsymbol{\Omega}_b + \mathbf{h}_{pk}\dot{q}_p\dot{q}_k + \mathbf{h}_{pk}q_p\dot{q}_k - \dot{\mathbf{V}}_b \times \left[\overline{\mathbf{r}\mathbf{m}} + {}^p\overline{\boldsymbol{\Phi}\mathbf{m}} q_p \right] + {}^p\overline{\mathbf{r}\boldsymbol{\Phi}\mathbf{m}} \ddot{q}_p \\ & + \mathbf{V}_b \times \left[\boldsymbol{\Omega}_b \times \left[\overline{\mathbf{r}\mathbf{m}} + {}^p\overline{\boldsymbol{\Phi}\mathbf{m}} q_p \right] \right] \\ & + \boldsymbol{\Omega}_b \times \left[\mathbf{J}\boldsymbol{\Omega}_b + \mathbf{h}_{pk}q_p\dot{q}_k - \mathbf{V}_b \times \left[\overline{\mathbf{r}\mathbf{m}} + {}^p\overline{\boldsymbol{\Phi}\mathbf{m}} q_p \right] + {}^p\overline{\mathbf{r}\boldsymbol{\Phi}\mathbf{m}} \dot{q}_p \right] = \mathbf{Q}_r , \end{aligned} \quad (2.66)$$

where the following definitions have been used [10]

$$\overline{\mathbf{J}} \equiv \mathbf{J} + \Delta\mathbf{J}_p q_p + \frac{1}{2}\Delta^2\mathbf{J}_{pk}q_pq_k , \quad (2.67)$$

$$\dot{\overline{\mathbf{J}}} \equiv \Delta\mathbf{J}_p\dot{q}_p + \Delta^2\mathbf{J}_{pk}q_p\dot{q}_k . \quad (2.68)$$

The governing equation of the elastic deformation for mode p is given as

$$\begin{aligned} & M_{pk}\ddot{q}_k + \dot{\mathbf{V}}_b^T {}^p\overline{\boldsymbol{\Phi}\mathbf{m}} + \dot{\boldsymbol{\Omega}}_b^T \left[{}^p\overline{\mathbf{r}\boldsymbol{\Phi}\mathbf{m}} - \mathbf{h}_{pk}q_k \right] - \mathbf{V}_b^T \left[\boldsymbol{\Omega}_b \times {}^p\overline{\boldsymbol{\Phi}\mathbf{m}} \right] - 2\boldsymbol{\Omega}_b^T \mathbf{h}_{pk}\dot{q}_k \\ & - \frac{1}{2}\boldsymbol{\Omega}_b^T \left[\Delta\mathbf{J}_p + \Delta^2\mathbf{J}_{pk}q_k \right] \boldsymbol{\Omega}_b + {}^pG_1^k q_k + {}^pG_2^{ki} q_k q_i + {}^pG_3^{kij} q_k q_i q_j + {}^p\overline{\boldsymbol{\Phi}\mathbf{m}}^T (\mathbf{M}_{bg}\mathbf{g}) = Q^p . \end{aligned} \quad (2.69)$$

2.2.6 Matrix Form of the Equations of Motion

To simplify the solution process, the final form of the coupled, combined first and second-order (hybrid) nonlinear equations of motion will be written in matrix notation with the mass $\overline{\mathbf{M}}$, the gyroscopic $\overline{\mathbf{D}}$, and the stiffness matrix $\overline{\mathbf{K}}$ according to their degrees of freedom as follows:

$$\underbrace{\begin{bmatrix} M_{tt} & M_{tr} & {}^pM_{te} \\ M_{rt} & M_{rr} & {}^pM_{re} \\ {}^pM_{et} & {}^pM_{er} & {}^pM_{ee} \end{bmatrix}}_{\overline{\mathbf{M}}} \begin{bmatrix} \dot{\mathbf{V}}_b \\ \dot{\boldsymbol{\Omega}}_b \\ \ddot{\mathbf{q}}_k \end{bmatrix} + \underbrace{\begin{bmatrix} \mathbf{0} & \mathbf{D}_{tr} & \mathbf{0} \\ \mathbf{D}_{rt} & \mathbf{D}_{rr} & {}^p\mathbf{D}_{re} \\ {}^p\mathbf{D}_{et} & {}^p\mathbf{D}_{er} & \mathbf{0} \end{bmatrix}}_{\overline{\mathbf{D}}} \begin{bmatrix} \mathbf{V}_b \\ \boldsymbol{\Omega}_b \\ \dot{\mathbf{q}}_k \end{bmatrix} + \underbrace{\begin{bmatrix} \mathbf{0} & \mathbf{0} & \mathbf{0} \\ \mathbf{0} & \mathbf{0} & \mathbf{0} \\ \mathbf{0} & \mathbf{0} & {}^p\mathbf{G} \end{bmatrix}}_{\overline{\mathbf{K}}} \begin{bmatrix} \mathbf{0} \\ \mathbf{0} \\ \mathbf{q}_k \end{bmatrix} = \begin{bmatrix} \mathbf{Q}_t \\ \mathbf{Q}_r \\ \mathbf{Q}^{p*} \end{bmatrix} . \quad (2.70)$$

Here, index t denotes translational, index r rotational, index e elastic degrees of freedom. The transformation matrix \mathbf{M}_{bg} is not explicitly written as function of the independent variables in Eq.(2.70), thus the generalized loads due to gravity are included in the generalized forces of the structural equation, denoted as Q^{p*} ,

$$Q^{p*} = \left({}^p\boldsymbol{\Phi}_0^T + {}^p\boldsymbol{\Phi}_1^T q_i \right) \mathbf{f} - {}^p\overline{\boldsymbol{\Phi}\mathbf{m}}^T (\mathbf{M}_{bg}\mathbf{g}) . \quad (2.71)$$

The mass $\overline{\mathbf{M}}$, the gyroscopic $\overline{\mathbf{D}}$, and the stiffness matrix $\overline{\mathbf{K}}$ are depicted in detail in Appendix A.

As can be seen from these equations, the coupling not only occurs by means of the aerodynamic forces applied to the aircraft, but also inertially by the terms defined in Eq.(2.56). In most aeroelastic applications, these terms are implicitly set to zero by the use of free-free mode shapes of an unrestrained vehicle. However, they are kept in this work due to the higher-order mode components used for the calculation of the physical displacement field, these mode components can be obtained for clamped structures only. Due to the tensor \mathbf{h} and the inertial coupling terms (Eq.(2.56)), both the mass and the gyroscopic matrix are a function of the structural state variables. Structural damping is omitted here, but can be considered by the component ${}^p D_{ee}$ in the gyroscopic matrix. However, the inclusion of structural damping is not part of this thesis since for highly flexible aircraft, the damping induced by the aerodynamic forces can be assumed to be much higher than the damping forces generated by the material of the structure. If the rigid-body degrees of freedom \mathbf{V}_b and $\mathbf{\Omega}_b$ (and their time derivatives) are set equal to zero, the equations of motion Eq.(2.70) reduce to the structural dynamics governing equation given by Eq.(2.29).

2.2.7 Simplified Equations of Motions

If the mean axes assumptions are applied and the corresponding terms in Eq.(2.56) are set to zero, the linearized equations of motions, as derived by Buttrill et al., are obtained [10, 50]:

$$\begin{bmatrix} M_{tt} & \mathbf{0} & \mathbf{0} \\ \mathbf{0} & M_{rr} & {}^p M_{re} \\ \mathbf{0} & {}^p M_{er} & {}^p M_{ee} \end{bmatrix} \begin{bmatrix} \dot{\mathbf{V}}_b \\ \dot{\mathbf{\Omega}}_b \\ \dot{\mathbf{q}}_k \end{bmatrix} + \begin{bmatrix} \mathbf{0} & D_{tr} & \mathbf{0} \\ \mathbf{0} & D_{rr} & {}^p D_{re} \\ \mathbf{0} & {}^p D_{er} & 0 \end{bmatrix} \begin{bmatrix} \mathbf{V}_b \\ \mathbf{\Omega}_b \\ \dot{\mathbf{q}}_k \end{bmatrix} + \begin{bmatrix} \mathbf{0} & \mathbf{0} & \mathbf{0} \\ \mathbf{0} & \mathbf{0} & \mathbf{0} \\ \mathbf{0} & \mathbf{0} & G \end{bmatrix} \begin{bmatrix} \mathbf{0} \\ \mathbf{0} \\ q_k \end{bmatrix} = \begin{bmatrix} Q_t \\ Q_r \\ Q^{p*} \end{bmatrix}, \quad (2.72)$$

where the mean axes conditions, i.e, $\overline{\mathbf{r}\mathbf{m}}$, ${}^p \overline{\mathbf{\Phi}\mathbf{m}}$, and ${}^p \overline{\mathbf{r}\mathbf{\Phi}\mathbf{m}}$ are equal to zero. Inertial coupling between angular momentum and structural deformation is still considered by the \mathbf{h} term defined in Eq.(2.51), also the tensor of inertia and its rate of change are functions of the structural deformation. The linearized mass and gyroscopic matrix are also given in detail in Appendix A.2.

2.2.8 First-Order System of the Equations of Motion

Finally, the equations of motion are converted into a system of coupled, nonlinear ordinary differential equations (ODEs). This form is used for the solution in the time domain using an appropriate numerical scheme. In residual form, the equations of motion can be written as

$$\dot{\mathbf{X}} - \mathbf{F}(\mathbf{X}, \dot{\mathbf{X}}) = \mathbf{0}. \quad (2.73)$$

The vectors of the independent state variables, $\dot{\mathbf{X}}$ and \mathbf{X} , and the generalized forces, \mathbf{Q} , are defined as follows:

$$\dot{\mathbf{X}} = \begin{bmatrix} \mathbf{V}_b \\ \boldsymbol{\Omega}_b \\ \dot{\mathbf{q}} \\ \dot{\mathbf{V}}_b \\ \dot{\boldsymbol{\Omega}}_b \\ \ddot{\mathbf{q}} \end{bmatrix}; \quad \mathbf{X} = \begin{bmatrix} \mathbf{P}_g \\ \boldsymbol{\Phi} \\ \mathbf{q} \\ \mathbf{V}_b \\ \boldsymbol{\Omega}_b \\ \dot{\mathbf{q}} \end{bmatrix}; \quad \mathbf{Q} = \begin{bmatrix} \mathbf{0} \\ \mathbf{0} \\ \mathbf{0} \\ \mathbf{Q}_t \\ \mathbf{Q}_r \\ \mathbf{Q}_e \end{bmatrix}, \quad (2.74)$$

where \mathbf{Q}_e denotes the column vector of the generalized structural forces.

The inertially coupled governing equations (Eq.(2.70)) can then be written in first-order form as

$$\dot{\mathbf{X}} - \begin{bmatrix} \mathbf{0} & \mathbf{I} \\ \hline -\overline{\mathbf{M}}^{-1}\overline{\mathbf{K}} & -\overline{\mathbf{M}}^{-1}\overline{\mathbf{D}} \end{bmatrix} \mathbf{X} - \overline{\mathbf{M}}^{-1}\mathbf{Q} = \mathbf{0}. \quad (2.75)$$

2.3 Calculation of the Linear and Higher-Order Stiffness and Mode Components

A general and crucial issue for the proposed method is the determination of the linear and the higher-order stiffness terms and mode components, which must be done in preprocessing. Both the nonlinear strain energy and the nonlinear deformation field are differentiated with respect to the scaling parameter \mathbf{q} to calculate the stiffness terms ${}^p\mathbf{G}_n$ and the mode components ${}^p\boldsymbol{\Phi}_n$, cf. Eq.(2.17) and Eq.(2.24). Depending on the structural model considered, different approaches exist for the determination of the nonlinear stiffness terms. Methods that calculate the higher-order terms by a series of nonlinear, static FE solutions are in general favorable since static solutions are computationally cheap [23]. This approach is followed in this work and a commercial FE program (MSC Nastran) is used which provides the strain energy and, of course, the nonlinear deformation field as part of the solution. A procedure for the calculation of the linear and quadratic mode components based on a series of static nonlinear FE solutions and numerical differentiation is proposed by Segalman and Dohrmann, where formulas for the numerical evaluation of the components ${}^p\boldsymbol{\Phi}_0^i$ and ${}^p\boldsymbol{\Phi}_1^{ij}$ based on finite differences of second and fourth-order are given [31]. Expressions for higher-order derivatives (third and fourth-order) can be derived from Taylor series expansions. The disadvantage of finite differences is the strong dependence on the stepping parameter that is used as well as the large effort which is involved with the implementation if expressions with higher-order accuracy are desired, especially for the third and fourth-order stiffness and mode components. In this work, another

method is proposed for the evaluation of the strain energy and deformation field derivatives, which is introduced in this section.

2.3.1 Two-dimensional Polynomial Surface Fitting to Nonlinear Solutions

Applying the nodal force field defined by Eq.(2.15) in a nonlinear static FE simulation yields the corresponding strain energy. Now the force field is extended and expressed as function of two variables (${}^a s_i$ and ${}^b s_j$) and two natural modes (ϕ^i and ϕ^j),

$${}^{ab}\mathbf{F}_{ij} = \mathbf{K} \left({}^a s_i \phi^i + {}^b s_j \phi^j \right), \quad (a, b = 1, \dots, \eta), \quad (i, j = 1, \dots, m). \quad (2.76)$$

The parameters ${}^a s_i$ and ${}^b s_j$, which correspond to elements of the vector \mathbf{s} defined in Eq.(2.14), are taken as scaling factors of the two structural eigenvectors ϕ^i and ϕ^j which can be combined in this way. Therefore, η^2 force fields are obtained for each combination of i and j . These force fields are applied in a series of nonlinear static FE simulations from which η^2 values for the strain energy and the deformation field are obtained. These nonlinear solutions are collected in vector \mathbf{N}_{ij} ,

$$\mathbf{N}_{ij} = [N_1({}^1 s_i, {}^1 s_j) \dots N_{\eta*\eta}(\eta s_i, \eta s_j)]^T, \quad (2.77)$$

where N_i represents a nonlinear operator mapping the force field to a strain energy or displacement field. The operator is of course realized by a nonlinear FE solution in this work. In the following, η will also be denoted as *stencil size*, since the η^2 scaling factors can be seen as a two-dimensional grid centered at zero on which the nonlinear operator is executed for each combination of a and b , as shown in Fig. 2.9. Now a quartic polynomial is defined in the

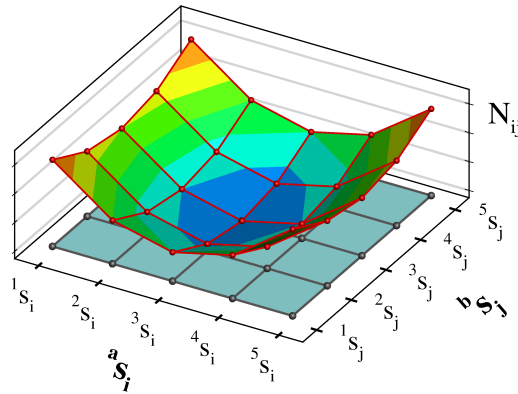


Figure 2.9: Stencil of width five (grey spheres) for ${}^a s_i$ and ${}^b s_j$ with $(a, b = 1, \dots, 5)$ and exemplary solutions of N_{ij} (red spheres).

following way for the nonlinear solutions in vector \mathbf{N}_{ij} with $^a s_i$ and $^b s_j$ as parameters:

$$\mathbf{N}_{ij} = \sum_{t=1}^4 ({}^a s_i + {}^b s_j)^t \quad (2.78)$$

The individual terms of this polynomial are inserted columnwise in Matrix \mathbf{P} as follows:

$$\mathbf{P} = \begin{bmatrix} {}^1 s_i^4 & 4 {}^1 s_i^3 {}^1 s_j & {}^1 s_i^3 & 6 {}^1 s_i^2 {}^1 s_j^2 & 3 {}^1 s_i^2 {}^1 s_j & {}^1 s_i^2 & 4 {}^1 s_i {}^1 s_j^3 & 3 {}^1 s_i {}^1 s_j^2 & 2 {}^1 s_i {}^1 s_j & {}^1 s_i & {}^1 s_j^4 & {}^1 s_j^3 & {}^1 s_j^2 & {}^1 s_j \\ \vdots & & & & & & \vdots & & & & & & & \vdots \\ \eta s_i^4 & 4 \eta s_i^3 \eta s_j & \eta s_i^3 & 6 \eta s_i^2 \eta s_j^2 & 3 \eta s_i^2 \eta s_j & \eta s_i^2 & 4 \eta s_i \eta s_j^3 & 3 \eta s_i \eta s_j^2 & 2 \eta s_i \eta s_j & \eta s_i & \eta s_j^4 & \eta s_j^3 & \eta s_j^2 & \eta s_j \end{bmatrix} \quad (2.79)$$

This matrix contains 14 columns because the polynomial defined in Eq.(2.78) contains 14 terms. Using the matrix \mathbf{P} with all entries well-defined by $^a s_i$ and $^b s_j$, as well as the vector of known nonlinear solutions, \mathbf{N}_{ij} , a linear system with η^2 equations can be defined,

$$\mathbf{P}_{ij} \mathbf{x}_{ij} = \mathbf{N}_{ij} \quad , \quad (2.80)$$

where the solution vector \mathbf{x} contains 14 unknown coefficients to be solved for

$$\mathbf{x}_{ij} = [{}^1 x_{ij} \dots {}^{14} x_{ij}]^T \quad . \quad (2.81)$$

Depending on the number of scaling parameters η used for the nonlinear FE simulations, the system of equations in Eq.(2.80) will mostly be over-determined (as will be shown, $\eta \geq 4$ must hold). Matrix \mathbf{P}_{ij} is not a square matrix, but a solution can be found by e.g. the calculation of the pseudo-inverse of \mathbf{P}_{ij} . This corresponds to solving an optimization problem, where the polynomial defined in Eq.(2.78), which depicts a two-dimensional surface, is fitted into the solutions of the vector \mathbf{N}_{ij} by minimizing an error norm. Higher precision in the sense of a more accurate calculation of the derivatives can be obtained by using more evaluations of the nonlinear operator, i.e., a higher value for η (i.e., $\eta > 4$). Once a solution is found for the vector of coefficients, \mathbf{x}_{ij} , the higher-order stiffness and mode components are obtained by differentiation of the polynomial defined in Eq.(2.78), without considering the index a :

- Symmetric derivatives w.r.t. s_i :

$$\frac{\partial \mathbf{N}_{ij}}{\partial s_i} = 4s_i^3 + 12s_i^2 s_j + 3s_i^2 + 12s_i s_j^2 + 6s_i s_j + 2s_i + 4s_j^3 + 3s_j^2 + 2s_j + 1 \quad (2.82)$$

$$\frac{\partial^2 \mathbf{N}_{ij}}{\partial s_i^2} = 12s_i^2 + 24s_i s_j + 6s_i + 12s_j^2 + 6s_j + 2 \quad (2.83)$$

$$\frac{\partial^3 \mathbf{N}_{ij}}{\partial s_i^3} = 24s_i + 24s_j + 6 \quad (2.84)$$

$$\frac{\partial^4 \mathbf{N}_{ij}}{\partial s_i^4} = 24 \quad (2.85)$$

- Coupled derivatives w.r.t. s_i and s_j :

$$\frac{\partial^2 \mathbf{N}_{ij}}{\partial s_i \partial s_j} = 12s_i^2 + 24s_i s_j + 6s_j + 12s_j^2 + 6s_j + 2 \quad (2.86)$$

$$\frac{\partial^3 \mathbf{N}_{ij}}{\partial s_i^2 \partial s_j} = 24s_i + 24s_j + 6 \quad (2.87)$$

$$\frac{\partial^3 \mathbf{N}_{ij}}{\partial s_i \partial s_j^2} = 24s_i + 24s_i + 6 \quad (2.88)$$

$$\frac{\partial^4 \mathbf{N}_{ij}}{\partial s_i^3 \partial s_j} = \frac{\partial^4 \mathbf{N}_{ij}}{\partial s_i^2 \partial s_j^2} = \frac{\partial^4 \mathbf{N}_{ij}}{\partial s_i \partial s_j^3} = 24 \quad (2.89)$$

2.3.2 Calculation of the Higher-Order Stiffness and Mode Tensors from Polynomial Coefficients

Because the higher-order stiffness tensors (${}^p G_1^i$, ${}^p G_2^{ij}$, and ${}^p G_3^{ijk}$) as well as the higher-order mode components (${}^p \Phi_0$ thru ${}^p \Phi_3^{ijk}$) were defined by Taylor series expansions centered at zero (cf. Eq.(2.18) and (2.24), the following expressions are obtained for the linear, quadratic, and cubic stiffness terms, assuming the vector of the nonlinear solutions \mathbf{N}_{ij} holds the strain energies U_{ij} , and two modes are involved:

- Linear stiffness term ${}^p G_1$

$${}^p G_1^i \equiv \frac{1}{2} \frac{\partial^2 U_{pi}}{\partial s_p \partial s_i} \Big|_{(s_{p,i}=0)} = {}^6 x_{pi} \quad (p, i = 1, \dots, m; p = i) \quad (2.90a)$$

$${}^p G_1^i \equiv \frac{1}{2} \frac{\partial^2 U_{pi}}{\partial s_p \partial s_i} \Big|_{(s_{p,i}=0)} = {}^9 x_{pi} \quad (p \neq i) \quad (2.90b)$$

- Quadratic stiffness term pG_2

$${}^pG_2^{ii} \equiv \frac{1}{6} \frac{\partial^3 U_{pi}}{\partial s_p \partial^2 s_i} \Big|_{(s_{p,i}=0)} = {}^3x_{pi} \quad (p = i) \quad (2.91a)$$

$${}^pG_2^{ij} \equiv \frac{1}{6} \frac{\partial^3 U_{pj}}{\partial s_p \partial s_i \partial s_j} \Big|_{(s_{p,i,j}=0)} = {}^5x_{pj} \quad (p = i, i \neq j) \quad (2.91b)$$

$${}^pG_2^{jj} \equiv \frac{1}{6} \frac{\partial^3 U_{pj}}{\partial s_p \partial^2 s_j} \Big|_{(s_{p,j}=0)} = {}^8x_{pj} \quad (p \neq j) \quad (2.91c)$$

- Cubic stiffness term pG_3

$${}^pG_3^{iii} \equiv \frac{1}{24} \frac{\partial^4 U_{pi}}{\partial s_p \partial^3 s_i} \Big|_{(s_{p,i}=0)} = {}^1x_{pi} \quad (p = i) \quad (2.92a)$$

$${}^pG_3^{iij} \equiv \frac{1}{24} \frac{\partial^4 U_{pj}}{\partial s_p \partial^2 s_i \partial s_j} \Big|_{(s_{p,i,j}=0)} = {}^2x_{pj} \quad (p = i, i \neq j) \quad (2.92b)$$

$${}^pG_3^{ijj} \equiv \frac{1}{24} \frac{\partial^4 U_{pj}}{\partial s_p \partial s_i \partial^2 s_j} \Big|_{(s_{p,i,j}=0)} = {}^4x_{pj} \quad (p = i, i \neq j) \quad (2.92c)$$

$${}^pG_3^{jjj} \equiv \frac{1}{24} \frac{\partial^4 U_{pj}}{\partial s_p \partial^3 s_j} \Big|_{(s_{p,j}=0)} = {}^7x_{pj} \quad (p \neq j) \quad (2.92d)$$

A similar procedure is followed to calculate the linear and higher-order mode components given the vector of coefficients, x_{ij} (which is of course different from x_{ij} defined for the strain energy above), but now the vector \mathbf{N}_{ij} holds the nodal displacements in physical coordinates, \mathbf{u} . For the case of two modes, the mode components are given as:

- Linear mode component ${}^p\Phi_0$

$${}^p\Phi_0 \equiv \frac{\partial \mathbf{u}_{pi}}{\partial s_p} \Big|_{(s_{p,i}=0)} = {}^{10}x_{pi} \quad (p, i = 1, \dots, m; p = i) \quad (2.93)$$

- Quadratic mode component ${}^p\Phi_1$

$${}^p\Phi_1^i \equiv \frac{1}{2} \frac{\partial^2 \mathbf{u}_{pi}}{\partial s_p \partial s_i} \Big|_{(s_{p,i}=0)} = {}^6x_{pi} \quad (p = i) \quad (2.94a)$$

$${}^p\Phi_1^i \equiv \frac{1}{2} \frac{\partial^2 \mathbf{u}_{pi}}{\partial s_p \partial s_i} \Big|_{(s_{p,i}=0)} = {}^9x_{pi} \quad (p \neq i) \quad (2.94b)$$

- Cubic mode component ${}^p\Phi_2$

$${}^p\Phi_2^{ii} \equiv \frac{1}{6} \frac{\partial^3 \mathbf{u}_{pi}}{\partial s_p \partial^2 s_i} \Big|_{(s_{p,i}=0)} = {}^3x_{pi} \quad (p = i) \quad (2.95a)$$

$${}^p\Phi_2^{ij} \equiv \frac{1}{6} \frac{\partial^3 \mathbf{u}_{pi}}{\partial s_p \partial s_i \partial s_i} \Big|_{(s_{p,i,j}=0)} = {}^5x_{pj} \quad (p = i, i \neq j) \quad (2.95b)$$

$${}^p\Phi_2^{jj} \equiv \frac{1}{6} \frac{\partial^3 \mathbf{u}_{pi}}{\partial s_p \partial^2 s_j} \Big|_{(s_{p,j}=0)} = {}^8x_{pj} \quad (p \neq j) \quad (2.95c)$$

- Fourth-order mode component ${}^p\Phi_3$

$${}^p\Phi_3^{iii} \equiv \frac{1}{24} \frac{\partial^4 \mathbf{u}_{pi}}{\partial s_p \partial^3 s_i} \Big|_{(s_{p,i}=0)} = {}^1x_{pi} \quad (p = i) \quad (2.96a)$$

$${}^p\Phi_3^{ijj} \equiv \frac{1}{24} \frac{\partial^4 \mathbf{u}_{pj}}{\partial s_p \partial^2 s_i \partial s_j} \Big|_{(s_{p,i,j}=0)} = {}^2x_{pj} \quad (p = i, i \neq j) \quad (2.96b)$$

$${}^p\Phi_3^{ijj} \equiv \frac{1}{24} \frac{\partial^4 \mathbf{u}_{pj}}{\partial s_p \partial s_i \partial^2 s_j} \Big|_{(s_{p,i,j}=0)} = {}^4x_{pj} \quad (p = i, i \neq j) \quad (2.96c)$$

$${}^p\Phi_3^{jjj} \equiv \frac{1}{24} \frac{\partial^4 \mathbf{u}_{pj}}{\partial s_p \partial^3 s_j} \Big|_{(s_{p,j}=0)} = {}^7x_{pj} \quad (p \neq j) \quad (2.96d)$$

Due to Schwartz's exchange theorem the tensors containing the mixed derivatives are symmetric, assuming continuity in the point of evaluation [75]. Using a polynomial function of two variables, only two modes can be coupled. The cubic stiffness tensor and the fourth-order mode component defined in Eq.(2.28) contain mixed partial derivatives with respect to three variables and thus a coupling of three modes can be considered. For simplicity, only two modes are taken into account in the formulation above. An upgrade to three coupled modes by an expansion of the polynomial defined in Eq.(2.76) is straightforward, but the cost for the evaluation of all derivatives increases. Both the strain energy and the deformation field that are obtained from a single FE simulation can be differentiated simultaneously with respect to the scaling parameters s_i and s_j .

Applying the procedure defined above for the calculation of the higher-order components on different structural models shows that the parameter G_1^i matches the eigenvalue of the structural model obtained from a FE eigenvalue analysis. Also ${}^p\Phi_0^i$ matches the structural mode shapes. In this way, the linear case (structural governing equation in modal coordinates with linear terms only) is recovered by neglecting the terms of higher order in Eq.(2.19). Furthermore, it is possible to derive the higher-order stiffness and mode component tensors by

differentiation of the nonlinear strain energy and displacement field at a point unequal to zero. This approach can be used for example to identify the higher-order components of a flexible aircraft in a steady, geometrically nonlinear trim state.

2.3.3 Exemplary Calculation of the Higher-Order Components for a Beam Structure

This subsection illustrates the calculation of the higher-order stiffness and mode components of a simple beam structure applying the approach introduced in the last subsection. The structure is described in detail in Section 4.1 and serves here as a simple but descriptive test case. Parameter studies are carried out to identify the convergence behavior of the higher-order terms as function of the stencil size η and the amplitudes s_i and s_j chosen for the calculation of the nonlinear strain energies and deformation fields (vector \mathbf{N}_{ij}).

First, a number of geometrically nonlinear solutions is calculated and the strain energies as well as nodal deformations and rotations are saved. MSC Nastran was used as structural solver and all simulations were done by solution sequence *SOL 106* (nonlinear static). The force fields chosen for the excitation are calculated according to Eq.(2.76). Here, the first out-of-plane and in-plane bending mode are used and the amplitude of the force fields were chosen large enough to obtain significant nonlinear deflections. The stencil size η is seven in this example. For the first out-of-plane bending mode, the 49 force fields are thus given as

$${}^{ab}\mathbf{F}_{11} = \mathbf{K} \left({}^a s_1 \phi^1 + {}^b s_1 \phi^1 \right) , \quad (a, b = 1, \dots, 7) . \quad (2.97)$$

It must be mentioned that the amplitudes ${}^a s_1$ are varying from negative to positive values, centered symmetrically about zero, as depicted schematically in Fig. 2.9. Thus only 13 values unequal zero are obtained for the strain energies and the deformation fields. The strain energies of the nonlinear simulations are plotted in Fig. 2.10 as function of the amplitudes ${}^a s_1$ and ${}^b s_1$, and in a two-dimensional plot in Fig. 2.11 as function of ${}^a s_1$ for ${}^b s_1 = 0$. In addition, the linear strain energy, given by

$$U_{linear} = \frac{1}{2} ({}^a s_1 \phi^1)^T \mathbf{K} ({}^b s_1 \phi^1) = \frac{1}{2} {}^a s_1 {}^b s_1 \Omega_1^2 , \quad (2.98)$$

and the difference between the nonlinear and the linear strain energies is plotted. In Eq.(2.98), Ω_1^2 denotes the natural eigenvalue of the first bending mode. As can be identified from the left plot of Fig. 2.11, the strain energy difference is a symmetric function about the origin, as is expected, but resembles a function which is of higher than second order. This clearly indicates that the nonlinear strain energy contains a term of (at least) fourth order which – after processing – yields the cubic stiffness term ${}^1 G_3^{111}$. However, the difference of the strain energies is very low, and consequently the magnitude of this cubic stiffness term is very low as well (and

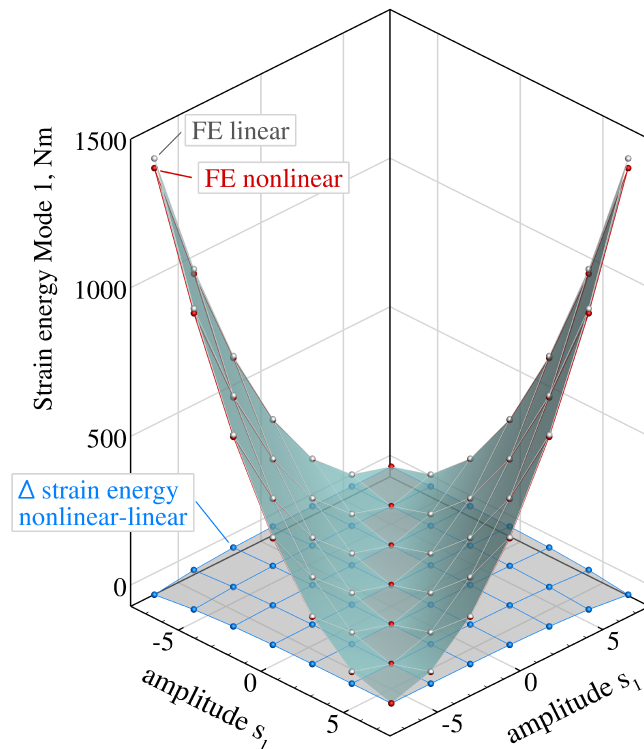


Figure 2.10: Nonlinear and linear strain energies, and their difference as function of the amplitudes a_{s_1} and b_{s_1} for the first out-of-plane bending mode of the beam test case and a stencil size of seven.

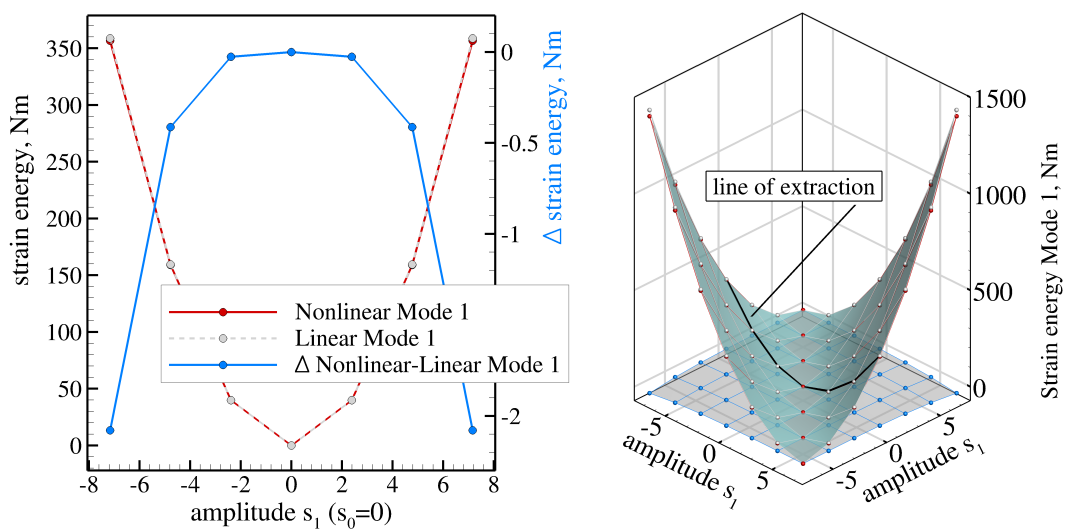


Figure 2.11: Nonlinear and linear strain energies, and their difference as function of the amplitude a_{s_1} ($b_{s_1} = 0$).

has negative sign) in this case. Figure 2.12 shows the corresponding displacements, where the first out-of-plane bending mode is clearly visible. For the sake of clarity, linear displacements

are not plotted in this chart. A similar result is obtained for the second mode shape of the

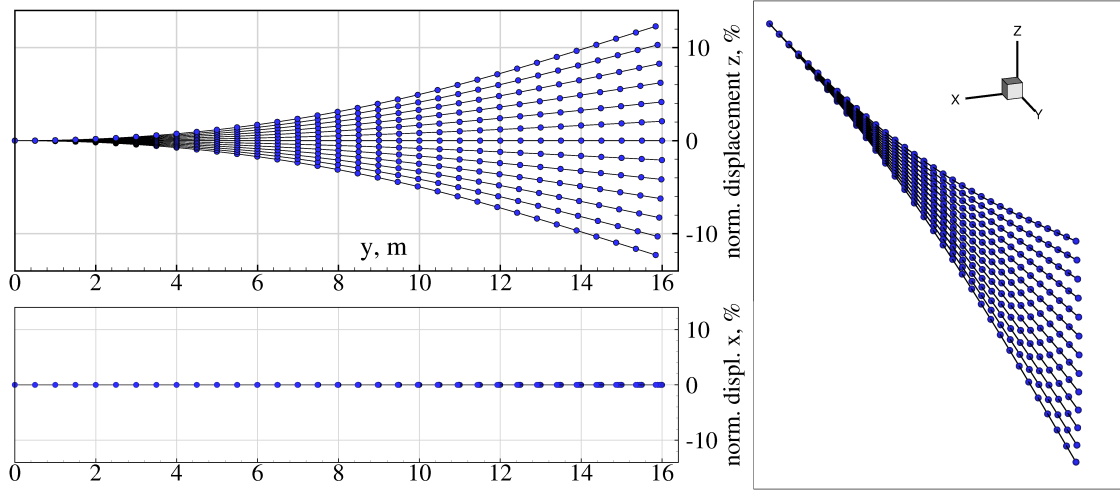


Figure 2.12: Displacements calculated by a geometrically nonlinear FE simulation as function of the amplitude a_{s_1} and b_{s_1} for the first out-of-plane bending mode of the beam test case and a stencil size of seven.

model, which is the first in-plane bending mode. The strain energy plotted in Fig. 2.13 shows higher overall values than for the first out-of-plane bending mode, but the dependence on the amplitudes a_{s_2} and b_{s_2} is similar. The corresponding deformation field, plotted in Fig. 2.14, is comparable to that of the first out-of-plane bending mode (with displacements in the direction of the x-axis). A combination of the first out-of-plane and in-plane bending mode is necessary to identify the coupling terms in the higher-order stiffness and mode components. The force field is then given as

$${}^{ab}\mathbf{F}_{12} = \mathbf{K} \left(a_{s_1} \phi^1 + b_{s_2} \phi^2 \right), \quad (a, b = 1, \dots, 7). \quad (2.99)$$

For this force field, the strain energies and deformations as results of the corresponding non-linear simulations are shown in Fig. 2.15 and 2.16, respectively. The coupling of the modes is evident both in the strain energy and the deformations. However, the magnitude of the differences of the nonlinear and the linear strain energies is very low compared to their overall value at the highest amplitudes of excitation for all three evaluations (first out-of-plane bending, first in-plane bending, and the coupling of both).

2.3.4 Residual-based Evaluation of the Stencil Size and the Amplitude Dependency

Once the nonlinear strain energies and nodal deformation fields for all modes of interest are determined, the linear system of equations (2.80) can be solved for the coefficient vector x_{ij} . As mentioned above, one vector x_{ij} is obtained for the strain energy for each combination of

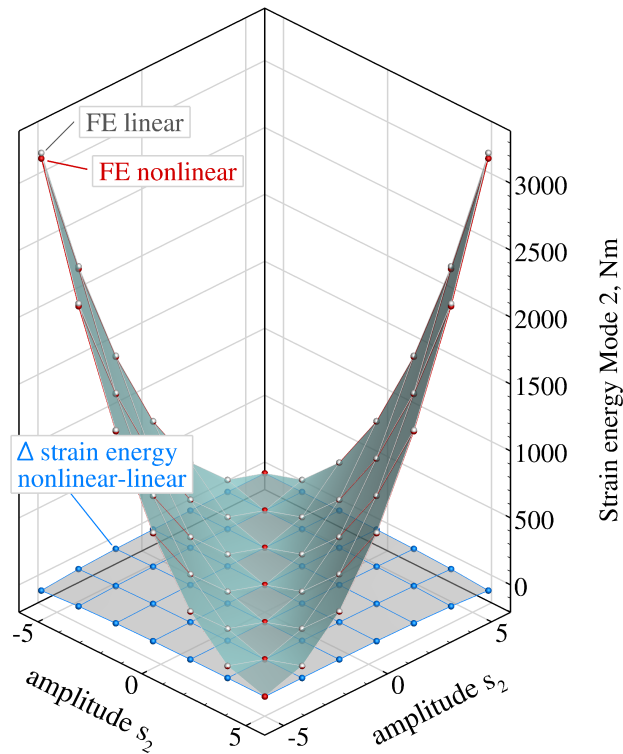


Figure 2.13: Strain energies as function of the amplitudes a_{s_2} and b_{s_2} for the first in-plane bending mode of the beam test case.

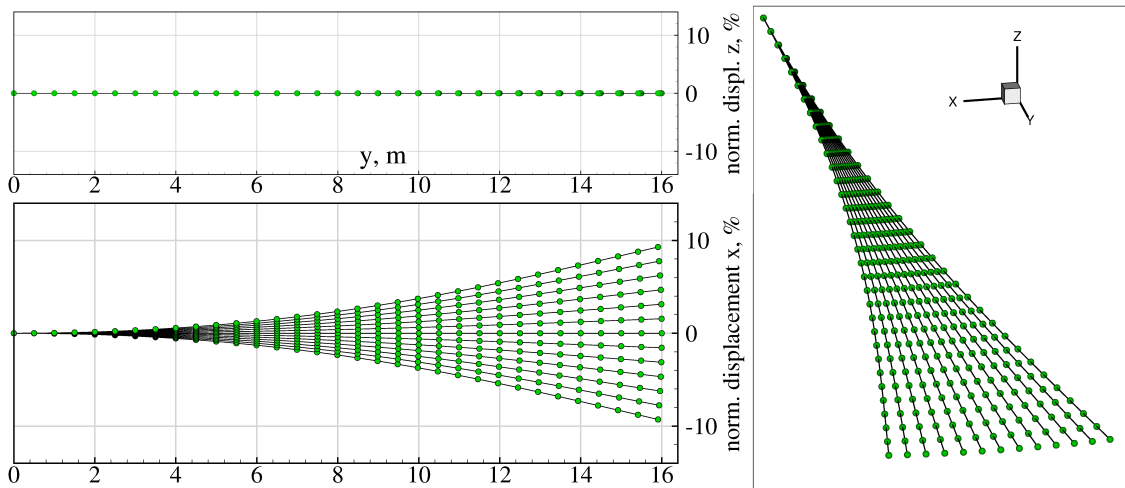


Figure 2.14: Nonlinear displacements as function of a_{s_2} and b_{s_2} for the first in-plane bending mode of the beam test case.

i and j , and one vector x_{ij} is obtained for the nodal displacements of each node and each combination of i and j . For a stencil of size seven, as is the case for the beam test case, matrix \mathbf{P} is composed of 49 rows and 14 columns, thus the resulting linear system is over-determined.

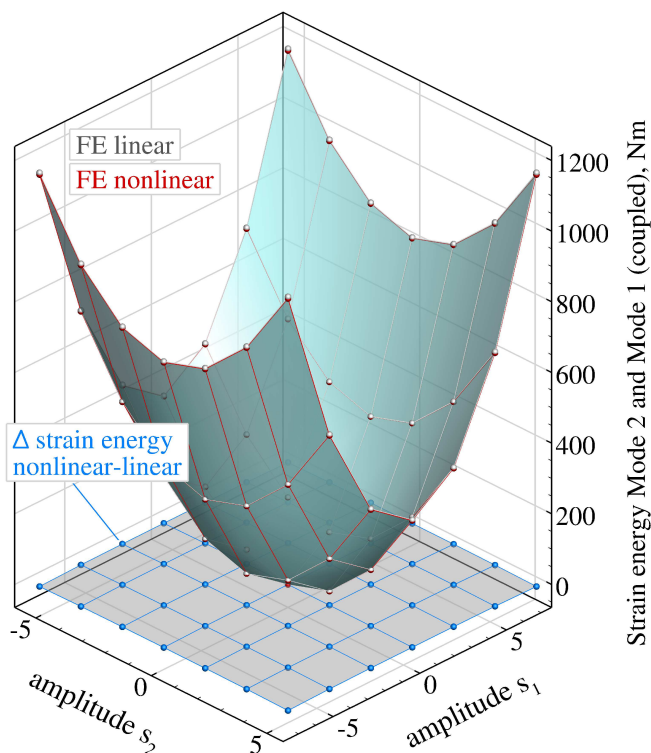


Figure 2.15: Strain energies as function of the amplitudes a_{s_1} and b_{s_2} for a combination of the first out-of-plane and in-plane bending mode of the beam test case.

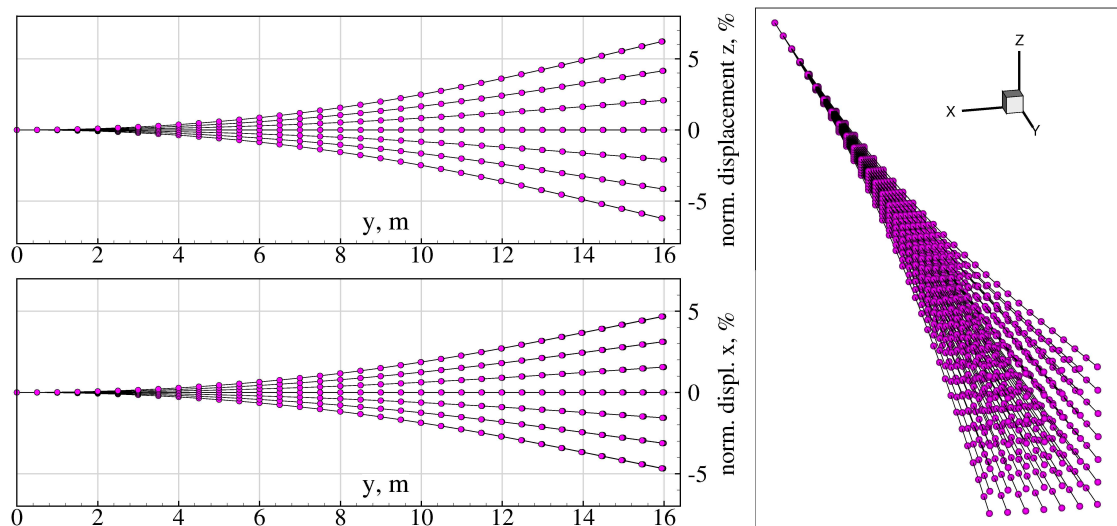


Figure 2.16: Nonlinear displacements as function of a_{s_1} and b_{s_2} for a combination of the first out-of-plane and in-plane bending mode of the beam test case.

Since the size of the stencil, η , and thus the number of nonlinear simulations per combination of a_{s_1} and b_{s_2} , η^2 , can be arbitrary, the question about the dependence of the higher-order

stiffness terms and mode components on the size of the stencil arises. The same applies to the magnitude of the amplitudes a_{s_1} and b_{s_2} which scale the force field. To this end, parameter studies using the beam test case are carried out to analyze the stencil size and amplitude dependency.

In the first study, the magnitude of the amplitudes a_{s_1} and b_{s_2} is kept constant, but the stencil size is increased from four to ten. The ten eigenvectors with the lowest eigenvalues are used for comparison of the ratios of the linear stiffness terms pG_1 to the corresponding eigenvalues calculated by Nastran. The results are plotted in Fig. 2.17. As can be seen, all ten

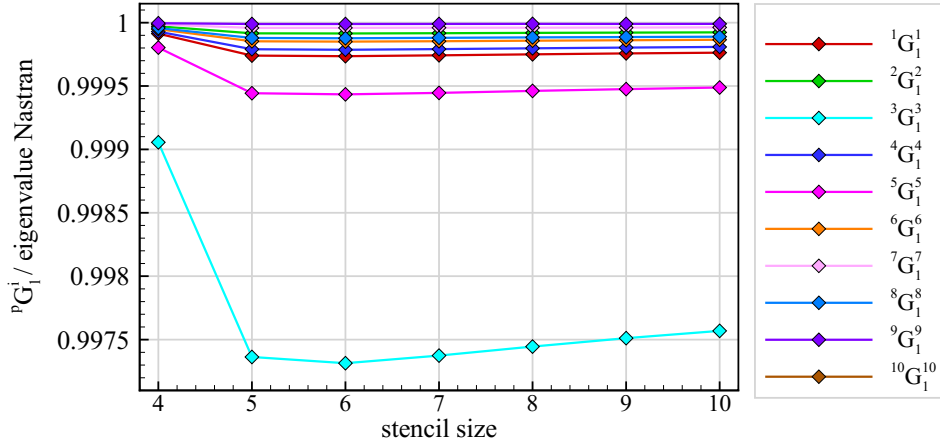


Figure 2.17: Dependency of the ratio of the ten lowest identified linear stiffness terms pG_1 to reference values from a Nastran eigenvalue analysis on the stencil size.

pG_1 stiffness terms could be determined with a ratio higher than 99,7%. However, the highest ratio for all modes is obtained from the stencil of size four. The ratio decreases as the stencil size is increased from four to five, and it increases continuously but slightly from that point on. Considering that the linear stiffness term is evaluated by a second partial derivative, cf. Eq. 2.90, the stencil of size four, which results in the lowest number of nonlinear simulations ($\eta^2=16$), obviously yields the best ratios because the solution of the linear system of equations, Eq.(2.80), is more unique.

The convergence of the linear mode components ${}^p\Phi_0$ of the beam test case was analyzed separately for the translational and the rotational DOFs. A measure for the difference between

the particular terms of ${}^p\Phi_0$ and the eigenvectors from Nastran is defined by the following residuals:

$${}^pR_0^{trans} = \sum_{k=1}^n \sqrt{\left({}^p\Phi_{0,x}^k - \phi_x^{p,k}\right)^2 + \left({}^p\Phi_{0,y}^k - \phi_y^{p,k}\right)^2 + \left({}^p\Phi_{0,z}^k - \phi_z^{p,k}\right)^2}, \quad (p = 1, \dots, m) \quad (2.100)$$

$${}^pR_0^{rot} = \sum_{k=1}^n \sqrt{\left({}^p\Phi_{0,rx}^k - \phi_{rx}^{p,k}\right)^2 + \left({}^p\Phi_{0,ry}^k - \phi_{ry}^{p,k}\right)^2 + \left({}^p\Phi_{0,rz}^k - \phi_{rz}^{p,k}\right)^2}. \quad (2.101)$$

Here, index k denotes a structural node, (x, y, z) denote the axes of the translational DOFs, and (rx, ry, rz) denote the axes of the rotational DOFs. The residuals ${}^pR_0^{trans}$ and ${}^pR_0^{rot}$ are plotted in Fig. 2.18. The plots show a moderate convergence of the residuals, both for the translational

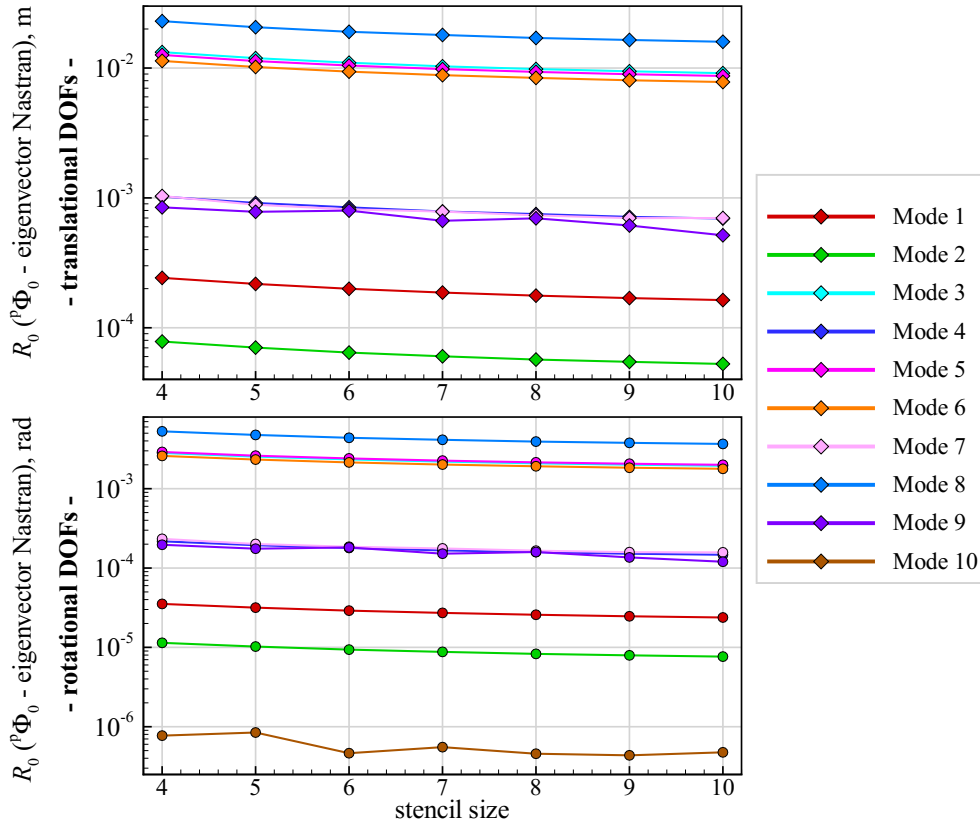


Figure 2.18: Difference between identified linear mode components ${}^p\Phi_0$ and references from Nastran modal analysis (translational and rotational DOFs).

and the rotational DOFs. For instance, the translational residual of the first bending mode decreases from 0.000242 m (stencil size four) to 0.000163 m (stencil size ten), which corresponds to a reduction of approximately 33%. The residuals of the rotational DOFs are more than one

magnitude lower than the residuals of the translational DOFs (for the same mode). Obviously, a further increase of the size of the stencil (greater than ten) does not provide a significant improvement for this test case for both the translational and the rotational DOFs.

The convergence of the higher-order mode components is analyzed next. Unfortunately, a reference – such as eigenvectors calculated by Nastran as for the linear mode components – is not available for the higher-order mode components and a measure for the convergence is now formulated in terms of a residual which is evaluated again each time the stencil size is increased. Considering, for simplicity, only the individual (uncoupled) quadratic mode components, the residual of the translational DOFs of the quadratic mode component, ${}^p R_1^{trans}$, is defined as

$${}^p R_1^{trans} = \sum_{k=1}^n \sqrt{\left({}^\eta \Phi_{0,x}^{p,k} - {}^{\eta-1} \Phi_{0,x}^{p,k} \right)^2 + \left({}^\eta \Phi_{0,y}^{p,k} - {}^{\eta-1} \Phi_{0,y}^{p,k} \right)^2 + \left({}^\eta \Phi_{0,z}^{p,k} - {}^{\eta-1} \Phi_{0,z}^{p,k} \right)^2} \quad (p = 1, \dots, m), \quad (2.102)$$

where the lower left index η denotes the stencil size. These residuals are plotted in Fig. 2.19 for the beam test case. A significant decrease of the residuals over several orders of magnitude

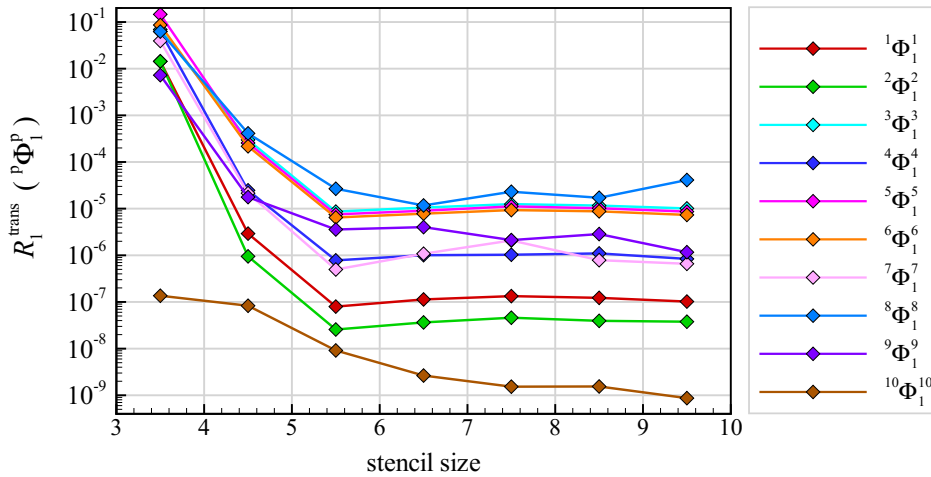


Figure 2.19: Convergence of the quadratic mode components defined by ${}^p R_1^{trans}$ (translational DOFs of individual, uncoupled modes) as function of the stencil size.

(except for mode ten, which is the first torsion mode) is obtained for an increase of the stencil size from three to six. The reason therefore is that only nine nonlinear solutions are available from a stencil of size three, and the accuracy of the quadratic mode components is increased considerably if 16 or 25 nonlinear solutions are available for the evaluation of the coefficients in Eq.(2.80). On the other hand, stencil sizes greater than seven do not improve the convergence of this test case.

Similar results are obtained for the cubic and fourth-order mode components of the beam test case. The evaluation of the convergence was done with an equation similar to Eq. 2.102, and again for the higher-order components of individual modes only. The results are shown in

Fig. 2.20 and Fig. 2.21. For the cubic mode components, the strongest decrease of the residual is obtained for an increase of the stencil size from three to five. Stencils larger than five decrease

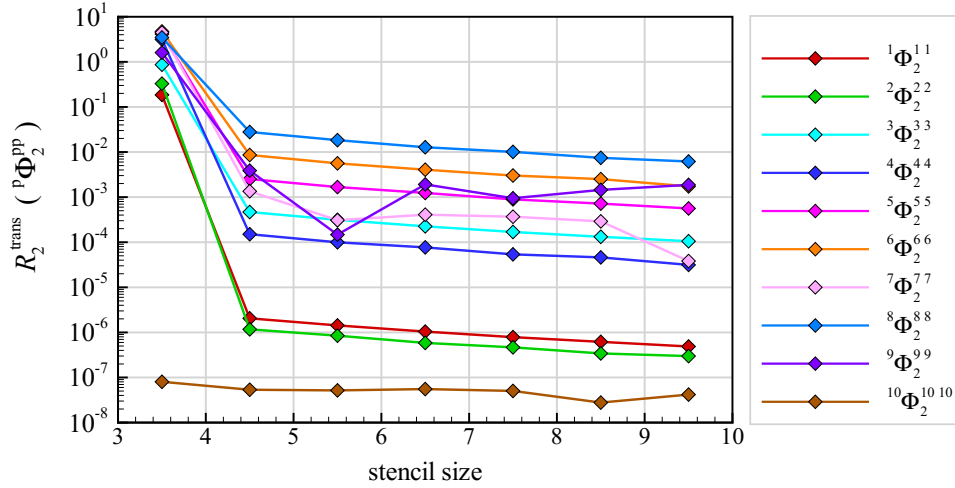


Figure 2.20: Convergence of the cubic mode components defined by ${}^p R_2^{trans}$ (translational DOFs of individual, uncoupled modes) as function of the stencil size.

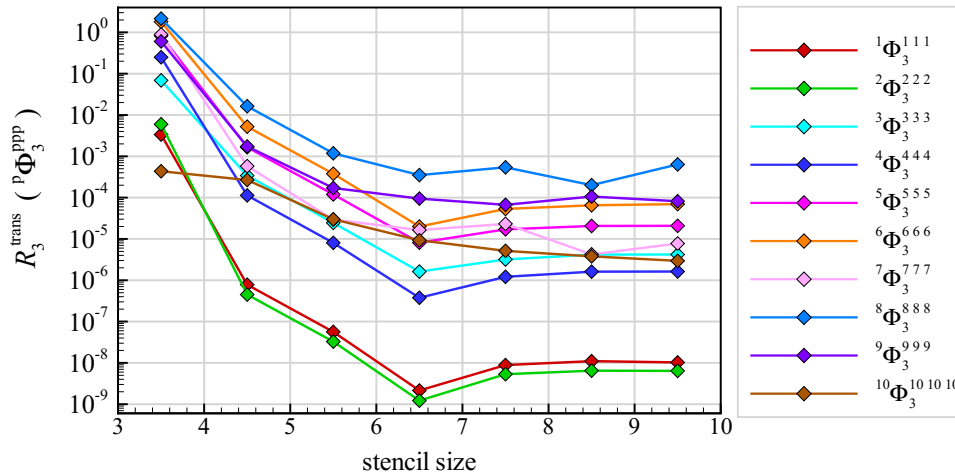


Figure 2.21: Convergence of the fourth-order mode components defined by ${}^p R_3^{trans}$ (translational DOFs of individual, uncoupled modes) as function of the stencil size.

the residual only gradually. Considering the fourth-order mode components of the beam test case, increasing the stencil size up to seven yields a significant decrease of the residual.

In addition to the size of the stencil, the magnitudes of ${}^a s_i$ and ${}^b s_j$, which scale the force field defined in Eq.(2.76), can be optimized to increase the accuracy of the higher-order stiffness and mode components. A parameter study in which these amplitudes are varied is shown in Fig. 2.22 for the first out-of-plane bending mode of the beam test case. The stencil size is fixed at seven, and the amplitudes are varied within limits that correspond to normalized tip

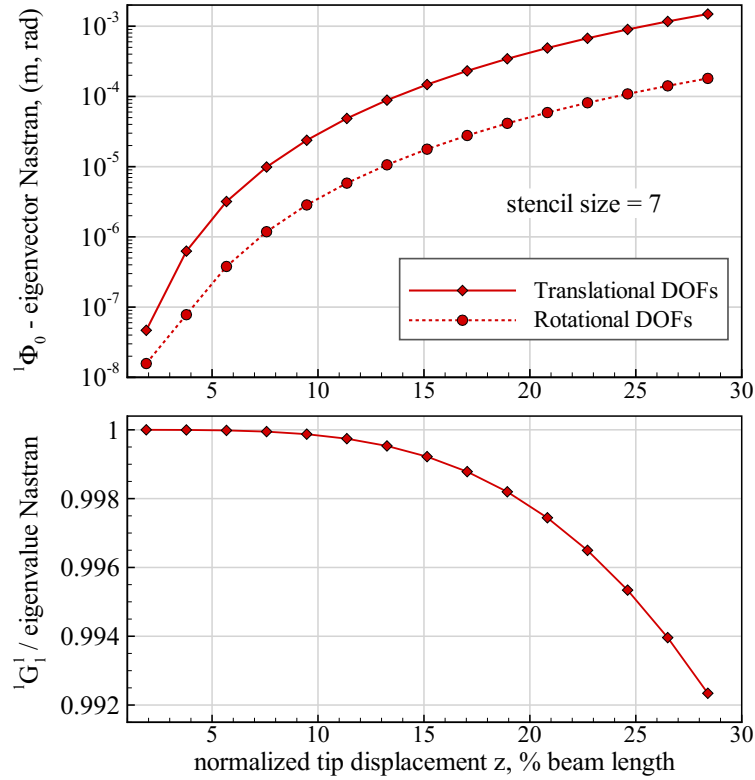


Figure 2.22: Residuals of eigenvectors and eigenvalues for the first out-of-plane bending mode as defined in Eq.(2.100) as function of the amplitudes and a fixed stencil of size seven.

displacements ranging from 2% up to almost 29% with respect to the length of the beam. The plots show a significant increase of the residuals and thus a decrease of the accuracy of the linear mode component ${}^1\Phi_0$ and the linear stiffness term 1G_1 with increasing amplitude. Thus for the evaluation of the linear mode component and the linear stiffness term, comparatively lower values for ${}^a s_i$ and ${}^b s_j$ are advantageous because the evaluation of the second-order derivatives, Eq.(2.90) for the linear stiffness term, and the first-order derivatives, Eq.(2.93), for the linear mode components, yields better results in this case. The reason therefore is that with lower amplitudes, the nonlinear strain energy and the nonlinear displacement field are closer to the linear ones, i.e., their differences are lower, and the quadratic function fitted to these results is close to a quadratic function fitted to the linear results (which would yield the eigenvectors and eigenvalues exactly). Nevertheless, if comparatively small (approximately less than 5% normalized tip displacement) deformations are applied in the nonlinear simulations for the solution vector N_{ij} , accurate results are obtained for the linear stiffness terms and mode components.

A similar result is obtained for the evaluation of the quadratic, cubic, and fourth-order mode components for this test case, as shown in Fig. 2.23. The residual is calculated by an equation similar to the one defined in Eq.(2.102), but the differences in the x , in the y , and in the z direction are now taken from one deformation increment to the next. The result

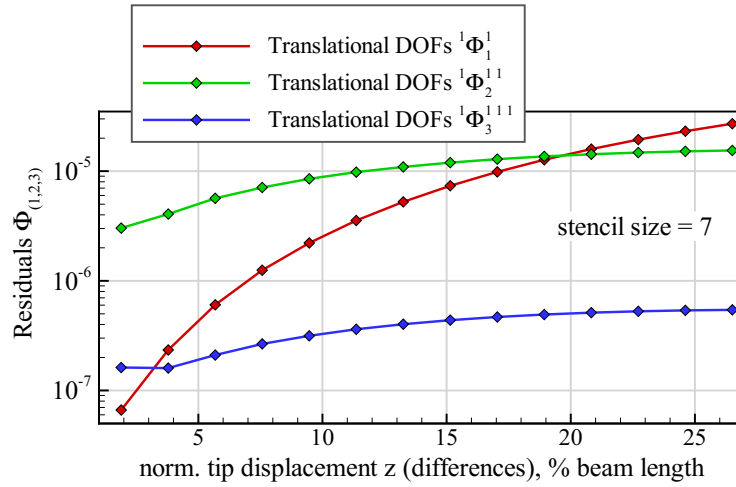


Figure 2.23: Residuals of quadratic, cubic, and fourth-order mode components of the first out-of-plane bending mode for varying amplitudes and a fixed stencil of size seven.

is rather remarkable because it is expected that comparatively large deformations would be necessary to excite nonlinear effects in terms of geometric displacements. On the other hand, the nonlinear solution sequence of Nastran, which is used for the calculation of the solution vector \mathbf{N}_{ij} , always considers geometrical nonlinearities, even in the case of very low magnitudes of the overall displacements [14]. The residual of the quadratic mode components shows a stronger dependence on the amplitude compared to the residual from the cubic and fourth-order mode components, which reveals that also in this case small amplitudes for a_{s_i} and b_{s_j} are appropriate.

In general the size of the stencil can be arbitrary, but regarding the computational effort which depends quadratically on the stencil size, a value of seven seems reasonable. As mentioned above, the amplitudes used for the nonlinear simulations, a_{s_i} and b_{s_j} , should be rather small, a value of approximately 5% tip displacement with respect to the length of the beam can be taken as an adequate starting point.

Chapter 3

The Aeroelastic Model of the Free-flying Aircraft

This chapter describes the setup of the aeroelastic model which is used for the numerical solution of the static and dynamic structural governing equation, Eq.(2.28) and Eq.(2.29), respectively, as well as for the inertially coupled flight dynamic equations of the free-flying elastic aircraft, Eq.(2.70). The theory and the implementation of the steady and unsteady vortex-lattice method (VLM) for the calculation of the aerodynamic forces are explained in Section 3.1. A coupling model approach is used for the data transfer between the aerodynamic and the structural model, it is described in Section 3.2. The unsteady solution sequence in the time domain is summarized in Section 3.3, and the approach for trimming the aircraft in steady horizontal flight is outlined in Section 3.4.

3.1 Calculation of Aerodynamic Forces by a Vortex-lattice Method

Although various aeroelastic simulation toolboxes with different aerodynamic methods have been presented, as described in Section 1.2, the following reasons support the choice of a vortex-lattice method for the aeroelastic model of this thesis [44]:

- Aerodynamic panels can undergo large translations and rotations in all directions. This is one of the greatest advantages of the vortex-lattice method compared to the *doublet-lattice method* (DLM), which is valid for small out-of-plane displacements of lifting surfaces only.
- The method is comparatively fast (even for unsteady calculations) and computationally much cheaper than solutions of the unsteady Euler or Navier-Stokes equations using a volume-grid CFD approach.
- It is a medium fidelity method that accounts for 3D effects (e.g. at wingtips) and interactions of lifting surfaces (which are particularly developed in terms of the time-dependent

downwash from wing to tail). This is in contrast to the widely applied 2D strip theories, which per se disregard such effects.

A large amount of literature about the vortex-lattice method is available. The theoretical basis explained in the following is taken from the detailed and descriptive book of Katz and Plotkin [76]. Although only few contributions to the theory of the vortex-lattice method were made in the context of this thesis, the description of the method itself and important details of the implementation are included for the sake of completeness. The focus is first on the theory and implementation of the unsteady vortex-lattice method (UVLM), the conversions necessary for the simulation of steady flows are described thereafter.

3.1.1 Basics of Aerodynamic Potential Theory

Starting with the Navier-Stokes equations that describe the conservation of mass, momentum, and energy for a viscous, compressible fluid (continuum), assumptions about the flow field are introduced from the beginning for simplification. These assumptions are based on expected physical properties of the aerodynamic flow of the test cases that will be analyzed. In general, they are characterized by such low speeds that the flow field can be taken as divergence free and thus incompressible, the Mach number stays well below 0.3. On the other hand, the Reynolds number is expected large enough to neglect the viscosity of the fluid, although an estimation for the viscous drag will be included in the calculation of the aerodynamic forces¹.

For an incompressible fluid, the continuity equation, which governs the conservation of mass, reduces to [76]

$$\nabla \cdot \mathbf{u} = \frac{\partial u}{\partial x} + \frac{\partial v}{\partial y} + \frac{\partial w}{\partial z} = 0 \quad , \quad (3.1)$$

where \mathbf{u} denotes the flow velocity vector, and u, v, w denote its components along the Cartesian axes x, y , and z , respectively. Equation(3.1) expresses the necessary condition that the divergence of the flow field is equal to zero. It is important to mention that this equation contains no time derivatives; an appropriate formulation of the boundary conditions is thus required to account for the time-dependent motion of exposed boundaries, such as solid walls. Assuming irrotational motion of the fluid particles, which is justified if high Reynolds number flows outside of shear layers are considered, the vorticity of the flow field, ζ , vanishes,

$$\zeta = \nabla \times \mathbf{u} = \mathbf{0} \quad . \quad (3.2)$$

It can be shown that the velocity field $\mathbf{u}(x, y, z)$ of an incompressible and irrotational flow can be obtained by the gradient of a scalar function Φ (the velocity potential) at each point in the flow domain,

$$\mathbf{u} = \nabla \Phi \quad . \quad (3.3)$$

¹However, due to Kelvin's theorem the influence of viscosity in the infinitesimal thin wake cannot be neglected and is of course taken into account.

Inserting Eq.(3.3) into Eq.(3.1) leads to *Laplace's equation*, which is the governing equation for the velocity of an incompressible and irrotational flow:

$$\nabla \cdot \mathbf{u} = \nabla \cdot \nabla \Phi = \nabla^2 \Phi = 0 . \quad (3.4)$$

Laplace's equation is a linear, elliptic differential equation that describes a boundary-value problem, where the values at the boundaries must be specified at solid walls and at infinity for typical aerodynamic problems [76]. For a space-fixed reference frame and if the flow is exterior to the body, boundary conditions of the Neumann type can be specified

$$\frac{\partial \Phi}{\partial n} = \mathbf{n} \cdot \mathbf{u}_b , \quad \text{on the surface of the body} , \quad (3.5a)$$

$$\nabla \Phi \rightarrow 0 , \quad \text{at infinity} , \quad (3.5b)$$

where $\frac{\partial \Phi}{\partial n}$ denotes the normal derivative of the potential, \mathbf{n} the surface normal, and \mathbf{u}_b the velocity at a point on the surface. The first boundary condition usually specifies a zero normal flow on solid boundaries (non-penetration condition). Following the calculation of the velocity field, the pressure field is obtained from the (time-dependent) Bernoulli equation, since the pressure field of an incompressible flow is a pure kinematic value that directly results from the velocity field. The key feature of Laplace's equation is linearity which allows the superposition of elementary solutions. In the context of aerodynamic flows, important elementary solutions are uniform flow, sources and doublets. They can be formulated not only to fulfill Laplace's Equation (3.1), but also the boundary condition specified by Eq.(3.5), their strength is determined as part of the solution of the entire flow field. The basic idea for the calculation of the flow field over e.g. an entire aircraft using potential-based methods is the proper choice of elementary solutions to Laplace's equation (singularity elements) and their distribution over the boundary of the object submerged to the flow. This approach almost naturally leads to a discretization of the flow domain by the singularities. Since the singularity elements are influencing each other (without preferred direction or time dependence because of the ellipticity of Laplace's equation), a set of algebraic equations is solved to determine the circulation Γ of each element:

$$\mathbf{AIC} \cdot \Gamma = \mathbf{RHS} \quad (3.6)$$

The *aerodynamic influence coefficients* (AIC) matrix \mathbf{AIC} relates the velocity that is induced at certain points in the flow domain (the *collocation points*) to the circulation of all elementary solutions. The right hand side \mathbf{RHS} of this set of equations consists of the kinematic boundary condition, which includes the non-penetration condition (zero flow velocity in normal direction) at solid walls and the Kutta condition. Once the circulation of each element is determined, the dependent variables, such as aerodynamic loads, pressures, and velocity components are calculated as function of the circulation.

3.1.2 Spatial Discretization and Details of the Unsteady Vortex-lattice Implementation

In the case of the vortex-lattice method, the body considered is composed of lifting surfaces (wings) of infinitesimal thickness, i.e. no thickness effects are modeled. Therefore, the singularity elements chosen are *vortex rings*. These elements are based on the elementary solution of a vortex line and capable of producing lift by bound circulation along a line. In this case, they are formulated to have a constant distribution of vorticity². Each lifting surface is discretized by a number of plane quadrilateral panels in the spanwise and the chordwise direction. The discretization process places the panels on the camber surface of the wing, which can be of arbitrary shape, but is preferably bounded by four sides without excessive twist. Increasing the panel density at particular positions of the wing where the circulation shows strong local gradients (e.g. near kinks or near wingtips) increases the accuracy of the solution. At this point, the grid metric is calculated including the panel areas, normal vectors, and the location of the collocation points (at the center of the three quarter chord line). An exemplary discretization of a wing by aerodynamic panels and vortex rings is depicted in Fig. 3.1. A vortex ring is placed in a quadrilateral panel such that one of the four vortex lines coincides with the quarter chord line of the panel. The reason for this location is that the two-dimensional Kutta condition will be satisfied along the chord for each aerodynamic panel [76]. The two adjacent vortex rings are collinear with the edges of the panel in flow direction, and the fourth ring coincides with the quarter chord line (and thus with the vortex ring) of the neighboring panel in chordwise direction. At the trailing edge, the last vortex line in chordwise direction is placed as shown in Fig. 3.1, by an offset of approximately 0.3 times the distance traveled during one time step with respect to the trailing edge of the wing. The three-dimensional trailing edge condition, which requires that the circulation at the trailing edge vanishes, is thereby fulfilled. Given the grid metric, the AIC matrix is calculated, which will be used to determine the velocity that is induced by vortex ring i with circulation Γ_i at collocation point j . The calculation of the AIC matrix is based on the evaluation of the *Biot-Savart Law* for each of the straight vortex segments of each bound vortex ring. Since the circulation of each vortex ring is unknown at this point, it is set to unity. The shape of the AIC matrix is $N \times N$, where N denotes the total number of aerodynamic panels. The AIC matrix only depends on the grid metric of the aircraft. Not only the bound circulation of the wing is discretized by vortex rings, but also the circulation of the wake.

The further solution process is based on a time-stepping technique with time step size Δt . At the beginning of each time step, the right hand side of Eq.(3.6) is evaluated for each panel i using the normal vector of the panel, \mathbf{n}_i , the velocity $\mathbf{V}_{RB,i}$ due to onflow and rigid-body

²Higher-order vortex ring elements with linearly or quadratically varying vorticity can be formulated at significantly higher implementation effort and computational costs. A good example for a higher-order implementation is the work of Horstmann [77].

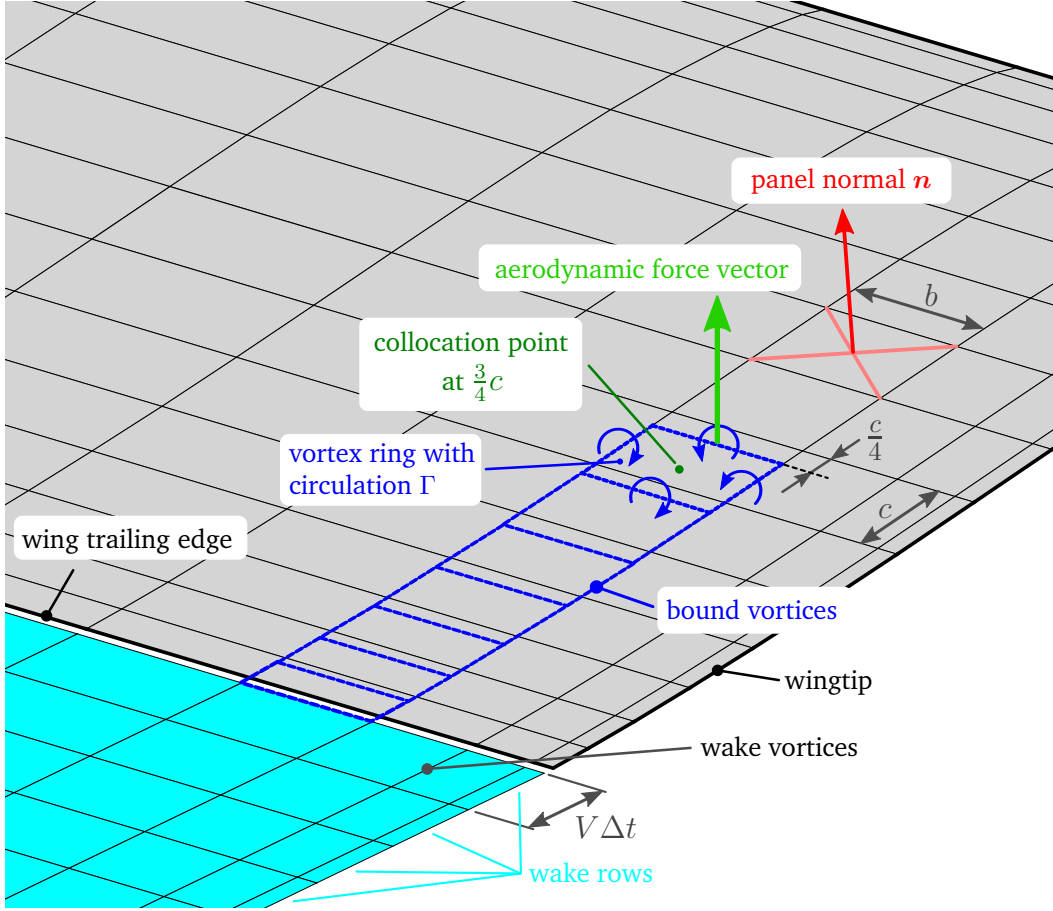


Figure 3.1: Discretization of a cambered lifting surface with vortex rings and details of the grid metric.

motion of the wing, and the velocity induced by all wake vortices at the collocation point of the panel. Further disturbance velocities, such as those induced by gusts or elastic deformation of the structure can be added,

$$RHS_i = -(\mathbf{V}_{RB,i} + \mathbf{V}_{wake,i} + \mathbf{V}_{gust,i} + \mathbf{V}_{elastic,i}) \cdot \mathbf{n}_i \quad (3.7)$$

All boundary conditions RHS_i of the wing are collected in vector \mathbf{RHS} of Eq.(3.6). Equation(3.6) can now be written – with both the AIC matrix and the kinematic boundary conditions known – as follows:

$$\begin{pmatrix} AIC_{11} & AIC_{12} & \cdots & AIC_{1N} \\ AIC_{21} & AIC_{22} & \cdots & AIC_{2N} \\ \vdots & \vdots & \ddots & \vdots \\ AIC_{N1} & AIC_{N2} & \cdots & AIC_{NN} \end{pmatrix} \begin{pmatrix} \Gamma_1 \\ \Gamma_2 \\ \vdots \\ \Gamma_N \end{pmatrix} = \begin{pmatrix} RHS_1 \\ RHS_2 \\ \vdots \\ RHS_N \end{pmatrix} \quad (3.8)$$

This algebraic system of equations is solved for the unknown circulation Γ_i of each panel. The aerodynamic loads in terms of a force vector with three components of each panel can be calculated as function of the circulation. Here, the method proposed by Mauermann was used for the calculation of the aerodynamic forces \mathbf{F}^A [58],

$$\mathbf{F}_i^A = \mathbf{F}_{S,i}^A + \mathbf{F}_{U,i}^A . \quad (3.9)$$

The steady force contribution $\mathbf{F}_{S,i}^A$ is calculated as

$$\mathbf{F}_{S,i}^A = \rho_\infty \Gamma_{eff,i} (\mathbf{V}_{RB,i} + \mathbf{V}_{gust,i} + \mathbf{V}_{elastic,i}) \times \mathbf{r}_i , \quad (3.10)$$

where ρ_∞ denotes the onflow velocity, and \mathbf{r}_i is the vector of length b (see Fig. 3.1) that is identical to the quarter chord line of the corresponding i -th aerodynamic panel. The effective circulation $\Gamma_{eff,i}$ equals the circulation of the corresponding aerodynamic panel if the panel is located at the leading edge of the lifting segment, otherwise it is the difference of the circulation of the i -th panel and the circulation of the neighboring panel in chordwise (downstream) direction. The unsteady contribution of the aerodynamic forces $\mathbf{F}_{U,i}^A$ is calculated as follows [58]:

$$\mathbf{F}_{U,i}^A = \rho_\infty A_i \frac{\partial \Gamma_{eff,i}}{\partial t} \mathbf{n}_i , \quad (3.11)$$

where A_i is the area of panel i and \mathbf{n}_i its normal vector. As can be seen from Eq.(3.11) the unsteady force component acts in the direction of the normal vector of the panel. The time derivative of the circulation can be discretized using e.g. backward-differential formulas of appropriate order. In the current implementation, a second-order backward scheme was applied [58],

$$\frac{\partial \Gamma}{\partial t} \approx \frac{3\Gamma^n - 4\Gamma^{n-1} + \Gamma^{n-2}}{2\Delta t} , \quad (3.12)$$

where the superscript n denotes the current time step and Δt the time step size. Both the steady and unsteady aerodynamic force act at the center of the quarter-chord line of each aerodynamic panel, i.e., at the center of each bound vortex ring, see Fig. 3.1.

Every new time step, a wake panel is shed from each trailing-edge vortex panel. The wake panel is assigned the same vortex strength as the circulation of the panel it was shed from in the previous time step. This process automatically fulfills the *Kelvin theorem* (conservation of angular momentum), which states that the total circulation surrounding the wing and the wake does not change with time,

$$\frac{D}{Dt} (\Gamma_{aircraft} + \Gamma_{wake}) = 0 , \quad (3.13)$$

where $\frac{D}{Dt}$ denotes the substantial derivative [76]. Thus every time-dependent change of the circulation of the wing is associated with a change in the circulation of the wake, the appearance of a starting vortex is the result of Kelvin's theorem. It must be mentioned that the strength of

each wake vortex remains unchanged during all subsequent time steps, and the wake carries no aerodynamic loads (it can be relaxed to move with the streamlines of the flow behind the wing). Furthermore, the propagation of the circulation from each vortex ring at the trailing edge to the wake vortex rings corresponds to the unsteady equivalent of the Kutta condition. The wake shedding process accounts for the influence of the history of the motion of the wing onto the actual bound circulation of the wing, since the disturbance velocities from all wake panels is taken into account, as can be seen from Eq.(3.7). However, taking into account a large amount of wake panels highly increases the computational costs, whereas the influence of wake rows far behind the wing can be neglected – the influence of a vortex filament in terms of its induced velocity at a certain point decreases with the square of the distance of that point to the vortex. In practice, the wake can be truncated after it has developed a certain length in order to speed up the calculation. An exemplary wing with evolved wake panels of an unsteady vortex-lattice solution is depicted in Fig. 3.2.

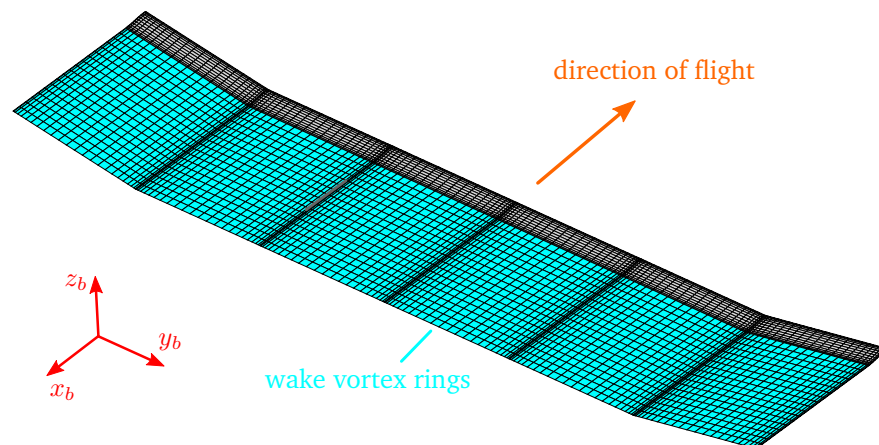


Figure 3.2: Wing and wake of the vortex-lattice method discretized by vortex rings. The wake panels evolve with the solution.

Subsequent to each time step, the metric of the aerodynamic grid is calculated again, including updates of e.g. the panel areas and the normal vectors. To this end, translations and rotations of aerodynamic panels due to structural deformations are always taken into account and no linearization or assumption is made in this regard. In general, also the AIC matrix can be updated at every new time step or based on physical considerations, such as deflections of the wing due to structural deformations. Aeroelastic simulations of typical wing-like structures showed that an update of the AIC matrix is not necessary even at large deformations. The solution sequence of the unsteady vortex-lattice method is illustrated in Fig. 3.3.

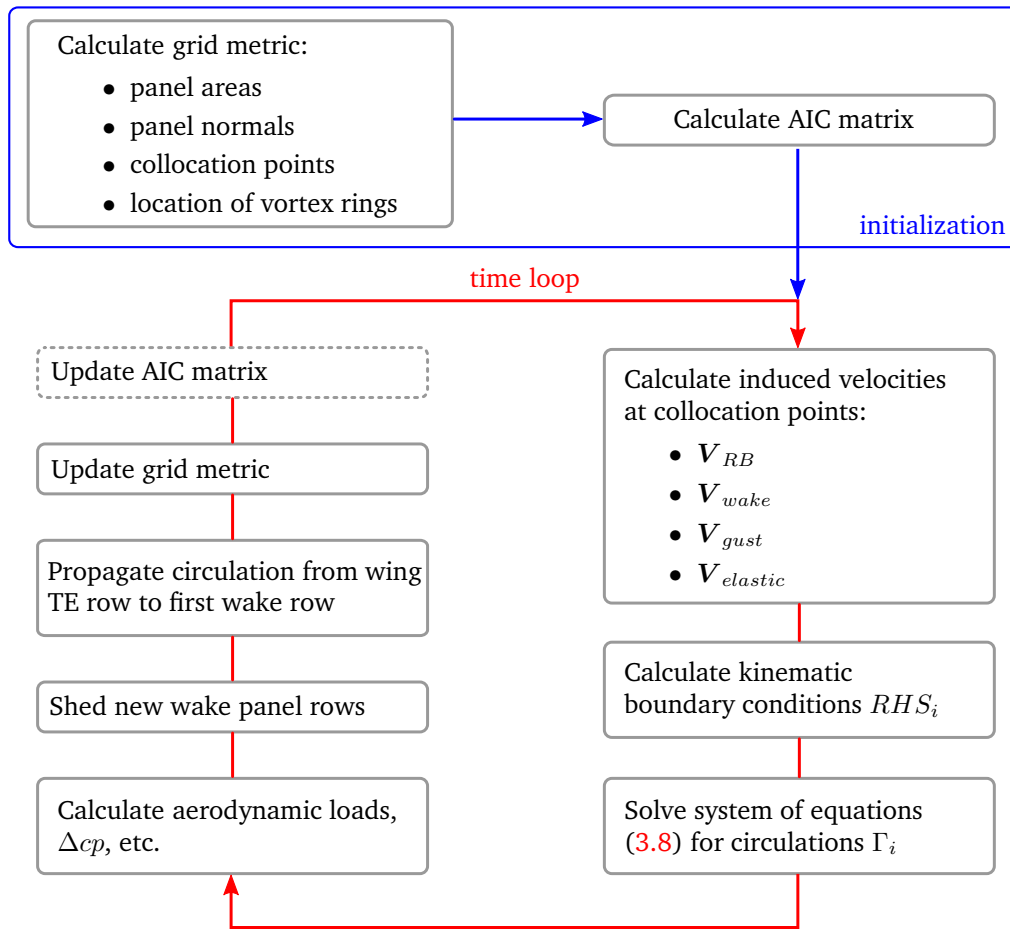


Figure 3.3: Solution sequence of the unsteady vortex-lattice method.

3.1.3 Steady Vortex-lattice Method

If a steady aerodynamic solution is desired, the solution sequence will simplify considerably compared to the unsteady case. The circulation of the wake is equal in all vortex rings in flow direction, i.e., no streamwise gradient in the circulation of the wake exists. Thus the contribution of each trailing vortex filament of a wake vortex ring cancels the circulation of the leading segment of the neighboring panel downstream. The strength of each wake panel is equal to the strength of the corresponding wing panel at the trailing edge of the wing to fulfill the three-dimensional trailing edge condition. The result is that the wake panels can be seen as lengthy vortex rings with side vortex filaments parallel to the free stream. The trailing vortex line represents the starting vortex, which is preferably located far downstream of the wing to minimize its influence. An example of a wake of the steady vortex-lattice method is shown in Fig. 3.4.

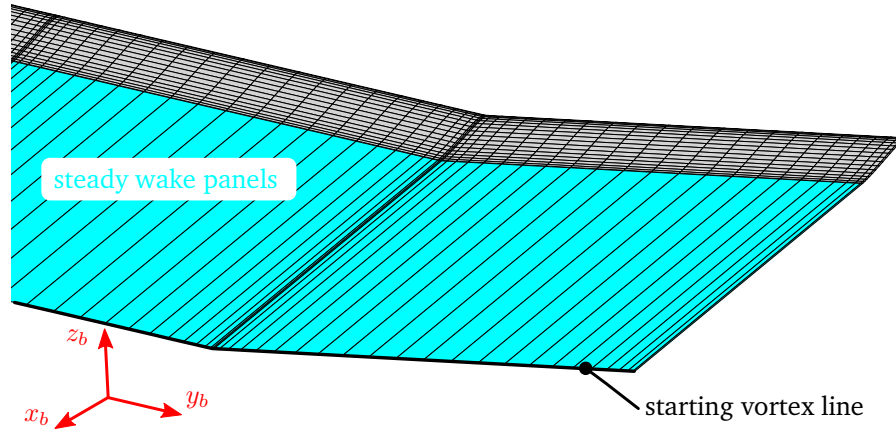


Figure 3.4: Wake panels of the steady vortex-lattice method.

3.1.4 Enhancements of the Steady and Unsteady Vortex-lattice Method

One drawback of the aerodynamic method described is that the aerodynamic forces, defined by Eq. 3.10, are at any time perpendicular to the sum of the rigid-body, gust, and elastic velocity contributions. Thus no induced drag is calculated because the effect of the induced velocity of the wake and bound panels is not included in this expression. The calculation of the induced drag, $F_{D,i}^A$, is done separately by summing the velocities that are induced by the streamwise segments of the bound vortex rings and all segments of the wake vortex rings:

$$\mathbf{F}_{D,i}^A = \rho_{\infty} \Gamma_{eff,i} (\mathbf{V}_{bodystreamwise,i} + \mathbf{V}_{wake,i}) \times \mathbf{r}_i . \quad (3.14)$$

This follows the approach proposed by Katz and Plotkin [76]. The induced drag becomes a quadratic function of the lift coefficient, as will be shown for the calculation of aerodynamic coefficients of the X-HALE aircraft discussed in Section 4.3. However, this method gives correct results for unswept wings only and yields small errors for swept wings when compared to vortex-lattice methods based on horseshoe vortices.

An aerodynamic method based on potential theory is per definitionem not able to calculate viscous forces because vorticity is neither generated nor transported in the flow field. Of course boundary layer analysis can be included and coupled to potential methods, but their application would require a 3D panel method which discretizes the upper and the lower side of the wing to obtain the velocity distribution around the airfoil of the wing. Viscous forces can have significant contributions to the overall drag balance of an aircraft, though. Since the vortex-lattice method and the aeroelastic program developed for this thesis will be applied to aircraft operating at low speeds, problems arise because the regime of low Reynolds numbers is entered. In particular, the flight speed of the X-HALE UAV at the beginning of the maneuvers (cf. Section 4.3) is 16 m/s. Given the fluid air at 20° C at sea level conditions and a chord

length of the main wing of 0.2 m yields a Reynolds number of approximately $2.1 \cdot 10^5$. The thickness of the boundary layer increases at such low Reynolds numbers, which results in significant viscous drag contributions. Regarding a typical airfoil section used for radio controlled model aircraft with a thickness of 10-14%, laminar separation bubbles are likely to occur (as will be shown in Section 4.3 for the X-HALE's *EMX07* airfoil) [78]. The consideration of such effects in an aeroelastic software for UAV modeling is desirable, but their explicit calculation by sophisticated models representing the very complex physical behavior is not possible for the vortex-lattice method. Nevertheless, an approach based on the estimation of the viscous drag forces using the drag polars of the airfoil of the wing was implemented. To this end, numerous drag polars are calculated in a preprocessing step using *XFOIL* for a series of Reynolds numbers and angles of attack. The range of Reynolds numbers is given by the anticipated flight (or onflow) velocity, the kinematic viscosity of the fluid, and the particular chord lengths of each lifting segment's tip and root section. Subsequent to the calculation of the steady loads for each aerodynamic panel, the local Reynolds number and the local effective angle of attack are calculated for each column (strip) of aerodynamic panels – from leading edge to trailing edge – along the span. Given the drag polars of the airfoil and the local Reynolds number and effective angle of attack for each strip, a two-dimensional interpolation is applied to calculate the local drag coefficient. The viscous drag force is then calculated for each strip based on the geometry of the strip, the local dynamic pressure, and the interpolated drag coefficient. This method is implemented and validated for the steady solver so far only. A validation of aerodynamic coefficients of a forward-swept wing at low speeds calculated by this method shows good agreement to reference data calculated by a CFD method, especially for the drag coefficient [79].

3.2 Interface of Aerodynamic and Structural Model

In this thesis, independent solution methods are applied to the structural and the aerodynamic part of the aeroelastic model. The unavoidable problem of this approach is that a further methodology is required to handle the fluid-structure interface of the model. In the case of aeroelastic simulations, this implies the data transfer from the aerodynamic to the structural model, and vice versa. Considering the vortex-lattice model described in Section 3.1, the aerodynamic forces \mathbf{F}^A are calculated at the center of the quarter-chord line of each aerodynamic panel, whereas the nodes of the structural model are in almost all cases located at different positions. This classical fluid-structure-interaction problem can be expressed by the following two equations:

$$\mathbf{u}^A = \mathbf{H} \mathbf{u}^S , \quad (3.15)$$

$$\mathbf{F}^S = \mathbf{H}^T \mathbf{F}^A . \quad (3.16)$$

The first equation relates the (dependent) displacements of the points of the aerodynamic grid \mathbf{u}^A to the (independent) displacements of the structural nodes \mathbf{u}^S by a linear mapping with the operator \mathbf{H} , the *coupling matrix*. The second equation describes the transformation of the aerodynamic loads \mathbf{F}^A to *equivalent* structural loads \mathbf{F}^S . The linear mapping must ensure at least a global conservation of work between the aerodynamic and the structural part (this is meant by the expression equivalent loads) and correctly consider rigid-body motions of the structure. As can be shown by the principle of virtual work, the coupling matrix \mathbf{H} used for the interpolation of deformations can also be used (in transposed form) for the transfer of forces [80]. The coupling matrix is based on the evaluation of either two- or three-dimensional *radial basis functions* (RBF), where a variety of suitable RBFs can be applied, e.g. ones with local or global support [80]. The only information necessary to build the coupling matrix is the location of the structural nodes and the location of the aerodynamic grid points (the four points of each aerodynamic panel). In this thesis, a *thin-plate-spline* (TPS) basis function was used which provides global support and can be used for three-dimensional structural models [80, 40].

A problem arises if a beam-type structural model is to be used with panel methods in aeroelastic computations, as is often the case. In general, not only forces but also moments must be applied to the nodes of the beam. The coupling matrix based on the TPS can only transfer discrete forces from the aerodynamic grid to the structural grid, but moments are disregarded. Several possibilities are available to overcome this issue. Commercial aeroelastic toolboxes for instance provide a *beam spline* method for the coupling of 3D aerodynamic models with beam-type finite element structural models [18, 40]. In this work, another approach was applied. The beam-type model is enhanced by a number of coupling points which are located at the aerodynamic surface and are connected to the nodes of the beam via massless bars of infinite stiffness. In this sense, the one-dimensional beam structural model is expanded to a three-dimensional model for which the TPS-based coupling matrix can be used. This approach is illustrated in Fig. 3.5 and was successfully used for coupled aeroelastic simulations of free-flying elastic aircraft where condensed structural models were used [11]. For beam models to be used with MSC Nastran, *RBE2* or beam elements with special properties are typically used for such purposes [18]. It must be mentioned that the extra *RBE2* elements attached to the model do not change the structural properties of the beam structure (no stiffness and mass are added). From a practical point of view, the coupling points are added to the beam finite element model in preprocessing before the calculation of the higher-order mode components.

3.3 The Aeroelastic Model – Simulations in the Time Domain

Combining the vortex-lattice method with either the proposed method for the structural dynamics, Eq.(2.29), or the equations of motion of the free-flying elastic aircraft, Eq.(2.70), yields the

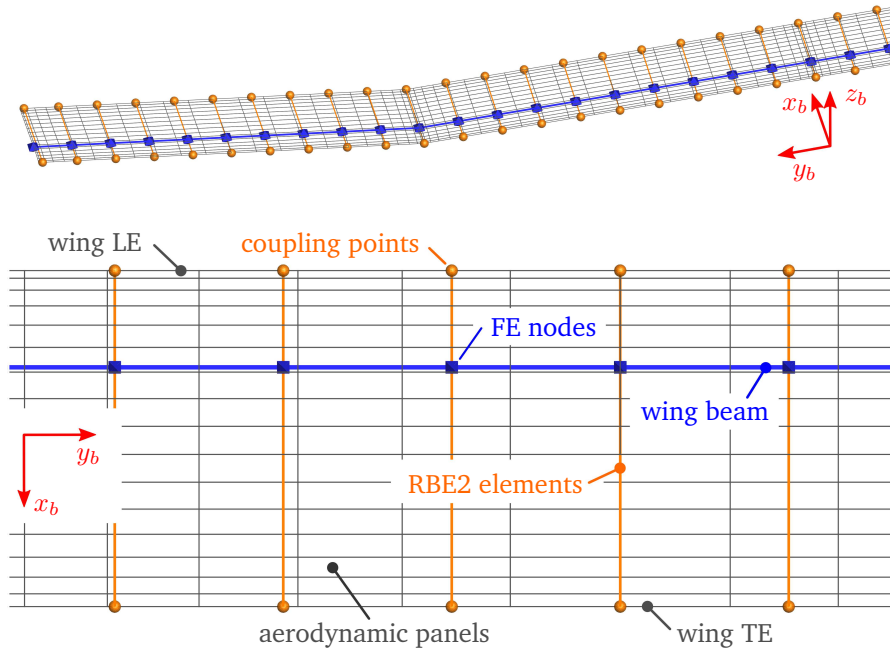


Figure 3.5: Setup of the coupling model. The beam-type FE model is extended by RBE2 elements, aerodynamic forces are transferred to the FE nodes and to the coupling points.

aeroelastic model. Depending on the structural model used (3D FEM or beam-type), a coupling model provides the interface between aerodynamic and structural model. In the case a free-flying flexible aircraft is to be simulated, control surface deflections are necessary for trim, maneuvering, or load alleviation. Several approaches can be used to consider and deflect control surfaces in the vortex-lattice method. The most accurate way would be the rotation of the aerodynamic panels of the corresponding control surface around a specified hinge line. This approach is costly, since a rotation matrix must be calculated in every time step for each column of aerodynamic panels of the control surface. A simplified but effective approach for control surface deflection is the modification of the kinematic boundary condition at the collocation points by tilting the normal vectors of the corresponding panels³:

$$RHS_i = -(\mathbf{V}_{RB,i} + \mathbf{V}_{wake,i} + \mathbf{V}_{gust,i} + \mathbf{V}_{elastic,i}) \cdot \tilde{\mathbf{n}}_i, \quad (3.17)$$

where $\tilde{\mathbf{n}}_i$ denotes the tilted panel normal. This method is illustrated in Fig. 3.6. Since it represents a linearization compared to a true rotation of the control surface, the range of application is limited to small values of deflection angles.

The solution sequence of the aeroelastic program is depicted at a glance in Fig. 3.7. In terms of the flight mechanic part of the program, the kinematic relations, coordinate systems,

³This approach is very similar to the one that is used by MSC Nastran and ZAERO for the deflection of control surfaces (and even for elastic structural deformations) [40].

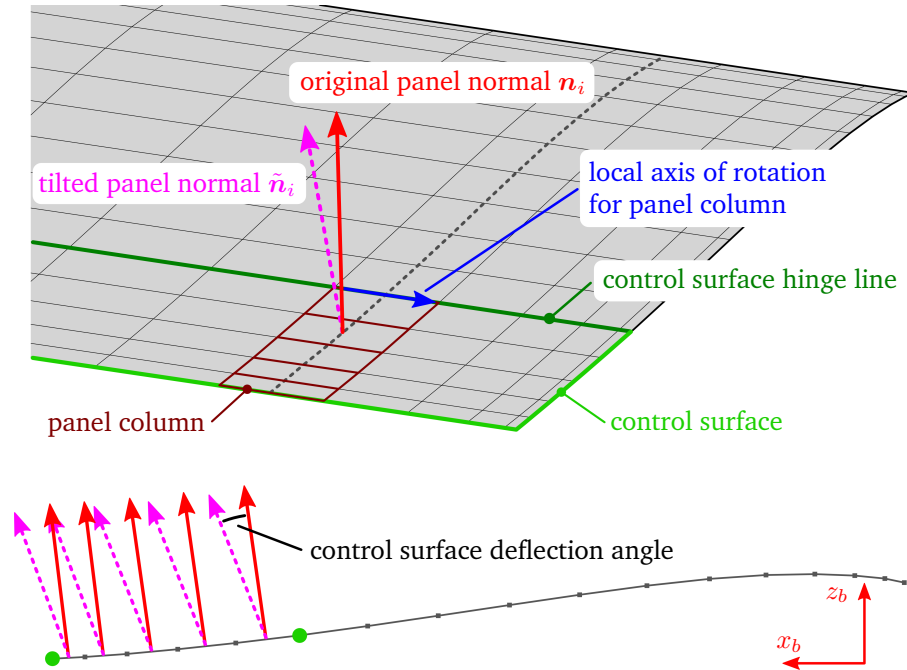


Figure 3.6: Deflection of a control surface by means of tilting the normal vectors of its panels.

and degrees of freedom of the free-flying aircraft are based on the definitions introduced in Section 2.2.1. The explicit quantities of the rigid-body motion are given in Eq.(2.70), these are the rotational rates of the body frame p , q , and r collected in vector Ω_b , as well as the translational velocities of the body frame u , v , and w collected in V_b and resolved in the body-fixed frame. The structural solution variables are the generalized coordinates q_k of each elastic mode. The dependent solution variables are obtained from the independent ones by either algebraic relations or by means of a first-order differential equation, as detailed in Section 2.2.1. Definitions for other important flight mechanic states derived from vector X (Eq. 2.74) are given in Appendix B.

3.4 Trim Approach for Steady Straight Horizontal Flight

All unsteady maneuver simulations are started from a trimmed, i.e. steady straight, horizontal flight. Initial values must be given for the translational and rotational velocities of the body-fixed frame, V_b and Ω_b , for the location and orientation of the body frame in the geodetic frame, P_g and Φ , and for the generalized coordinates and their rates, q_p and \dot{q}_p . Considering a steady straight, horizontal flight without sideslip and wind, all rotational velocities of the body frame, Ω_b , the translational velocity in the y direction, $V_{b,y}$, the bank and the yaw angle, Φ and Ψ , and the generalized velocities, \dot{q}_p , are zero. This corresponds to an unaccelerated flight state where a trim algorithm must solve for the pitch angle Θ – which yields the body

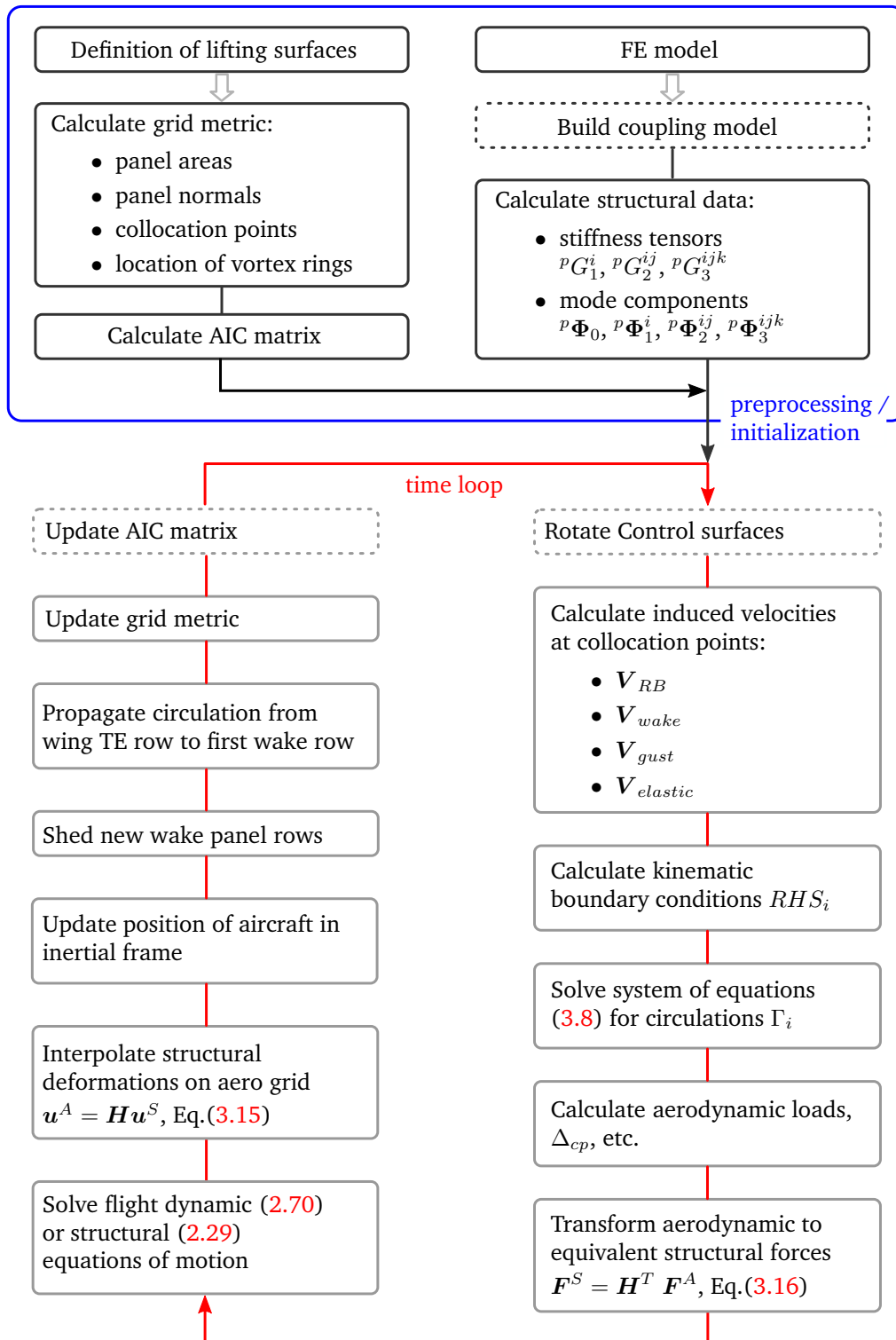


Figure 3.7: Solution sequence of the aeroelastic program with aerodynamic forces calculated by an unsteady vortex-lattice method.

translational velocities $V_{b,x}$ and $V_{b,z}$, the thrust, and the generalized coordinates to account for the structural deformations. In general, the location of the origin of the body frame, P_g , can be chosen arbitrarily, but coincides for convenience with the location of the origin of the geodetic frame at the beginning of an unsteady flight simulation. Based on the flight dynamic equations of motion given in Eq.(2.70), the trim problem to be solved for is defined in terms of constraints on particular variables as

$$\begin{bmatrix} \dot{\mathbf{V}}_b \\ \dot{\boldsymbol{\Omega}}_b \\ \ddot{q}_k \end{bmatrix} \stackrel{!}{=} \begin{bmatrix} \mathbf{0} \\ \mathbf{0} \\ 0 \end{bmatrix}; \quad \boldsymbol{\Omega}_b \stackrel{!}{=} \mathbf{0}; \quad \dot{q}_k \stackrel{!}{=} 0; \quad \dot{\mathbf{P}}_g = \begin{bmatrix} V_A \\ 0 \\ 0 \end{bmatrix}, \quad (3.18)$$

where V_A denotes the desired initial air speed in flight direction, which coincides with the x direction of the geodetic system. The last expression (the constraint on $\dot{\mathbf{P}}_g$) forces the aircraft to a steady horizontal, straight flight with respect to the geodetic system. Using Eqs.(2.37) and (B.6) with the bank and the yaw angle equal to zero yields the translational velocities of the body frame as function of the pitch angle of the aircraft,

$$\mathbf{V}_b = \begin{bmatrix} \cos(\Theta) V_A \\ 0 \\ \sin(\Theta) V_A \end{bmatrix}. \quad (3.19)$$

In order to simplify the fulfillment of the restriction on $\dot{\mathbf{P}}_g$ (the velocity of the aircraft resolved in the geodetic frame does not appear explicitly in the EOMs), the translational governing equation is expressed in the geodetic frame (this does not pose a problem since the equation is reduced significantly if the constraints are imposed). The trim problem is then defined mathematically by the constraints given in Eq.(3.18) together with the governing equation of translational motion expressed in the geodetic frame and the rotational governing equation (which reduces to $\mathbf{Q}_r = \mathbf{0}$):

$$\begin{bmatrix} \mathbf{R}_t \\ \mathbf{R}_r \end{bmatrix} = \begin{bmatrix} \mathbf{M}_{bg}^T \mathbf{Q}_t \\ \mathbf{Q}_r \end{bmatrix} \stackrel{!}{=} \begin{bmatrix} \mathbf{0} \\ \mathbf{0} \end{bmatrix}. \quad (3.20)$$

Here, the residual vectors of the translational and the rotational degrees of freedom are denoted by \mathbf{R}_t and \mathbf{R}_r , respectively. The forces \mathbf{Q}_t and \mathbf{Q}_r are defined in Eq.(2.60). The structural governing equation is not included in Eq.(3.20) explicitly, it is solved independently at each iterative trim step (the rigid-body and elastic degrees of freedom are coupled by the aerodynamic forces).

The trim algorithm implemented in the aeroelastic program is based on Newton's method to solve for the roots of this equation iteratively. This is necessary because the aerodynamic forces are a nonlinear function of the velocities and the structural deformations. Considering the case that both the aerodynamic forces and the structural deflections are represented as linear

functions with respect to any input parameters – as is the case for instance for the Nastran SOL 144 (steady aeroelastic) solution sequence – no iterative method is needed but a linear system of equations is solved [18].

The trim variables (or parameters) that were chosen to solve Eq.(3.20) are the following:

- The pitch angle Θ (which corresponds to the angle of attack in this case),
- The deflection of control surfaces (e.g. tail plane rotation η),
- External forces and moments which can be specified for particular axes of the body frame (this includes thrust forces).

The first and the second parameter implicitly influence the aerodynamic forces acting on the aircraft. The last trim variable, the external forces and moments, are included because of two reasons. First, the vector equation (3.20) is composed of six scalar equations. Thus only considering the pitch angle, the tail plane rotation, and the thrust force would yield an under-determined system. Second, the aircraft considered may have an asymmetric mass distribution (the center of mass is not located in the xz -plane) or is asymmetric with respect to the aerodynamic lifting surfaces. This will inevitably lead to non-zero residual moments about the x and the z axis because there might be no aerodynamic parameter (e.g. a control surface) to compensate for this. To this end, additional forces and moments that are directly applied to the body frame can be specified as trim parameters to account for asymmetric aircraft configurations. An important example for the necessity of such additional forces and moments is the X-HALE aircraft analyzed in Section 4.3. Its mass model is slightly asymmetric which leads to small differences in the structural deflections of the right and the left wing under aerodynamic loading. Furthermore, no ailerons exists to compensate for the rolling moment about the x axis. Both problems can be handled conveniently by using external forces and moments as additional trim parameters. Violating the force and moment equilibrium defined in Eq.(3.20) by not balancing forces and moments entirely would lead to undesirable drifts at the beginning of unsteady maneuver simulations.

Application of Newton's method requires a Jacobian composed of the partial derivatives of the residual vectors \mathbf{R}_t and \mathbf{R}_r with respect to the specified trim parameters (Θ , control surface deflections, external forces and moments) denoted by v_i ,

$$\mathbf{J} = \begin{bmatrix} \frac{\partial R_{t,x}}{\partial v_1} & \dots & \frac{\partial R_{t,x}}{\partial v_6} \\ \vdots & \ddots & \vdots \\ \frac{\partial R_{r,z}}{\partial v_1} & \dots & \frac{\partial R_{r,z}}{\partial v_6} \end{bmatrix}. \quad (3.21)$$

The Jacobian is calculated at each iterative step by a finite difference approach in the program. The iterative solution procedure using Newton's method is then expressed as

$$\mathbf{v}_{n+1} = -\mathbf{J}_n^{-1} \begin{bmatrix} \mathbf{R}_t \\ \mathbf{R}_r \end{bmatrix} + \mathbf{v}_n, \quad (3.22)$$

where \mathbf{J}_n and \mathbf{v}_n denote the Jacobian and the solution vector of the last iteration, respectively.

The vortex-lattice method and the aeroelastic program introduced here were programmed from scratch in Python applying object-oriented programming techniques. The Python extensions *NumPy* and *SciPy* are used to support and ease high-level array and mathematical calculations⁴. Furthermore, high performance implicit ODE solvers based on the backward differential formula (BDF) are available in *SciPy* to solve the flight dynamic governing equations of motion⁵.

⁴<http://numpy.org/>

⁵<http://scipy.org/>

Chapter 4

Numerical Studies

The goal of this chapter is the validation of the proposed method by means of three selected test cases. This comprises the setup of the simulation models, the numerical simulation, and the comparison of the results. As mentioned in the introduction, the simulation results of the proposed method are not presented on its own, the focus is on the comparison with nonlinear reference solutions wherever possible. Depending on the test case and the particular solution sequence (e.g. static or dynamic structural response, steady or unsteady aeroelastic coupling, steady trim or unsteady maneuver), the reference solutions are obtained either from MSC Nastran (clamped structures) or from UM/NAST (free-flying aircraft). In the case of a clamped structural model (no rigid-body motions) without aerodynamic interaction, the nonlinear reference solutions are obtained by MSC Nastran solution sequences SOL 106 (nonlinear static) or SOL 400 (nonlinear static and implicit transient). If a clamped structural model is to be used for nonlinear aeroelastic coupling or trim analyses, the vortex-lattice solver can be coupled to Nastran using the methods for data transfer described in Subsection 3.2. Reference data for the unsteady maneuver simulations were simulated at the University of Michigan using the UM/NAST toolbox since no other software is available by now for such kind of simulations.

The three test cases are of increasing complexity. The simple cantilever beam model in static structural response, analyzed in Section 4.1, allows for a comprehensible understanding of the basic concepts of the proposed method. Important features of the higher-order mode components and the coupling terms as well as the force-dependent linear stiffness term are emphasized and outlined in detail. The second test case is a slender wing box made from carbon fiber reinforced plastic and represented by a full 3D finite element model. This structure uses plate elements and serves as a test case to demonstrate the intended applicability of the proposed method to more complex and general finite element structural models. It is detailed in Section 4.2. The third test case is the very flexible *X-HALE* UAV from the University of Michigan, introduced in Section 4.3. Although its structure is represented by a beam model, the unique design and its structural properties turned out to be challenging. Results of static and dynamic aeroelastic responses as well as free-flight unsteady simulations with this model are discussed.

The finite element models of the beam and the wingbox test cases were built from scratch based on generic designs serving special needs. The beam-type Nastran structural model of the X-HALE UAV was also built from scratch, the stiffness and mass properties were taken from a corresponding input file of the UM/NAST toolbox the University of Michigan provided.

4.1 Cantilever Beam Test Case

The first test case is a cantilever beam with a length of 16 meters that resembles a generic, slender aircraft wing [81]. It is discretized by 32 finite beam elements (here, Nastran *CBEAM* beam elements were used) and 33 nodes, all properties of the FE model are listed in Appendix D. The moments of inertia of the cross section of the beam vary quadratically along the axis of the beam. This setup was chosen to obtain bending deformations with almost constant curvature as the beam is subjected to forces with elliptic distribution (similar to aerodynamic forces). Discrete mass elements were used to tune the dynamic structural behavior. The layout of the model is shown in Fig. 4.1.

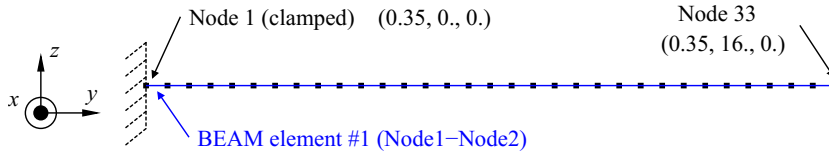


Figure 4.1: FE model of the 16 m beam test case composed of 33 nodes and 32 elements, clamping at Node 1.

Following a study to select the mode shapes with the highest contribution to the static deformation field as function of a generic elliptical loading applied to the beam, seven modes were used for which the higher-order stiffness tensors and mode components (G and Φ , respectively) were calculated. This reduction of the degrees of freedom of the system significantly reduces the computational effort for all the simulations described in the following.

The values of ${}^pG_1^i$ and ${}^p\Phi_1^i$, which were calculated with the method described in subsection 2.3, are in perfect agreement with the corresponding natural eigenvalues of the beam. Table 4.1 lists the types and frequencies of the ten lowest mode shapes of the beam model obtained from a modal analysis using MSC Nastran and from the reconstruction method for the seven selected modes. The second, third, and fourth in-plane bending mode were omitted since their contribution to the deformation field resulting from the generic loading is almost negligible. The quadratic stiffness term ${}^pG_2^{ij}$ is zero for this model (as is in general the case for isotropic structures). The diagonal entries of the cubic stiffness term ${}^pG_3^{ijk}$ are comparatively small (in the order of 10^{-3} for the first bending mode). Neither follower forces nor gravity were taken into account in the static simulations of the beam test cases of this subsection.

Table 4.1: Eigenvalues of the ten lowest modes of the beam model; values are obtained from a FE modal analysis and from the polynomial fitting method described in Section 2.3.

Mode	Type of mode shape	Eigenvalue FE analysis [Hz]	Eigenvalue (${}^pG_1^i$) reconstructed [Hz]
1	first bending	0.595	0.595
2	first bending in-plane	1.190	1.190
3	second bending	2.705	2.705
4	second bending in-plane	5.407	-
5	third bending	6.956	6.956
6	fourth bending	13.358	13.358
7	third bending in-plane	13.893	-
8	fifth bending	21.908	21.908
9	fourth bending in-plane	26.651	-
10	first torsion	27.132	27.132

4.1.1 Static Validation of the Higher-Order Stiffness Tensors and Mode Components

First, the beam test case shall illustratively introduce the concept of the higher-order mode components. The goal is to highlight how the representation of the nodal displacement field, as defined by Eq.(2.23), includes the desired geometrical nonlinearities. Furthermore, the importance of the coupling terms in the higher-order mode components, which are mandatory for the calculation of a displacement field in which several modes participate, is pointed out.

Single Mode Excitation

As described in the theoretical part, Section 2.1.1, and in the section about the calculation of the higher-order stiffness tensors and mode components, Section 2.3, the method applied for the calculation of the higher-order components is based on a series of nonlinear static simulations. The force field used to excite the structure is chosen such that the resulting deformation field equals either a particular mode or a combination of modes. For a single mode denoted by index i , Eq.(2.15) yields

$$\mathbf{F}_i = \mathbf{K} \phi^i q_i .$$

Such a force field was applied to the beam test case with five different values of q_1 : (8, 16, 24, 32, 40)¹. The eigenvector chosen for ϕ^i is the first bending mode shape, thus the resulting displacement field corresponds qualitatively to the first bending mode. The results of three different methods are depicted in Fig. 4.2, where the nonlinear and the linear reference were

¹The values of q_1 were chosen to obtain meaningful tip displacements, the particular magnitudes do not correspond to the resulting magnitudes of the tip displacements.

calculated by MSC Nastran solution sequences 400 and 101, respectively. The results of the proposed method were obtained by the solution of Eq.(2.28) using a Newton-Raphson scheme with a specified start estimate. As can be seen, the deformation field of the proposed method

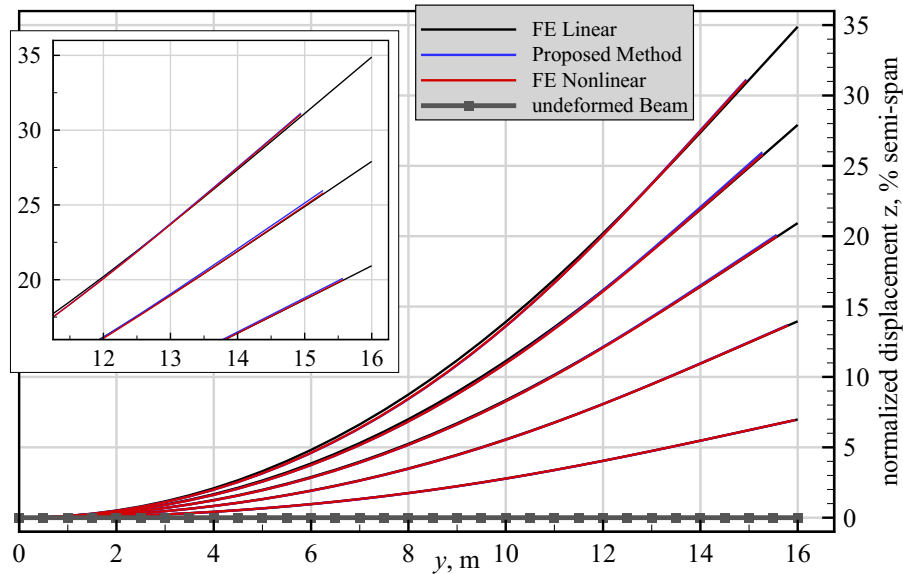


Figure 4.2: Comparison of the static displacement fields obtained by different methods for a force field defined by Eq.(2.15), the first bending mode shape was selected for ϕ^i .

and the nonlinear FE solution agree well up to tip displacements greater than 30% with respect to the semi-span. The result can be taken as a measure of the accuracy of the higher-order mode components. Note that the deformation of the linear FE solution is on top of the nonlinear ones, but the beam is stretched significantly at higher deformations. A similar result is obtained from the deformation field of the first in-plane bending mode shape, which is plotted in Fig. 4.3. The values for q_2 are: (7, 14, 21, 28, 35). A different result is obtained for the second bending mode shape, its validation is shown in Fig. 4.4. Here, q_3 was specified within the range of: (2, 4, 6, 8, 10). Due to the shape of the mode, reasonable values for the maximum deformation are not larger than a few percent of the semi-span. For this case, the nonlinearities are much more pronounced with respect to the magnitude of the deformation than for the last two modes. Starting at five percent tip displacement, the differences between the linear and the nonlinear results become significant. Note also that the nonlinear beam deformation is no longer on top of the linear one. The proposed method agrees well with the nonlinear reference, thus the higher-order components are also well represented for this mode.

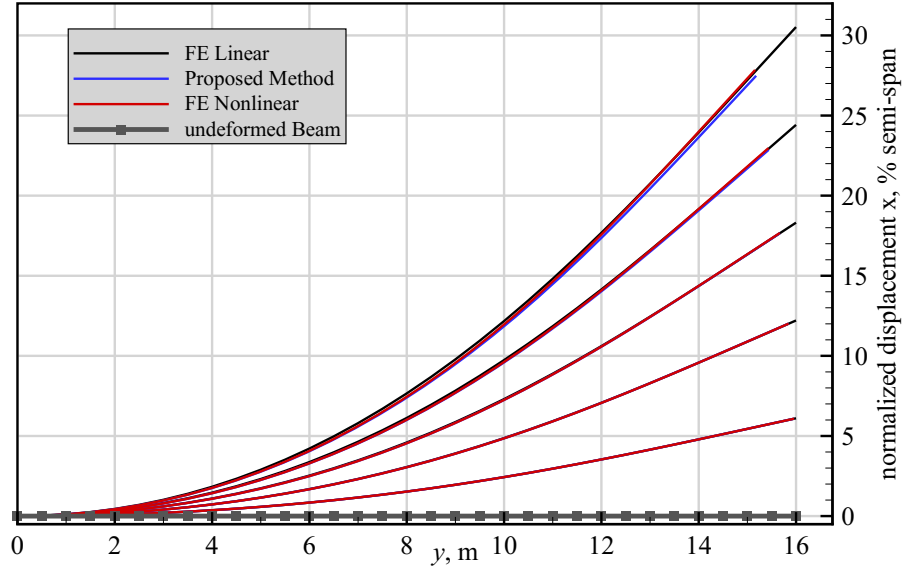


Figure 4.3: Comparison of the static displacement fields obtained by different methods for a force field defined by Eq.(2.15), the first in-plane bending mode shape was selected for ϕ^i .

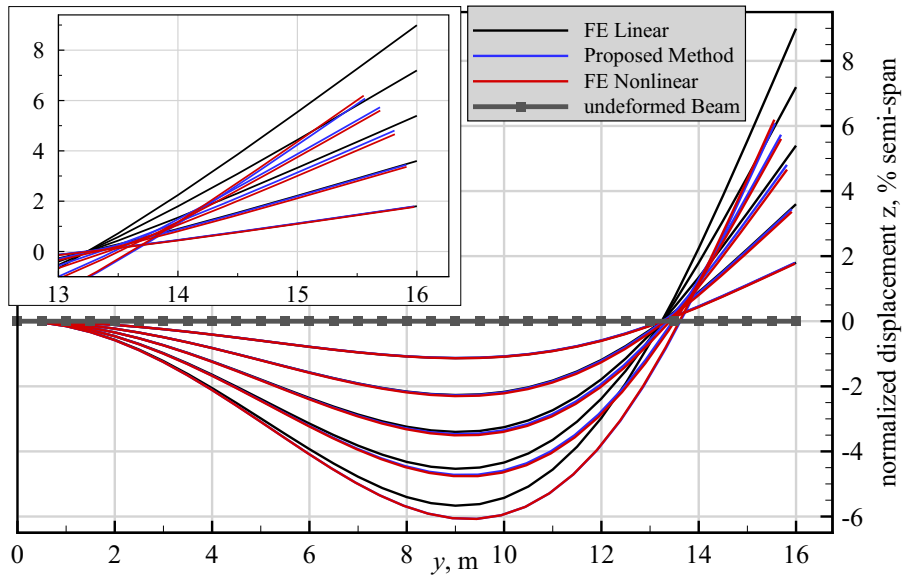


Figure 4.4: Comparison of the static displacement fields obtained by different methods for a force field defined by Eq.(2.15), the second bending mode shape was selected for ϕ^i .

Two Mode Excitation

A more interesting test case is the combined excitation of two modes. The force field is now defined by the sum of two modal contributions, each with their own scaling factors q_i and q_j , where $i \neq j$,

$$\mathbf{F}_{i,j} = \mathbf{K} (\phi^i q_i + \phi^j q_j) \quad (i \neq j) . \quad (4.1)$$

Figure 4.5 shows the deformation field that was obtained by a coupling of the first and the second out-of-plane bending mode:

$$\mathbf{F}_{1,3} = \mathbf{K} (\phi^1 q_1 + \phi^3 q_3) , \quad (4.2)$$

where the six particular values of the scaling factors q_1 and q_3 were chosen as follows to

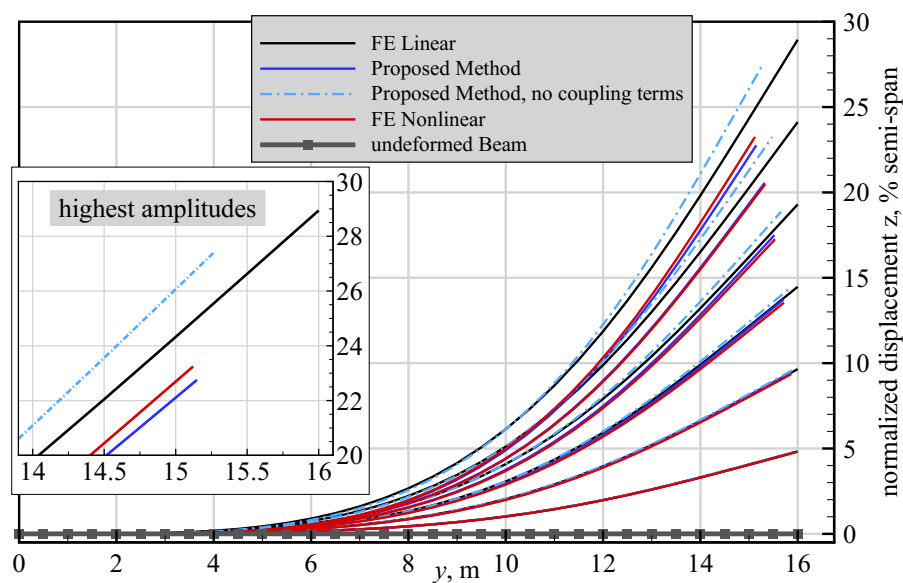


Figure 4.5: Comparison of the static displacement fields obtained by different methods for a force field defined by Eq.(4.2) with a combination of the first and the second out-of-plane bending mode.

excite significant nonlinearities: $q_1 = (4.5, 9, 13.5, 18, 22.5, 27)$, and $q_3 = (1, 2, 3, 4, 5, 6)$. As can be seen from the results, although similar up to deformations slightly over 15% of the semi-span, the differences between the linear and the two nonlinear solutions increase significantly at larger deformations, i.e., higher than approximately 20% semi-span in this case. Additional results are shown in this figure, labeled by *Proposed Method, no coupling terms*. These results were obtained by solving the governing equations of the proposed method, but all coupling terms of the higher-order mode components of the first and the second bending mode were equal to zero. The results show large differences to the case in which the coupling terms are included, and thus highlight their importance. In contrast to the case of linear, small deformations, which allows the application of the principle of superposition, the coupling terms of the higher-order mode components must be considered in the case of large deformations. An additional case is calculated, also with the first and the second bending mode, but this time the sign of q_3 is inverted, i.e. the second bending mode acts in the opposite direction. The results are shown in Fig. 4.6. However, in this case the nonlinearities are less pronounced.

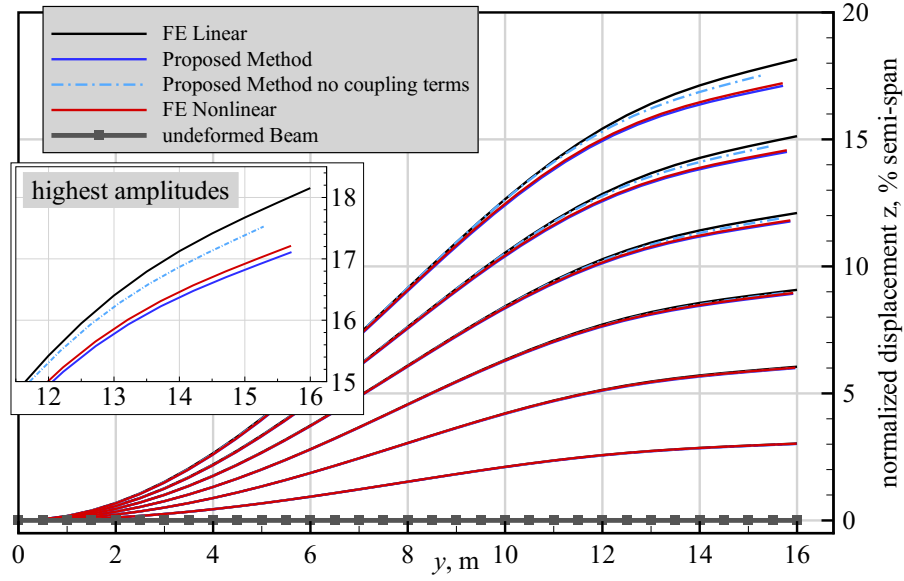


Figure 4.6: Comparison of the static displacement fields obtained by different methods for a force field defined by Eq.(4.2), with a combination of the first and the second out-of-plane bending mode.

Another combination of two modes is analyzed, the sum of the first vertical bending and the first in-plane bending mode:

$$\mathbf{F}_{1,2} = \mathbf{K} (\phi^1 q_1 + \phi^2 q_2) . \quad (4.3)$$

The values chosen for the amplitudes are: $q_1 = q_2 = (7, 14, 21, 28, 35, 42)$, the results are plotted in Fig. 4.7. Good agreement with the nonlinear reference solution is obtained by the proposed method in this test case, the differences between the linear and the nonlinear results are more pronounced compared to a single excitation of the two particular modes.

The last test case with force fields defined by modal contributions uses a combination of the first vertical bending and the first torsion mode, the force field is given as

$$\mathbf{F}_{1,10} = \mathbf{K} (\phi^1 q_1 + \phi^{10} q_{10}) , \quad (4.4)$$

with the following amplitudes: $q_1 = (12, 16, 20, 24, 28, 32)$, and $q_{10} = (0.2, 0.3, 0.4, 0.5, 0.6, 0.7)$. This case, whose results are shown in Fig. 4.8, illustrates the appearance of particular effects which cannot be approximated by linear solutions. The displacement in the x direction and the associated rotation of the structural nodes about the z axis are not accounted for by the linear solutions at all. In addition, especially the rotation about the y axis (the twist) of the linear FE solution shows large differences to the nonlinear results. This would lead to a

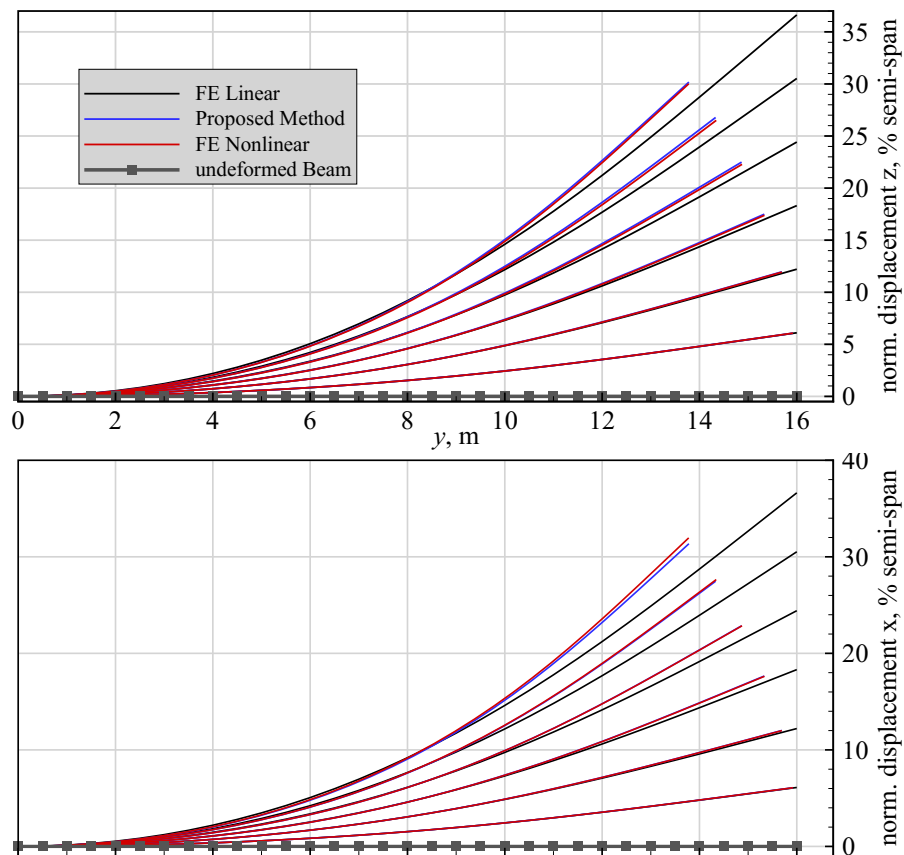


Figure 4.7: Comparison of the static displacement fields obtained by different methods for a force field defined by a combination of the first vertical and the first horizontal (in-plane) bending mode.

different variation of the local angle of attack along the span for example in the case of an aircraft wing and in turn to different bending deformations.

4.1.2 Static Simulations and Validation with Selected Force Fields

In this subsection, static simulations and validations are discussed where arbitrary force fields are applied to the beam structure. Focus is on the analyses of the differences between the nonlinear and the linear solutions with respect to the deformation field, especially for the case of combined loadings (forces and moments).

For the first validation, a constant tip force in the z direction was applied at the outermost node of the beam with assumed values between 1100 N and 3850 N to simulate a constant static loading. As before, the static governing equation is nonlinear and was solved by a Newton-Raphson method. The results of this test case are plotted in Fig. 4.9. Load stepping procedures (incremental loads) are used in the Nastran nonlinear solutions, the force applied to the beam is increased stepwise and equilibrium is ensured in every intermediate step until the total specified

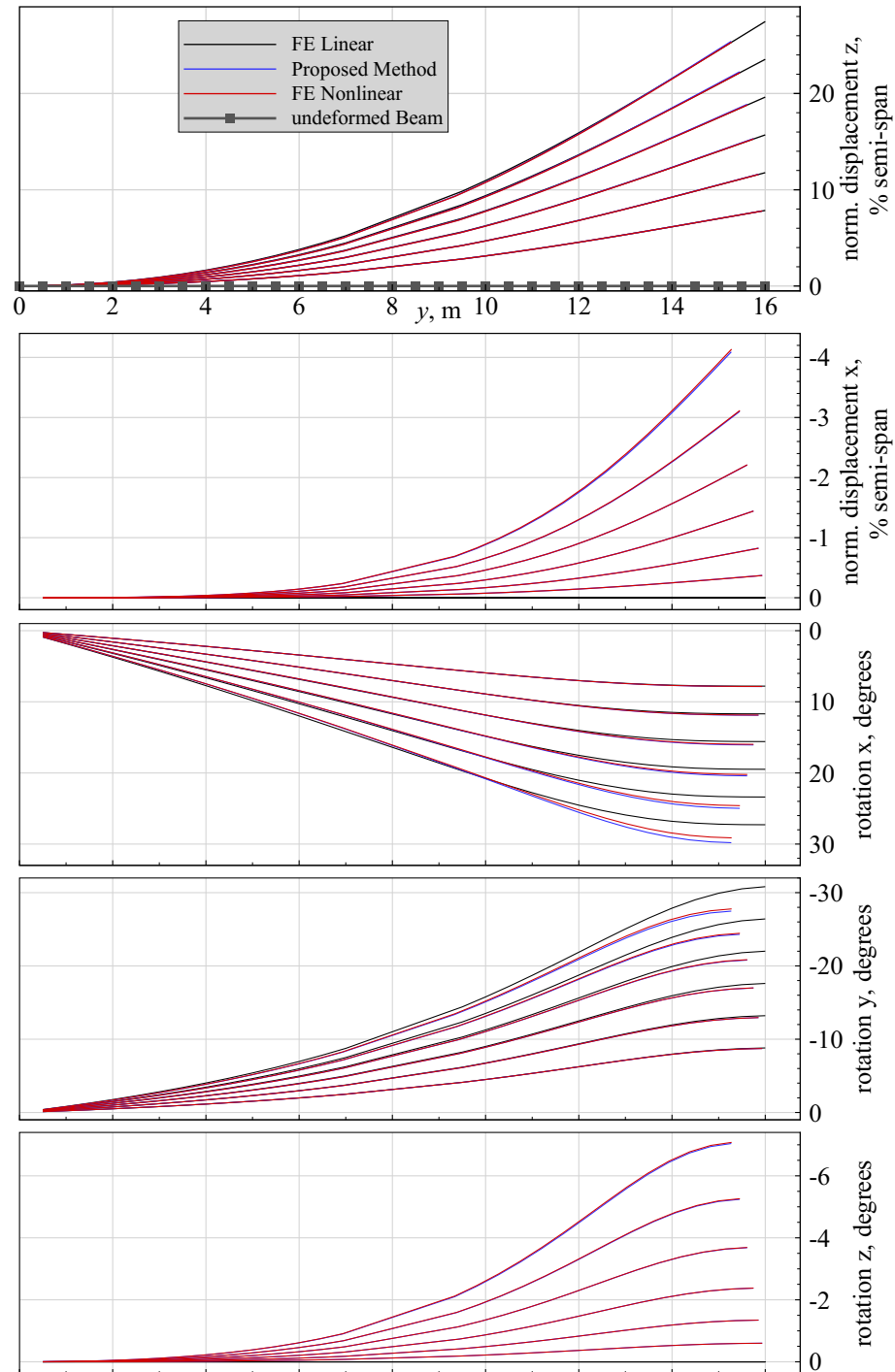


Figure 4.8: Comparison of the static displacement fields obtained by different methods for a force field defined by a combination of the first vertical bending and the first torsion mode.

load is applied. In the solution sequence used for the proposed method, the specified value of the force is applied always onto the undeformed (initial) configuration of the beam. The values

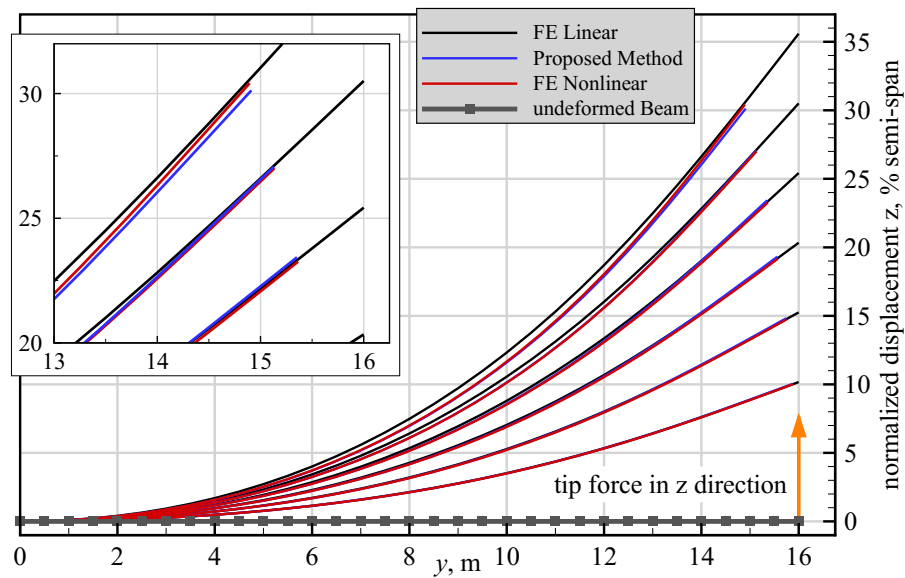


Figure 4.9: Comparison of the static displacement fields obtained by different methods for forces with values of 1100, 1650, 2200, 2750, 3300, and 3850 N applied along the z direction at the end of the beam.

of the force were chosen to excite deformations beyond the limit of structural linearity. This can be seen in terms of the nodal displacement field of the beam in the z and in the y direction. As for the other test cases, the displacements in the z direction obtained from the linear FE solution are much higher than the nonlinear reference, whereas displacements in the y direction are nonexistent. The results of the proposed method are in good agreement with the nonlinear reference data from Nastran, and the displacements in the z and in the y direction are captured well up to the highest tip force of 3850 N, resulting in normalized bending deformations in the z direction of approximately 30% with respect to the semi-span of the beam. The next test case is similar, a constant force field is applied in the z direction, but now at each node of the beam. The values are increased from 50 N to 300 N in steps of 50 N. The results are shown in Fig. 4.10. Again, good agreement between the nonlinear results from Nastran and the proposed method is obtained for tip displacements up to 30% of the semi-span. The nonlinear results are nearly on top of the linear ones but the length of the beam is kept.

The effects of combined force fields acting in different spatial directions increase the complexity of the simulations and are analyzed in the following. Fig. 4.11 depicts the results of simulations obtained for a tip load in both the x and the z direction. The values of the tip forces applied in the x direction are increased from 1000 N to 6000 N in steps of 1000 N, and in the z direction from 500 N to 3000 N in steps of 500 N. This force field yields displacements up to approximately 28% semi-span in the z and 15% semi-span in the x direction in terms of the nonlinear simulations, which show good agreement in this test case. Differences between

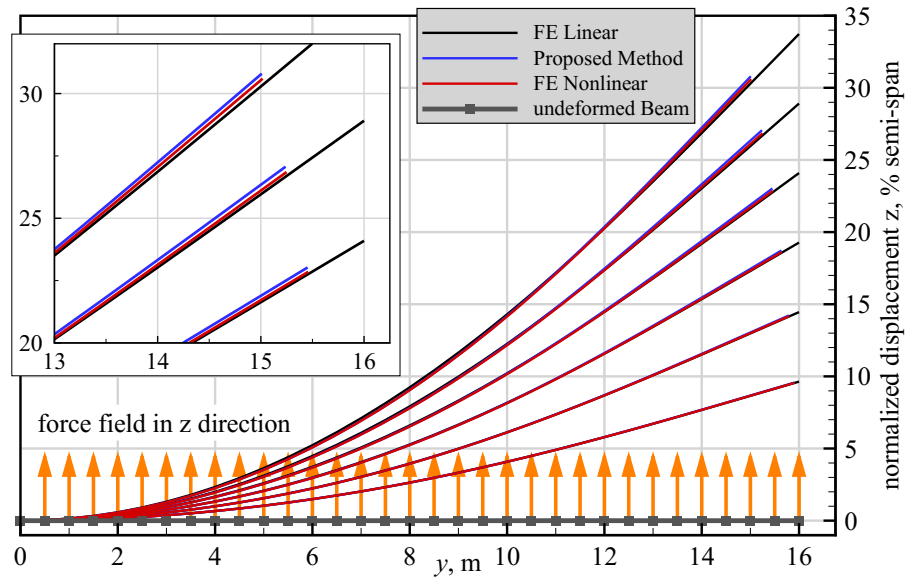


Figure 4.10: Comparison of the static displacement fields obtained by different methods for forces with values of 50, 100, 150, 200, 250, and 300 N applied along the z direction at each node of the beam.

the nonlinear and the linear results become significant mainly for the displacements in the x direction, a similar result was obtained for the deformations shown in Fig. 4.7.

Applying a combined force field with loading in the x and in the z direction at each node of the beam leads to the deformations shown in Fig. 4.12, where the forces were increased in six steps, respectively, from 100 N to 600 N (x direction), and from 50 N to 300 N (z direction). The agreement between the nonlinear results is comparable to the last test case. Applying a constant force field in the y and in the z direction depicts significant differences between the nonlinear and the linear results. Deformations of the beam structure are shown in Fig. 4.13 for a constant force field applied at each node in the negative y and in the positive z direction in six steps from 50 N to 300 N, respectively. Good agreement between the results of the proposed method and the nonlinear FE solution is achieved. For this type of loading, the force component in the y direction takes no effect in the linear solution. The reason is that the force is applied onto the undeformed structure, and the component in the y direction leads to a very small deformation (compression) in the axial direction of the beam only. By contrast, the proposed method is able to account for the forces acting in the axial direction because of the the linear stiffness term which becomes a function of the applied force field, as defined by Eq.(2.28). A similar test with a force field acting both in the y and in the z direction is carried out with the wingbox structure in Section 4.2.2.

The last steady test case is obtained by a combined loading of shear forces acting in the x , in the y , and in the z direction, as well as a torsion moment about the y axis applied at each

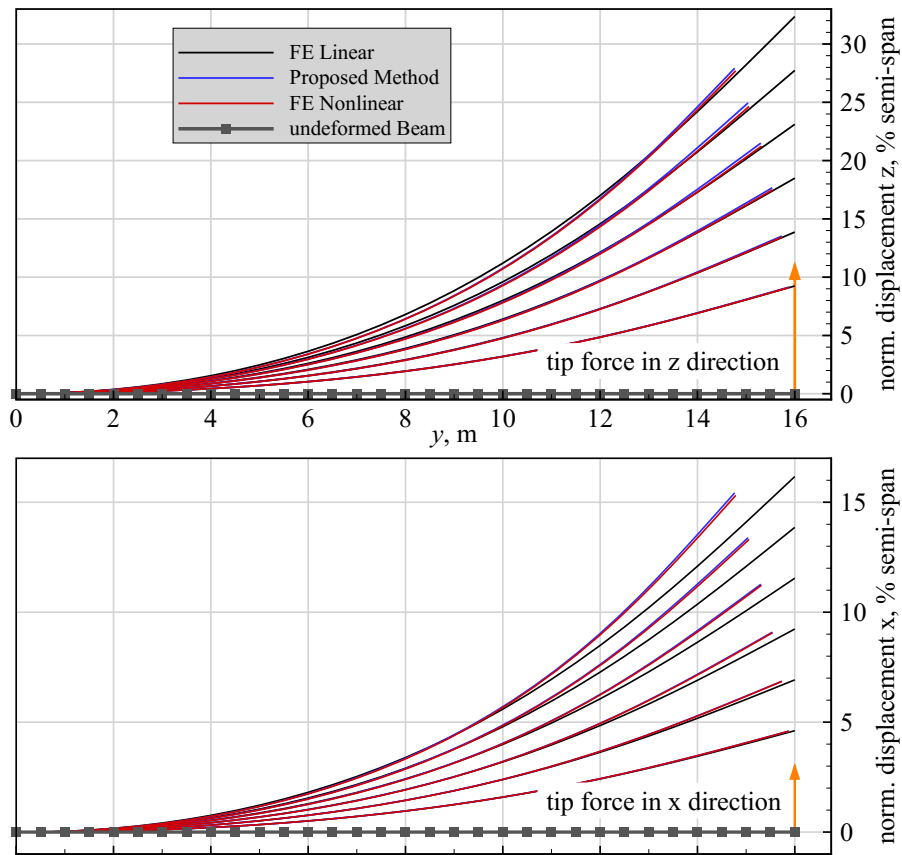


Figure 4.11: Comparison of the static displacement fields for a combination of forces in the x and in the z direction applied at the tip of the beam.

node of the beam. Six load steps are used where the values of all shear forces are varied from 100 N to 600 N, and the torsion moment was varied from 100 Nm to 600 Nm. The results are plotted in Fig. 4.14 in terms of displacements in the x and in the z direction, as well as rotations about the x , the y , and the z axis of each node. Considerable differences between the linear simulations and the nonlinear ones manifest for this test case. The agreement between the proposed method and the nonlinear reference is acceptable, but significant differences occur for the nodal rotations about the x and the y axis (this deficiency could possibly be overcome by using higher torsion modes). The most important aspect of this test case is that the coupling terms of different modes of the quadratic, cubic, and fourth-order mode components play a decisive role for the resulting nonlinear deformation field since all modes participate significantly. The loading can be seen as a limit for the capabilities of the proposed method for this structure. However, for typical aeroelastic applications and test cases the applied forces from aerodynamic and inertia loading act in different spatial regions, but out-of-plane forces (in the z direction in this case) will dominate.

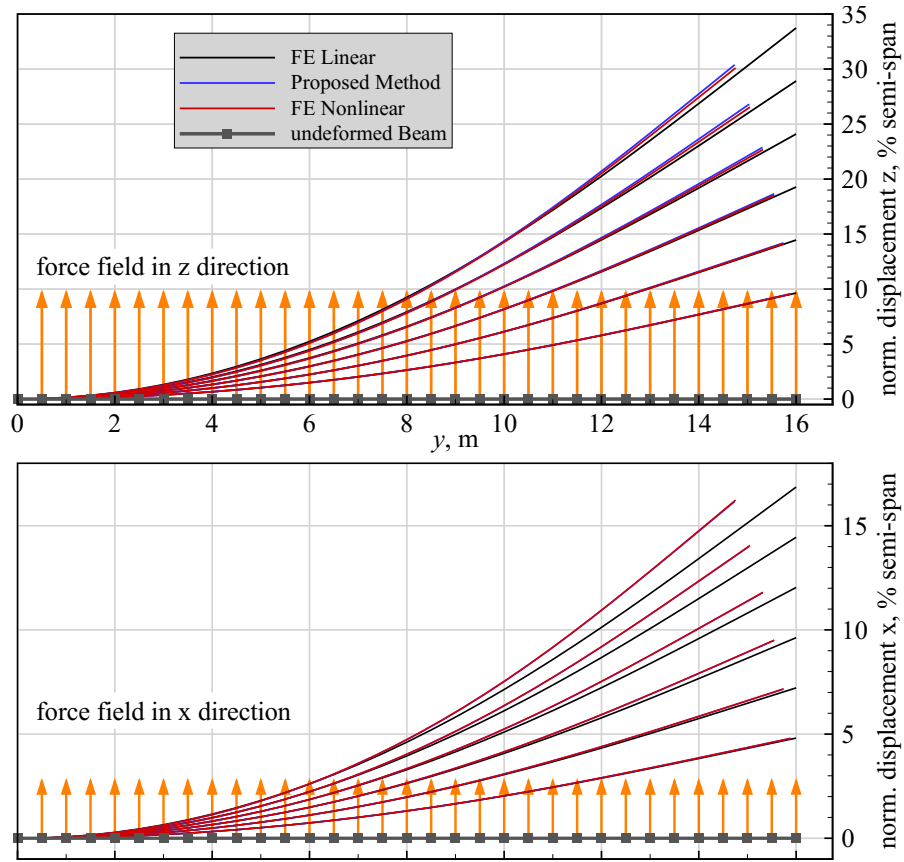


Figure 4.12: Comparison of the static displacement fields for a combination of forces in the x and in the z direction applied at each node of the beam.

As mentioned above, the linear stiffness term of the proposed method, ${}^pG_1^i - {}^p\Phi_1^{iT} \mathbf{f}$, becomes a function of the applied force field \mathbf{f} , cf. Eq.(2.28). The impact of this term manifests, amongst others, in the correct consideration of axial loading as depicted in Fig. 4.13, but also in a change of the eigenvalue of a particular mode itself. Since all modes of the beam test case with exception of the first torsion are bending modes, their corresponding quadratic mode components have components in the y direction only. Thus the product ${}^p\Phi_1^{iT} \mathbf{f}$, which is subtracted from the eigenvalue ${}^pG_1^i$, can be changed simply by applying a force field \mathbf{f} with components in the y direction. An interesting validation of the proposed method is thus a comparison of the changes in the eigenvalues of the mode shapes as function of axial loading. This is shown in Fig. 4.15, where a force field in the positive y direction is applied at each node of the beam with magnitudes ranging from 0 to 2000 N. An eigenvalue analysis with preload was performed with Nastran to obtain the nonlinear reference results. In nonlinear FE analyses, a tangent stiffness matrix is used to account for changes in the structure's stiffness due to structural deformation, as described by Eq.(1.6) in the introduction. The counterpart of the tangent stiffness matrix in modal space is the set of the quadratic mode components [39]. As can be seen, good agreement

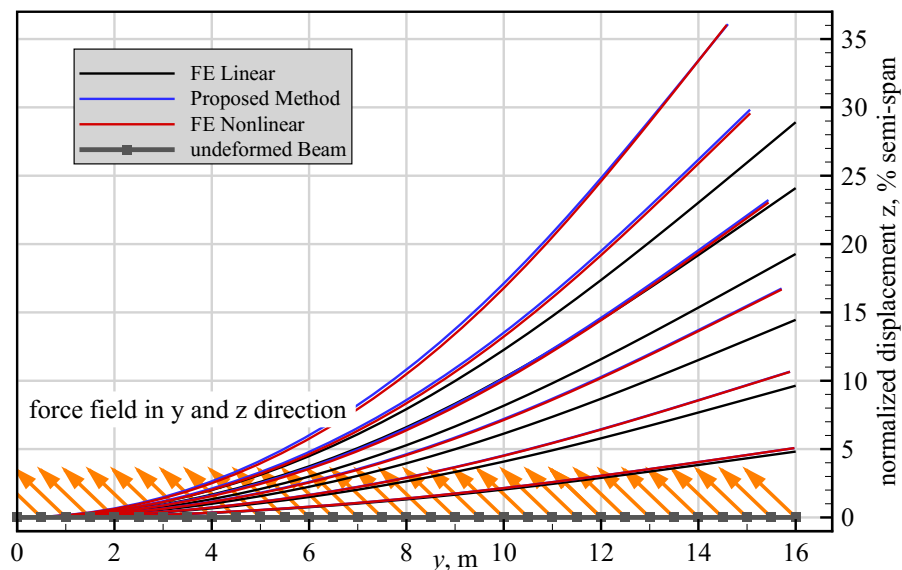


Figure 4.13: Comparison of the static displacement fields for a combination of forces in the negative y and in the positive z direction applied at each node of the beam.

is obtained for all modes except the first torsion modes. However, the variation of the frequency as calculated by the nonlinear Nastran solution is very low. The practical importance of such a loading is given for example in the case of a translational acceleration of the beam in the y direction or a rotation about the x or z axis of the clamping section.

4.2 High Aspect Ratio Composite Wingbox Test Case

The second test case is a 20 meter span, generic wingbox configuration with a sweep angle of 1.8 degrees [82]. This structural model resembles a real aircraft wing more than the cantilever beam of Section 4.1. It is entirely built from quadrilateral shell elements defining the three spars, the ribs, as well as the upper and lower skins. The anisotropic properties of the carbon fiber reinforced plastic (CFRP) material of all elements are specified by means of Nastran *MAT2* cards. Furthermore, the thicknesses of the shell elements are reduced from root to tip to obtain a smooth bending deformation with almost constant curvature for elliptical (aerodynamic) loading. No additional discrete mass elements were used for this test case, the density of all materials is 2700 kg/m^3 , the total mass of the wingbox is 489 kg. The model consists of 1950 nodes, 2005 elements, and 254 different anisotropic materials. It was generated using the DLR in-house model generator *ModGen* which generates parametrized structural and aerodynamic models to be used with the structural and aeroelastic solution sequences of MSC Nastran [83]. The outer shape of the wingbox is defined by a NACA 4415 airfoil at the root of the wing and a NACA4412 airfoil at the tip. The model and selected details are illustrated in Fig. 4.16.

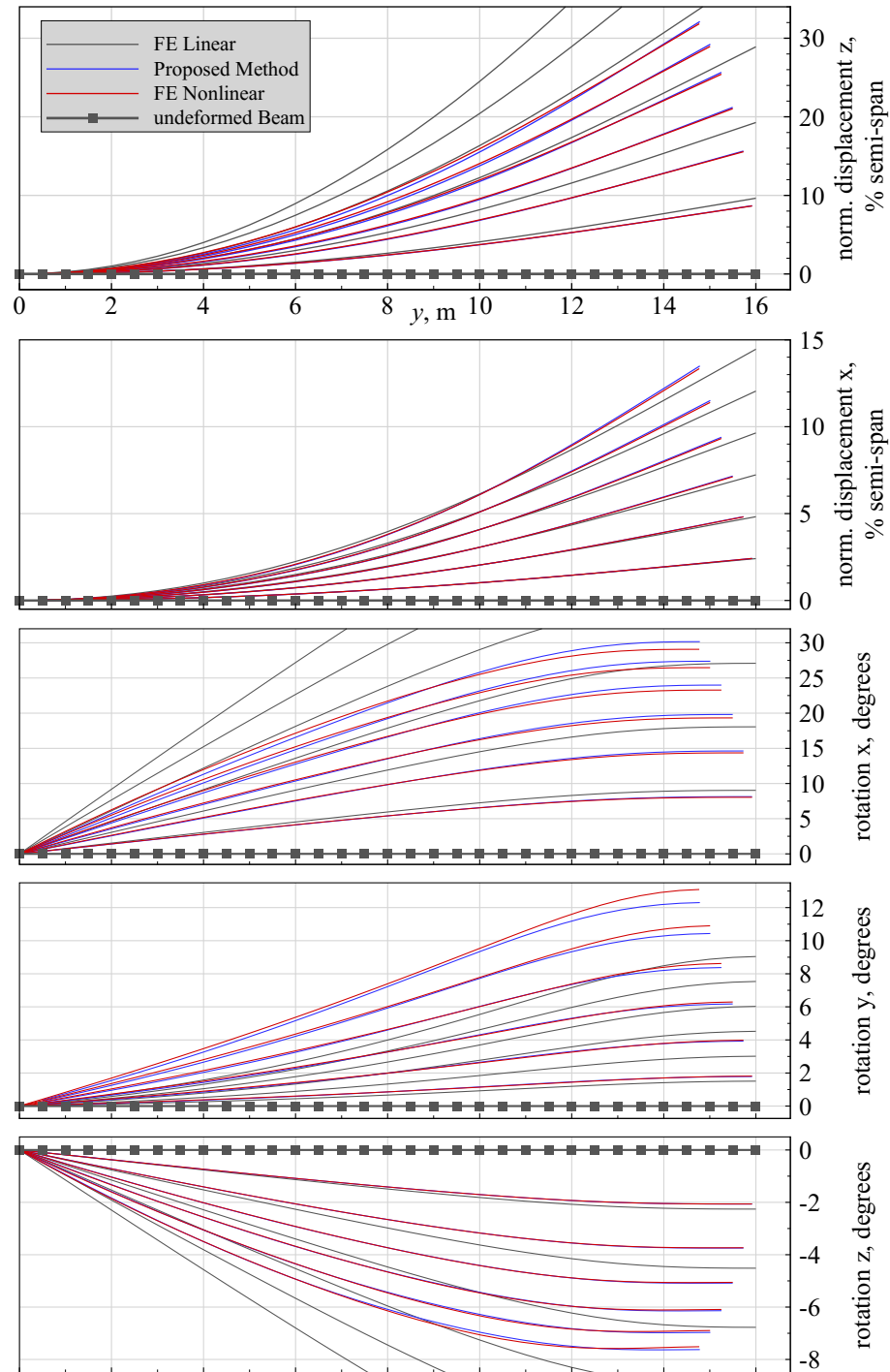


Figure 4.14: Comparison of the static displacement fields for a combination of forces along the x , the y , and the z axes and a torsion moment applied at each node of the beam.

Higher-order stiffness terms and mode components were calculated for eight modes. The linear stiffness components ${}^p G_1^i$ are close to the corresponding natural eigenvalues of the struc-

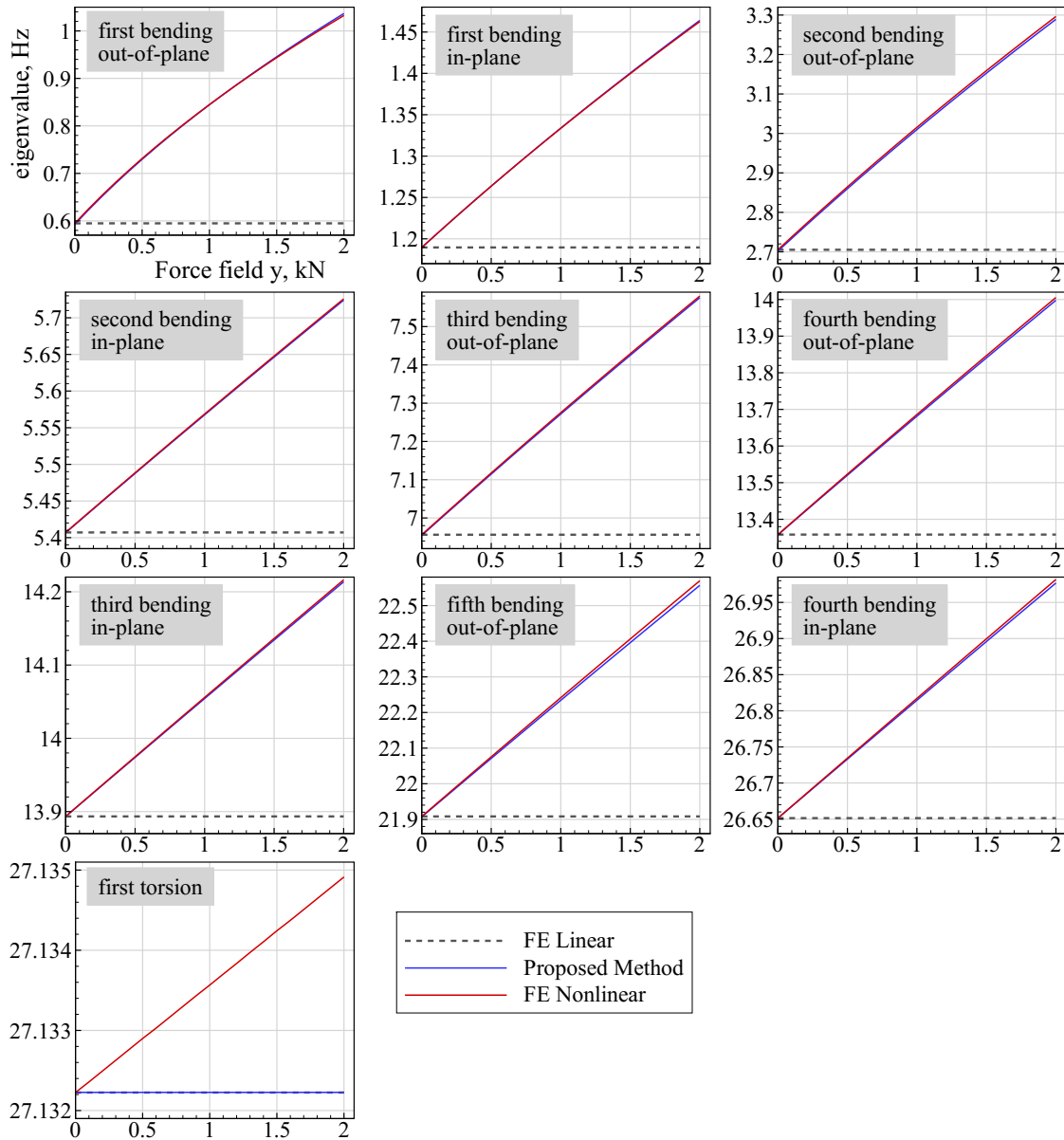


Figure 4.15: Changes in linear stiffness of ten modes of the beam test case as function of a constant force field applied in the y direction at each node.

ture, but with slightly larger differences compared to the beam test case of Section 4.1. Table 4.2 lists the types and frequencies of the eight selected mode shapes of the wingbox model obtained from the FE modal analysis and from the polynomial fitting approach described in Section 2.3. The corresponding mode shapes are plotted in Fig. 4.17.

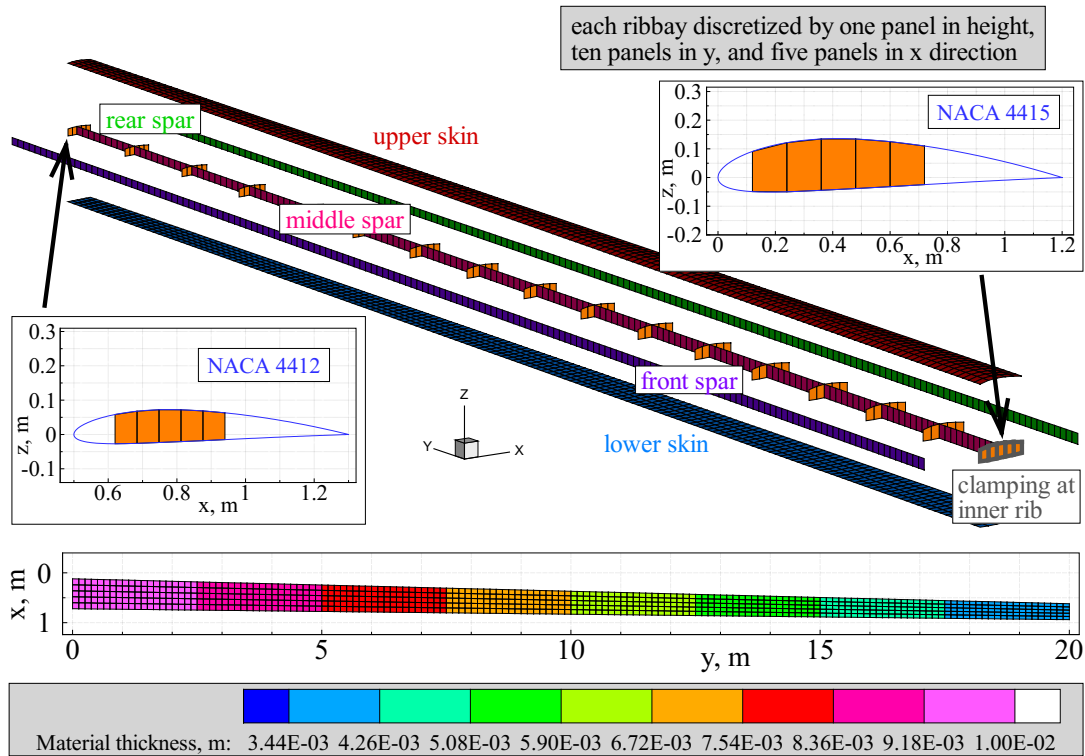


Figure 4.16: Layout of the wingbox made from CFRP shell elements with details and material thicknesses.

Table 4.2: Eigenvalues of eight selected modes of the generic wingbox model; values are obtained from a FE modal analysis and from the polynomial fitting method described in Section 2.3.

Mode	Type of mode shape	Eigenvalue FE analysis [Hz]	Eigenvalue (${}^p G_1^i$) reconstructed [Hz]
1	first bending	0.884	0.880
2	first bending in-plane	3.218	3.135
3	second bending	3.602	3.575
4	third bending	8.755	8.677
5	fourth bending	16.180	16.109
6	fifth bending	25.543	25.612
7	first torsion	28.302	28.386
8	sixth bending	36.171	37.411

4.2.1 Static Response Simulations and Validation

The structural deformations of the load cases shown in the following are plotted for selected nodes located on the upper side of the wing, depicted in Fig. 4.18. First, a constant force in

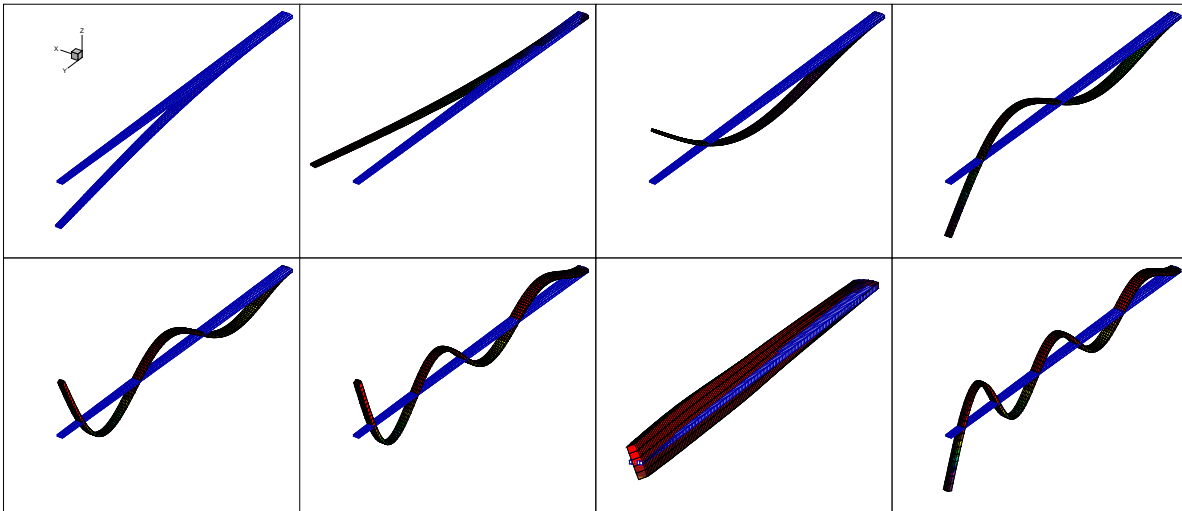


Figure 4.17: Selected normal mode shapes of the wing box test case; the corresponding eigenvalues are listed in Table 4.2.

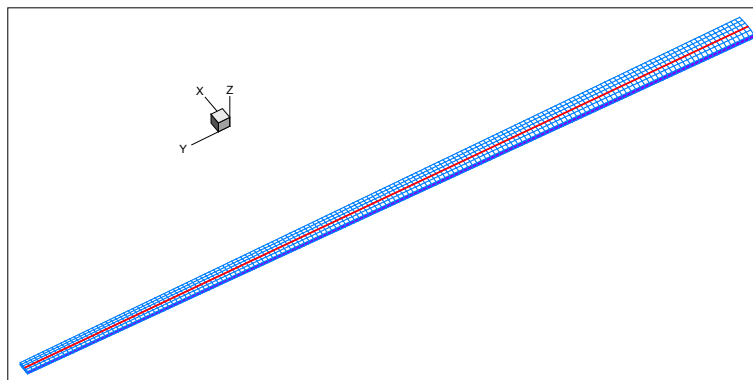


Figure 4.18: Nodes on the upper side of the wingbox for which deformations will be plotted.

the z direction was applied at the nodes of the outermost rib with assumed values between 1000 N and 7000 N to simulate a static tip loading. The results are plotted in Fig. 4.19. No follower forces and no gravity were considered, the force field is applied always onto the undeformed initial configuration of the wingbox. The amplitude of the force was scaled to excite deformations of the wing beyond the limit of structural linearity (up to almost 30% with respect to the semi-span), as can be seen in terms of the displacements in the z and the y direction. As for the beam test case, the linear FE solution calculates too large displacements in the z direction and completely omits the displacement in the y direction. The results of the proposed method are in fair agreement with the nonlinear reference solution from Nastran, differences are increasing however for the last two force fields where the displacements in the z and in the y direction are overestimated. The proposed method has attained its limit with this loading since the deviations from the Nastran solution are increasing further. It must be

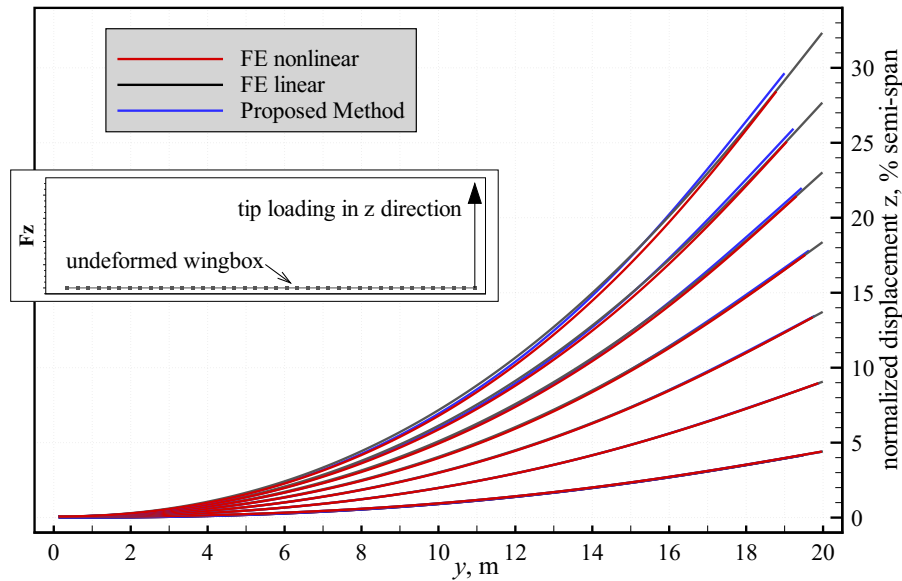


Figure 4.19: Comparison of the static displacement fields obtained by different methods for tip forces with values from 1000 to 7000 N applied in the z direction at the wingtip.

mentioned that the upper skin of the wingbox close to the root starts buckling if higher loads are applied. Of course only the fully nonlinear solution from Nastran is able to represent such behavior.

An elliptically shaped, static force field in the z direction was applied for the next test with the objective to resemble a load distribution typical of aerodynamic forces. The magnitude was scaled to reveal the limits of the proposed method. In contrast to real aerodynamic forces, which are perpendicular to the surface of the wing and thus rotate as the wing deforms, the force field is not rotated for this test and no follower force function is used. The results of the simulations are shown in Fig. 4.20. Similar to the last case, the nonlinear reference solution from Nastran and the results of the proposed method show a fair agreement regarding the displacements in the z and in the y direction. Here, the limit for the proposed method is approximately 20% tip displacement with respect to the span of the wingbox.

Tilting the elliptical force field of each node around the local x axes to obtain components in the y direction yields a more interesting test case. As mentioned, the proposed method is able to properly account for the y components due to the quadratic mode components and the force-dependent linear stiffness term, cf. Eq.(2.28). The result of this comparison is shown in Fig. 4.21, where the forces in the z direction are tilted by ± 45 degrees but the magnitudes remain unchanged. The tilt angle remains constant throughout the test. Overall displacements in the z direction are reduced for both the positive and the negative tilt angles. The linear FE solution shows large differences to the respective nonlinear results since the in-plane components of the force field have no effect.

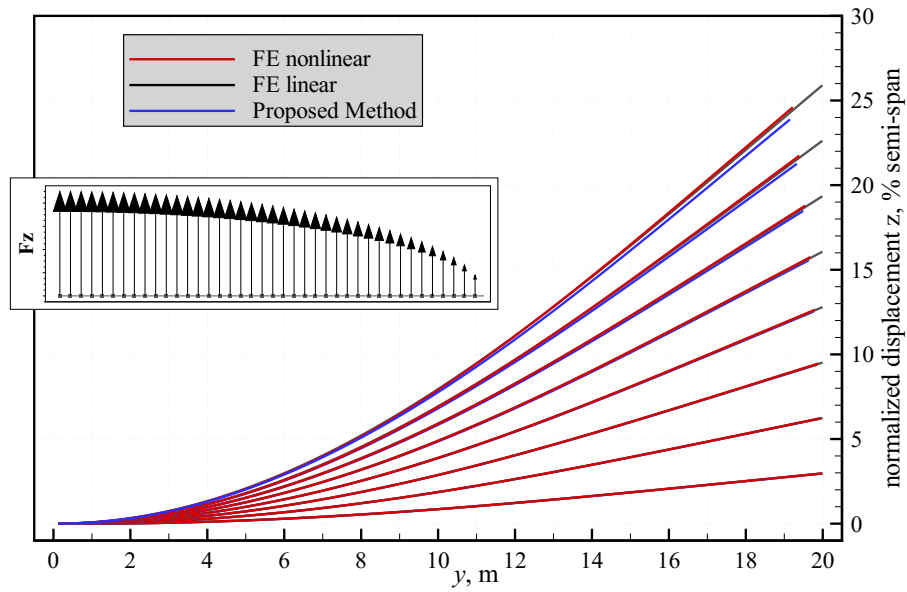


Figure 4.20: Comparison of the static displacement fields obtained by different methods for different elliptical force fields applied along the z direction at each node of the wingbox.

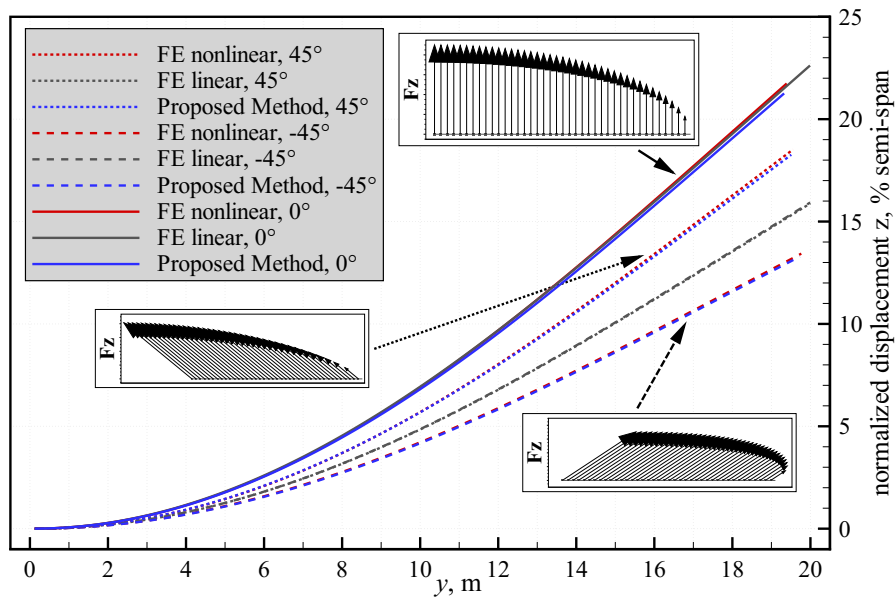


Figure 4.21: Comparison of the static displacement fields obtained by different methods for different elliptical force fields with components in z and y direction applied at each node of the wingbox. Forces are also tilted around the x axis by the angle given in the legend.

4.2.2 Static Aeroelastic Simulations and Validation

Static coupling simulations were conducted to evaluate the potential of the proposed method in terms of large deformations excited by real aerodynamic loadings calculated by the vortex-

lattice method detailed in Section 3.1. Aerodynamic forces calculated by this method are non-linear functions of the structural deformation since the vortex-lattice method allows for almost arbitrary displacements and rotations of the panels and calculates aerodynamic loads based on the current (deformed) aerodynamic grid. A coupling matrix based on a thin-plate-spline radial basis function enables the data transfer between the aerodynamic and the structural grid. No specific coupling model was built for the wingbox, but all FE nodes were used as coupling nodes. The aerodynamic grid representing the lifting surface is uncambered for easier comparison with Nastran and discretized by 64 panels in spanwise and 16 panels in chordwise direction. Its aspect ratio is 25. Induced drag is not calculated by the VL solver for this test case since its contribution is expected to be negligible (furthermore, this approach results in a better comparability to Nastran where induced drag is not calculated either).

Aeroelastic results for validation of the proposed method were calculated with Nastran solution sequence SOL 144 (static aeroelastic). To this end, a wing with exactly the same geometry and panel discretization as the VL-grid was built for Nastran. For the transfer of forces and the interpolation of displacements, the *SPLINE1* method was used where the thin-plate-spline was used as radial basis function. Since Nastran uses a vortex-lattice method for static aeroelastic simulations and the spline methods are similar for both methods, the results are expected to be identical in the linear regime, i.e. for small structural deflections². The VL model and an exemplary aerodynamic solution in terms of the pressure coefficient difference Δc_p is illustrated in Fig. 4.22.

The first aeroelastic comparison is shown in Fig. 4.23 by a plot of the structural deformations of the nodes shown in Fig. 4.18 as function of the root angle of attack which is varied from 1 to 4.5 degrees in steps of 0.5 degrees. Both the VL solver and the Nastran solution sequence SOL 144 apply incompressible aerodynamics, the Mach number in Nastran is therefore set to zero. The dynamic pressure is 3750 Pa. Nastran and the VL solution in combination with a linear structural solution yield comparable results for all angles of attack. The difference is most likely to come from the solution process. The VL aeroelastic solution is a static coupling process in which aerodynamic forces and structural deformations are converged iteratively. However, two effects acting against each other are involved. First, the increase of the wing area due to the linear structural solution, depicted in Fig. 4.24, and second, the tilting of the aerodynamic forces due to structural deformation resulting in a load component in the y direction. The nonlinear reference displacements (obtained by static coupling of the VL solver with Nastran solution sequence 400) and the deformations of the proposed method are in good agreement up to approximately 25% tip displacement with respect to the semi-span. However, differences are increasing from this region on.

²The vortex-lattice method of Nastran SOL 144 makes use of a geometrical linearization. Structural deformations are considered by tilting of the normal vectors to modify the downwash at the collocation points of the aerodynamic panels, cf. Section 3.3.

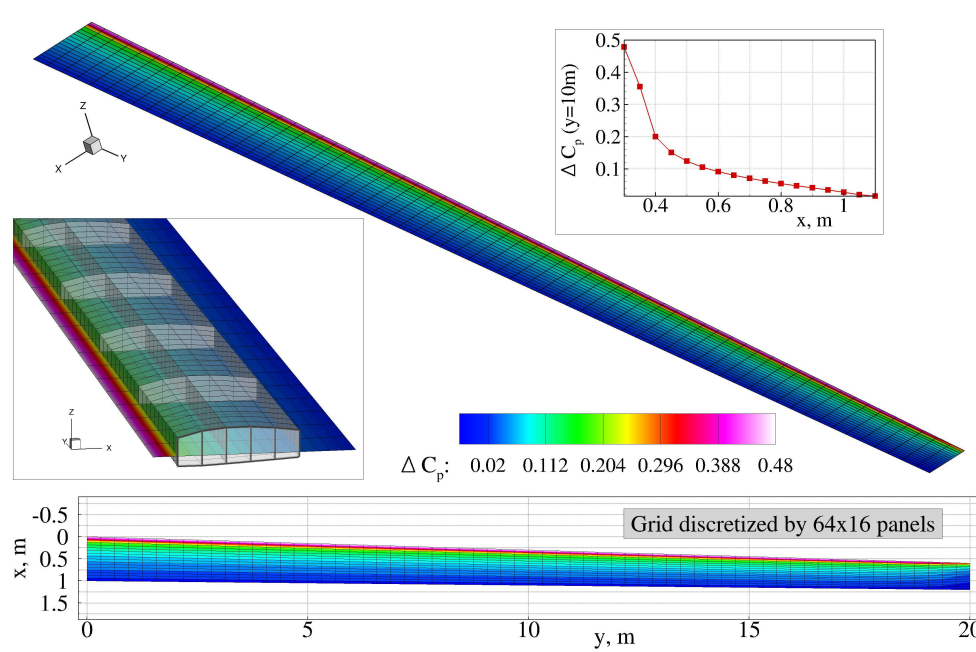


Figure 4.22: Vortex-lattice aerodynamic model of the wingbox test case with ΔC_p distribution (incompressible solution, dynamic pressure=3750 Pa, AoA=1 degree).

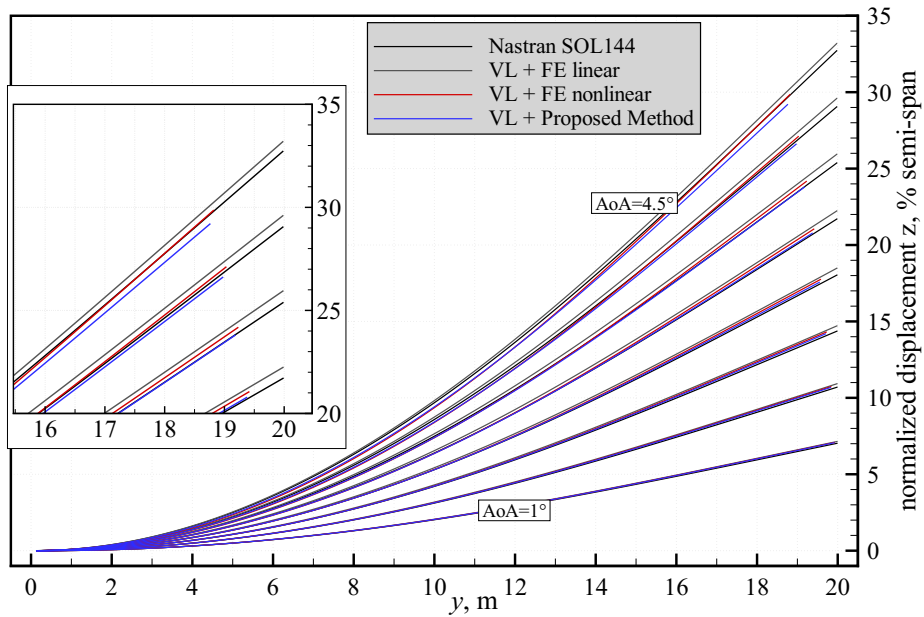


Figure 4.23: Comparison of static aeroelastic coupling results of the wingbox calculated by different methods.

The linear and nonlinear static aeroelastic simulations are further analyzed in the following with the focus on the impact of deformations on structural loads. Therefore, the structural

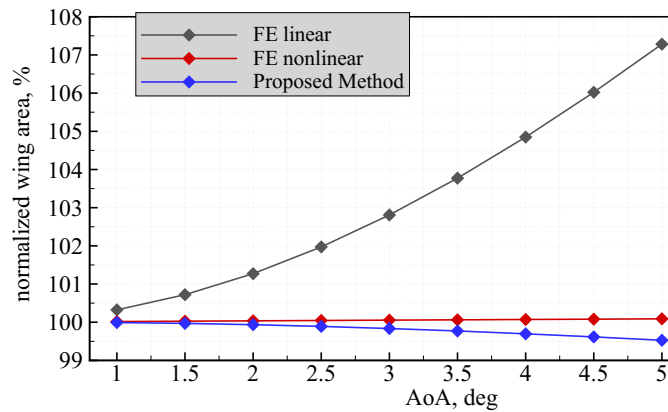


Figure 4.24: Increase of the aerodynamically effective surface area of the wing due to structural deformation.

forces and moments at the wing root resolved in the body-fixed frame are compared and plotted as function of the root angle of attack. Figure 4.25 shows the cut loads in the x , the y , and the z direction. Large differences between the two linear and the two nonlinear solutions are

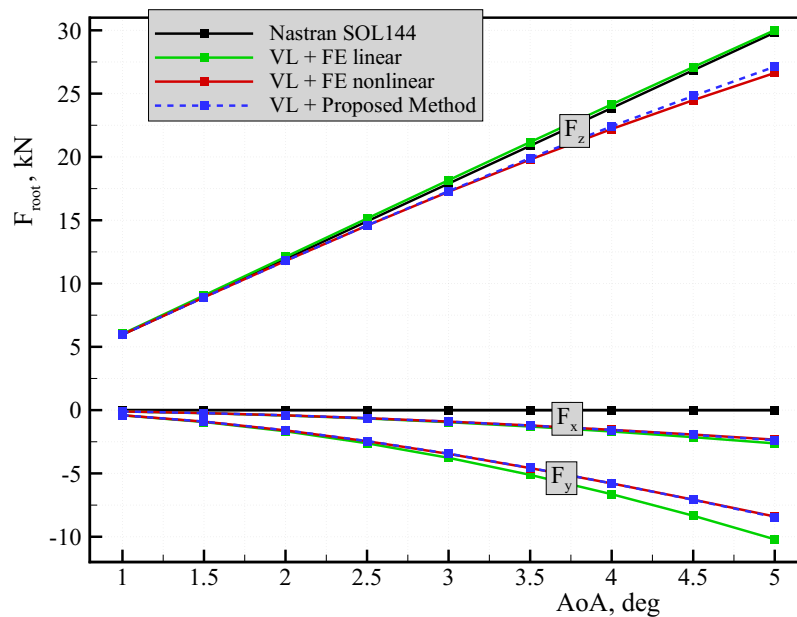


Figure 4.25: Cut loads (forces) at the wing root as function of AoA.

obtained for the shear force F_z at the wing root. This effect can be clearly attributed to the simultaneous increase of the surface area (shown in Fig. 4.24) which, in turn, increases the magnitude of the aerodynamic forces by the same amount. However, the structural forces of the two nonlinear solutions in the z direction decrease since the vector of aerodynamic forces of each panel is rotated towards the negative y direction as the structural deformation is increased.

The proposed method is in good agreement with the nonlinear reference solution with respect to F_z , although it yields slightly higher loads (which can be taken as conservative in this case). The linear Nastran SOL 144 results have no force components in the x and the y direction due to the way the aerodynamic forces are calculated – neither induced drag nor the rotation of the aerodynamic panels are taken into account. The forces F_x of the three VL solutions all agree well, but the forces in the y direction calculated by the VLM coupled with the linear FE solver show large differences with increasing root AoA. The reason therefore is again the increase of the surface area as the result of the linear FE solution. As expected, good agreement of the moments at the wing root about the y and the z axes is obtained, as is depicted in Fig. 4.26. It must be mentioned that F_x is negative and M_z positive with increasing AoA since

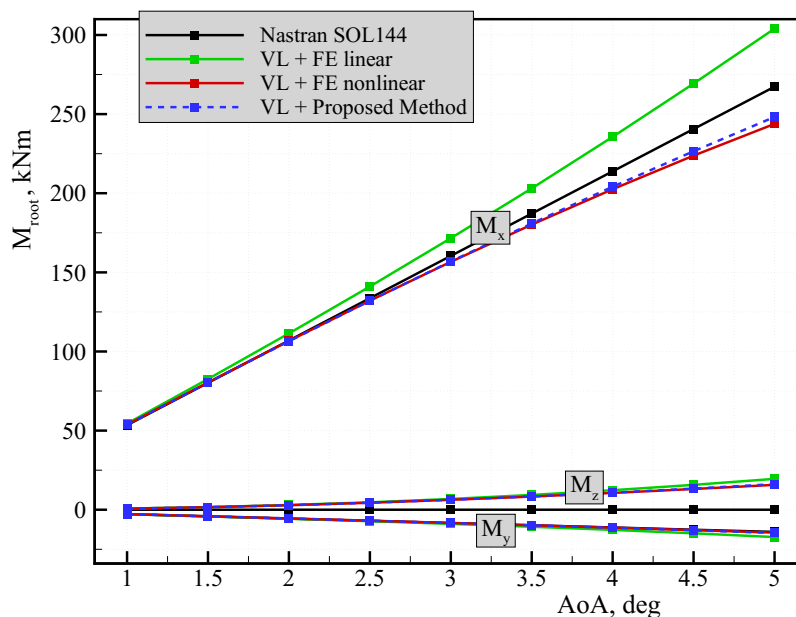


Figure 4.26: Cut loads (moments) at the wing root as function of AoA.

the lift force has a positive component in the x direction with respect to the body-fixed frame. The moment about the y axis is negative due to the slight positive sweep angle of the wing. Most important is the comparison of the wing root bending moment M_x . Here, the VL and linear structural solution yields a much higher bending moment compared to the nonlinear and even to the Nastran solution. The tilting of the aerodynamic force vectors, as it is considered by the VL solution, keeps them perpendicular to the panels of the wing and thus leads to higher bending moments along the wing span and at the root. However, the increased wing area additionally increases this bending moment. The aerodynamic forces from the Nastran solution only have a component in the z direction, thus lowering the bending moment M_x . The bending moment from the nonlinear Nastran solution and the proposed method are in fair agreement, but again the proposed method calculates larger values. The most important

conclusion from the structural loads point of view is that a geometrically nonlinear aerodynamic method (such as the VLM) should not be used in combination with a linear structural solution. This overestimates the bending moment M_x as discussed above.

4.3 X-HALE UAV Test Case

In the previous sections, the proposed method was validated statically with a slender cantilever beam and a 3D wingbox built from shell elements. The X-HALE UAV from the University of Michigan is the final test case in this thesis to demonstrate and validate steady and unsteady simulation results [84, 85, 86]. The complexity is further increased by the inclusion of rigid-body DOFs and the simulation of a highly flexible, free-flying elastic aircraft undergoing large deformations in maneuvering flight.

4.3.1 Key Features of the X-HALE UAV

The X-HALE UAV is a very flexible, high aspect ratio wing-boom-tail type aircraft. In this work, the *Risk Reduction Vehicle* (RRV) version is considered, which has a wing span of six meters, five booms with all-moving horizontal tails (with symmetrical section), and five motor pods with propellers, batteries, speed controllers, and processor boards. Composite materials (mainly glass fiber reinforced plastic) wrapped around a Rohacell foam core are used for the fabrication of the wings and the tails. The aircraft can either be remotely piloted from ground or flown autonomously by a flight controller using data from the GPS, the IMU, and the INS. Figure 4.27 illustrates details of the X-HALE's design and construction. The goal of the corresponding activities at the University of Michigan is to design and build a very flexible UAV for nonlinear aeroelastic tests³. It should serve as a low-cost platform to obtain relevant nonlinear aeroelastic data to support validation of nonlinear aeroelastic codes and as platform for control law studies in the future. The unique nonlinear aeroelasticity/flight dynamic interaction of very flexible aircraft not easily obtainable from wind tunnel tests are to be captured. Elaborated on-board measurement systems with complex sensor arrays are collecting data during the flight tests [1]. Figure 4.28 shows the X-HALE 6 meter span RRV on the ground and in flight during a turn maneuver with considerable wing deflection. The UM/NAST toolbox is the standard software package used by the University of Michigan for aeroelastic simulations of the X-HALE [1, 62].

The mass of the aircraft is 10.86 kg with an anticipated flight speed ranging from 10 to 19 m/s [1]. The wing and the four tails are of rectangular planform with constant airfoil sections along the span. Important aerodynamic and structural properties of the X-HALE are listed in Table 4.3.

³University of Michigan Aerospace Engineering, <https://a2srl.engin.umich.edu/research/flexible/xhale>

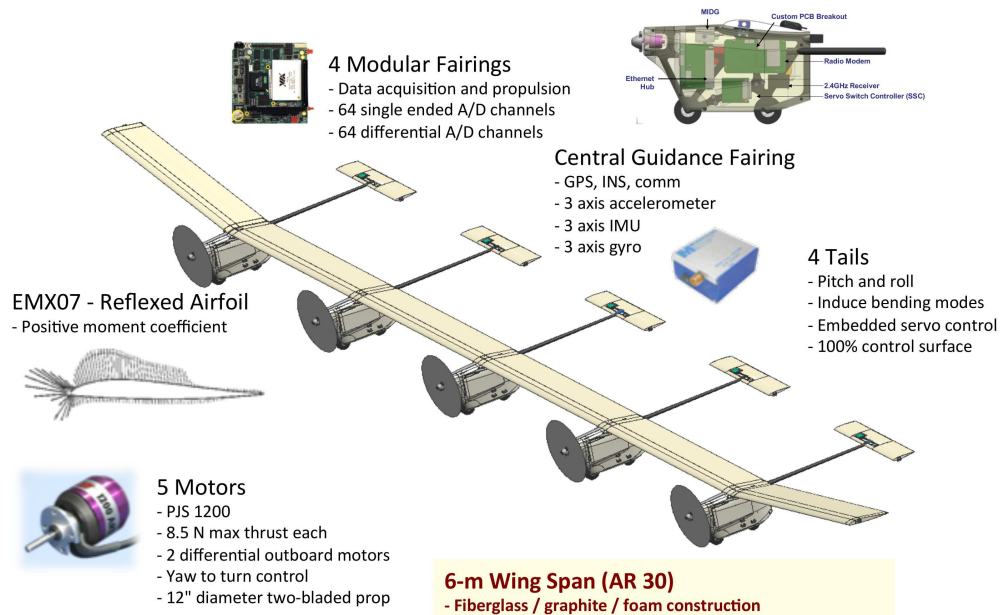


Figure 4.27: Concept of the X-HALE UAV developed by the University of Michigan [87].

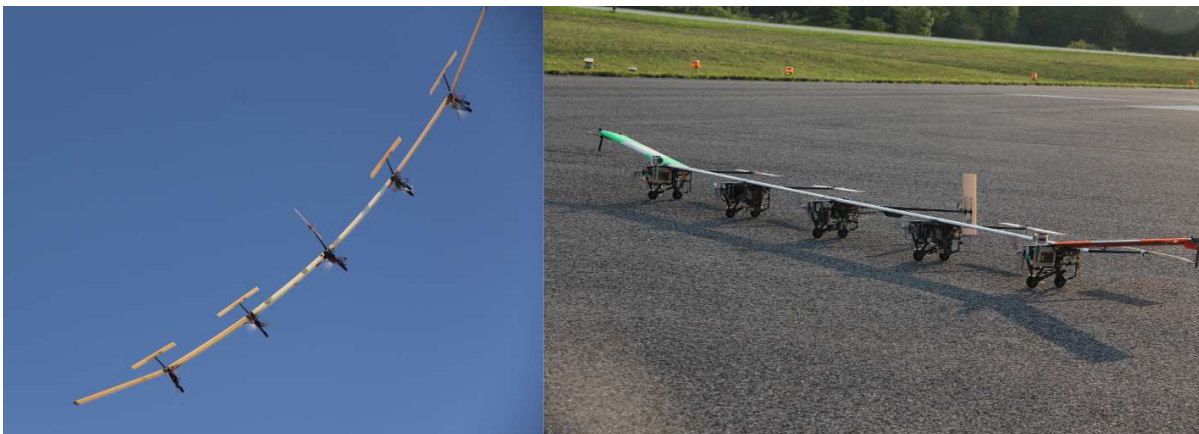


Figure 4.28: X-HALE 6 meter span RRV in turn maneuver and on ground.

4.3.2 Setup of the Structural and Aerodynamic Simulation Models

Nastran FEM of the X-HALE UAV

A MSC Nastran 3D finite beam element model of the X-HALE was built from scratch based on input files for UM/NAST with the intention to match the stiffness and mass properties as well as the eigenvalues and eigenvectors as accurately as possible (the corresponding data from UM/NAST were taken as reference). The UM/NAST solver uses a distinct format for the definition of the simulation model including the beam properties, the aerodynamic lifting surfaces, and the definition of parameters for the solution process. Any beam-like members (wings, booms, and tails) are modeled by beam-type elements (Nastran *CBEAM* elements in this case),

Table 4.3: Aerodynamic and mass properties of the X-HALE UAV (mass properties for undeformed configuration). Tensor of inertia entries according to body-fixed frame axes orientation depicted in Fig. 2.8.

Property	Symbol	Unit	X-HALE FEM
Span (wing)	b	m	6
Mean Chord (wing)	\bar{c}	m	0.2
Area (wing)	S	m ²	1.2
Aspect Ratio (wing)	Λ	-	30
Airfoil (wing)	-	-	EMX07
Flight velocity (trim)	V_0	m/s	16
Air density (trim and maneuver)	ρ	kg/m ³	1.2216
Lift coefficient (trim)	C_{L0}	-	0.524
Mass	m	kg	10.862
Inertia (xx)	J_{xx}	m ² kg	25.012
Inertia (yy)	J_{yy}	m ² kg	0.595
Inertia (zz)	J_{zz}	m ² kg	25.517
Inertia (xy)	J_{xy}	m ² kg	0.00312
Inertia (xz)	J_{xz}	m ² kg	0.00115
Inertia (yz)	J_{yz}	m ² kg	0.000115
c.m. x (w.r.t body frame origin)	cm_x	m	0.00865
c.m. y (w.r.t body frame origin)	cm_y	m	-0.00095
c.m. z (w.r.t body frame origin)	cm_z	m	0.00118

discrete mass elements (Nastran *CONM2* elements) were added to condense distributed masses of structural members (e.g. booms or tails) and to consider particular ballast masses such as batteries, engines, and servos. Only one mass configuration of the model is defined and the mass of the aircraft remains constant during flight. The structural model is depicted in Fig. 4.29, where the masses of the discrete mass points are visualized by spheres with aluminum equivalent density. The origin of the body-fixed frame is located at (x,y,z = 0,0,0 m) with respect to the coordinate system of the structural model defined in Nastran (to setup the model).

The UM/NAST structural model uses various mass offsets to account for different locations of the elastic axis of a beam and its center of mass. To avoid mass offsets in the nonlinear solutions of Nastran, they are eliminated by additional massless beam elements as depicted in detail in Fig. 4.29 at the right wing. It must be mentioned that the structural model is clamped at the origin of the body frame and thus the flexible main beam of the wing is clamped at the center. The reason for the clamping is, as mentioned in the previous sections, the calculation

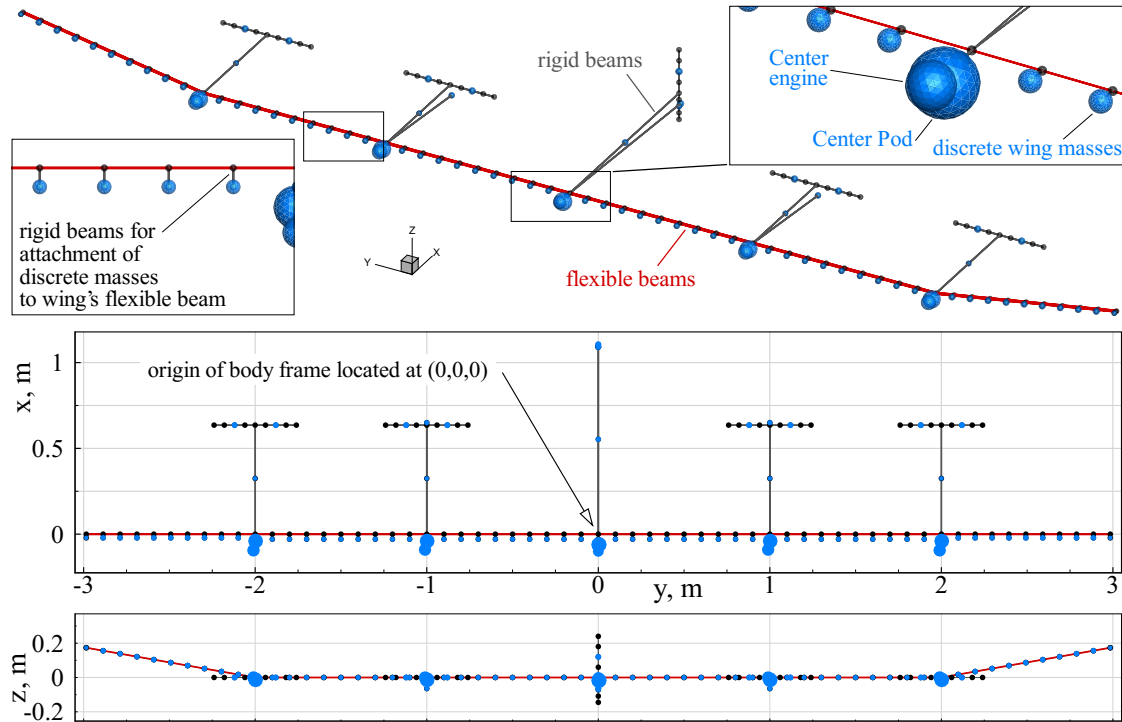


Figure 4.29: Structural model of the X-HALE UAV build with flexible (red lines) and rigid (grey lines) beam finite elements. Discrete mass points are visualized by spheres with aluminum equivalent density.

of the higher-order stiffness and mode components which requires a clamped structural model. Table 4.4 lists the lowest twelve modes with the corresponding natural frequencies and the types of the modes both from the FE modal analysis and from the polynomial fitting method. Due to the clamping of the model at the center of the wing beam, the modes appear in pairs for the right and the left wing. However, due to the asymmetric setup of the mass model, the eigenvalues of the left and the right wing of the same mode are slightly different. The high flexibility of this configuration can be seen in terms of the first bending mode, which has a frequency of about 0.6 Hz only. Furthermore, a specific characteristic of the model is that the second mode of each wing is the first torsion mode. The lowest twelve natural modes of the FE model are plotted in Fig. 4.30 with the corresponding frequencies of the FE eigenvalue analysis listed in Hz. Higher-order stiffness and mode components were calculated for these modes and used for all static and dynamic simulations of the following sections.

VL Aerodynamic and Coupling Model

The VL model is composed of different lifting surfaces for the wings, the tails, the spines, and the fins. The VL method is advantageous for the aerodynamic modeling of the X-HALE since it accounts for the mutual interaction of the numerous lifting surfaces and due to the

Table 4.4: Eigenvalues of the twelve lowest modes of the X-HALE FE model; values are obtained from a FE modal analysis and from the polynomial fitting method described in Section 2.3.

Mode	Type of mode shape	Eigenvalue FE analysis [Hz]	Eigenvalue (${}^pG_1^i$) reconstructed [Hz]
1	first bending left	0.598	0.598
2	first bending right	0.600	0.600
3	first torsion right	2.605	2.604
4	first torsion left	2.605	2.605
5	second bending left	3.677	3.676
6	second bending right	3.681	3.680
7	first bending in-plane left	4.486	4.486
8	first bending in-plane right	4.491	4.491
9	second torsion right	6.685	6.685
10	second torsion left	6.687	6.688
11	third bending right	8.199	8.198
12	third bending left	8.220	8.220

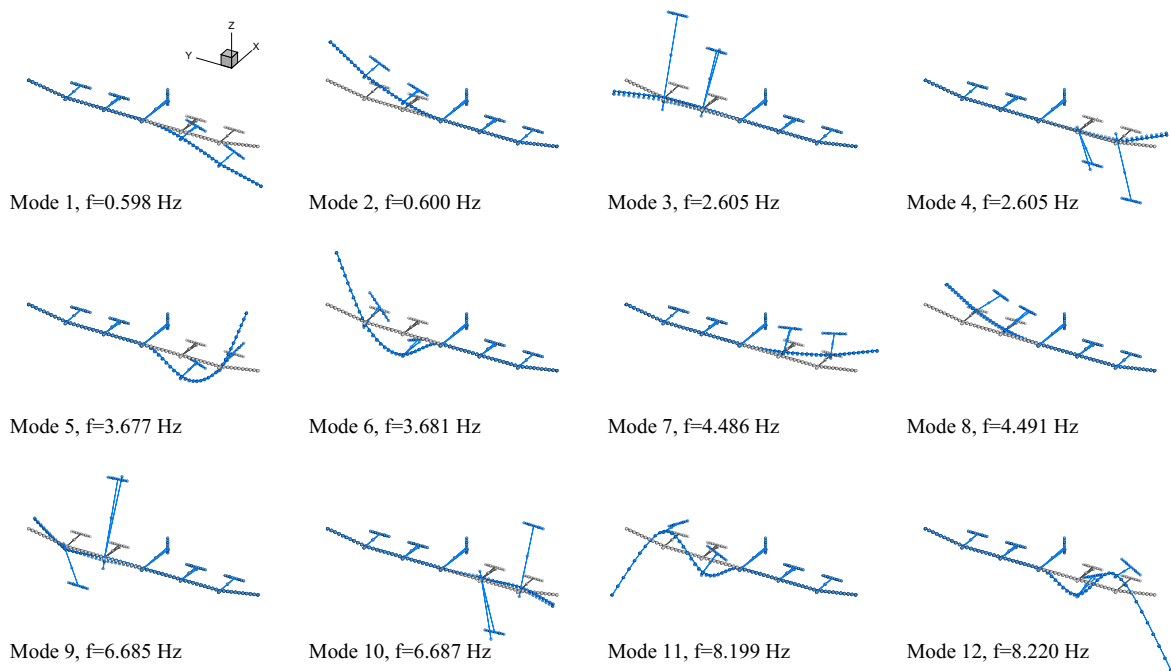


Figure 4.30: The lowest twelve mode shapes of the X-HALE structural model obtained from a normal modes analysis (the model is clamped at the origin).

comparatively low computational costs even for the unsteady simulations. The VL grid of the X-HALE model is shown in Fig. 4.31. The section of the wing is the *EMX07* reflex airfoil⁴, the

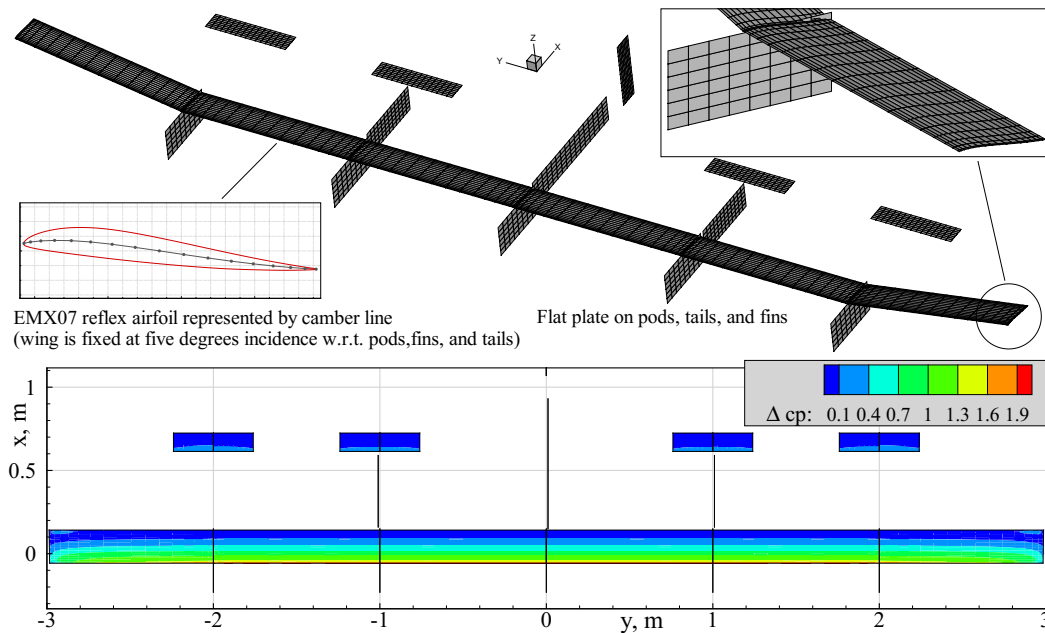


Figure 4.31: Vortex-lattice grid of the X-HALE composed of several lifting surfaces for the wings, the tails, the pods, and the fins with exemplary pressure coefficient (Δc_p).

VL solver uses its camber line – calculated by the mean of the coordinates describing the upper and the lower side of the airfoil – to define the actual surface of the wing. Any other lifting surfaces (the pods, the tails, and the fins) are modeled as flat plates. It must be mentioned that the incidence of the wing is five degrees with respect to the body-fixed reference frame, as can be seen in Fig. 4.31. A cosine spacing is applied to the panels on the wing in the spanwise direction to better resolve the wing tip effect as well as the transition at the dihedral wing elements and at the pods. All lifting surfaces share wake panels as described in Section 3.1.2. An example of the pressure coefficient distribution on the wing is shown in the same plot. As can be seen, three-dimensional aerodynamic effects are pronounced at the wing tips and at the tails.

As mentioned in Section 3.1.4, the accuracy of the VLM can be improved by the calculation of the induced drag and an estimation of the viscous drag. The estimation of the viscous drag is implemented for steady aerodynamic analysis so far only, but the induced drag is calculated in steady and unsteady solutions. For the estimation of the viscous drag, a number of drag polars of the EMX07 airfoil was calculated with XFOIL for Reynolds numbers varying from $1.95 \cdot 10^5$ to $2.5 \cdot 10^5$ in steps of 5000. This corresponds to flight velocities from approximately 14 to 18 m/s, a reference length of 0.2 m (which corresponds to the chord length of the airfoil), and a kinematic viscosity of $1.421 \cdot 10^{-5} \text{ m}^2/\text{s}$. A set of lift, drag, and moment polars is plotted in Fig. 4.32

⁴A reflex airfoil for the wing section of an aircraft with tails is unusual. The reason for this choice is that the X-HALE was originally designed without horizontal tailplanes (unswept flying wing).

together with an inviscid and a viscous pressure distribution for the range of Reynolds numbers mentioned above and AoAs from two to eight degrees (the anticipated range of the AoA during maneuvers). The objective of this plot is to depict that the lift slope can be approximated well

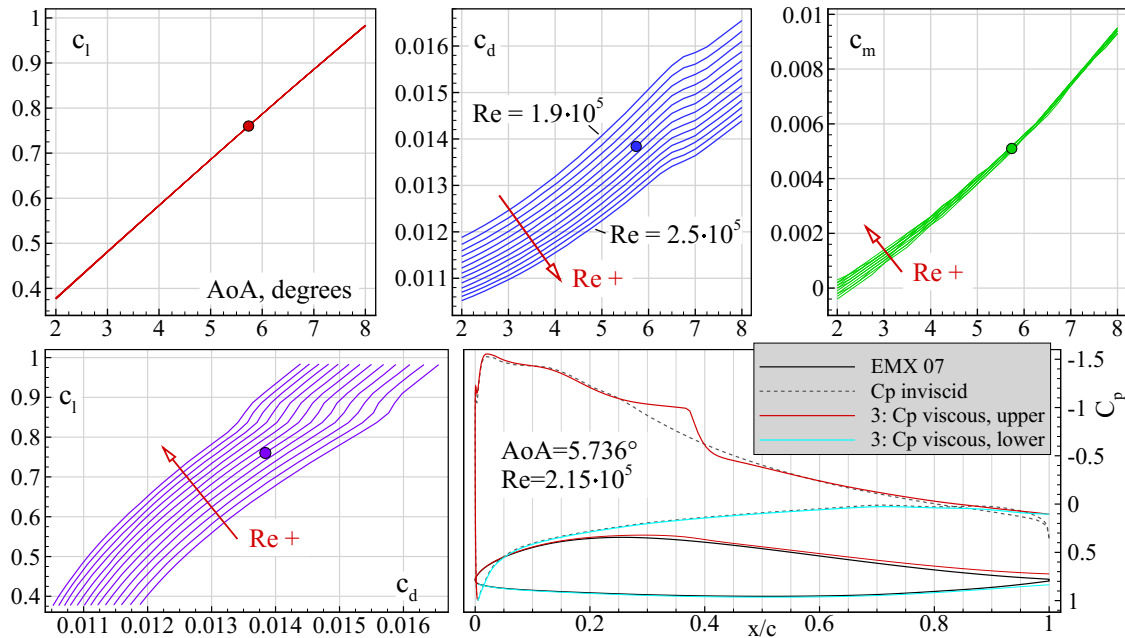


Figure 4.32: Lift, drag, and moment coefficients of the EMX 07 reflex airfoil for Reynolds number varying from $1.95 \cdot 10^5$ to $2.5 \cdot 10^5$ in steps of 5000 calculated by XFOIL (circles correspond to the steady trim condition at 16 m/s flight velocity). Pressure distribution and boundary layer show laminar separation bubble at $x/c=0.35$ for trim AoA.

by a linear function and also the drag coefficient shows a smooth behavior with the exception of minor bumps within an AoA from 6.5 to 7.5 degrees (which can be attributed to the movement of the region of transition). This behavior can partly be attributed to the small leading edge radius and the location of the maximum thickness at 28.4% resulting in a gentle adverse pressure gradient aft the point of maximum thickness. However, due to the low Reynolds number, a laminar separation bubble develops on the upper side of the airfoil between approximately 30% and 40% of the chord as can be seen in the pressure distribution and the boundary layer thickness. These benign airfoil characteristics – mainly the nearly constant lift slope – endorse the use of the VL method in general for the simulation of the X-HALE wing and the estimation of the viscous drag based on the interpolation of the drag polars. Although these detailed airfoil analyses are not essential for this thesis, future flight dynamic simulations of the X-HALE model will be validated with flight test data for which these particular aerodynamic effects induced by the low Reynolds numbers are expected to play an important role.

To evaluate the aerodynamic characteristics of the entire aircraft, a static polar was calculated using the rigid VL model for an airspeed of 16 m/s and a density of 1.2216 kg/m^3 .

The AoA (measured with respect to the body frame) was varied between -10 and 4 degrees in steps of 0.5 degrees (it should be mentioned again that the wing is fixed at an incidence of five degrees with respect to the body frame). The lift, the drag, and the pitching moment coefficients are plotted in Fig. 4.33. The slopes of the lift and the moment coefficients are almost constant, the large contribution of the estimated viscous drag is significant. Clearly the induced drag shows a quadratic dependence on the AoA. As can be seen, the lift coefficient required to balance the weight of the aircraft (0.524) is reached at an AoA of approximately 0.5 degrees.

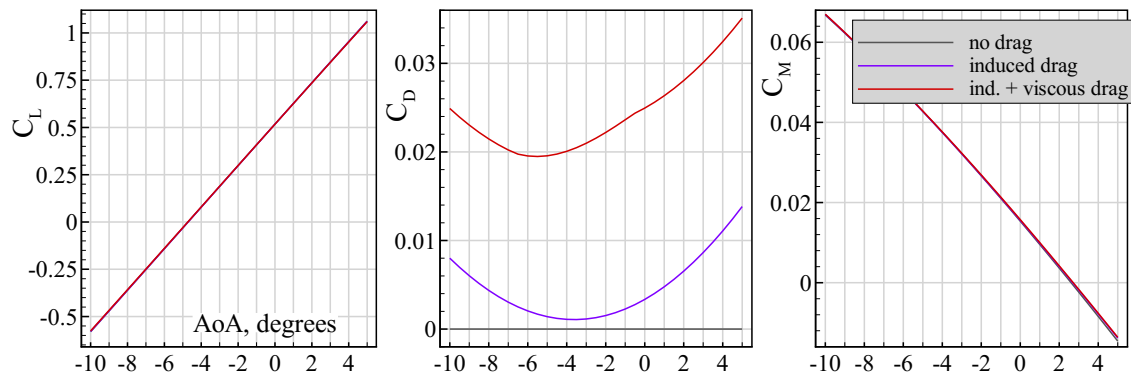


Figure 4.33: Lift, drag, and pitching moment coefficients of the rigid X-HALE model as function of the AoA. Airspeed=16 m/s, density=1.2216 kg/m³.

The lift force distribution in the z direction is shown in Fig. 4.34 for AoAs from -3 to 3 degrees in steps of one degree. The linear characteristic of the lift with respect to the AoA

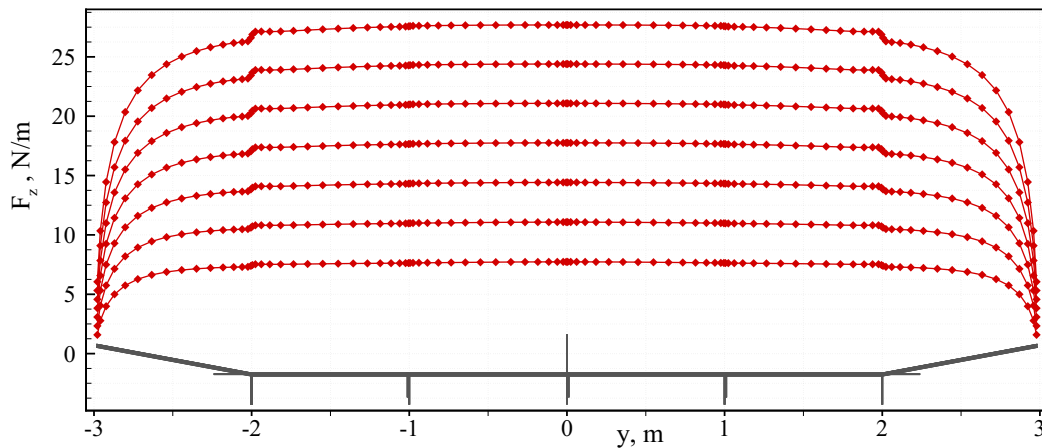


Figure 4.34: Lift force per length in the z direction of the rigid X-HALE aerodynamic model for AoAs between -3 and 3 degrees shows pronounced wingtip effects and discontinuities at the dihedral intersection. Airspeed=16 m/s, density=1.2216 kg/m³.

is obvious. Because it uses linear potential flow theory, the vortex lattice method is based on a linear relationship between the circulation of the panels of the wing and the corresponding

kinematic boundary condition. Since no stall effects are modeled in this implementation, the lift of a particular panel is always a linear function of the circulation of the panel.

Because the FE model of the X-HALE is built from beam elements, a coupling model, described in Section 3.2, is necessary. The coupling model built for the X-HALE is illustrated in Fig. 4.35.

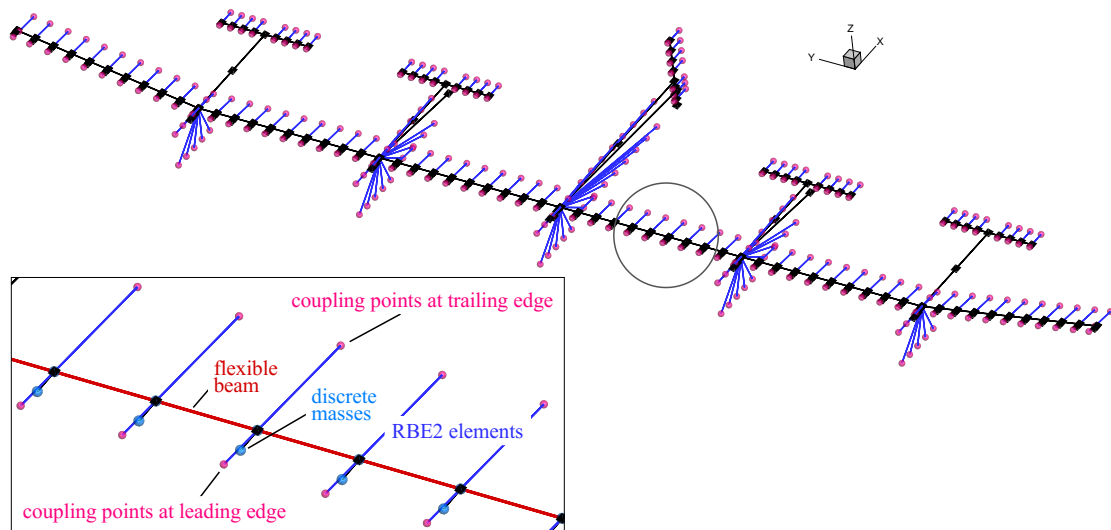


Figure 4.35: Coupling model of the X-HALE UAV. Nastran RBE2 elements (massless and rigid bars) are used to introduce the aerodynamic forces into the nodes of the beam [18].

4.3.3 Verification of the Structural Model

Static Response of the Structural Model

Two simple static structural response simulations are carried out to verify that the FE model in general and especially the higher-order stiffness and mode components yield satisfying results. First, a constant tip load in the z direction is applied at the wingtip. Second, a constant loading, also in the z direction, is applied at each node of the wing beam. Neither gravity nor follower forces are considered. The magnitudes of the forces are scaled to reach a deformation in the z direction of more than 35% of the semi-span. Results from a nonlinear Nastran solution are compared to results of the proposed method and shown in Fig. 4.36 and Fig. 4.37, respectively. Good agreement between the nonlinear reference solution and the proposed method is obtained up to a maximum tip displacement of about 30% semi-span. For reference, the solution of a linear FE simulation is added for the highest force field, but it shows large deviations to the nonlinear results.

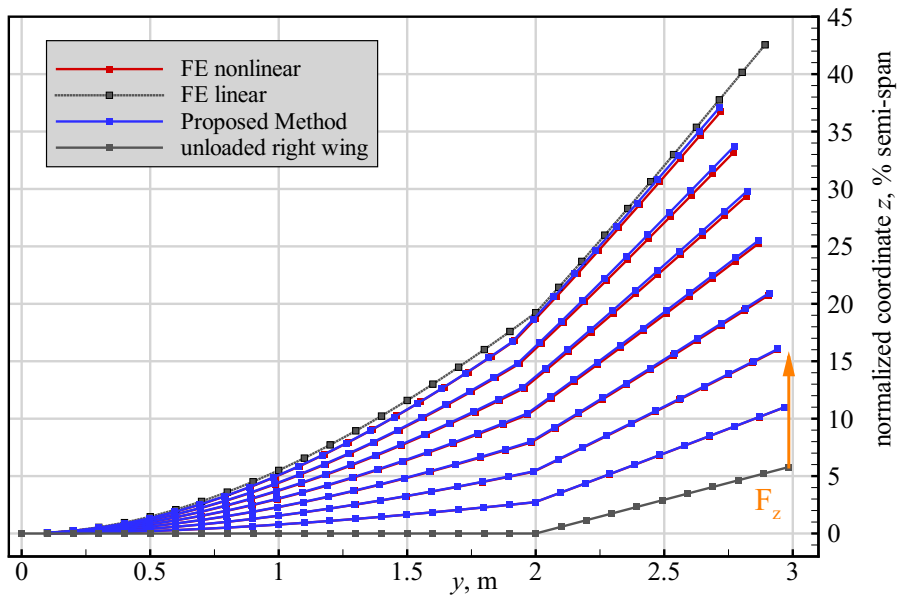


Figure 4.36: Comparison of the static displacement field obtained by different methods for forces from 2 N to 14 N (in steps of 2 N) applied along the z direction at the wingtip.

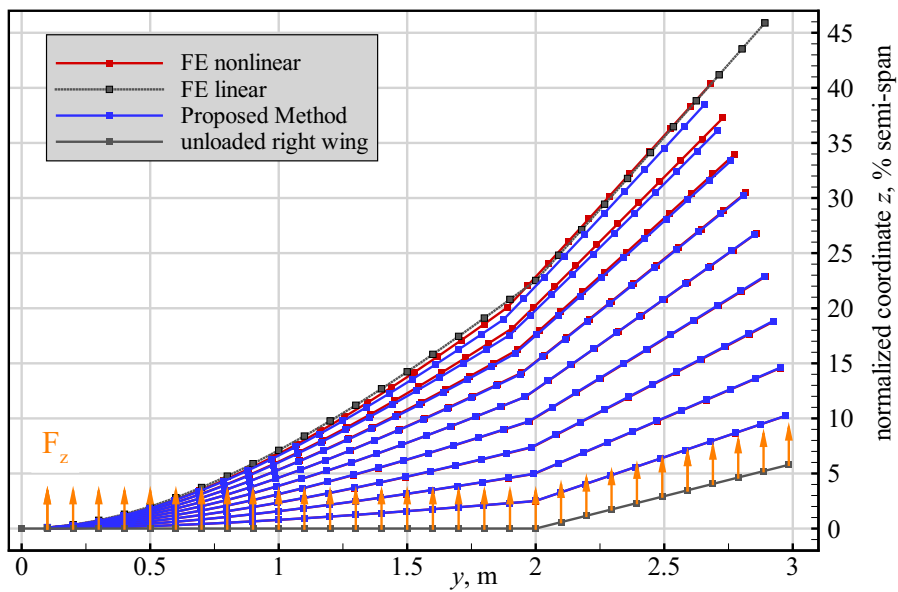


Figure 4.37: Comparison of the static displacement field obtained by different methods for forces from 0.2 N to 1.8 N (in steps of 0.2 N) applied along the z direction at each node of the wing beam.

Static Aeroelastic Response

In order to verify the static aeroelastic response of the structural model (only elastic DOFs are considered), static coupling simulations were performed in which Nastran in-the-loop and the

proposed method were used as structural solvers. This test is indispensable because differences in the static deformation field will impact the unsteady maneuver results as well. Furthermore, a nonlinear aeroelastic reference solution is given by the Nastran in-the-loop results. For the first test, the elastic beam of the wing is clamped at the root and the AoA is increased from -2 to 4 degrees to excite significant structural deflections. The airspeed is set to 16 m/s, this value is also set as (initial) flight speed for the unsteady maneuver simulations. Results of this test are shown in Fig. 4.38 in terms of the normalized displacements in the z direction of a number of structural nodes of the flexible beam located along the span, as shown in the figure. A good

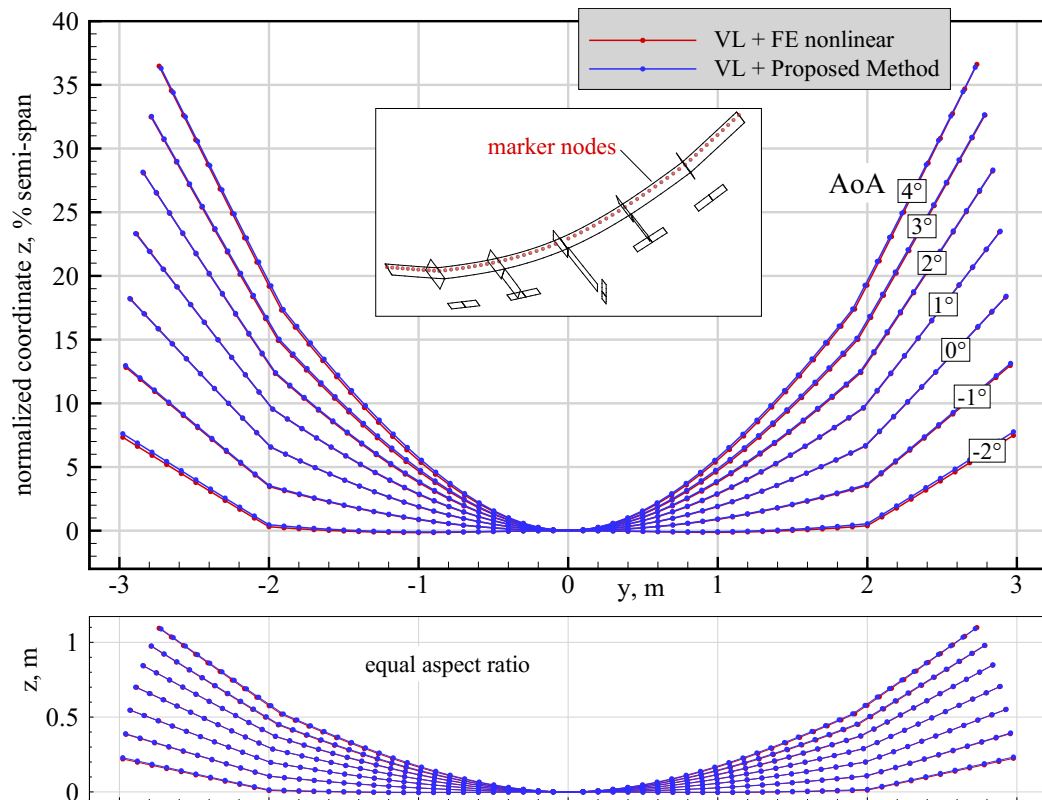


Figure 4.38: Displacement field of two methods from static coupling simulations for different AoAs. Airspeed = 16 m/s, density = 1.2216 kg/m³.

agreement between the Nastran in-the-loop and the results of the proposed method is given for the displacements in the z direction. Smaller differences occur at the lowest angle of attack. It must be mentioned that a positive deflection in the z direction is obtained even at negative angles of attack because the wing is fixed at an incidence of five degrees with respect to the x axis of the body frame. The corresponding total lift is plotted Fig. 4.39 in aerodynamic axes; the decrease of the lift slope is pronounced, and, since no nonlinearities are considered for the calculation of the aerodynamic forces, this effect can be attributed to the structural deformation because the forces in the z direction are rotated towards the center.

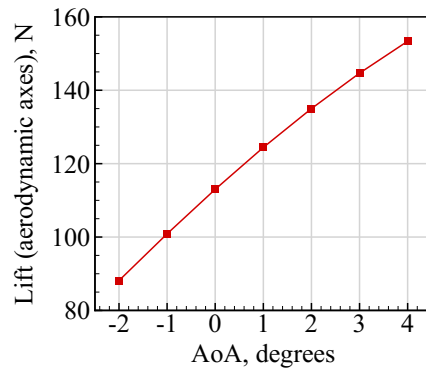


Figure 4.39: Lift in aerodynamic axes for AoAs corresponding to Fig. 4.38.

The second verification is of equal importance. Now the AoA is fixed to zero degrees and all four tails are deflected symmetrically by 4, 2, 0, -2, and -4 degrees. All other parameters remain the same. This test case is of high relevance because the interaction between the bending and the torsion deformation of the wing must be captured accurately. The validation results are shown in Fig. 4.40 again in terms of the displacements of selected nodes of the wing beam in the z direction. Good agreement is obtained between the nonlinear results and those of

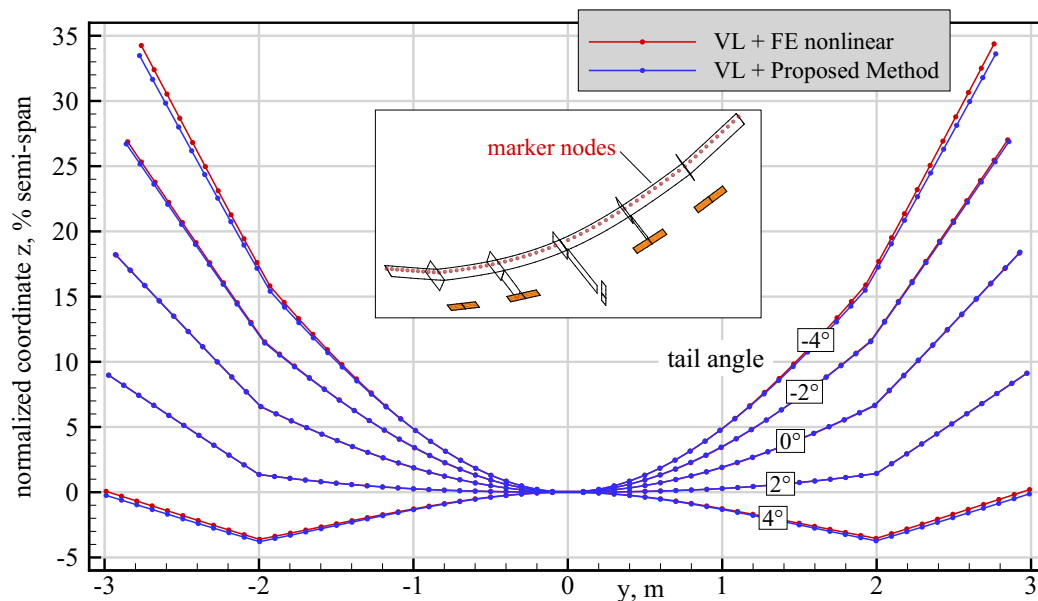


Figure 4.40: Displacement fields of two methods from static coupling simulations with varying tail deflections (positive tail angle yields negative pitching moment). AoA=0 degrees, air-speed=16 m/s.

the proposed method; however, differences are significant at the lowest and the highest tail deflections. Nevertheless, this agreement is acceptable and it can be expected that the structural model yields reliable results in the steady trim and unsteady maneuver simulations.

4.3.4 Validation of Static Coupling Simulations with UM/NAST Results

Nonlinear static coupling simulations were conducted at the University of Michigan using the UM/NAST toolbox. Originally based on 2D strip theory aerodynamics, an unsteady vortex-lattice method has recently been implemented in this toolbox with the goal to better capture 3D aerodynamic effects (e.g. at wingtips and pod-wing-fin junctions) notably pronounced at the X-HALE configuration [64]. Thus the aerodynamic model of the method introduced in Section 3 is very similar to the one used by UM/NAST. A comparison of the static coupling results of the proposed method (depicted in Fig. 4.38) with results from UM/NAST is shown in Fig. 4.41. Results of the linear FE method are plotted additionally for reference. For the

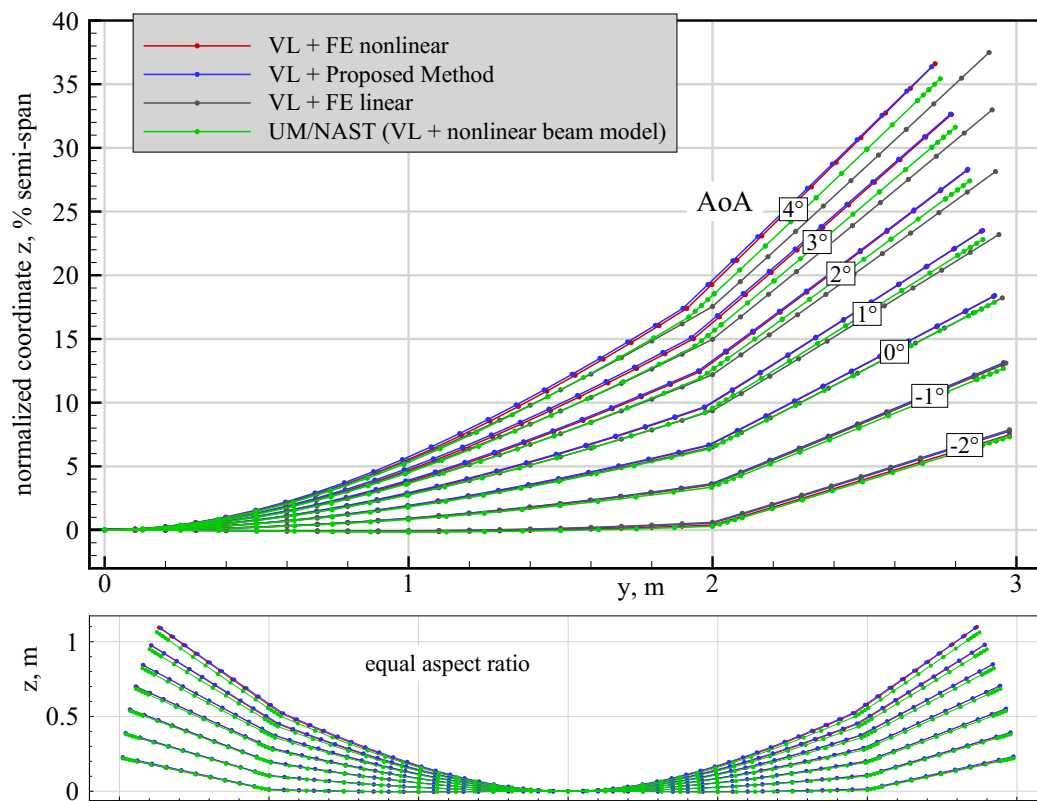


Figure 4.41: Displacement fields of static coupling simulations from four methods for different AoAs. Airspeed=16 m/s.

static coupling, the differences between the nonlinear and the linear results are more distinct for the displacements in the y direction than in the z direction (when compared for example to the structural response results shown in Fig. 4.37). The distribution of the aerodynamic forces, the dihedral of the outer sections of the wings wing and the follower-type aerodynamic forces lead to pronounced in-plane displacements. Comparing the UM/NAST results with those of the proposed method reveals a good agreement of the displacements in the y direction, but smaller differences in the z direction. These differences could be attributed to the different methods

that the two programs use for the data transfer between the aerodynamic and the structural model. The aerodynamic methods (VL) are similar, and the structural models (strain-based beam theory and Nastran nonlinear) are similar as well when considering the simulations using VL and Nastran in-the-loop. However, the validation of simulations from the aeroelastic model and the program of this work with UM/NAST results is currently an ongoing effort.

4.3.5 Trim Simulations for Steady Straight Horizontal Flight

Steady trim simulation results are discussed in the following. Different flight velocities in the x direction of the geodetic frame were specified: 15, 16, 17, and 18 m/s, together with an air density of 1.2216 kg/m^3 . The approach applied for the X-HALE trim is described in Section 3.4. The AoA, the angle (deflection) of the tail planes, and the thrust of the engines must be set to achieve a steady straight horizontal flight for which all angular rates as well as all translational and angular accelerations are equal to zero. Three trim simulations were performed for each flight velocity to analyze the impact of drag forces on the trim parameters: No drag forces, induced drag, as well as induced plus viscous drag. The results of the elastic trim simulations in terms of these parameters are shown in Fig. 4.42. As is expected, the AoA decreases quadrat-

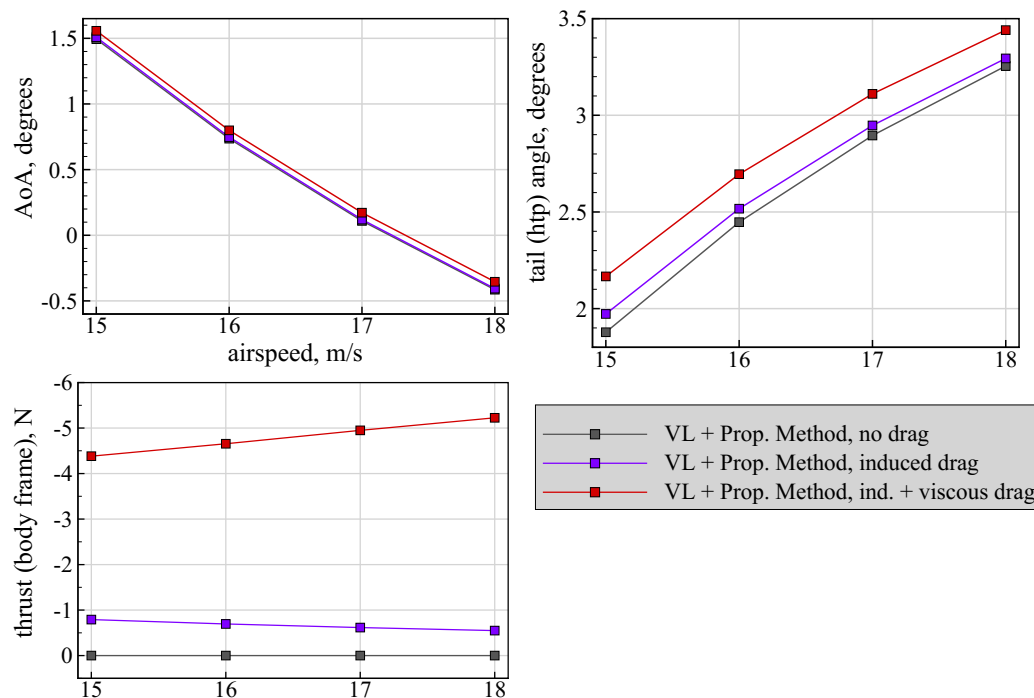


Figure 4.42: Results of the trim simulations (steady straight horizontal flight) of the X-HALE for flight velocities of 15, 16, 17, and 18 m/s. Aerodynamic forces from VL without drag, with induced, and with induced and viscous drag.

ically for all three types of drag as the aircraft is trimmed for a higher flight velocity. The lift

forces are a linear function of the dynamic pressure which in turn depends quadratically on the flight velocity. Taking induced and viscous drag into account requires a slightly higher AoA for all flight velocities compared to the case without drag and with induced drag only. The distribution of the viscous drag forces on the airframe obviously leads to slightly different structural deformations and pitching moments which requires a higher AoA. Concerning the values of the AoA, which are in the range of approximately 1.5 to -0.5 degrees, one must again keep in mind the five degrees wing incidence. The deflection of all four tails to balance the moment about the y-axis of the body frame increases with increasing airspeed for all types of drag. The tail deflection is defined such that a positive angle yields a negative pitching moment. For steady trim, the AoA decreases with increasing flight speed, and the pitching moment of the aircraft increases because the angle of attack of the tails is decreased as well. An increased (more positive) tail deflection is thus necessary for equilibrium of moments about the y-axis. It seems remarkable at first sight that the tail angles are positive, but, as mentioned before, the five degrees incidence of the wing w.r.t the body frame (and thus to the tails) must be considered. The viscous drag case requires a comparatively larger tail deflection compared to the induced and no drag case. The viscous drag forces generate a positive pitching moment mainly due to the dihedral of the wing, the elastic deformation of the wing further increases the lever arm in the z direction with respect to the origin of the body frame, which is located at the center of the wing (cf. Fig. 4.29).

Thrust is required to balance the drag forces of the aircraft, it is modeled – for simplicity – as a discrete force acting at the center of mass of the undeformed aircraft collinear with the x-axis of the body-fixed frame⁵. Thus the thrust force generates a moment with respect to the actual/instantaneous location of the center of mass if the airframe is deformed. As is expected, no thrust is required if no aerodynamic drag is calculated, as is proved by the grey line on the lower left plot of Fig. 4.42. The thrust decreases (negative slope) for the induced drag case if the flight velocity is increased since the induced drag is a (quadratic) function of the lift coefficient. Clearly, the largest amount of thrust is needed if both induced and viscous drag is included in the trim simulation, where the gradient of the thrust is positive because of the quadratic dependence of the viscous drag forces on the airspeed (the dependence of the airfoil drag on the Reynolds number, as shown in Fig. 4.32, is also included in these results, but less pronounced). It must be mentioned that the thrust has negative sign which is a result of the orientation of the x-axis of the body frame, which points positive from nose to tail (cf. Fig. 2.8).

Besides the rigid-body trim parameters, the question of how the structural deformations depend on the trim velocity and the drag approach arises. At first, the structural deformation of the right wing is analyzed as function of the trim speed, where any drag forces are neglected. The result is depicted in Fig. 4.43. As can be seen from the plot with equal aspect ratio, the

⁵The consideration of engine thrust can be improved in the aeroelastic model by applying it at the structural nodes to which the engines are assigned to. It can be expected that this approach yields more realistic results for the trim and maneuver simulations and will be implemented in the future.

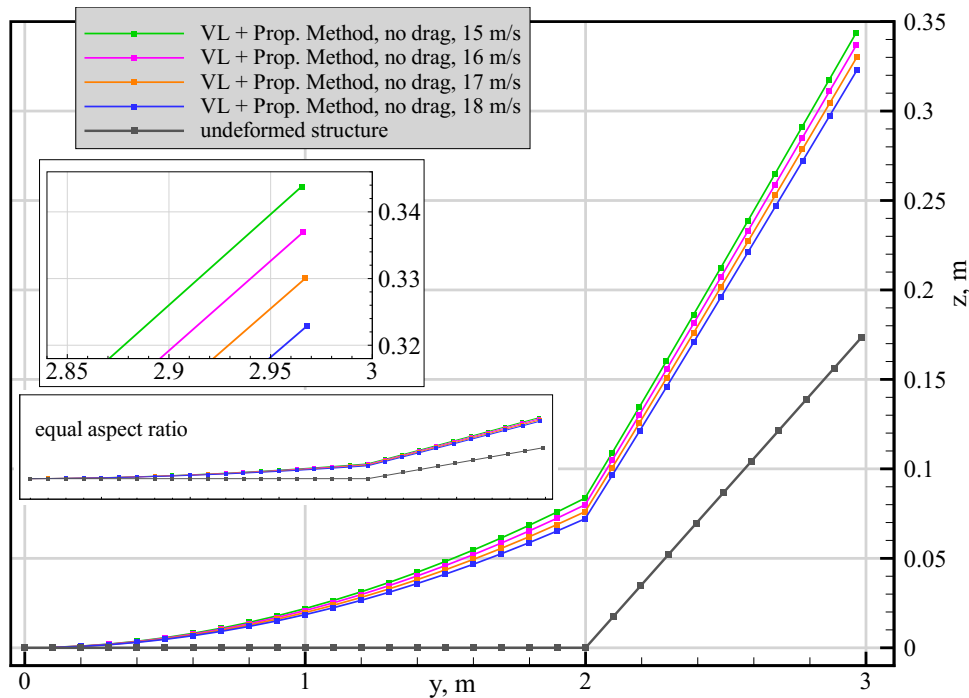


Figure 4.43: Structural deformation of the right wing of the X-HALE for four trim velocities. Drag forces are omitted.

magnitude of the overall structural deformation in steady horizontal flight (approximately five percent normalized tip displacement with respect to the semi-span) is low compared to the deflections during maneuvering flight (as will be shown in the following section). This can be attributed to the equal distribution of the structural and ballast masses along the wing. The structural deflections show only little variation with the trim speed, simply because the mass of the aircraft and thus the lift force necessary to balance the weight is independent of the flight speed. However, the lift distribution will change slightly since the tail deflection is different at different trim speeds which leads to a (slightly) different twist distribution of the wing. The difference between 15 m/s and 18 m/s trim speed in terms of elastic deformations is approximately 21 millimeters at the wingtip.

The influence of drag on the structural deflections is lower than would be expected. Fig. 4.44 shows the same plot but with both induced and viscous drag forces included. The results in terms of structural deflections are very similar to the case without drag. This time, the difference of the elastic deformations from 15 m/s to 18 m/s is approximately 23 millimeters. For the X-HALE model in steady horizontal flight, the main effect of drag is the higher thrust force that is required for the force balance.

Finally, the effects of different structural methods are analyzed. The trim speed is set to 16 m/s (corresponding to the initial speed of the maneuver simulations), and the results of a nonlinear FE solution used within the trim process are compared to the solution from the

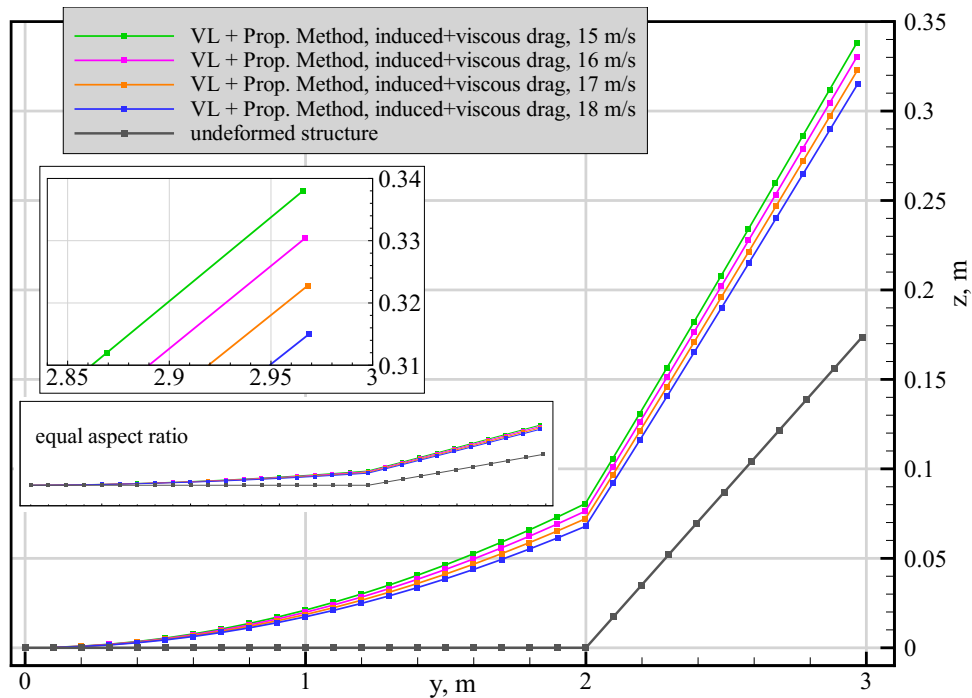


Figure 4.44: Structural deformation of the right wing of the X-HALE for four trim velocities. Both induced and viscous drag forces are included.

proposed and the linear FE method. Both induced and viscous drag are taken into account. As is expected because of the low overall displacements in trimmed flight, the effects in terms of structural deflections are small, the differences of the deformations are within a range of approximately six millimeters, depicted in Fig. 4.45.

4.3.6 Unsteady Maneuver Simulations

Results of open loop, unsteady sinusoidal tail input and gust encounter scenarios are shown in the following. Tail deflections and gust disturbance velocities (as well as gust widths) were chosen to excite structural deflections up to the nonlinear regime. However, the maneuvers are simulated with increasing magnitude of deformation such that the effects caused by the structural nonlinearities can be comprehended step by step. Furthermore, all unsteady simulations were performed additionally with linear mode shapes (clamped modes, but no higher-order mode components) as a reference. This approach ensures that the dynamics of the system and the differences between linear and nonlinear solutions are comprehensible. Nonlinear solutions from the UM/NAST toolbox are used for validation of the results. Unfortunately, only few nonlinear solutions are available so far because of the ongoing implementation work; the validation activities of the proposed method and the UM/NAST toolbox are pursued and further results are expected to be available in near future.

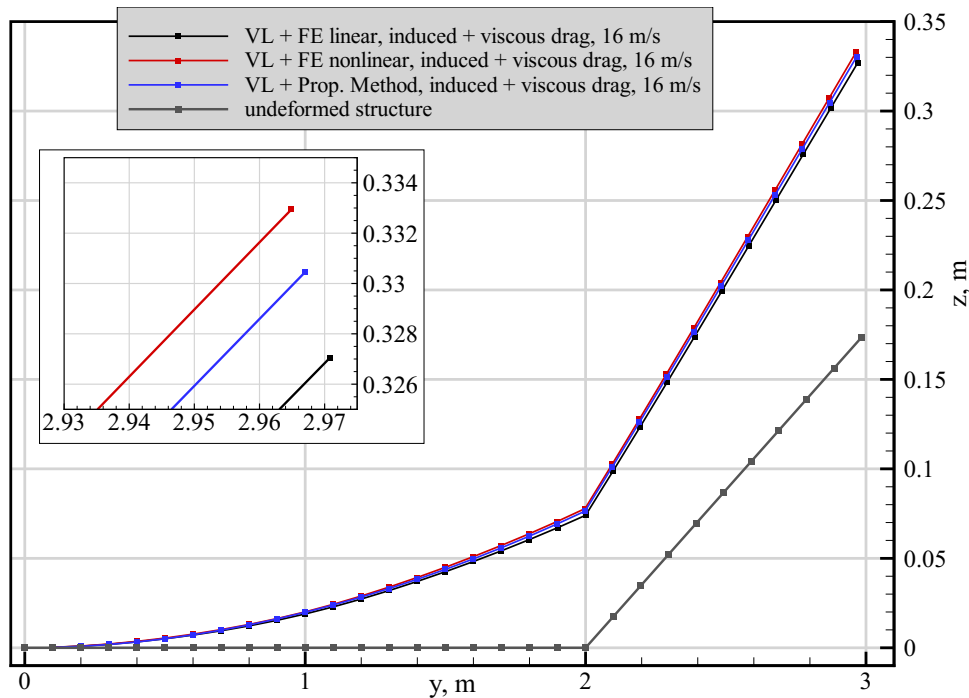


Figure 4.45: Structural deformation of the right wing of the X-HALE for a trim velocity of 16 m/s and three different structural solutions. Both induced and viscous drag forces are included.

An implicit *BDF* scheme of second-order accuracy was used to solve the governing equations of motion (Eq. 2.2.6) in the time domain with a timestep size of 0.005 s. The governing equations define an initial value problem, thus a steady trim simulation was performed for a flight velocity of 16 m/s and the results (AoA, tail deflections, and thrust) prescribed as initial conditions for the unsteady simulations. This approach ensures that no rigid-body or elastic motions are excited within the first time steps of the unsteady simulations, which could result in small drifts or oscillations of rigid-body and elastic degrees of freedom. Only induced drag is included in the unsteady simulations since the viscous drag estimation is only implemented in the steady aeroelastic solver. Time histories of selected elastic and rigid-body DOFs will be shown in the following plots. It must be mentioned that the rigid-body quantities are plotted with respect to the axes of the geodetic and body-fixed frames introduced in Figure 2.8 of Section 2.2. In particular, the z axes of the inertial and the body-fixed system point positive upwards, and the x axes of the body frame points positive from nose to tail.

Validation of Unsteady Tail Input Simulations with UM/NAST Results

Results of a symmetric, sinusoidal rotation of the four outer tails of the X-HALE model are plotted within a time interval from 0 to 13 seconds. The first amplitude of the rotation is one degree with a period of four seconds (one cycle only, no continuous deflection of the

tails). The rotation of the tails is positive at the beginning and then negative, which leads to a maneuver in which the aircraft first pitches downwards and then upwards. The amplitude of the tail rotation is comparatively small and was chosen to obtain results within the linear regime of structural deformations and small rigid-body motions. Selected rigid-body states and structural deformations (in terms of the unsteady displacements of the right wingtip, i.e. without trim deflection) are plotted as function of time in Fig. 4.46. As is expected, only small unsteady structural deflections in the z direction of approximately 1.6% of the semi-span are excited in the nonlinear case by this tail rotation maneuver (7% including the trim deflection). The difference between the proposed method and the linear structural solution in terms of structural deformations is small, the nonlinear solution yields larger displacements. A similar trend is obtained for the rigid-body degrees of freedom. Differences between the methods are hardly noticeable in all states. The end of the tail input at four seconds is recognizable in both the structural deformations and the rigid-body states, mainly in the pitch acceleration, which shows oscillations induced by the short-period mode and the inertial coupling of the elastic and rigid-body modes. Subsequent to the tail input, the phugoid develops which is clearly recognizable in the plots of the airspeed, the altitude, the pitch angle, and the elastic deformations (the frequency is approximately 8.5 seconds). An estimation of the frequencies of the short-period mode and the phugoid of the X-HALE based on stability derivatives is given in Appendix C.

The results of this test case are compared with those from the UM/NAST toolbox in Fig. 4.47 for the unsteady displacements of the right wing in the z and in the y direction as well as for the pitch angle and the location of the aircraft (origin of the body frame) in the geodetic frame (the trim altitude is subtracted since it is arbitrary). Good agreement is obtained for both the elastic and rigid-body degrees of freedom considering that different structural and flight dynamic methods are applied. During the first four seconds of the maneuver, the nonlinear structural deformations calculated by the proposed method are closer to the UM/NAST results than the linear ones but after that time interval the linear deformations agree better with UM/NAST data.

The second unsteady maneuver uses the same type of excitation, but this time the amplitude of the tail deflection is twice as high. All other simulation parameters are kept the same. The results of the nonlinear (proposed method) and structurally linear simulations are shown in Fig. 4.48. Compared to the one degree tail amplitude case, the unsteady nonlinear deformations reach values of approximately 3% (about 9% including trim deflection) with respect to the semi-span. The difference to the results obtained with the linearized structural solution are increased, as are the magnitudes of the other elastic and rigid-body state reactions. However, considerable oscillations of the pitch acceleration occur between two and four seconds. The magnitudes are significantly larger in this period compared to those at the beginning and the end of the (not differentiable) sinusoidal tail input at zero and four seconds. A particular physical reason for these oscillations cannot be determined due to the complex interactions of

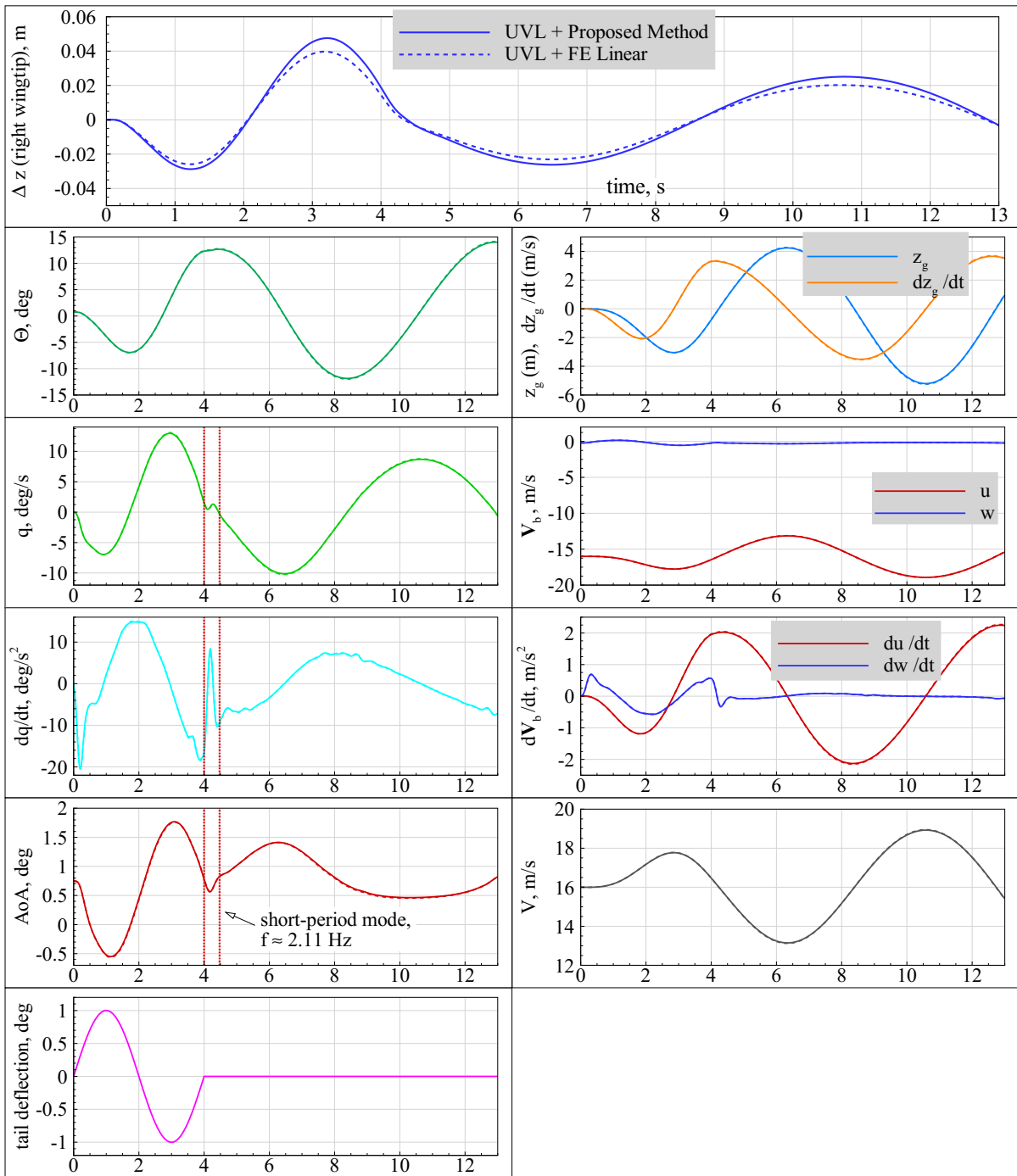


Figure 4.46: Time histories of the elastic and rigid-body responses of symmetric tail input maneuver with tail rotation of one degree (solid lines represent structurally nonlinear, dashed lines linear solutions). The short-period mode and the phugoid develop subsequently to the tail input. Steady trim velocity is 16 m/s.

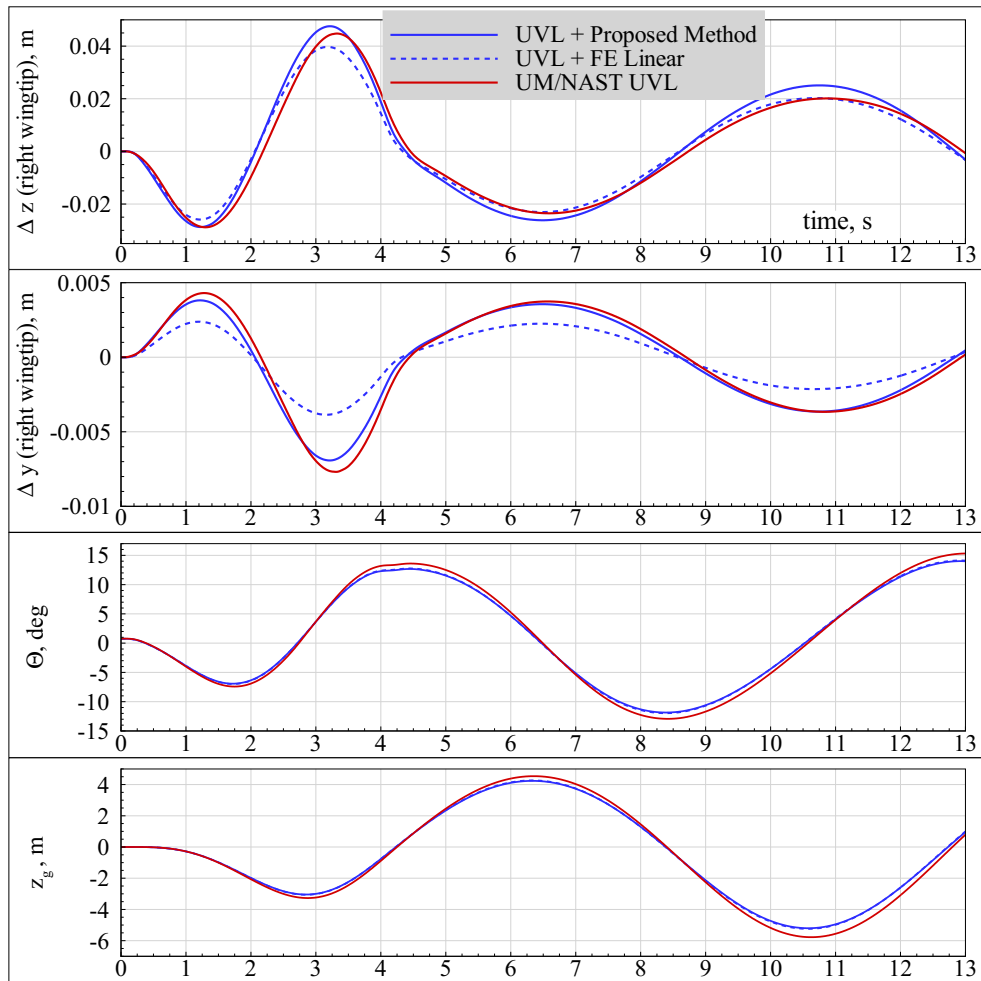


Figure 4.47: Comparison of the responses from the proposed method and UM/NAST in terms of elastic deformation and rigid-body reaction. Amplitude of the tail rotation is one degree.

aerodynamics, flight dynamics, and structural dynamics in this maneuver, but several single reasons (combinations of them are possible as well) can be proposed. Interactions between higher-order structural modes appear possible; furthermore, interactions between the wake of the wing and the tails and fins can lead to discontinuous aerodynamic forces (the high pitch angles during the maneuver lead to multiple crossings of the wake and the tails) which excite large pitch accelerations due to the lever arm of the tails. It must be mentioned that, in addition to the pitch angle, the aircraft encounters a wide range of flight velocities (magnitude shown in the plot at the bottom right in Fig. 4.48) with a minimum of 10 m/s at six seconds and a maximum of 22 m/s at ten and a half seconds. The AoA ranges from -2 to 3 degrees during the maneuver which results in an AoA of the wing of 3 to 8 degrees due to the five degrees wing incidence. Transferring this to a real flight test, it can be assumed that the airfoil just operates in the linear regime, i.e. without stalling, in such a maneuver. The comparison of elas-

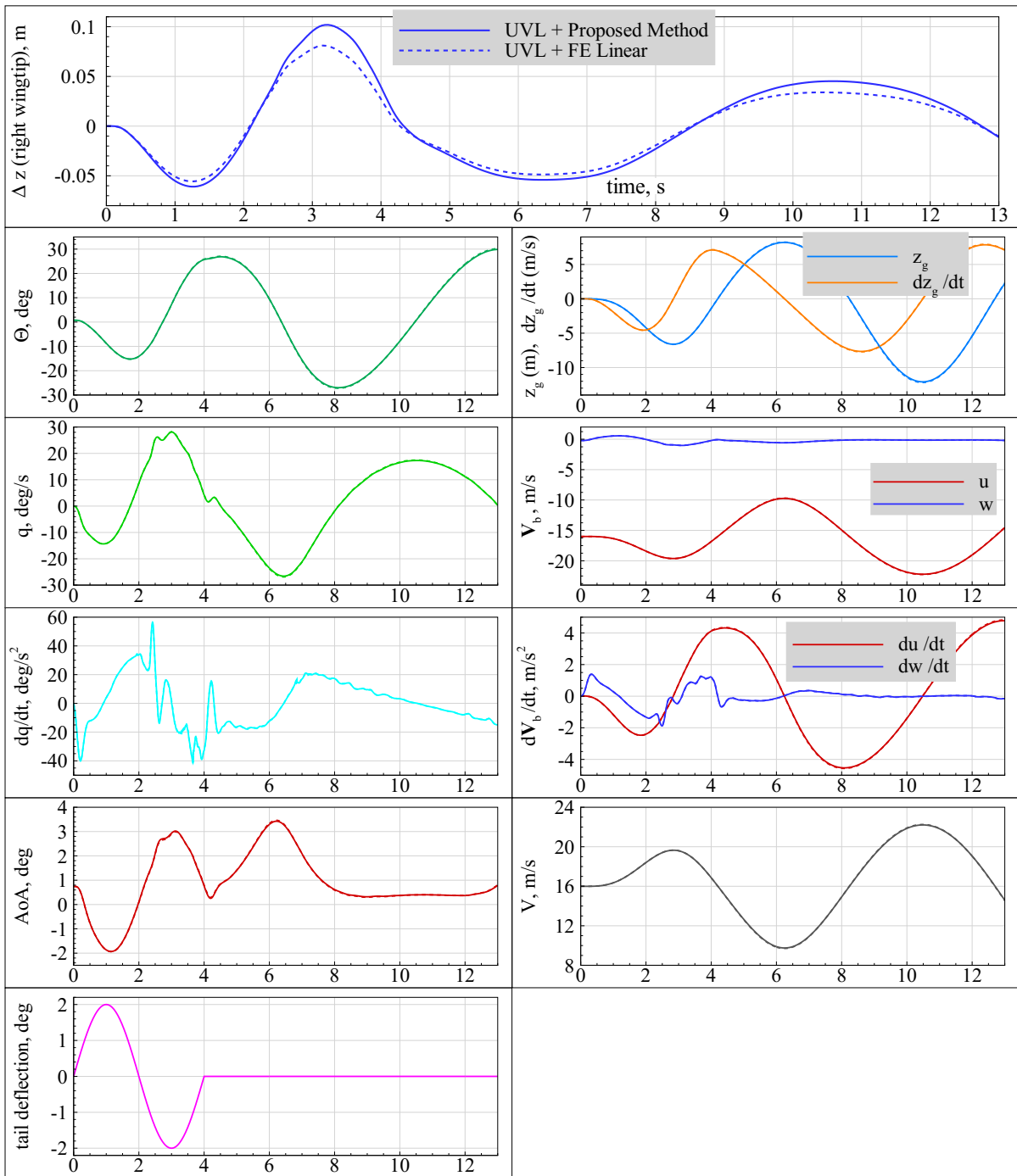


Figure 4.48: Time histories of the elastic and rigid-body responses of symmetric tail input maneuver with tail rotation of two degrees (solid lines represent structurally nonlinear, dashed lines linear solutions). Steady trim velocity is 16 m/s.

tic displacements, pitch angle and altitude with results from UM/NAST is shown in Fig. 4.49. In general, the agreement is good and comparable to the one degree tail amplitude test case,

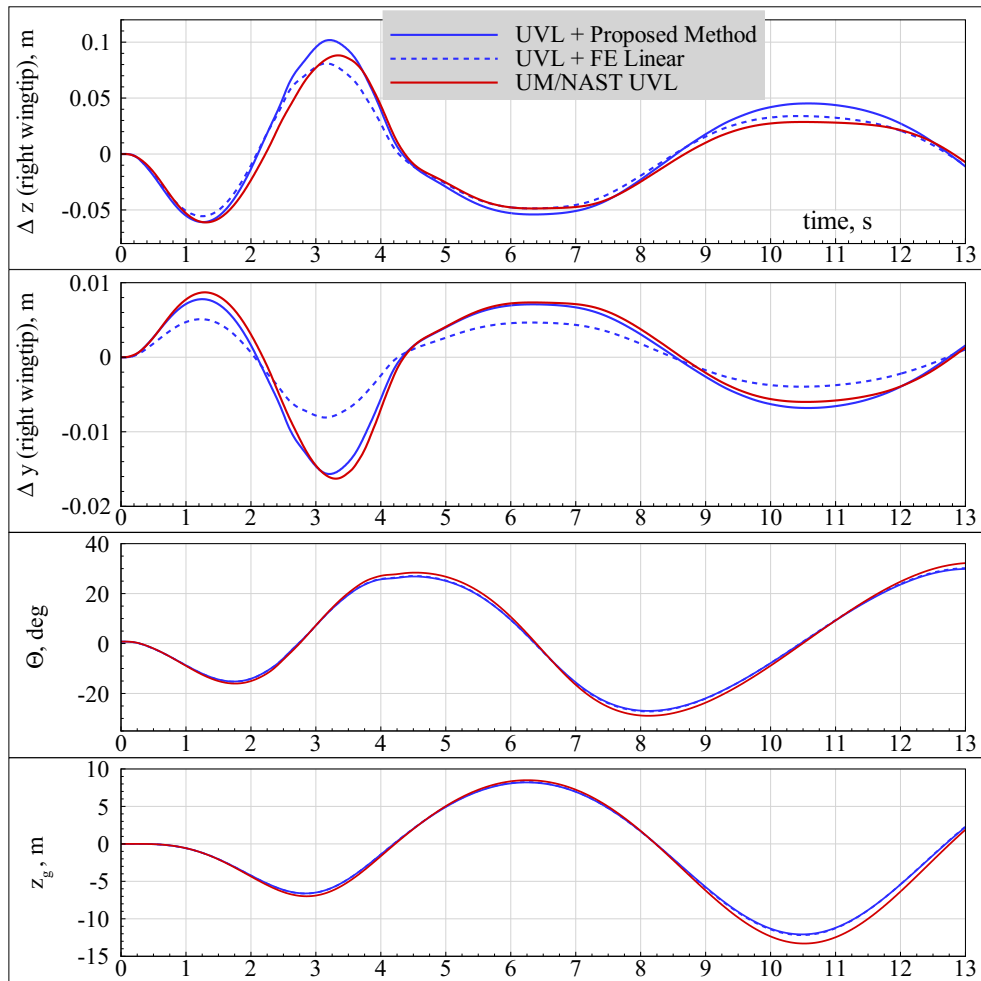


Figure 4.49: Comparison of the responses from the proposed method and UM/NAST in terms of elastic deformation and rigid-body reaction. Amplitude of the tail rotation is two degrees.

especially for the rigid-body data. However, the linear structural deformations in the z direction are a bit closer to the UM/NAST results. Given the deformations from the static coupling validations plotted in Fig. 4.41, which show larger displacements of the UM/NAST results, it appears plausible that also the unsteady deflections in the z direction of the proposed method will be less than those calculated by UM/NAST.

Unsteady DARPA Gust Simulations

The two tail rotation maneuvers were shown and discussed to provide validations for the aeroelastic model and the extended modal approach. Rigid-body responses are much more pronounced whereas the structural dynamic reactions are comparatively low. Unfortunately, a further increase of the tail rotation amplitude leads to very high pitch rates and pitch angles in combination with a largely varying magnitude of the flight speed but structural deforma-

tions remain comparatively low. Thus other types of maneuvers were sought in which large structural deformations but bounded rigid-body motions can be excited. Gust encounter scenarios using specially shaped disturbance velocity profiles are much more suitable to excite large amplitude structural deformations and low rigid-body motions. The *DARPA* gust profile yields parametrized disturbance velocities with *1-cos*-shape in the flight direction and a cosine distribution over the wingspan, as illustrated in Fig. 4.50. The spatial distribution of the gust

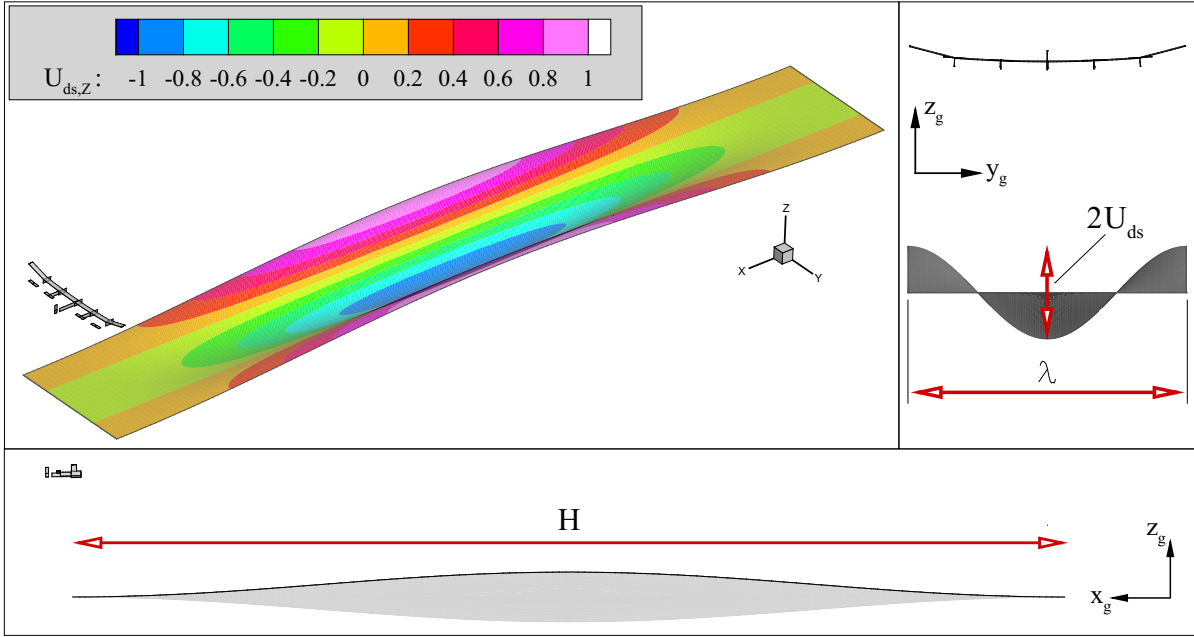


Figure 4.50: Illustration of the DARPA gust with disturbance velocity $U_{ds,Z}$ varying in the flight and in the spanwise direction and defined by parameters λ and H .

disturbance velocity $U_{ds,Z}(x_g, y_g)$ in the z direction of the geodetic frame is defined as:

$$U_{ds,Z}(x_g, y_g) = \frac{1}{2}U_{ds} \left(1 - \cos \left(\frac{2\pi x_g}{H} \right) \right) \cos \left(\frac{\pi y_g}{\lambda} - \phi \right) . \quad (4.5)$$

The parameter H determines the length of the gust in flight direction, λ and ϕ vary the disturbance velocity in the y_g direction. Considering the shape of the gust with respect to the yz -plane displays similarities to the first bending mode shape, thus it can be expected that high generalized forces are generated for that DOF when the aircraft encounters the gust field. For the calculation of the aerodynamic forces, the gust disturbance velocities, which are expressed in the geodetic frame, are transformed into the body-fixed frame using the transformation matrix M_{bg} (Eq. B.6) and become part of the kinematic boundary condition at the collocation points defined by Eq. 3.7.

Two gust scenarios are presented in the following with increasing disturbance velocities. In the first case, U_{ds} is set to -0.5 m/s. The results are plotted in Fig. 4.51 in terms of the unsteady

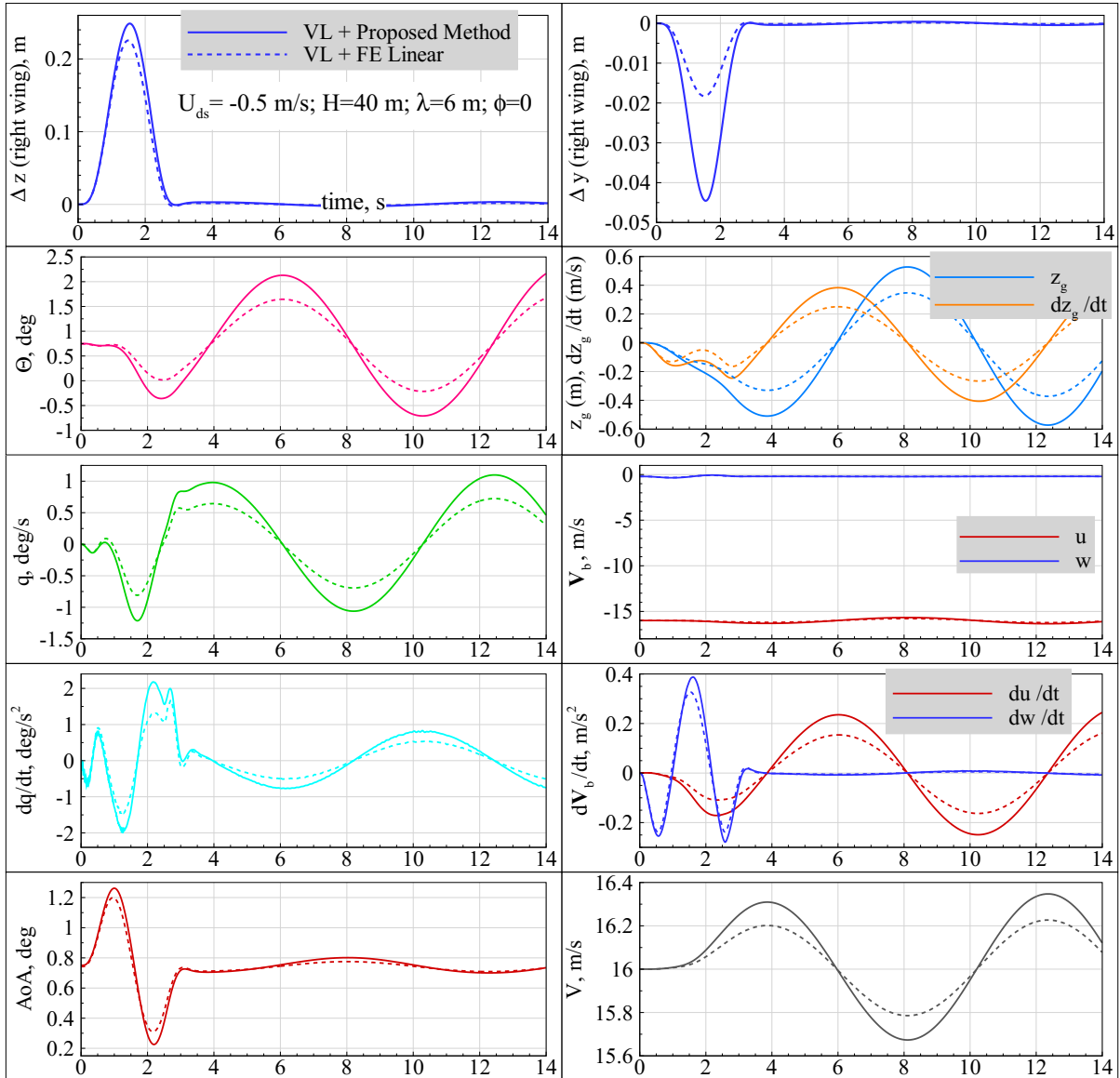


Figure 4.51: Time histories of rigid-body and elastic DOFs of DARPA gust encounter simulation with disturbance velocity in the z_g direction of -0.5 m/s (solid lines represent structurally nonlinear, dashed lines linear solutions). Steady trim velocity is 16 m/s.

displacement of the right wingtip resolved in the body frame as well as selected rigid-body states. Regarding the structural deformation, the selected value of the disturbance velocity yields a maximum normalized deflection in the z direction of approximately 14% semi-span for the proposed method and 12% for the linear FE solution, both values including the static trim deflection. The time histories of the deformations show similar trends for the nonlinear and the linear results, solely the peaks differ in amplitude and (slightly) in phase. Larger differences between the two methods are obtained for the displacements of the wingtip in

the y direction. This effect (larger differences for the displacements in the y than in the z direction) was obtained likewise for the tail input maneuvers. It is interesting to note that the nonlinear deformations in the z direction are higher than the linear ones, similar to the deflections calculated for the steady trim (cf. Fig. 4.43), but opposed to the deformations of the static coupling simulations (cf. Fig. 4.41). The reason for this behavior can be attributed to the lift distribution of the wing which shows significant differences between the clamped (static coupling) and the free-free model (steady trim) because of the different aerodynamic forces acting on the tails. As mentioned in Section 4.3.2, the wings of the X-HALE are characterized by comparatively low torsional stiffness, thus the lift distribution and the associated deformation of the wing are highly dependent on the moments generated by the tails with respect to the elastic axes of the wing.

Increasing the amplitude of the gust disturbance velocity increases the magnitude of the responses of both structural and rigid-body DOFs. Fig. 4.52 shows simulation results for $U_{ds}=1.5$ m/s. For the 1.5 m/s gust encounter, the normalized structural deformation in the z direction reaches approximately 29% semi-span for the nonlinear and 27% for the linear case (including trim deflections), hence clearly in the nonlinear regime. Considering the gust maneuvers with increasing amplitude shows that nonlinear effects (i.e. significant differences between the nonlinear and the linear solution) are pronounced mainly in terms of the displacement of the wingtip in the y direction and the flight mechanic states of the longitudinal motion. For the last scenario with the highest disturbance velocity, both the pitch acceleration and the translational acceleration in the z direction of the body-fixed frame show large differences between nonlinear and linear solution, not only in terms of the amplitude but especially in terms of the frequencies.

As mentioned above, no further validation results are available for the DARPA gust scenarios at this time. However, an important finding of the static coupling, the trim, and the maneuver simulations is that for the X-HALE, the nonlinearities in terms of the elastic structural deflections are more pronounced in the y than in the z direction. Furthermore, the tail input maneuvers showed nearly identical rigid-body reactions for the nonlinear and the linear results – mainly due to the low level of excitation. Unfortunately, increasing the amplitude of the tail deflection leads to large rigid-body reactions with varying air speed but comparatively low structural deformations. The DARPA gust scenario, on the other hand, serves as very good means to enforce large elastic deflections in combination with limited flight mechanic reactions.

For future validations, the simulation of real flight tests in which the pilot commands (recorded by a flight measurement unit) for the control surfaces and the engines are fed into the simulation model is indispensable. This would enable a comprehensive validation of the aeroelastic model and the proposed method. Since discrete gusts are not encountered in real flight and the measurement of e.g. disturbance velocities of turbulent air ahead of the aircraft poses several problems, other ways for the excitation of large structural deformations with limited rigid-body motions must be found. An approach could be the symmetric, but independent

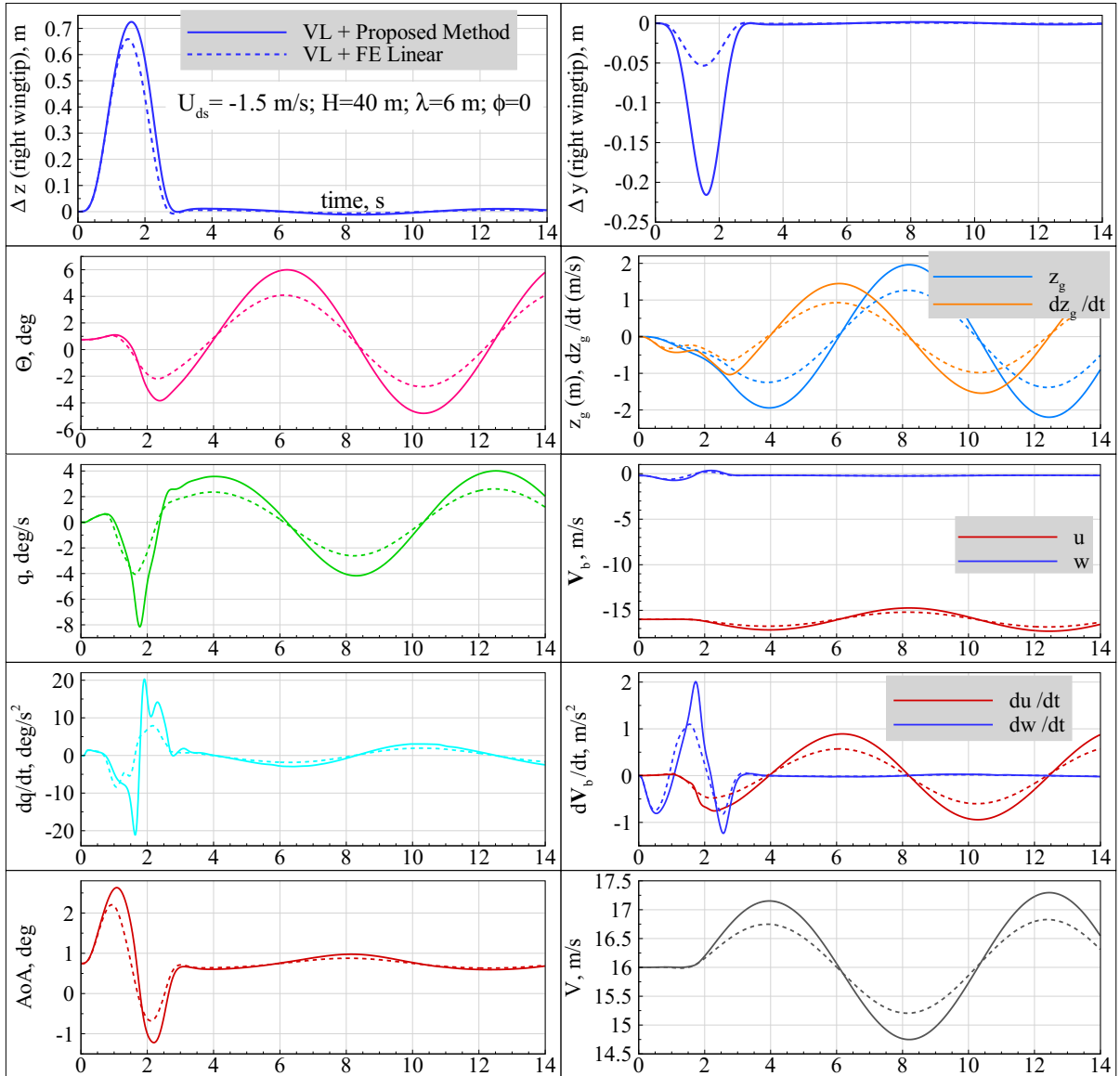


Figure 4.52: Time histories of rigid-body and elastic DOFs of DARPA gust encounter simulation with disturbance velocity in the z_g direction of -1.5 m/s (solid lines represent structurally nonlinear, dashed lines linear solutions). Steady trim velocity is 16 m/s.

actuation of the tails in such a way that the outer tails are generating a force downwards in order to twist the outer section of the wing leading to a locally increased AoA and thus to increased structural deformations.

Chapter 5

Conclusion and Outlook

This chapter summarizes the method proposed in this thesis for the nonlinear aeroelastic modeling of highly flexible aircraft structures. The main scientific contributions of this work and advantages of the method are highlighted; ideas for particular research topics and possible improvements are offered for future activities.

5.1 Summary and Main Conclusions

The goal of this thesis was the development of a method for the nonlinear aeroelastic simulation of highly flexible aircraft structures. The nonlinearities considered evolve from nonlinear load-displacement relations and geometrically nonlinear deformation fields. A modal based method that accounts for these shortcomings by higher-order stiffness and mode components is shown to represent the nonlinearities up to displacements of approximately 25% with respect to the semi-span of a wing. In contrast to the widely used geometrically exact beam theories, the proposed method can be applied to more complex FE models, built for instance from shell elements. A number of nonlinear static FE simulations – performed with a commercial structural solver capable of handling complex FE models – is necessary to calculate the higher-order stiffness and mode components in a preprocessing step. Higher-order polynomials are fitted into the resulting nonlinear strain energies and deformation fields, where the coefficients of the fitted polynomials are directly related to the higher-order stiffness and mode components. A special feature of the proposed method is the linear stiffness term which is a function of the external force field applied to the structure. It was highlighted that this feature is crucial in aeroelastic applications with large deformations since it accounts for the rotation of applied loads, as is the nature of aerodynamic forces. In nonlinear FE analyses, a tangent stiffness matrix is used to account for changes of the stiffness matrix as function of the applied loads and the deformation of the structure. In modal space, the set of the quadratic mode components is the counterpart of the tangent stiffness matrix. A set of inertially coupled EOMs for the free-flying elastic aircraft were derived using Lagrange's equations of the second kind. The higher-order

stiffness terms are used in the expression of the potential energy, the calculation of the nodal displacement field uses the higher-order mode components. No mean axes constraints are applied for the derivation of the EOMs and all gyroscopic and inertial coupling terms between rigid-body and elastic DOFs are kept to enable the use of mode shapes of clamped structural models. This is necessary because the structural solver (MSC Nastran in this case) used for the calculation of the higher-order components requires the model to be clamped in geometrically nonlinear structural simulations.

The proposed method was then combined with a vortex-lattice aerodynamic solver to build an aeroelastic model for the implementation in a program for the numerical simulation. A coupling-model approach with a radial basis function based interpolation method is used for the data exchange between the aerodynamic and the structural model. The program enables static trim and flight dynamic simulations of very flexible aircraft. For the nonlinear time domain simulations, the EOMs are integrated in time using an implicit ODE solver based on a second-order BDF-scheme.

Numerical simulations with three different test cases were introduced to demonstrate the power but also the limits of the proposed method. At first, a cantilever beam, subjected to different kinds of static loading with force fields acting in all spatial directions was analyzed. Depending on the loading applied, the proposed method captures the nonlinear displacement field well compared to the nonlinear reference solutions up to approximately 25% tip displacement with respect to semi-span. It was pointed out that the coupling terms of the individual modes in the higher-order mode components are crucial to correctly reconstruct the displacement field especially if several modes participate in the nodal deformation field. This is in contrast to the classical linear modal approach, where the nodal deformations of the individual modes are superimposed without considering cross-coupling terms. The second test case is the FE model of a more complex wingbox made from shell elements with anisotropic materials. The proposed method shows good agreement to nonlinear reference solutions from Nastran also for this test case with normalized deflections up to approximately 20% of the semi-span. Static coupling simulations were performed in which pronounced differences to the linear simulation results became evident, both in terms of structural displacements and loads. The importance of the force-dependent linear stiffness term in aeroelastic analyses was illustrated by this test case.

The third test case is the 6 meter span X-HALE UAV from the University of Michigan. For this model, the results of static structural response and static coupling simulations showed good agreement with nonlinear reference solutions. The elastic deflections of the model in trimmed, steady straight horizontal flight are comparatively low, approximately 5% tip displacement of the semi-span. Similar results are thus obtained from the nonlinear and the linear simulations. The effect of drag forces on the elastic deformations and the trim parameters was analyzed and showed minor influence. Results of the trim simulations were used as initial conditions for two types of unsteady maneuver simulations. First, sinusoidal tail inputs with tail deflections of one and two degrees were simulated. Second, two gust encounter scenarios were performed with

the DARPA gust profile and two levels of magnitude of the disturbance velocity. The unsteady deformations of the tail input scenarios are low, but differences between the nonlinear and the linearized simulations are noticeable, although the rigid-body results are virtually the same. Validation with UM/NAST results showed good agreement both for the elastic deformations and the rigid-body motions. The DARPA gust profile proved beneficial for the excitation of large structural deformations with low rigid-body reactions. Furthermore, the differences between nonlinear and linear simulation results are significant for this test case. It should be mentioned that in the case of the X-HALE model – and in contrast to the other test cases – the differences between the nonlinear and the linear solutions are larger for the out-of-plane deformations (in the y direction) than for the in-plane deformations (in the z direction).

Based on the results and experience with the three test cases, the proposed method can be seen to provide meaningful results for nonlinear aeroelastic simulations with moderately large deformations, roughly in the order of 25% of the semi-span. The computational costs of this method are only slightly higher than for the classical modal approach. This advantage is of importance particularly for unsteady aeroelastic or flight dynamics simulations. However, the calculation of the higher-order stiffness and mode components requires a series of nonlinear FE simulations and also a careful evaluation of the results. Further unsteady maneuver simulations are essential for the validation of the proposed method, though. Simulations of real flight experiments in which the control surface inputs of the pilot are fed into the numerical simulation should provide an excellent basis for future validations.

5.2 Key Contributions of this Dissertation

The new contributions of this thesis can be summarized as follows:

- Expansion of the linear relation between load and structural displacements given in the classical modal approach. The expansion yields a generalized stiffness term that depends quadratically and cubically on the generalized coordinates.
- Expansion of the linear geometrical relation between modal and nodal (cartesian) space. Higher-order mode components are used to reconstruct the geometrically nonlinear displacement field at large deformations. The modal expansion used in this work includes second, third, and fourth-order terms.
- Calculation of the higher-order stiffness and mode component tensors based on a polynomial fitting approach.
- Introduction of higher-order stiffness and mode components in the flight dynamic EOMs that account for inertially coupled rigid-body and elastic DOFs without using the mean axes assumptions. The inertial coupling is necessary for mode shapes of clamped structural models.

- Implementation of an aeroelastic program for the time-domain simulation of the free-flying highly flexible aircraft based on the proposed method as structural solver and a geometrically nonlinear, unsteady vortex-lattice method.

5.3 Outlook and Future Research

In retrospect, a number of ideas and topics for further research could be identified not only for the proposed method, but also for the aeroelastic program and the test cases. The following items are grouped according to the different sections of the thesis.

Further Improvements and Extensions of the Proposed Method

- Other methods for the excitation of the structure to obtain deformation fields that equal the particular modes can be evaluated. Not only the stiffness matrix, but also the mass matrix can be used for the generation of the corresponding force field (which would then correspond to an inertial loading). This approach is described in literature and used by several researchers mainly for plate-like structures, and an application to the proposed method should be tested.
- Regarding the displacement field of the proposed method near the highest levels of deformation reveals that especially the cubic and the fourth-order mode components emerge significantly because their associated displacements are cubic and fourth-order functions of the generalized coordinates. This drawback could be overcome by limiting the contributions of these terms to the nodal displacement field once a certain level is exceeded.
- The results of nonlinear dynamic simulations with carefully selected force fields could be used to identify possible dependencies of the generalized mass and gyroscopic matrices on the amplitude of deformation and the velocity of deformation. So far, state-dependent mass and gyroscopic matrices have not been considered.
- Higher-order mode components have not been introduced into the flight dynamic EOMs to extend the expressions for the kinetic energy. Only the representation of the nonlinear displacement field is based on the higher-order mode components. By considering these terms, especially the dependency of the tensor of inertia of the aircraft on the structural deformations would be taken into account more accurately.
- Any higher-order mode and stiffness components were derived by Taylor series expansions centered at zero, i.e. with respect to the undeformed and unstressed structure. One advantage of this approach is that the higher-order components can then be used for any steady (trimmed) flight state and unsteady maneuvers. However, deriving the higher-order components for instance about a steady, trimmed flight state (possibly with

large deformations) would have the advantage that even higher deformations could be considered in heavy maneuvers.

Extensions of the Aeroelastic Program

- In order to become an established program for nonlinear aeroelastic simulations, additional features are required. The most important is the possibility to perform stability analysis of the aircraft at a particular (trimmed) state. Therefore, the aerodynamic solver must be linearized to obtain a state-space representation for the unsteady aerodynamic forces. The same must be done for the structural and the fluid-structure coupling part in order to build an integrated simulation model in linear state-space form. Stability analysis for both flight mechanic and aeroelastic DOFs can then be performed by an eigenvalue analysis of the dynamics matrix of the integrated model.
- Considering the kinematical relations used for the flight mechanical calculations, a more general and versatile approach would be the use of quaternions to enable simulations with unbounded angles of orientation of the aircraft with respect to the geodetic system. Thus the implementation of this feature is seen as mandatory for future versions of the software.
- Using a higher-order shape function for the circulation of each aerodynamic panel in the vortex-lattice code can improve both the accuracy of the lift forces and also of the induced drag. Furthermore, computational costs can be reduced because less panels are needed for the same accuracy compared to the current implementation which uses constant circulation for each panel. A further aerodynamic improvement is given by the implementation of the *Vortex Particle Method*, in which the wake is converted into vortex particles shortly behind the lifting surfaces. The advantage is that the vortex particles, which then represent the vorticity of the wake, can be convected arbitrarily with the flow, i.e. they have no connectivity that must be kept. This would be especially suitable for complex configurations with a large number of lifting surfaces and interacting wakes, such as the X-HALE. Also the propeller downwash can be modeled, and the effects of thrust from the propellers can be simulated much more realistically.
- To further validate the proposed method, the implementation of another unsteady nonlinear structural solver in the software is mandatory. For beam-type structural models, either an intrinsic or a strain-based beam formulation would provide appropriate means. Another idea is the development and implementation of a nonlinear inertia relief in combination with the unsteady nonlinear solution capabilities of Nastran (solution sequence SOL 400). Then, also complex 3D FEMs could be used for nonlinear flight dynamics analysis.

Further Applications of the Method

- Rotating structures could serve as interesting test cases for the proposed method. The possibility to account for axial loads which change the eigenvalues of the structure are indispensable for calculating the structural dynamics behavior of e.g. wind turbines or helicopter rotor blades. Modern wind turbines are increasing continuously in size, the slenderness of their rotors provoke large deflections in operation. Additionally, the high centrifugal loading demands the nonlinear calculation of the structural dynamics.
- Complex and detailed transport aircraft FEMs are another field of application. Such an application is not part of this thesis, simply because so far no nonlinear reference solutions for the flight dynamics of such aircraft exist. If such solutions were available, they could provide valuable validation data for the proposed method.
- Additionally, flight dynamics and loads analysis of jet transports operating at transonic Mach numbers require aerodynamic methods able to account for complex geometries and nonlinear flow features caused by compressible and viscous effects. CFD is the preferred method to handle such requirements; combining an appropriate CFD solver with the proposed method yields a comprehensive software for aeroelastic analysis which considers both aerodynamic and structural nonlinearities with a high degree of accuracy.

Appendix A

Matrices of the Nonlinear Flight Dynamics EOMs

A.1 Matrices of the Nonlinear Flight Dynamics EOMs without mean axes assumptions

The mass matrix \overline{M} , the gyroscopic matrix \overline{D} , and the stiffness matrix \overline{K} given in compact matrix notation in Section 2.2.6 are given here in detail with expanded submatrices. To this end, any vector cross products of the governing equations (2.65, 2.66, and 2.69) were converted into matrix-vector products using the skew-symmetric operator.

- The mass matrix \overline{M} defined in Eq.(2.2.6) can be written as:

$$\overline{M} = \begin{bmatrix} m\mathbf{I} & -\widetilde{\mathbf{r}\overline{m}} - {}^p\overline{\Phi}\overline{m}q^p & {}^p\overline{\Phi}\overline{m} \\ \widetilde{\mathbf{r}\overline{m}} + {}^p\overline{\Phi}\overline{m}q^p & \overline{\mathbf{J}} & \mathbf{h}_{pk}q^p + {}^p\overline{\mathbf{r}\Phi}\overline{m} \\ {}^p\overline{\Phi}\overline{m}^T & -(\mathbf{h}_{pk}q^k)^T + {}^p\overline{\mathbf{r}\Phi}\overline{m}^T & M_{pk} \end{bmatrix}. \quad (\text{A.1})$$

- The gyroscopic matrix \overline{D} is given as:

$$\overline{D} = \begin{bmatrix} \mathbf{0} & \widetilde{r\dot{m}\Omega_b} + {}^p\widetilde{\Phi\dot{m}q^p\Omega_b} & \mathbf{0} \\ \widetilde{r\dot{m}\Omega_b} + {}^p\widetilde{\Phi\dot{m}q^p\Omega_b} & \overset{\circ}{\widetilde{J}} - \widetilde{J\Omega_b} - \widetilde{h_{pk}q^p\dot{q}^k} & \mathbf{h_{pk}\dot{q}^p} \\ (\overset{p}{\widetilde{\Phi\dot{m}\Omega_b}})^T & -\widetilde{r\dot{m}V_b} - {}^p\widetilde{\Phi\dot{m}q^pV_b} - {}^p\widetilde{r\dot{m}q^p} & \mathbf{0} \\ (\overset{p}{\widetilde{\Phi\dot{m}\Omega_b}})^T & -2(\widetilde{h_{pk}\dot{q}^k})^T - \frac{1}{2}(\Omega_b^T[\Delta J_p + \Delta^2 J_{pkq^k}])^T & \mathbf{0} \end{bmatrix}. \quad (\text{A.2})$$

- The stiffness matrix \overline{K} contains the linear, quadratic, and cubic stiffness terms as follows:

$$\overline{K} = \begin{bmatrix} \mathbf{0} & \mathbf{0} & \mathbf{0} \\ \mathbf{0} & \mathbf{0} & \mathbf{0} \\ \mathbf{0} & \mathbf{0} & {}^pG_1^k + {}^pG_2^{ki}q_i + {}^pG_3^{kij}q_iq_j \end{bmatrix}. \quad (\text{A.3})$$

A.2 Matrices of the Linearized Flight Dynamics EOMs

Using the practical mean axes assumptions to linearize the nonlinear flight dynamics EOMs (Eq. 2.72 of Section 2.2.7) yields the following expressions for the mass and the gyroscopic matrices.

- The linearized mass matrix is given as:

$$\overline{\mathbf{M}}' = \begin{bmatrix} m\mathbf{I} & \mathbf{0} & \mathbf{0} \\ \mathbf{0} & \overline{\mathbf{J}} & \mathbf{h}_{pk}q^p \\ \mathbf{0} & -(\mathbf{h}_{pk}q^k)^T & M_{kp} \end{bmatrix}. \quad (\text{A.4})$$

- Omitting structural damping, the linearized gyroscopic matrix becomes:

$$\overline{\mathbf{D}}' = \begin{bmatrix} \mathbf{0} & -\widetilde{\mathbf{V}}_b m & \mathbf{0} \\ \mathbf{0} & \overset{\circ}{\mathbf{J}} - \widetilde{\mathbf{J}}\Omega_b - \widetilde{\mathbf{h}}_{pk} q^p \dot{q}^k & \mathbf{h}_{pk} \dot{q}^p \\ \mathbf{0} & -2(\mathbf{h}_{pk} \dot{q}^k)^T - \frac{1}{2}(\Omega_b^T [\Delta \mathbf{J}_p + \Delta^2 \mathbf{J}_{pk} q^k])^T & \mathbf{0} \end{bmatrix}. \quad (\text{A.5})$$

Appendix B

Frames of Reference and Flight Mechanic Matrices

The inertial and the body-fixed coordinate frame, both introduced in Section 2.2.1, will be discussed in more detail here because the orientation of their axes is not conform with those of reference frames typically applied to flight dynamics analyses, such as the *ISO-1151*¹. The reference frames used for the kinematic descriptions in this thesis and the frames described in the ISO-1151 standard are illustrated in Fig. B.1. In particular, the orientation of the x and the z axes is switched in both the inertial and the body-fixed frames of reference. However, the respective axes of the inertial and body-fixed frames are collinear and the z_g and the z_o axis are collinear to the gravity vector. As mentioned, the reason for this axes orientation is the setup and construction of the structural (FE) model, which is typically based on a coordinate system in which the x axis points positive from nose to tail and the z axis points positive upwards. This convention was adopted for the extension of the proposed method by rigid-body DOFs, as detailed in Section 2.2. The choice of the axes has an impact on the representation of the results of the flight dynamics simulations shown in Section 4.3.6 where the time histories of the rigid-body quantities are plotted with respect to the inertial and body-fixed systems indexed by g and b , respectively. It should be mentioned that the rotation matrices $M_{b\Phi}$ and M_{bg} , as well as the AoA and the angle of sideslip (depicted in the following) take identical forms in the (g, b) - and in the (o, f) -frames.

As mentioned in Section 3.3, definitions for useful flight mechanic states and rotation matrices derived from vector \mathbf{X} (Eq. 2.74) are given in the following for the sake of completeness. All quantities are defined with respect to the (g, b) -frame. The states comprise the airspeed V

¹<https://www.iso.org/standard/5699.html>

(measured at the origin of the body-fixed frame), as well as the AoA and the angle of sideslip, denoted as α and β , respectively [73]:

$$V = \|\mathbf{V}_b\| = \sqrt{u^2 + v^2 + w^2} , \quad (\text{B.1})$$

$$\alpha = \arctan\left(\frac{w}{u}\right) , \quad (\text{B.2})$$

$$\beta = \arcsin\left(\frac{v}{V}\right) . \quad (\text{B.3})$$

The relation between the time derivative of the Euler angles and the rotational rates of the body frame is given by a differential equation with matrix $M_{b\Phi}$:

$$\dot{\underline{\Phi}} = M_{b\Phi}^{-1} \underline{\Omega}_b .$$

The set of Euler angles is not an explicit quantity of the equations of motion, it is obtained as time integral of its time derivative:

$$\underline{\Phi} = \int \dot{\underline{\Phi}} dt + \underline{\Phi}^0 , \quad (\text{B.4})$$

where $\underline{\Phi}^0$ denotes the initial attitude of the body-fixed frame with respect to the geodetic frame (this includes, for instance, the trim states). Similar, a differential equation relates the time derivative of the position vector of the airframe (\mathbf{P}_g) in the geodetic frame with the vector of the translational velocities of the body frame, \mathbf{V}_b :

$$\dot{\mathbf{P}}_g = M_{bg}^T \mathbf{V}_b .$$

The location of the body-fixed frame, resolved in the inertial frame, is given as the following time integral:

$$\mathbf{P}_g = \int \dot{\mathbf{P}}_g dt + \mathbf{P}_g^0 , \quad (\text{B.5})$$

where \mathbf{P}_g^0 denotes the initial location of the origin of the body-fixed frame in the geodetic frame. The orthogonal rotation matrix M_{bg} is given as [73]:

$$M_{bg} = \begin{bmatrix} \cos \Psi \cos \Theta & \sin \Psi \cos \Theta & -\sin \Theta \\ \cos \Psi \sin \Theta \sin \Phi - \sin \Psi \cos \Phi & \sin \Psi \sin \Theta \sin \Phi + \cos \Psi \cos \Phi & \cos \Theta \sin \Phi \\ \cos \Psi \sin \Theta \cos \Phi - \sin \Psi \sin \Phi & \sin \Psi \sin \Theta \cos \Phi + \cos \Psi \sin \Phi & \cos \Theta \cos \Phi \end{bmatrix} . \quad (\text{B.6})$$

Matrix $M_{b\Phi}$ is given as [73]:

$$M_{b\Phi} = \begin{bmatrix} 1 & 0 & -\sin \Theta \\ 0 & \cos \Phi & \sin \Phi \cos \Theta \\ 0 & -\sin \Phi & \cos \Phi \cos \Theta \end{bmatrix}. \quad (\text{B.7})$$

Note that this is not an orthogonal matrix because the rotational axes of the Euler angles do not define an orthogonal coordinate system. The inverse of $M_{b\Phi}$ is given as [73]:

$$M_{b\Phi}^{-1} = \begin{bmatrix} 1 & \sin \Phi \tan \Theta & \cos \Phi \tan \Theta \\ 0 & \cos \Phi & -\sin \Phi \\ 0 & \frac{\sin \Phi}{\cos \Theta} & \frac{\cos \Phi}{\cos \Theta} \end{bmatrix}. \quad (\text{B.8})$$

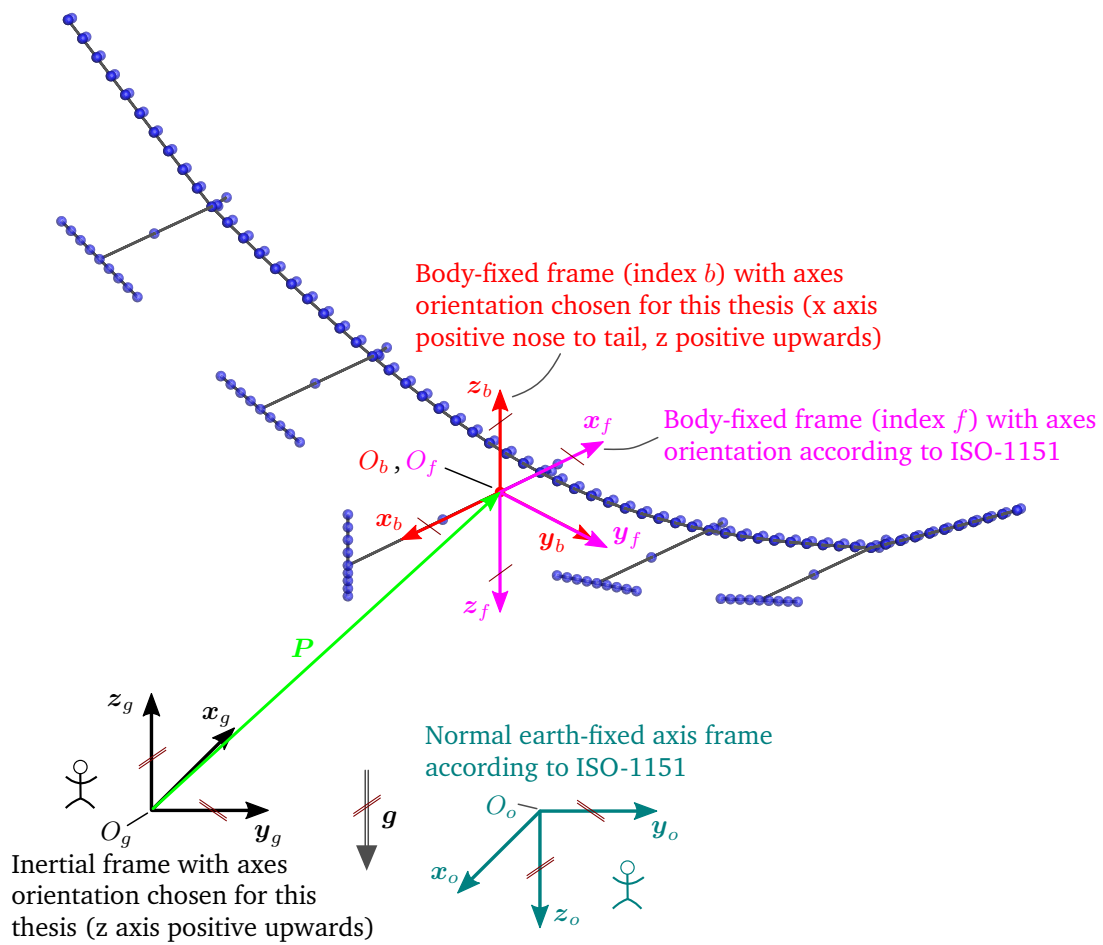


Figure B.1: Two Inertial (geodetic) and body-fixed frames with different axes orientations. The axes of the inertial frame indexed g and the body-fixed frame indexed b are oriented for convenience (in contrast to the ISO-1151 standard).

Appendix C

Longitudinal Dynamics of the X-HALE

The simulations of longitudinal maneuvers of the X-HALE shown in Section 4.3.6 use a prescribed tail input or an external disturbance (gust) to excite unsteady motions. Subsequent to the end of the tail input or the gust, the longitudinal dynamics of the aircraft evolve in terms of the short-period and the phugoid motion. These distinctive eigenmodes can be identified, for instance, from the time histories of particular rigid-body DOFs plotted in Fig. 4.46. The fast and well-damped short-period mode can be recognized by means of the pitch rate (and its time derivative), and, of course, the AoA. This mode is more pronounced in the tail input maneuvers than in the gust encounter scenarios, though. The slow and weakly damped phugoid is easily recognizable from the structural deformations, the pitch angle, and the airspeed. The frequencies of these modes will be calculated in the following based on aerodynamic and structural properties of the aircraft and the approximations given by Brockhaus [73]. For the short-period mode, the frequency (in rad/s) can be calculated as:

$$\omega_{0,SP} \approx \sqrt{Z_\alpha M_q - M_\alpha} \quad , \quad (\text{C.1})$$

where the normalized quantities that characterize the longitudinal motion are given as follows [73]:

$$Z_\alpha = -\bar{q} \frac{S}{mV_0} [C_{L\alpha} + C_{D0} + \alpha_0 C_{D\alpha}] \quad , \quad (\text{C.2a})$$

$$M_q = \bar{q} \frac{S\bar{c}}{J_y} \frac{\bar{c}}{V_0} [C_{mq} + C_{m\dot{\alpha}}] \quad , \quad (\text{C.2b})$$

$$M_\alpha = \bar{q} \frac{S\bar{c}}{J_y} C_{m\alpha} \quad . \quad (\text{C.2c})$$

The expression for $\omega_{0,SP}$ can be simplified by neglecting the derivatives with respect to drag (their values are small compared to $C_{L\alpha}$) and the $C_{m\dot{\alpha}}$ derivative, which is small compared to C_{mq} . Table C.1 lists the stability derivatives $C_{L\alpha}$, C_{mq} , and $C_{m\alpha}$ calculated by the steady vortex-lattice solver described in Section 3. The frequency and period of the short-period mode

of the X-HALE can then be estimated using the reference quantities V_0 , ρ , S , m , \bar{c} , and J_y listed in Table 4.3 and the derivatives from Table C.1. An estimation for the frequency of the phugoid motion is given by a simple expression which uses the flight velocity and the magnitude of the gravity vector as parameters [73]:

$$\omega_{0,P} \approx \sqrt{2} \frac{g}{V_0} . \quad (\text{C.3})$$

Table C.2 lists the estimated frequencies and periods for the short-period and the phugoid of the X-HALE.

Table C.1: Selected longitudinal stability derivatives of the X-HALE.

Derivative	Value
$C_{L\alpha}$	6.3026
C_{mq}	-16.5278
$C_{m\alpha}$	-1.7426

Table C.2: Short-period mode and phugoid of the X-HALE.

Data	Unit	Value
$f_{0,SP}$	Hz	≈ 2.1095
$T_{0,SP}$	s	≈ 0.4741
$f_{0,P}$	Hz	≈ 0.1380
$T_{0,P}$	s	≈ 7.2488

The short-period mode develops subsequently to the end of the tail input, as marked in the plots of the pitch rate, the pitch acceleration, and the AoA in Fig. 4.46. Also the phugoid can be identified well in several plots of the elastic and the rigid-body DOFs in the same figure. The estimated frequency of the short-period mode agrees well with the frequency that can be identified from the time history of the pitch acceleration, for instance. Considering the lowest frequencies of the elastic structural modes shows that an interaction of the rigid-body dynamics in terms of the short-period mode and the lowest elastic modes must be expected. However, a slight difference is obtained between the estimated frequency of the phugoid and the frequency that can be read from the plots (approximately 8.5 seconds).

Appendix D

Properties of the Cantilever Beam Test Case

The structural properties of the 16 m beam testcase (Fig. 4.1) introduced in Section 4.1 are given here as reference. The geometrical data (e.g. sectional moments of inertia) and mass properties are chosen to yield a homogeneous curvature of the bending line of the beam for typical aerodynamic loads (with elliptical distribution). The beam was modeled for MSC Nastran using *CBEAM* elements with beam properties defined by *PBEAM* cards [18]. This beam element can be used to model tapered beams and is the preferred beam element type for geometrically nonlinear analysis. The *id* and the location of the FE nodes in the Nastran frame of reference are listed in Table D.1.

The geometric properties I_{zz} (moment of inertia for bending in the *xy*-plane), I_{xx} (moment of inertia for bending in the *xz*-plane), and J (moment of inertia for torsion around the *y*-axis) of the cross-sections at the FE nodes are listed in Table D.2 (the values of J are identical to those of I_{zz}). The sectional area of 0.008 m^2 is constant along the span of the beam. The Young's modulus of the material is $7.1 \cdot 10^{10} \text{ N/m}^2$, the shear modulus is $2.67 \cdot 10^{10} \text{ N/m}^2$, and the density is 800 kg/m^3 . Additional discrete mass elements (Nastran *CONM2* elements) are used to tune the structural dynamic properties of the beam, they are listed in Table D.3.

Table D.1: Node ids and locations (with respect to the Nastran basic coordinate system) of the nodes of the beam test case FE model introduced in Section 4.1.

Node	Global id	Location (x, y, z)
1	1	0.35, 0.0, 0.0
2	2	0.35, 0.5, 0.0
3	3	0.35, 1.0, 0.0
4	4	0.35, 1.5, 0.0
5	5	0.35, 2.0, 0.0
6	6	0.35, 2.5, 0.0
7	7	0.35, 3.0, 0.0
8	8	0.35, 3.5, 0.0
9	9	0.35, 4.0, 0.0
10	10	0.35, 4.5, 0.0
11	11	0.35, 5.0, 0.0
12	12	0.35, 5.5, 0.0
13	13	0.35, 6.0, 0.0
14	14	0.35, 6.5, 0.0
15	15	0.35, 7.0, 0.0
16	16	0.35, 7.5, 0.0
17	17	0.35, 8.0, 0.0
18	18	0.35, 8.5, 0.0
19	19	0.35, 9.0, 0.0
20	20	0.35, 9.5, 0.0
21	21	0.35, 10., 0.0
22	22	0.35, 10.5, 0.0
23	23	0.35, 11.0, 0.0
24	24	0.35, 11.5, 0.0
25	25	0.35, 12.0, 0.0
26	26	0.35, 12.5, 0.0
27	27	0.35, 13.0, 0.0
28	28	0.35, 13.5, 0.0
29	29	0.35, 14.0, 0.0
30	30	0.35, 14.5, 0.0
31	31	0.35, 15.0, 0.0
32	32	0.35, 15.5, 0.0
33	33	0.35, 16.0, 0.0

Table D.2: Moments of inertia of the cross-sections of the beam test case FE model.

Node	I_{zz}, m^4	I_{xx}, m^4	J, m^4
1	$1.1106 \cdot 10^4$	$2.7765 \cdot 10^5$	$1.1106 \cdot 10^4$
2	$1.0445 \cdot 10^4$	$2.6112 \cdot 10^5$	$1.0445 \cdot 10^4$
3	$9.8054 \cdot 10^5$	$2.4514 \cdot 10^5$	$9.8054 \cdot 10^5$
4	$9.1884 \cdot 10^5$	$2.2971 \cdot 10^5$	$9.1884 \cdot 10^5$
5	$8.5936 \cdot 10^5$	$2.1484 \cdot 10^5$	$8.5936 \cdot 10^5$
6	$8.0210 \cdot 10^5$	$2.0053 \cdot 10^5$	$8.0210 \cdot 10^5$
7	$7.4706 \cdot 10^5$	$1.8677 \cdot 10^5$	$7.4706 \cdot 10^5$
8	$6.9424 \cdot 10^5$	$1.7356 \cdot 10^5$	$6.9424 \cdot 10^5$
9	$6.4364 \cdot 10^5$	$1.6091 \cdot 10^5$	$6.4364 \cdot 10^5$
10	$5.9527 \cdot 10^5$	$1.4882 \cdot 10^5$	$5.9527 \cdot 10^5$
11	$5.4911 \cdot 10^5$	$1.3728 \cdot 10^5$	$5.4911 \cdot 10^5$
12	$5.0517 \cdot 10^5$	$1.2629 \cdot 10^5$	$5.0517 \cdot 10^5$
13	$4.6346 \cdot 10^5$	$1.1586 \cdot 10^5$	$4.6346 \cdot 10^5$
14	$4.2396 \cdot 10^5$	$1.0599 \cdot 10^5$	$4.2396 \cdot 10^5$
15	$3.8669 \cdot 10^5$	$9.6673 \cdot 10^6$	$3.8669 \cdot 10^5$
16	$3.5164 \cdot 10^5$	$8.7910 \cdot 10^6$	$3.5164 \cdot 10^5$
17	$3.1881 \cdot 10^5$	$7.9702 \cdot 10^6$	$3.1881 \cdot 10^5$
18	$2.8820 \cdot 10^5$	$7.2049 \cdot 10^6$	$2.8820 \cdot 10^5$
19	$2.5981 \cdot 10^5$	$6.4951 \cdot 10^6$	$2.5981 \cdot 10^5$
21	$2.0969 \cdot 10^5$	$5.2422 \cdot 10^6$	$2.0969 \cdot 10^5$
22	$1.8796 \cdot 10^5$	$4.6990 \cdot 10^6$	$1.8796 \cdot 10^5$
23	$1.6845 \cdot 10^5$	$4.2113 \cdot 10^6$	$1.6845 \cdot 10^5$
24	$1.5117 \cdot 10^5$	$3.7792 \cdot 10^6$	$1.5117 \cdot 10^5$
25	$1.3610 \cdot 10^5$	$3.4026 \cdot 10^6$	$1.3610 \cdot 10^5$
26	$1.2326 \cdot 10^5$	$3.0814 \cdot 10^6$	$1.2326 \cdot 10^5$
27	$1.1263 \cdot 10^5$	$2.8159 \cdot 10^6$	$1.1263 \cdot 10^5$
28	$1.0423 \cdot 10^5$	$2.6058 \cdot 10^6$	$1.0423 \cdot 10^5$
29	$9.8049 \cdot 10^6$	$2.4512 \cdot 10^6$	$9.8049 \cdot 10^6$
30	$9.4088 \cdot 10^6$	$2.3522 \cdot 10^6$	$9.4088 \cdot 10^6$
31	$9.2348 \cdot 10^6$	$2.3087 \cdot 10^6$	$9.2348 \cdot 10^6$
32	$9.2828 \cdot 10^6$	$2.3207 \cdot 10^6$	$9.2828 \cdot 10^6$
33	$9.5530 \cdot 10^6$	$2.3882 \cdot 10^6$	$9.5530 \cdot 10^6$

Table D.3: Properties of concentrated masses defined at particular nodes of the beam test case FE model.

Assigned to node	m, kg	I_{22} , kg·m ²
2	5.0000	0.20000
3	4.9697	0.19879
4	4.9394	0.19758
5	4.9091	0.19636
6	4.8788	0.19515
7	4.8485	0.19394
8	4.8182	0.19273
9	4.7879	0.19152
10	4.7576	0.19030
11	4.7273	0.18909
12	4.6970	0.18788
13	4.6667	0.18667
14	4.6364	0.18545
15	4.6061	0.18424
16	4.5758	0.18303
17	4.5455	0.18182
18	4.5152	0.18061
19	4.4848	0.17939
20	4.4545	0.17818
21	4.4242	0.17697
22	4.3939	0.17576
23	4.3636	0.17455
24	4.3333	0.17333
25	4.3030	0.17212
26	4.2727	0.17091
27	4.2424	0.16970
28	4.2121	0.16848
29	4.1818	0.16727
30	4.1515	0.16606
31	4.1212	0.16485
32	4.0909	0.16364
33	4.0606	0.16242

Bibliography

- [1] Cesnik, C. E. S., Senatore, P. J., Su, W., Atkins, E. M., and Shearer, C. M., “X-HALE: A Very Flexible Unmanned Aerial Vehicle for Nonlinear Aeroelastic Tests,” *AIAA Journal*, Vol. 50, No. 12, Dec 2012, pp. 2820–2833.
- [2] Noll, T. E., Brown, J. M., Perez-Davis, M. E., Ishmael, S. D., and Tiffany, G. C., *Investigation of the Helios Prototype Aircraft Mishap - Volume I Mishap Report*, CreateSpace Independent Publishing Platform, 2012.
- [3] Patil, M. J., Hodges, D. H., and Cesnik, C. E. S., “Nonlinear Aeroelasticity and Flight Dynamics of High-Altitude Long-Endurance Aircraft,” *Journal of Aircraft*, Vol. 38, No. 1, Jan 2001, pp. 88–94.
- [4] Shearer, C. M. and Cesnik, C. E. S., “Nonlinear Flight Dynamics of Very Flexible Aircraft,” *Journal of Aircraft*, Vol. 44, No. 5, Sep 2007, pp. 1528–1545.
- [5] Palacios, R., Murua, J., and Cook, R., “Structural and Aerodynamic Models in Nonlinear Flight Dynamics of Very Flexible Aircraft,” *AIAA Journal*, Vol. 48, No. 11, Nov 2010, pp. 2648–2659.
- [6] Kroll, N. et al., “DLR Project Digital-X: towards virtual aircraft design and flight testing based on high-fidelity methods,” *CEAS Aeronautical Journal*, Vol. 7, No. 1, 2016, pp. 3–27.
- [7] Weigold, W., Stickan, B., Travieso-Alvarez, I., Kaiser, C., and Teufel, P., *Linearized Unsteady CFD for Gust Loads with TAU - IFASD 2017*, International Forum on Aeroelasticity and Structural Dynamics, Como, Italy, 2017.
- [8] Etkin, B., *Dynamics of Atmospheric Flight*, Dover Books on Aeronautical Engineering, Dover Publications, 2012, Unabridged republication of the work originally published by John Wiley and Sons, Inc., New York, in 1972.
- [9] Waszak, M. R. and Schmidt, D. K., “Flight Dynamics of Aeroelastic Vehicles,” *Journal of Aircraft*, Vol. 25, No. 6, Jun 1988, pp. 563–571.

- [10] Buttrill, C., Arbuckle, P., and Zeiler, T., *Nonlinear Simulation of a Flexible Aircraft in Maneuvering Flight*, Guidance, Navigation, and Control and Co-located Conferences, American Institute of Aeronautics and Astronautics, Monterey, California, Aug 1987.
- [11] Reimer, L., Ritter, M., Heinrich, R., and Krüger, W., *CFD-based Gust Load Analysis for a Free-flying Flexible Passenger Aircraft in Comparison to a DLM-based Approach*, 22nd AIAA Computational Fluid Dynamics Conference, American Institute of Aeronautics and Astronautics, Dallas, Texas, Jun 2015.
- [12] Su, W. and Cesnik, C. E. S., *Strain-Based Analysis for Geometrically Nonlinear Beams: A Modal Approach*, 53rd AIAA/ASME/ASCE/AHS/ASC Structures, Structural Dynamics and Materials Conference, Honolulu, Hawaii, April 2013.
- [13] Bathe, K. and Zimmermann, P., *Finite-Elemente-Methoden*, Springer, 2002.
- [14] MSC, *MSC Nastran 2017 Nonlinear User's Guide SOL 400*, MacNeal-Schwendler Corporation, 2014.
- [15] Felippa, C. A. and Haugen, B., "Unified Formulation of Small-Strain Corotational Finite Elements: I. Theory," *Computer Methods in Applied Mechanics and Engineering*, Vol. 194, June 2005, pp. 2285–2335.
- [16] Schwertassek, R. and Wallrapp, O., *Dynamik flexibler Mehrkörpersysteme: Methoden der Mechanik zum rechnergestützten Entwurf und zur Analyse mechatronischer Systeme*, Grundlagen und Fortschritte der Ingenieurwissenschaften, Vieweg+Teubner Verlag, 1999.
- [17] Wallrapp, O., "Review of Past Developments in Multibody System Dynamics at DLR - From FADYNA to SIMPACK," *Vehicle System Dynamics*, Vol. 41, No. 5, 2004, pp. 339–348.
- [18] MSC, *MSC Nastran 2012 Quick Reference Guide*, MacNeal-Schwendler Corporation, 2011.
- [19] Palacios, R., "Nonlinear normal modes in an intrinsic theory of anisotropic beams," *Journal of Sound and Vibration*, Vol. 330, No. 8, Apr 2011, pp. 1772 – 1792.
- [20] Jones, J. and Cesnik, C. E. S., *Nonlinear Aeroelastic Analysis of the X-56 Multi-Utility Aeroelastic Demonstrator*, 15th Dynamics Specialists Conference, San Diego, California, Jan 2016.
- [21] Muravyov, A., Turner, T., Robinson, J., and Rizzi, S., *A new Stochastic Equivalent Linearization Implementation for Prediction of Geometrically Nonlinear Vibrations*, 40th Structures, Structural Dynamics, and Materials Conference and Exhibit, St. Louis, Missouri, Apr 1999.

- [22] Muravyov, A. A. and Rizzi, S. A., "Determination of nonlinear stiffness with application to random vibration of geometrically nonlinear structures," *Computers and Structures*, Vol. 81, No. 15, 2003, pp. 1513 – 1523.
- [23] Mignolet, M. P., Przekop, A., Rizzi, S. A., and Spottswood, S. M., "A review of indirect/non-intrusive reduced order modeling of nonlinear geometric structures," *Journal of Sound and Vibration*, Vol. 332, No. 10, May 2013, pp. 2437 – 2460.
- [24] Kim, K., Radu, A. G., Wang, X. Q., and Mignolet, M. P., "Nonlinear reduced order modeling of isotropic and functionally graded plates," *International Journal of Non-Linear Mechanics*, Vol. 49, 2013, pp. 100 – 110.
- [25] Wang, X. Q., Perez, R. A., and Mignolet, M. P., *Nonlinear Reduced Order Modeling of Complex Wing Models*, 54th AIAA/ASME/ASCE/AHS/ASC Structures, Structural Dynamics, and Materials Conference, Boston, Massachusetts, Apr 2013.
- [26] Medeiros, R. R., Cesnik, C. E. S., and Coetzee, E. B., *Modal Formulation for Geometrically Nonlinear Structural Dynamics*, International Forum on Aeroelasticity and Structural Dynamics, Como, Italy, 2017.
- [27] Kerschen, G., Peeters, M., Golinval, J., and Vakakis, A., "Nonlinear normal modes, Part I: A useful framework for the structural dynamicist," *Mechanical Systems and Signal Processing*, Vol. 23, No. 1, 2009, pp. 170 – 194, Special Issue: Non-linear Structural Dynamics.
- [28] Kuether, R. J. and Allen, M. S., *Nonlinear Modal Substructuring of Systems with Geometric Nonlinearities*, Structures, Structural Dynamics, and Materials and Co-located Conferences, 54th AIAA/ASME/ASCE/AHS/ASC Structures, Structural Dynamics, and Materials Conference, Boston, Massachusetts, Apr 2013.
- [29] Kuether, R. J. and Allen, M. S., *Substructuring with Nonlinear Reduced Order Models and Interface Reduction with Characteristic Constraint Modes*, AIAA SciTech, 55th AIAA/ASME/ASCE/AHS/ASC Structures, Structural Dynamics, and Materials Conference, National Harbor, Maryland, Jan 2014.
- [30] Kuether, R. J., Deaner, B. J., Hollkamp, J. J., and Allen, M. S., "Evaluation of Geometrically Nonlinear Reduced-Order Models with Nonlinear Normal Modes," *AIAA Journal*, Vol. 53, No. 11, Nov 2015, pp. 3273–3285.
- [31] Segalman, D. J. and Dohrmann, C. R., "Dynamics of Rotating flexible Structures by a Method of Quadratic Modes," Sandia National Laboratories, Structural Dynamics Division, Albuquerque, New Mexico, 1990.

- [32] Segalman, D. J. and Dohrmann, C. R., "A Method for Calculating the Dynamics of Rotating Flexible Structures, Part 1: Derivation," *Journal of Vibration and Acoustics*, Vol. 118, No. 3, Jul 1996, pp. 313–317.
- [33] Segalman, D. J., Dohrmann, C. R., and Slavin, A. M., "A Method for Calculating the Dynamics of Rotating Flexible Structures, Part 2: Example Calculations," *Journal of Vibration and Acoustics*, Vol. 118, No. 3, Jul 1996, pp. 318–322.
- [34] Robinett, R. D., Feddema, J., Eisler, G. R., Dohrmann, C., Parker, G. G., Wilson, D. G., and Stokes, D., "The Method of Quadratic Modes," *Flexible Robot Dynamics and Controls*, Vol. 19, IFSR International Series on Systems Science and Engineering, 2002.
- [35] van Zyl, L. H., Sutherland, A. N., and Rossouw, P. S., *Parabolic Mode Shapes: What they are, where to get them and what to do with them*, International Forum on Aeroelasticity and Structural Dynamics, Seattle, Washington, 2009.
- [36] van Zyl, L. H. and Mathews, E. H., "Quadratic Mode Shape Components From Linear Finite Element Analysis," *ASME Journal of Vibration and Acoustics*, Vol. 134, No. 1, Dec 2011.
- [37] Farao, J. C., Malan, A. G., and Gambioli, F., *Towards a Non-linear Full Aircraft Model for Passenger Aircraft Loads Calculations*, International Forum on Aeroelasticity and Structural Dynamics, Como, Italy, 2017.
- [38] Wallrapp, O., "Standardization of Flexible Body Modeling in Multibody System Codes, Part I: Definition of Standard Input Data," *Mechanics of Structures and Machines*, Vol. 22, No. 3, 1994, pp. 283–304.
- [39] Wallrapp, O. and Wiedemann, S., "Comparison of Results in Flexible Multibody Dynamics Using Various Approaches," *Nonlinear Dynamics*, Vol. 34, No. 1, 2003, pp. 189–206.
- [40] ZONA Technology, *ZAERO Theoretical Manual Version 8.4*, ZONA Technology Inc., 2011.
- [41] Meirovitch, L. and Tuzcu, I., "The Lure of the Mean Axes," *Journal of Applied Mechanics*, Vol. 74, No. 3, Apr 2006, pp. 497–504.
- [42] Ritter, M., *Nonlinear Numerical Flight Dynamics of Flexible Aircraft in the Time Domain by Coupling of CFD, Flight Mechanics, and Structural Mechanics*, New Results in Numerical and Experimental Fluid Mechanics VIII: Contributions to the 17th STAB/DGLR Symposium Berlin, Germany 2010, Springer Berlin Heidelberg, 2013, pp. 339–347.
- [43] Silvestre, F. J. and Luckner, R., "Experimental Validation of a Flight Simulation Model for Slightly Flexible Aircraft," *AIAA Journal*, Vol. 53, No. 12, Dec 2015, pp. 3620–3636.

- [44] Murua, J., Palacios, R., and Graham, J. M. R., "Applications of the unsteady vortex-lattice method in aircraft aeroelasticity and flight dynamics," *Progress in Aerospace Sciences*, Vol. 55, 2012, pp. 46 – 72.
- [45] Milne, R., *Dynamics of the Deformable Aeroplane, Parts I and II*, Aeronautical Research Council, 1964, Technical Report R&M 3345, London: Her Majesty's Stationery Office.
- [46] Bisplinghoff, R. and Ashley, H., *Principles of Aeroelasticity*, Dover Books on Aeronautical Engineering, Dover Publications, 2002, Unabridged, corrected republication of the edition published by John Wiley and Sons, Inc., New York, 1962.
- [47] Reschke, C., *Integrated Flight Loads Modelling and Analysis for Flexible Transport Aircraft*, Dissertation, Universität Stuttgart, 2006.
- [48] Milne, R., "Some Remarks on the Dynamics of Deformable Bodies," *AIAA Journal*, Vol. 6, No. 3, March 1968, pp. 556–558.
- [49] Waszak, M. R. and Schmidt, D. K., *On the Flight Dynamics of Aeroelastic Vehicles*, Astrodynamics Conference, Fluid Dynamics and Co-located Conferences, Williamsburg, Virginia, Aug 1986.
- [50] Waszak, M. R., Buttrill, C., and Schmidt, D. K., "Modeling and Model Simplification of Aeroelastic Vehicles: An Overview," *NASA Technical Memorandum 107691*, September 1992.
- [51] Meirovitch, L., "Hybrid State Equations of Motion for Flexible Bodies in Terms of Quasi-Coordinates," *Journal of Guidance, Control, and Dynamics*, Vol. 14, No. 5, Sep 1991, pp. 1008–1013.
- [52] Reschke, C., *Flight Loads Analysis with Inertially Coupled Equations of Motion*, Guidance, Navigation, and Control and Co-located Conferences, San Francisco, California, Aug 2005.
- [53] Looye, G., *Integrated Flight Mechanics and Aeroelastic Aircraft Modeling using Object-Oriented Modeling Techniques*, Guidance, Navigation, and Control and Co-located Conferences, Portland, Oregon, Aug 1999.
- [54] Meirovitch, L. and Tuzcu, I., *Time Simulations of the Response of Maneuvering Flexible Aircraft*, 44th AIAA/ASME/ASCE/AHS/ASC Structures, Structural Dynamics, and Materials Conference, Norfolk, Virginia, Apr 2003.
- [55] Meirovitch, L. and Tuzcu, I., *Integrated Approach to the Dynamics and Control of Maneuvering Flexible Aircraft*, NASA, 2003, NASA Technical Report CR-2003-211748.

- [56] Kier, T., *Comparison of Unsteady Aerodynamic Modelling Methodologies with Respect to Flight Loads Analysis*, Guidance, Navigation, and Control and Co-located Conferences, San Francisco, California, Aug 2005.
- [57] Silvestre, F. J. and Luckner, R., *Integrated Model for the Flight Mechanics of a Flexible Aircraft in the Time Domain*, International Forum on Aeroelasticity and Structural Dynamics, Seattle, Washington, 2009.
- [58] Mauermann, T., *Flexible Aircraft Modelling with Application to Flight Loads Analysis of Wake Vortex Encounters*, Dissertation, Technische Universität Carolo-Wilhelmina zu Braunschweig, 2010.
- [59] Ritter, M. and Dillinger, J., *Nonlinear numerical flight dynamics for the prediction of maneuver loads*, 15th International Forum on Aeroelasticity and Structural Dynamics, Paris, France, 2011.
- [60] Drela, M., *Integrated Simulation Model for Preliminary Aerodynamic, Structural, and Control-Law Design of Aircraft*, 40th Structures, Structural Dynamics, and Materials Conference and Exhibit, St. Louis, Missouri, Apr 1999.
- [61] Cesnik, C. and Su, W., *Nonlinear Aeroelastic Modeling and Analysis of Fully Flexible Aircraft*, 46th AIAA/ASME/ASCE/AHS/ASC Structures, Structural Dynamics and Materials Conference, Austin, Texas, Apr 2005.
- [62] Su, W. and S. Cesnik, C. E., “Dynamic Response of Highly Flexible Flying Wings,” *AIAA Journal*, Vol. 49, No. 2, Feb 2011, pp. 324–339.
- [63] Su, W. and Cesnik, C. E. S., “Nonlinear Aeroelasticity of a Very Flexible Blended-Wing-Body Aircraft,” *Journal of Aircraft*, Vol. 47, No. 5, Sep 2010, pp. 1539–1553.
- [64] Teixeira, P. and Cesnik, C. E. S., *Inclusion of Propeller Effects on Aeroelastic Behavior of Very Flexible Aircraft*, International Forum on Aeroelasticity and Structural Dynamics, Como, Italy, 2017.
- [65] Palacios, R. and Epureanu, B., *An Intrinsic Description of the Nonlinear Aeroelasticity of Very Flexible Wings*, 52nd AIAA/ASME/ASCE/AHS/ASC Structures, Structural Dynamics and Materials Conference, Denver, Colorado, Apr 2011.
- [66] Murua, J., *Flexible Aircraft Dynamics with a Geometrically-Nonlinear Description of the Unsteady Aerodynamics*, Dissertation, Imperial College London, Department of Aeronautics, 2012.
- [67] Howcroft, C. et al., *Aeroelastic Modelling of Highly Flexible Wings*, 15th Dynamics Specialists Conference, San Diego, California, Jan 2016.

- [68] Krüger, W. R., *Multibody Dynamics for the Coupling of Aeroelasticity and Flight Mechanics of Highly Flexible Structures*, International Forum on Aeroelasticity and Structural Dynamics, Stockholm, Sweden, 2007.
- [69] Castellani, M., Cooper, J. E., and Lemmens, Y., “Nonlinear Static Aeroelasticity of High-Aspect-Ratio-Wing Aircraft by Finite Element and Multibody Methods,” *Journal of Aircraft*, Vol. 54, No. 2, Mar 2017, pp. 548–560.
- [70] Shames, I. H. and Dym, C. L., *Energy and Finite Element Methods in Structural Mechanics*, Hemisphere Publishing Corporation, 1985.
- [71] Washizu, K., *Variational Methods in Elasticity and Plasticity*, Vol. 9, Pergamon Press Ltd., 2nd ed., 1975.
- [72] Meirovitch, L., *Methods of analytical dynamics*, Advanced engineering series, McGraw-Hill, 1970.
- [73] Brockhaus, R., *Flugregelung*, Springer Berlin Heidelberg, 2013.
- [74] Goldstein, H., *Classical Mechanics*, Addison-Wesley series in physics, Addison-Wesley Publishing Company, 1980.
- [75] Bronstein, I., Semendjajew, K., Musiol, G., and Mühlig, H., *Taschenbuch der Mathematik*, Verlag Harri Deutsch, 2001.
- [76] Katz, J. and Plotkin, A., *Low-Speed Aerodynamics*, Cambridge Aerospace Series, Cambridge University Press, 2001.
- [77] Horstmann, K.-H., “Ein Mehrfach-Traglinienverfahren und seine Verwendung für Entwurf und Nachrechnung nichtplanarer Flügelanordnungen,” 1987, DFVLR, Institut für Entwurfsaerodynamik, Braunschweig.
- [78] Selig, M., *Summary of low speed airfoil data Vol. 1*, SoarTech Publications, 1995.
- [79] Ritter, M., Dillinger, J., and Meddaikar, Y. M., *Static and Dynamic Aeroelastic Validation of a Flexible Forward Swept Composite Wing*, 58th AIAA/ASCE/AHS/ASC Structures, Structural Dynamics, and Materials Conference, Grapevine, Texas, Jan 2017.
- [80] Beckert, A. and Wendland, H., “Multivariate interpolation for fluid-structure-interaction problems using radial basis functions,” *Aerospace Science and Technology*, Vol. 5, No. 2, 2001, pp. 125 – 134.
- [81] Ritter, M., Cesnik, C. E. S., and Krüger, W. R., *An Enhanced Modal Approach for Large Deformation Modeling of Wing-Like Structures*, 56th AIAA/ASCE/AHS/ASC Structures, Structural Dynamics, and Materials Conference, Kissimmee, Florida, Jan 2017.

-
- [82] Ritter, M. and Cesnik, C. E. S., *Large Deformation Modeling of a Beam Type Structure and a 3D Wingbox using an Enhanced Modal Approach*, 57th AIAA/ASCE/AHS/ASC Structures, Structural Dynamics, and Materials Conference, San Diego, California, Jan 2016.
- [83] Klimmek, T., *Parameterization of Topology and Geometry for the Multidisciplinary Optimization of Wing Structures*, Proceedings of CEAS European Air and Space Conference (CEAS2009), Manchester, UK, Oct 2009.
- [84] Ritter, M., Cesnik, C. E. S., and Jones, J., *Enhanced Modal Approach for Free-flight Nonlinear Aeroelastic Simulation of Very Flexible Aircraft*, 15th Dynamics Specialists Conference, San Diego, California, Jan 2016.
- [85] Ritter, M., Jones, J., and Cesnik, C. E. S., *Free-flight Nonlinear Aeroelastic Simulations of the X-HALE UAV by an Extended Modal Approach*, International Forum on Aeroelasticity and Structural Dynamics, Como, Italy, 2017.
- [86] Ritter, M., Teixeira, P. C., and Cesnik, C. E. S., *Comparison of Nonlinear Aeroelastic Methods for Maneuver Simulation of Very Flexible Aircraft*, AIAA/ASCE/AHS/ASC Structures, Structural Dynamics, and Materials Conference, Kissimmee, Florida, Jan 2018.
- [87] Cesnik, C. E. S., Palacios, R., and Reichenbach, E. Y., "Reexamined Structural Design Procedures for Very Flexible Aircraft," *Journal of Aircraft*, Vol. 51, No. 5, 2014, pp. 1580–1591.